

# **Development of MAS solid state NMR methods for structural and dynamical characterization of biomolecules**

Dissertation

zur Erlangung des akademischen Grades  
doctor rerum naturalium  
(Dr. rer. nat.)  
im Fach Biophysik

eingereicht an der  
Mathematisch-Naturwissenschaftlichen Fakultät I  
der Humboldt-Universität zu Berlin

von  
Herrn Veniamin Shevelkov

Präsident der Humboldt-Universität zu Berlin  
Prof. Dr. Christoph Marksches

Dekan der Mathematisch-Naturwissenschaftlichen Fakultät I  
Prof. Dr. Christian Limberg

Gutachter:

1. Prof. Dr. Klaus Peter Hofmann
2. Prof. Dr. Bernd Reif
3. Prof. Dr. Andreas Herrmann

Tag der mündlichen Prüfung: 22. April 2008



## ***Contents.***

<i>Acknowledgements.....</i>	<i>6</i>
<i>List of publications:.....</i>	<i>8</i>
<i>Abbreviations: .....</i>	<i>10</i>
<i>1 Chapter. General Introduction.....</i>	<i>11</i>
<b>1.1 Structural and dynamical investigations of biological systems by solid-state NMR spectroscopy. ....</b>	<b>11</b>
<b>1.2 Distances and angles in proteins and peptides.....</b>	<b>12</b>
<b>1.3 The dynamics of a quantum mechanical systems.....</b>	<b>16</b>
<b>1.4 Density operator. ....</b>	<b>18</b>
<b>1.5 The nuclear spin and NMR spectroscopy. ....</b>	<b>18</b>
<b>1.6 Spin one half in a static field.....</b>	<b>20</b>
<b>1.7 Operator algebra. ....</b>	<b>20</b>
<b>1.8 The nuclear spin Hamiltonian in the static field. ....</b>	<b>22</b>
<b>1.9 Spherical representation of the spin Hamiltonian.....</b>	<b>24</b>
<b>1.10 Reference frames and magic angle spinning in solid state NMR.....</b>	<b>25</b>
<b>1.11 Interaction frame.....</b>	<b>27</b>
<b>1.12 Average Hamiltonian theory. ....</b>	<b>29</b>
<b>1.13 Basic solid state NMR techniques. ....</b>	<b>29</b>
<b>1.14 Overview of the thesis. ....</b>	<b>36</b>
<i>2 Chapter. Proton detection in MAS solid state NMR of proteins. ...</i>	<i>38</i>

2.1	Introduction. ....	38
2.2	Sample preparation and NMR spectroscopy. ....	40
2.3	<sup>1</sup> H Detection in MAS ssNMR spectroscopy of proteins employing Pulsed Field Gradients for residual solvent suppression. ....	40
2.4	Ultra-high resolution in proton solid-state NMR at high levels of deuteration. ....	44
2.5	Conclusion. ....	51
3	<i>Chapter. Transverse relaxation optimized spectroscopy in MAS solid-state NMR of proteins. ....</i>	<i>52</i>
3.1	Introduction. ....	52
3.2	Experimental section. ....	54
3.3	Experimental results. ....	56
4	<i>Chapter. Quantitative analysis of backbone dynamics in microcrystalline sample of the SH3 domain of <math>\alpha</math>-spectrin by MAS solid-state NMR. ....</i>	<i>72</i>
4.1	Introduction. ....	72
4.2	Experimental section. ....	73
4.3	Theoretical background. ....	78
4.4	Experimental results. ....	81
4.5	Simulated results and discussions. ....	95
5	<i>Chapter. Detection of water molecules in a microcrystalline sample of the SH3 domain of <math>\alpha</math>-spectrin by MAS solid-state NMR. ....</i>	<i>105</i>
5.1	Introduction. ....	105
5.2	Materials and solid state NMR methods. ....	107



5.3	Results.....	108
5.4	Discussion. ....	114
6	<i>Chapter. Resolution enhancement in MAS solid-state NMR by application of <math>^{13}\text{C}</math> homonuclear scalar decoupling during acquisition. ....</i>	<i>124</i>
6.1	Introduction. ....	124
6.2	Experimental.....	126
6.3	Results and discussion.....	128
	<b>References:</b> .....	136
	<i>Appendix 1.1. Simulation of <math>^{15}\text{N}</math> peaks ratio. ....</i>	<i>155</i>
	<i>Appendix 2.1. Simulation of <math>^{15}\text{N}</math> line width. ....</i>	<i>158</i>
	<i>Appendix 2.2 Experimental values for <math>T_1</math>, <math>T_2</math> and <math>\eta</math> for SH3. ....</i>	<i>160</i>
	<i>Appendix 2.3 SIMPSON input file to extract <math>^{15}\text{N}</math>-<math>^1\text{H}</math> dipolar coupling values. ....</i>	<i>165</i>
	<i>Appendix 2.4. Fitting results for <math>^{15}\text{N}</math>-<math>^1\text{H}</math> dipolar coupling values.....</i>	<i>167</i>
	<i>Appendix 2.5 C++ code to fit correlation parameters. ....</i>	<i>169</i>
	<i>Appendix 2.6. Simulated results for motional parameters. ....</i>	<i>175</i>
	<i>Summary.....</i>	<i>178</i>
	<i>Zusammenfassung.....</i>	<i>180</i>

## *Acknowledgements.*

This research work was carried out under supervision of Prof. Dr. Bernd Reif at Department Chemie, Technische Universität München, from March 2002 to March 2003 and at the Leibniz-Institut für Molekulare Pharmakologie (FMP-Berlin) from April 2003 to June 2007. I would like to express my deepest gratitude to the people who supported and helped me during my doctoral research.

Firstly, I would like to thank my supervisor Prof. Dr. Bernd Reif. For his encouragement and support, which were invaluable all the time. His scientific guidance and fruitful ideas were base for my successful research work. Numerous interesting and stimulating discussions formed my scientific views and were a key point for my results. His trust and concerns on me allowed to keep my own scientific freedom and opinion. I thank him for excellent scientific environment and perfect working conditions.

A special thanks to Dr. Anne Diehl and Kristina Rehbein for preparing all SH3 samples used in my work. Without this collaboration many results of my research would not be possible.

Thanks to Prof. Dr. Horst Kessler for the perfect NMR facilities in München.

I am grateful to Prof. Dr. Hartmut Oschkinat for the state of art NMR facilities and for good scientific cooperation.

Thanks to Dr. Barth Jan van Rossum for help and guidance in struggling with NMR hardware problems, for scientific cooperation, helpful discussions and cheerful mood.

I thank Dr. Frank Eisenmenger for time and efforts he spend for tutorial and help in respect of computer's soft- and hardware.

Thanks to all former and current members of Bernd's group, for your help, support and just nice time. Jing and Sarav were persons who made friendly atmosphere in the group where I came. Thanks Maggy, Vipin, Juan Miguel and Rasmus also for solid state NMR discussions. My officemates Tomas and Rasmus for pleasant working and personal

atmosphere. Thanks to Murali, Mangesh, Katja, Uwe, Po and Stefan for good and interesting contacts.

I am also thankful for people in Hartmut's group, especially in solid state NMR division. I have to single out Stefan Jehle for scientific contacts.

Veniamin Shevelkov, Berlin June 2007.

### *List of publications:*

This thesis is based on the following papers and reviews:

1. Chevelkov V., Rossum B.J.v., Castellani F., Rehbein K., Diehl A., Hohwy M., Steuernagel S., Engelke F., Oschkinat H. and Reif B., *H-1 detection in MAS solid-state NMR Spectroscopy of biomacromolecules employing pulsed field gradients for residual solvent suppression*. Journal of the American Chemical Society (2003) Vol 125, pp 7788-7789.
2. Chevelkov V., Faelber K., Diehl A., Heinemann U., Oschkinat H. and Reif B., *Detection of Water Molecules in a polycrystalline sample of a chicken  $\alpha$ -spectrin SH3 domain*. Journal of Biomolecular NMR (2005) Vol 31, pp 295-310.
3. Chevelkov V., Chen Z.J., Bermel W. and Reif B., *Resolution enhancement in MAS solid-state NMR by application of C-13 homonuclear scalar decoupling during acquisition*. Journal of Magnetic resonance (2005) Vol 172, pp 56-62.
4. Chevelkov V., Rehbein K., Diehl A. and Reif B., *Ultrahigh resolution in proton solid-state NMR spectroscopy at high levels of deuteration*. Angewandte Chemie-International Edition (2006) Vol 45, pp 3878-3881.
5. Hologne M., Chevelkov V. and Reif B., *Deuterated peptides and proteins in MAS solid-state NMR*. Progress in Nuclear Magnetic Resonance Spectroscopy (2006) Vol 48, pp 211-232.
6. Chevelkov V. and Reif B., *TROSY type experiments in solid state MAS NMR*. Concepts in magnetic resonance Part A (2007), submitted.
7. Chevelkov V., Faelber K., Schrey A., Rehbein K., Diehl A. and Reif B., *Differential line broadening in MAS solid-state NMR due to dynamic interference*. Journal of the American Chemical Society (2007), in press.
8. Chevelkov V., Diehl A., Skrynnikov N. and Reif B., *Measurement of Differential  $^{15}\text{N}$ - $^1\text{H}$   $T_2$  Relaxation Times in a Perdeuterated Protein by MAS Solid-State NMR Spectroscopy*. Journal of the American Chemical Society (2007), submitted.

9. Chevelkov V., Diehl A. and Reif B., *Quantitative analysis of backbone dynamics in microcrystalline sample of the SH3 domain of  $\alpha$ -spectrin by MAS solid-state NMR*. Journal of Magnetic Resonance (2007), in preparation.

Further publications:

10. Magin I.M., Shevel'kov V., Obynochny A.A., Kruppa A.I. and Leshina T.V., *CIDNP study of the third spin effect on the singlet-triplet evolution in radical pairs*. Chemical Physics Letters (2002) Vol 357, pp 351-357.
11. Chevelkov V., Zhuravleva A.V., Reif B. and Skrynnikov N.R., *Combined analysis of  $^{15}\text{N}$  relaxation data from solid- and solution-state NMR*. Journal of the American Chemical Society (2007), submitted.

*Abbreviations:*

1D, 2D, 3D	one dimensional, two dimensional, three dimensional
CP	Cross Polarization
CSA	Chemical Shift Anisotropy
CW	Continuous Wave
FSLG	Frequency Switched Lee-Goldburg
HMQC	Heteronuclear Multiple Quantum Correlation
HSQC	Heteronuclear Single Quantum Correlation
Hz	Hertz
INEPT	Insensitive Nuclei Enhanced by Polarization Transfer
MAS	Magic Angle Spinning
ms	Millisecond, $10^{-3}$ , s
NMR	Nuclear Magnetic Resonance
ns	Nanosecond, $10^{-9}$ , s
PDSD	Proton Driven Spin Diffusion
PMLG	Phase Modulated Lee-Goldburg
ppm	Part Per Million
ps	Picosecond, $10^{-12}$ , s
RMSD	Root Mean Square Deviation
TPPM	Two-Pulse Phase Modulation
$\mu$ s	Microsecond, $10^{-6}$ , s

## *1 Chapter. General Introduction.*

### **1.1 Structural and dynamical investigations of biological systems by solid-state NMR spectroscopy.**

Understanding the mechanism how biological systems work is an important objective of current structural biology. Nuclear magnetic resonance (NMR) spectroscopy is a well suited technique to approach these goals and to study structure and dynamics of biomolecules.

The vast majority of protein's structures has been produced by X-ray crystallographic spectroscopy which is the leading technique, providing slightly higher audacity comparatively to NMR. Comparison of both methods has been done recently [1,2]. For attaining a high resolution structure X-ray technique requires well ordered 3D single crystals. Crystal growth is a time consuming procedure which is the major limitation of the technique.

Solution state NMR probes not only structure but also dynamic of biological systems, which gives complimentary information for understanding functionality of proteins.

Membrane proteins are 25-30% fraction of the genomes of mammals and they are of high importance playing a critical role in the cell, being involved in many processes as channels, pumps, receptors. The structure of only a few membrane proteins have been elucidated so far despite strong efforts. Production of membrane proteins in sufficient amounts is quite difficult. In addition, most of them are resistant to crystallization and are inherently not soluble, which is a major obstacle for X-ray and solution state NMR. Solid state NMR (ssNMR) is the method of choice for structural and dynamic characterization of membrane proteins and aggregated amyloid systems, which have lack in solubility and crystallization.

Access to high field ssNMR instruments, methodological advancements, isotope labeling techniques significantly assisted the rapid progress of ssNMR over the last few

years which resulted in complete structure elucidation of several peptides and small proteins [3,4,5,6], characterization of protein complex formation [4] and characterization dynamic properties of small proteins [7,8].

## **1.2 Distances and angles in proteins and peptides.**

Proteins and peptides are biopolymers composed of amino acid residues interlinked by amide bonds. Their structure can be discussed in terms of four levels of complexity defined as follows:

**Primary structure** denotes the amino acid sequence, and indicates the constitution of a protein.

**Secondary Structure** is the local structure which is typically recognized by specific backbone torsion angles and specific mainchain hydrogen bond pairings.

**Tertiary Structure** is the folding of the total chain, the arrangement of the elements of the secondary structure linked by turns and loops. Its stability is determined by non-bonding interactions and disulfide bonds.

**Quaternary Structure** is the combination of two or more chains, to form a complete unit. The interactions between the chains are not different from those in tertiary structure, but are distinguished only by being interchain rather than intrachain.

Figure 1.2.1 shows all 4 structural classes in proteins:



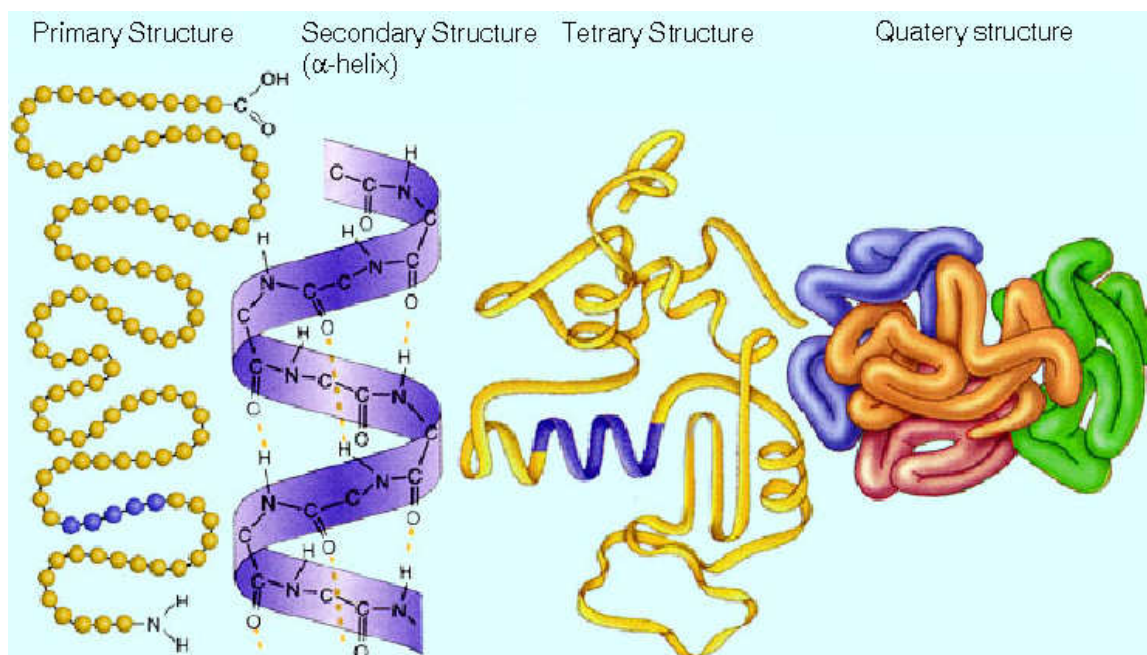


Figure 1.2.1. Schematic representation of primary, secondary, tertiary and quaternary structure of a protein.

In terms of the accuracy of protein structure determinations, all bond lengths are invariant. Bond angles are also essentially invariant. Only dihedral angles  $\phi$  around the  $\text{CO-N-C}^{\alpha}\text{-CO}$  bond and  $\psi$  around the  $\text{N-C}^{\alpha}\text{-CO-N}$  bond are the origin of variability in protein conformation. They are given by Figure 1.2.2.

The secondary structure of a segment of the polypeptide chain is the local spatial arrangement of its main-chain atoms without regard to the conformation of its side chains or to its relationship with other segments (IUPAC-IUB, 1970). There are three common secondary structures in proteins, namely alpha-helices, beta-sheets and turns. Secondary structure elements which cannot be classified as one of the standard three classes are usually grouped into a category called "other" or "random coil". This last designation is unfortunate as no portion of a protein three dimensional structure is truly random and it is not a coil either. Regular secondary structure conformations in segments of a polypeptide chain occur when all the  $\phi$  bond angles in that polypeptide segment are equal to each other, and all the  $\psi$  bond angles are equal. The rotational angles for  $\psi$  and  $\phi$  bonds for common regular secondary structures are shown in the table 1.2.1 below:

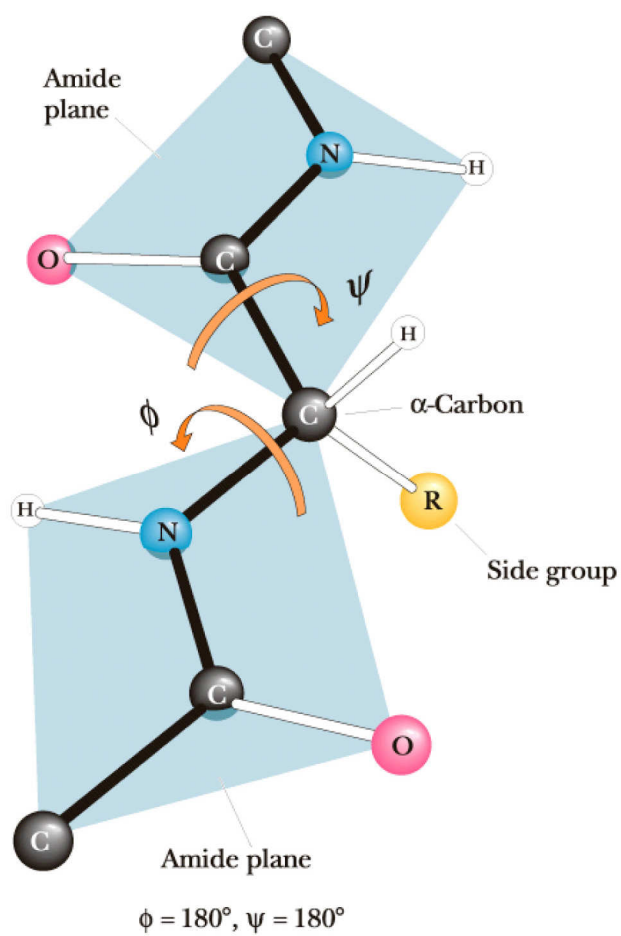


Figure 1.2.2. Representation of the dihedral angles  $\phi$  and  $\psi$  and in the peptide' bonds.

Table 1.2.1. Parameters of regular secondary structures.  $n$  is the number of residues per helical turn,  $p$  is the helical pitch, and  $A$  is the number of atoms in H-bonded loops.

Structure	$\phi$	$\psi$	$n$	$p(\text{\AA})$	$A$	H-bond(CO,HN)
$\alpha$ -helix	-57	-47	3.6	5.4	13	i,i+2
$3_{10}$ -helix	-74	-4	3.0	6.0	10	i,i+3
$\pi$ -helix	-57	-70	4.4	5.0	16	i,i+4
Parallel $\beta$ -sheet	-119	113	2.0	6.4		
Anti-parallel $\beta$ -sheet	-139	135	2.0	6.8		

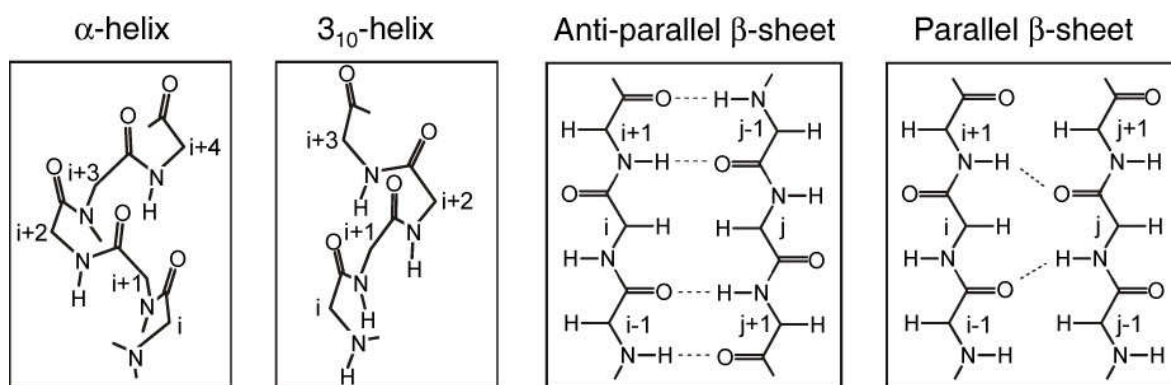


Figure 1.2.3. Schematic representation of a  $\alpha$ -helix,  $3_{10}$ -helix, anti-parallel  $\beta$ -sheet and parallel  $\beta$ -sheet secondary structure motives. The numbering of the residues (i and j) corresponds to the numbering in Tab. 1.2.2.

Table 1.2.2. Summary of the most characteristic, structure-defining  $^{13}\text{C}$ - $^{13}\text{C}$  distances in proteins. The four most commonly encountered secondary structure motifs are considered. For each secondary structure element, a set of structures was selected and distances between backbone-backbone and backbone side-chain carbons were measured. The errors are estimated from the dispersion of the distances in the selected structures [9]. The indices of the residues refer to the schematic representation of secondary structures shown in Figure 1.2.3.

Secondary structure	residue	$\text{C}^\alpha - \text{C}^\alpha$	$\text{CO} - \text{CO}$	$\text{C}^\alpha - \text{CO}$	$\text{CO} - \text{C}^\alpha$	$\text{C}^\alpha - \text{C}^\beta$	$\text{CO} - \text{C}^\beta$
$\alpha$ -helix	i,i+1	$3.8 \pm 0.1$	$3.0 \pm 0.1$	$4.4 \pm 0.1$	$2.4 \pm 0.1$	$4.9 \pm 0.1$	$3.7 \pm 0.1$
	i,i+2	$5.5 \pm 0.3$	$4.5 \pm 0.1$	$5.4 \pm 0.2$	$4.4 \pm 0.2$	$6.0 \pm 0.5$	$5.2 \pm 0.3$
	i,i+3	$5.0 \pm 0.2$	$4.7 \pm 0.1$	$5.5 \pm 0.2$	$4.4 \pm 0.2$	$4.4 \pm 0.5$	$4.3 \pm 0.4$
	i,i+4	$6.0 \pm 0.2$	$5.9 \pm 0.2$	$7.2 \pm 0.2$	$4.9 \pm 0.2$	$5.7 \pm 0.5$	$4.5 \pm 0.3$
$3_{10}$ -helix	i,i+1	$3.8 \pm 0.1$	$3.1 \pm 0.2$	$4.5 \pm 0.2$	$2.4 \pm 0.1$	$4.9 \pm 0.1$	$3.7 \pm 0.1$
	i,i+2	$5.3 \pm 0.3$	$4.6 \pm 0.2$	$5.6 \pm 0.2$	$4.3 \pm 0.3$	$5.6 \pm 0.5$	$5.0 \pm 0.5$
	i,i+3	$5.6 \pm 0.4$	$5.5 \pm 0.3$	$6.6 \pm 0.5$	$4.7 \pm 0.3$	$5.0 \pm 0.5$	$4.5 \pm 0.5$
	i,i+4	$8.1 \pm 0.4$	$7.9 \pm 0.4$	$9.2 \pm 0.5$	$6.8 \pm 0.4$	$8.3 \pm 0.5$	$6.9 \pm 0.5$
Anti-parallel $\beta$ -sheet	i,j	$4.6 \pm 0.3$		$5.4 \pm 0.5$		$5.4 \pm 0.7$	
	i-1,j+1	$5.4 \pm 0.3$	$5.0 \pm 0.4$				
	i-1,j		$4.9 \pm 0.4$		$4.7 \pm 0.5$		$5.4 \pm 0.7$
Parallel $\beta$ -sheet	i,j	$4.9 \pm 0.5$	$4.9 \pm 0.3$	$4.6 \pm 0.6$	$5.6 \pm 0.3$	$4.6 \pm 0.6$	$5.6 \pm 0.7$

Distances between carbons, which are the nuclei of highest interest for structure determination in ssNMR, for each regular secondary structure conformation are close to each other and listed in the Table 1.2.2.

### 1.3 The dynamics of a quantum mechanical systems.

Extensive description of the dynamic of physical systems in quantum mechanics, and of a nuclear spin system in particular, is given by a number of monographs [10,11,12,13,14]. The state of the physical system at a time point  $t$  is defined by its state function  $|\psi(t)\rangle$ , which evolution is governed by the time-dependent Schrödinger equation:

$$\frac{d}{dt}|\psi(t)\rangle = -\frac{i}{\hbar}H(t) \cdot |\psi(t)\rangle \quad (1.3.1)$$

where  $H(t)$  is the Hamiltonian, associated with total energy of the system and expressed by the hermitian operator. Planck's constant is denoted by  $\hbar = 1.05457168 \cdot 10^{-34}$  J·s. Further energy values are given in angular frequency units, and therefore  $\hbar$  is omitted in the Schrödinger equation. The state function  $|\psi(t)\rangle$  can be expanded in terms of a complete time independent orthogonal base  $\{|r\rangle, r=1\dots n\}$  in  $n$ -dimensional vector space of all admissible state functions:

$$|\psi(t)\rangle = \sum_r c_r(t) \cdot |r\rangle \quad (1.3.2)$$

where  $c_r(t)$  are time-dependent coefficients. We assume the state functions  $|\psi(t)\rangle$  to be normalized according to the scalar product defined in this space  $\langle\psi(t)|\psi(t)\rangle=1$ . The statistical expectation value  $\langle A \rangle$  of an arbitrary observable operator  $A$  is:

$$\langle A \rangle = \langle\psi(t)|A|\psi(t)\rangle \quad (1.3.3)$$

The dynamic evolution of the state  $|\psi(t)\rangle$  is determined by the solution of the Schrödinger equation (Eq. 1.3.1). The propagator  $U(t, t_0)$  is defined as the operator which transforms the state  $|\psi(t_0)\rangle$  at initial time point  $t_0$  into the spin state  $|\psi(t)\rangle$  at time  $t$ :

$$|\psi(t)\rangle = U(t, t_0)|\psi(t_0)\rangle \quad (1.3.4)$$

One can easily derive the equation of motion for the propagator  $U(t, t_0)$ :

$$\frac{d}{dt}U(t, t_0) = -iH(t) \cdot U(t, t_0) \quad (1.3.5)$$

In general, an analytical solution of this equation can not be obtained and the following cases may be considered:

1) If the Hamiltonian is time-independent, direct integration of Eq. 1.3.5 yields [12]:

$$U(t, t_0) = \exp(-iH(t-t_0)) = \sum_0^{\infty} \frac{1}{n!} [-iH(t-t_0)]^n \quad (1.3.6)$$

2) The Hamiltonian is inhomogeneous in the sense of Maricq and Waugh [15] and satisfies the condition  $[H(t_1), H(t_2)] \equiv H(t_1)H(t_2) - H(t_2)H(t_1) \equiv 0$ . Here  $[ , ]$  denote the commutator operation for two operators. The propagator can be written as:

$$U(t, t_0) = \exp(-i \int_{t_0}^t dt' \cdot H(t')) \quad (1.3.7)$$

3) The Hamiltonian is homogenous and  $[H(t_1), H(t_2)] \neq 0$  for at least one pair of time points  $t_1$  and  $t_2$ . In this case, an approximate solution can be obtained:

$$U(t, t_0) = \exp(-iH_n \cdot \tau_n) \dots \exp(-iH_k \cdot \tau_k) \dots \exp(-iH_1 \cdot \tau_1) \quad (1.3.8)$$

The time interval  $(t_0, t)$  can be divided into  $n$  small intervals of length  $\tau_k$  with  $k=1, 2, \dots, n$ . In each interval,  $H(t)$  is quasi time independent and has the constant value  $H_k(\tau_k) \equiv \text{const.}$

Cumulative expansion of the exponential product of two operators  $A$  and  $B$  is given by the Baker-Campbell-Hausdorff relation [12,14]:

$$\exp(B) \cdot \exp(A) = \exp \left\{ A + B + \frac{1}{2} [B, A] + \frac{1}{12} ([B, [B, A]] + [[B, A], A]) + \dots \right\} \quad (1.3.9)$$

## 1.4 Density operator.

Instead of using state functions, it is more practical to describe an ensemble of spins system by density operator, which can be expressed for an ensemble in mixed state as:

$$\rho(t) = \sum_k p^k |\psi_k(t)\rangle \langle \psi_k(t)| = \sum_k p^k \sum_r \sum_s c_r^k(t) \cdot c_s^{k*}(t) \cdot |r\rangle \langle s| \quad (1.4.1)$$

where  $p^k$  is the probability that a spin system of the ensemble is in one of several possible states  $|\psi_k(t)\rangle$ . The statistical expectation value for an operator  $A$  over the spin ensemble in terms of density operator is:

$$\langle A \rangle = \langle \psi_k(t) | A | \psi_k(t) \rangle = \text{Tr} \{ \rho(t) \cdot A \} \quad (1.4.2)$$

The equation of motion for the density operator can be derived from the Schrödinger equation (Eq.1.3.1 ):

$$\frac{d}{dt} \rho(t) = -i [H(t), \rho(t)] \quad (1.4.3)$$

The formal solution is given by:

$$\rho(t) = U(t, t_0) \rho(t_0) U^{-1}(t, t_0) \quad (1.4.4)$$

where the propagator  $U(t, t_0)$  solves Eq. (1.3.5)

## 1.5 The nuclear spin and NMR spectroscopy.

Nuclei have such property as a spin. The spin is an intrinsic angular momentum which is not produced by motion of the nucleus in space. The microscopic angular moment  $\mu$  of the nuclear is related to its spin by:

$$\mu = \gamma \cdot S \quad (1.5.1)$$

where  $\gamma$  is the gyromagnetic ratio, which is different for different nuclei.

According to quantum mechanics, the angular momentum  $S$  can only adopt certain values, given by  $\hbar(M(M+1))^{1/2}$  where  $M$  is the spin quantum number.  $M$  might be integer (0, 1, 2, ...) or half-integer (1/2, 3/2, ...).

Table 1.5.1 contains a list of ground-state nuclear spins of a few nuclear isotopes commonly used in biomolecular NMR:

Table 1.5.1. A selection of magnetic nuclei and their properties [16].

Isotope	Spin	Natural Abundance, %	Gyromagnetic ratio rad/(s·G)
$^1\text{H}$	1/2	~100	26753
$^2\text{H}$	1	0.015	4107
$^{12}\text{C}$	0	98.9	
$^{13}\text{C}$	1/2	1.1	6728
$^{14}\text{N}$	1	99.63	1934
$^{15}\text{N}$	1/2	0.37	-2712

In the external magnetic field  $B_0$ , the energy  $E$  of the nuclear magnetic momentum is given by:

$$E = -\mu \cdot B_0 \quad (1.5.2)$$

The energy is lower for the magnetic momentum oriented parallel to the external magnetic field. According to the Boltzman distribution, the number of parallel oriented spins is higher than the anti-parallel oriented ones. The difference in the occupancies of the energy states results in the macroscopic magnetic moment parallel to the external field and called longitudinal magnetization. The difference in anti- and parallel oriented spins is very tiny and on the order  $10^{-5}$  at room temperature. In NMR experiments, longitudinal magnetization is rotated by radio-frequency (rf) pulse into the plane perpendicular to the external field. The macroscopic magnetic momentum in the transversal plane is called transversal magnetization. The transversal magnetization starts to precess around the axis of the external magnetic field with the Larmor frequency  $\omega_0 = -\gamma \cdot B_0$ . The precession can be detected in a wire coil. The induced electric current is called free-induction decay (FID).

In general, the properties of a quantum mechanical system are represented by the total Hamiltonian, which includes all parameters and interactions describing the molecular system. For NMR, however, it is sufficient to derive a reduced spin Hamiltonian which only includes terms depending on the nuclear spins. The spin Hamiltonian does not take

into account possible time-dependent random interactions between the spin system and the environment, which could be introduced after time averaging as effective interactions. As an example, interactions with the electronic of a spin result in the specific chemical shift.

## 1.6 Spin one half in a static field.

Spin 1/2 nuclei are very common in biomolecular NMR. Only spins 1/2 problems are considered in this thesis. To simplify the quantum mechanical description of spin system in NMR only systems of nuclei one half will be considered.

The spin Hamiltonian for a single spin-1/2 in an external magnetic field  $B_0$  parallel to the axis  $Z$  of the introduced cartesian coordinate system is given by:

$$H = -\gamma \cdot B_0 \cdot S = -\gamma \cdot B_z \cdot S_z = \omega_0 \cdot S_z \quad (1.6.1)$$

where  $S$  is the spin operator and  $S_z$  is its  $Z$  component. The state function  $|\psi(t)\rangle$  may be expressed in the basis of eigenfunctions  $|M, m_z\rangle$  of the operator  $S_z$  which are called Zeeman states:

$$S_z |M, m_z\rangle = m_z |M, m_z\rangle \quad (1.6.2)$$

For a spin-1/2 one obtains two eigenvalues  $m_z = \pm 1/2$ . The corresponding eigenfunctions usually are denoted  $|\alpha\rangle = |1/2, 1/2\rangle$  and  $|\beta\rangle = |1/2, -1/2\rangle$ :

$$S_z |\alpha\rangle = \frac{1}{2} |\alpha\rangle \quad \text{and} \quad S_z |\beta\rangle = -\frac{1}{2} |\beta\rangle \quad (1.6.3)$$

In vector representation these eigenfunctions have the form:

$$|\alpha\rangle = \begin{pmatrix} 1 \\ 0 \end{pmatrix} \quad \text{and} \quad |\beta\rangle = \begin{pmatrix} 0 \\ 1 \end{pmatrix} \quad (1.6.4)$$

## 1.7 Operator algebra.

An elegant description of a NMR experiment can be given in terms of the momentum and polarization operators. In the basis introduced in the previous chapter, all operators can be expended in the following form [12,17]:



$$\begin{aligned}
S_z &= \frac{1}{2} \begin{pmatrix} 1 & 0 \\ 0 & -1 \end{pmatrix} = \frac{1}{2} (|\alpha\rangle\langle\alpha| - |\beta\rangle\langle\beta|) \\
S_x &= \frac{1}{2} \begin{pmatrix} 0 & 1 \\ 1 & 0 \end{pmatrix} = \frac{1}{2} (|\alpha\rangle\langle\beta| + |\beta\rangle\langle\alpha|) \\
S_y &= \frac{1}{2i} \begin{pmatrix} 0 & 1 \\ -1 & 0 \end{pmatrix} = \frac{1}{2i} (|\alpha\rangle\langle\beta| - |\beta\rangle\langle\alpha|)
\end{aligned} \tag{1.7.2}$$

These operators follow commutation rules:

$$[S_x, S_y] = i \cdot S_z \quad [S_y, S_z] = i \cdot S_x \quad [S_z, S_x] = i \cdot S_y \tag{1.7.3}$$

The raising  $S_+$  and lowering  $S_-$  operators can be introduced via the  $S_x$  and  $S_y$  operators:

$$\begin{aligned}
S_+ &= S_x + i \cdot S_y = \begin{pmatrix} 0 & 1 \\ 0 & 0 \end{pmatrix} = |\alpha\rangle\langle\beta| \\
S_- &= S_x^* = S_x - i \cdot S_y = \begin{pmatrix} 0 & 0 \\ 1 & 0 \end{pmatrix} = |\beta\rangle\langle\alpha|
\end{aligned} \tag{1.7.4}$$

They act on the basis functions in the following way:

$$\langle\alpha|S_+|\beta\rangle = \langle\beta|S_-|\alpha\rangle = 1 \tag{1.7.5}$$

And obey the commutation rules:

$$[S_+, S_z] = -S_+ \quad [S_-, S_z] = S_- \tag{1.7.6}$$

The polarization operators are defined as:

$$\begin{aligned}
S_\alpha &= \begin{pmatrix} 1 & 0 \\ 0 & 0 \end{pmatrix} = |\alpha\rangle\langle\alpha| \\
S_\beta &= \begin{pmatrix} 0 & 0 \\ 0 & 1 \end{pmatrix} = |\beta\rangle\langle\beta|
\end{aligned} \tag{1.7.7}$$

In the case of a system of  $N$  spins-1/2 nuclei, a possible choice of basis set is the direct product of Zeeman states of the single spins. Operators in this space are defined as the direct product of operators defined in the space of single spins.

## 1.8 The nuclear spin Hamiltonian in the static field.

The nuclear interactions that are of interest in ssNMR can be described by second-rank cartesian tensors. The spins interact with the external magnetic field  $B_0$ , and pair-wise by means of dipolar and  $J$  couplings. We do not consider quadrupolar couplings which are non-zero only for nuclei with spins higher than 1/2. The total spin Hamiltonian can be written as:

$$H = H_Z + H_{CS} + H_D + H_J \quad (1.8.1)$$

The Zeeman interaction term  $H_Z$  describes the interaction between the nuclear spin and the external magnetic field director along the  $Z$  axis  $B_0=B_z$ :

$$H_Z = -\gamma \cdot B_0 \cdot S = -\gamma \cdot B_z \cdot S_z = \omega_0 \cdot S_z \quad (1.8.2)$$

where  $S$  is the operator of the spin angular momentum and  $S_z$  is its  $Z$  projection.

According to first order perturbation theory [12,13,17,18] in high field NMR the spin Hamiltonian may be simplified by neglecting terms which do not commute with the Zeeman term, which is much stronger than others. The truncated Hamiltonian retains only terms which are referred as the secular terms.

The chemical shift (CS) interaction is induced by the electron environment, shielding the external magnetic field and can be described by the shielding tensor  $\sigma$ :

$$H_{CS} = -\gamma \cdot S \cdot \sigma \cdot B_0 \quad (1.8.3)$$

In the principal axis system (PAS) the tensor is diagonal  $\sigma=(\sigma_x, \sigma_y, \sigma_z)$ . The isotropic chemical shift is denoted as  $\sigma_{iso}=(\sigma_x+\sigma_y+\sigma_z)/3$ . By convention, the principal values are ordered such that  $|\sigma_z-\sigma_{iso}| \geq |\sigma_x-\sigma_{iso}| \geq |\sigma_y-\sigma_{iso}|$ . The chemical shift anisotropy parameter  $\delta$  and the asymmetry parameter  $\eta$  are defined as:

$$\delta = (\sigma_z - \sigma_{iso}) \quad \eta = (\sigma_y - \sigma_x) / (\sigma_z - \sigma_{iso}) \quad (1.8.4)$$

The  $H_{CS}$  in the high field approximation is given by:

$$H_{CS} = \omega_0 \cdot \sigma_{zz} \cdot S_z \quad (1.8.5)$$

where  $\sigma_{zz}$  is the corresponding element of the CSA tensor in the laboratory frame. The CS interaction is anisotropic and depends on molecular interaction relatively the

external magnetic field. With  $\mathbf{B}_0$  expressed in terms of its polar coordinates  $(\theta, \phi)$  in the PAS  $\sigma_{zz}$  can be written as [14]:

$$\sigma_{zz} = \sigma_x (\cos(\phi)\sin(\theta))^2 + \sigma_y (\sin(\phi)\sin(\theta))^2 + \sigma_z (\cos(\theta))^2 \quad (1.8.6)$$

The dipolar coupling between two spins S and K can be described by the traceless symmetric Cartesian tensor  $D$ :

$$H_{DD} = S * D \cdot K \quad (1.8.7)$$

and the tensor  $D$  in the laboratory frame has the form:

$$D_{ij} = \frac{\mu_0}{4\pi} \frac{\gamma_s \gamma_k \hbar}{r^3} \left[ \delta_{ij} - \frac{3x_i x_j}{r^2} \right] \quad (1.8.8)$$

where  $\delta_{ij}$  is the Kronecker delta,  $x_i$  and  $x_j$  the cartesian coordinates of the vector between two nuclei,  $r$  is the distance between them,  $\gamma_s$  and  $\gamma_k$  are corresponding nuclear gyromagnetic ratios,  $\mu_0 = 4\pi \cdot 10^{-7}$  is the permeability of the space.

In the high field approximation, the direct dipolar coupling of homonuclear interaction takes the form:

$$\begin{aligned} H_D &= \frac{\mu_0}{4\pi} \frac{\gamma_s \gamma_k \hbar}{r^3} \frac{1-3\cos^2(\theta)}{2} \left[ 2S_z K_z - \frac{1}{2}(S_+ K_- + S_- K_+) \right] = \\ &= \frac{\mu_0}{4\pi} \frac{\gamma_s \gamma_k \hbar}{r^3} \frac{1-3\cos^2(\theta)}{2} [3S_z K_z - S \cdot K] = \\ &= -b_{sk} \frac{1-3\cos^2(\theta)}{2} [3S_z K_z - S \cdot K] = \omega_{sk} [3S_z K_z - S \cdot K] \end{aligned} \quad (1.8.9)$$

where the relationship  $S_z K_z + 1/2(S_+ K_- + S_- K_+) = S_x K_x + S_y K_y = S \cdot K$  has been used.

For two heteronuclei in the high field approximation, the dipolar coupling may be written as:

$$\begin{aligned} H_D &= \frac{\mu_0}{4\pi} \frac{\gamma_s \gamma_k \hbar}{r^3} \frac{1-3\cos^2(\theta)}{2} \cdot 2S_z K_z \\ &= -b_{sk} \frac{1-3\cos^2(\theta)}{2} \cdot 2S_z K_z = \omega_{sk} S_z K_z \end{aligned} \quad (1.8.10)$$

The electron mediated  $J$  coupling (or scalar coupling) between two spins S and K is isotropic for most spin pairs and can be described by a constant  $J$ . For the homonuclear case, it takes the form:

$$H_J = 2\pi \cdot J \cdot S \cdot K \quad (1.8.11)$$

And for the heteronuclear interaction, it can be written as:

$$H_J = 2\pi \cdot J \cdot \mathbf{S}_z \cdot \mathbf{K}_z \quad (1.8.12)$$

## 1.9 Spherical representation of the spin Hamiltonian.

For the description of the spin Hamiltonian, the density and spin operators subjected to three-dimensional rotations, it is of advantage to use the representation of irreducible spherical tensor of rank 0, 1 and 2. An irreducible tensor  $A_p$  of rank  $p$  is composed of  $(2p+1)$  components  $A_{pq}$ , where  $q=(-p, -p+1, \dots, p)$ . The relation between the irreducible and cartesian tensors can be found in Ref.[11]. A general rotation transforms the coordinate system  $F$  into the system  $F^1$  and may be expressed by the three Euler angles  $\Omega=(\alpha, \beta, \gamma)$ . Under rotation, the irreducible tensor components transform in the following way:

$$A_{p,q}^F = \sum_{q'=-p}^p A_{p,q'}^{F_1} \cdot D_{q,q'}^p(\Omega) \quad (1.9.1)$$

where  $D_{qq'}^p$  is a Wigner matrix element [11,14,17].

The Hamiltonian of any spin interaction  $M$  can be written in terms of irreducible tensors:

$$H_M = \sum_{p=0}^2 \sum_{q=-p}^p (-1)^q A_{p,q} \cdot T_{p,-q} \quad (1.9.2)$$

where the tensor  $T_{p,-q}$  is composed out of spin operators and is called a spin tensor, while the spatial tensor  $A_{p,q}$  represents spatial part of an interaction. All NMR interactions are represented by spatial tensors of rank  $p$  equal to 0 or 2.

The exact form of the spatial and spin tensors for all interactions can be found in Ref. [11,14].

## 1.10 Reference frames and magic angle spinning in solid state NMR.

In MAS solid state NMR, the sample is rotated in the magnetic field to suppress anisotropic interactions. The spinning axis of the rotor is declined from the external magnetic field by “magic angle”  $\beta_{MAS} = \tan^{-1}(2^{1/2}) = 54.7356^\circ$ . The relevant reference frames in MAS ssNMR are depicted in the Figure 1.10.1.

The principal axis system (PAS) of each interaction is denoted  $P^A$ , and it is defined as the frame where the Cartesian tensor, representing the interaction is diagonal. The molecular frame  $M$  is fixed to the molecule and can be chosen arbitrarily. In the rotor frame  $R$ , the axis  $Z_R$  coincides with the rotational axis. The laboratory frame  $L$  is the reference frame in which the  $Z_L$  axis is pointing in the direction of the external magnetic field. The components of the spatial tensors in the total spin Hamiltonian are determined by a three step rotational transformation which can be described by Wigner matrix as given in Eq. 1.9.1.

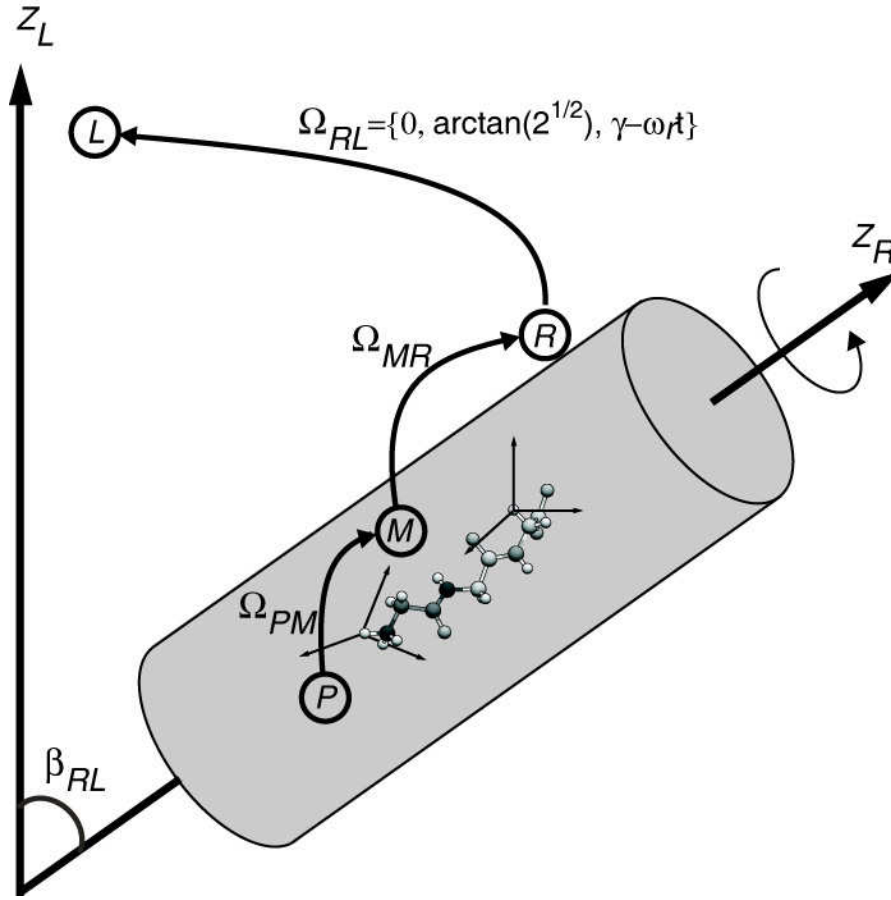


Figure 1.10.1. The relevant reference frames and transformations in MAS ssNMR

The transformation from the rotor frame to the laboratory for each interaction  $M$  can be written as:

$$H_M = \sum_{p=0,2} \sum_{m=-p}^p A_{p,q}^{M,R} d_{m0}^p(\beta_{RL}) \exp(im(\omega_r t - \gamma_{RL}^0)) \quad (1.10.1)$$

where  $A_{p,q}^{M,R}$  is  $q$ -th component of a tensor of rank  $p$ , determining the interaction  $M$  in the rotor frame  $R$  and  $d_{m0}^p(\beta_{RL})$  is a reduced Wigner matrix element. In case of exact MAS,  $d_{00}^2(\beta_{RL}) \equiv 0$  if  $\beta_{RL} = \tan^{-1}(\sqrt{2}) = 54.7356^\circ$ . All other components are oscillating with the frequencies  $\pm \omega_r$  and  $\pm 2\omega_r$ , resulting in averaging of the Hamiltonian to zero for all anisotropic interactions represented by a spatial tensor of rank 2.

### 1.11 Interaction frame.

Consider the situation where the Hamiltonian can be separated into two parts:

$$H(t) = H_0(t) + H_1 \quad (1.11.1)$$

Where  $H_1$  is time independent term. One can introduce a transformation of the density operator  $\rho$  into  $\rho^i$  as:

$$\rho^i = e^{iH_1 t} \rho e^{-iH_1 t} = U_1^{-1} \rho U_1 \quad (1.11.2)$$

where propagator  $U_1 = \exp(-iH_1 t)$ . According to Eq. 1.4.3  $\rho^i$  is a solution of the equation:

$$\frac{d}{dt} \rho^i = -i [H_0^i, \rho^i] \quad (1.11.3)$$

where  $H_0^i$  is the spin Hamiltonian in the interaction frame determined by the propagator  $U_1$ :

$$H_0^i = e^{iH_1 t} H_0 e^{-iH_1 t} = U_1^{-1} H_0 U_1 \quad (1.11.4)$$

As an example, we consider an interaction induced by an oscillating rf field in the transversal plane applied to a nucleus with the Larmor frequency  $\omega_0$ . The Hamiltonian can be written as:

$$\begin{aligned} H &= \omega_0 S_z + \omega_1 (S_x \cdot \cos(\omega t) + S_y \cdot \sin(\omega t)) = \\ &= \omega_0 S_z \pm \omega S_z + \frac{1}{2} \omega_1 (S_+ \cdot \exp(-i\omega t) + S_- \cdot \exp(i\omega t)) \end{aligned} \quad (1.11.5)$$

where  $\omega_1$  and  $\omega$  are the amplitude and the oscillating frequency of the rf field, respectively. One can divide this Hamiltonian into two parts:

$$\begin{aligned} H_1 &= \omega S_z \\ H_0 &= (\omega_0 - \omega S_z) + \frac{1}{2} \omega_1 (S_+ \cdot \exp(-i\omega t) + S_- \cdot \exp(i\omega t)) \end{aligned} \quad (1.11.6)$$

In the interaction frame determined by  $H_1 = \omega S_z$   $H_0$  takes the form:

$$H_{0,m} = (\omega_0 - \omega) S_z + \frac{1}{2} \omega_1 (S_{m,+} + S_{m,-}) = (\omega_0 - \omega) S_z + \omega_1 S_{m,x} \quad (1.11.7)$$

where the transformation for lowering and raising operators is given by the relationship:

$$\exp(i\omega t \cdot S_z) \cdot S_{\pm} \cdot \exp(-i\omega t \cdot S_z) = \exp(\pm i\omega t) \cdot S_{\pm} \quad (1.11.8)$$

which could be obtained using the expression from the operator's algebra:

$$\begin{aligned} \exp(-i\varphi \cdot C) \cdot A \cdot \exp(i\varphi \cdot C) = \\ \begin{cases} = A \cdot \cos(\varphi) - i[C, A \sin(\varphi)] = A \cdot \cos(\varphi) + B \sin(\varphi) & \text{if } B \neq 0 \\ = A & \text{if } B = 0 \end{cases} \end{aligned} \quad (1.11.9)$$

where the operators  $A$ ,  $B$  and  $C$  are related to each other by the commutation rule:

$$[C, A] = iB \quad (1.11.10)$$

From the Eq. (1.11.6) one can conclude that rf field acts on a nuclear when its oscillating frequency is close to the Larmor frequency of the nuclear of interest:  $\omega_1 \approx \omega_0 - \omega$ . Since the maximum applied rf power is of the order 100 kHz it can influence only on nuclei of one type, because of modern spectrometers operate at proton frequency of several hundreds megahertz.

The interaction frame can be considered in a more general case, when the perturbation  $H_I$  is time dependent. The general propagator  $U$  takes the form:

$$U = U_1 U^i \quad (1.11.11)$$

where  $U_1$  is determined by  $H_I$  and solves the equation:

$$\frac{d}{dt} U_1(t) = -iH_1(t)U_1(t) \quad (1.11.12)$$

The Hamiltonian  $H^i$  in the interaction frame can be obtained by the transformation:

$$H^i = U_1^{-1} H_0(t) U_1 \quad (1.11.13)$$

The propagator  $U^i$  determining the evolution of the spin system is a solution of the equation:

$$\frac{d}{dt} U^i(t) = -iH^i(t)U^i(t) \quad (1.11.14)$$

In NMR experiments the evolution of spin systems under a rf pulse train can be very efficient described in the interacting frame, which is determined by the rf pulses.



### 1.12 Average Hamiltonian theory.

If the Hamiltonian  $H_0$  has no analytical solution, the time-independent average Hamiltonian  $H_{0,Av}$  can be introduced over the time interval  $T$  as a series expansion of time-independent terms, called the Magnus expansion [19]:

$$H_{0,Av} = H_{0,1} + H_{0,2} + H_{0,3} + \dots \quad (1.12.1)$$

According to Eq. (1.3.8, 1.3.9), the first order term is given by:

$$H_{0,1} = \frac{1}{T} \left\{ H^{(1)} \tau^{(1)} + H^{(2)} \tau^{(2)} + \dots H^{(n)} \tau^{(n)} \right\} = \frac{1}{T} \int_0^T dt \cdot H_0(t) \quad (1.12.2)$$

The average Hamiltonian theory applied to a spin Hamiltonian in an interaction frame is a powerful tool in ssNMR to describe the evolution of spin systems under a rf pulse train. Consider a spin system described by the Hamiltonian  $H_0$  and the perturbation  $H_1(t)$  determined by an rf pulse train. Of practical interest are situations where the perturbation  $H_1(t)$  is periodic with period  $t_c$ :

$$H_1(t + nt_c) = H_1(t), \quad n = 0, 1, 2 \quad (1.12.3)$$

And  $H_1(t)$  is cyclic in the sense that:

$$U_1(t_c) = 1 \quad (1.12.4)$$

where  $U_1(t)$  is the propagator determined by  $H_1(t)$ .

Under this condition,  $H_1(t)$  has no overall direct effect in the course of one full cycle. For stroboscopic observation synchronized with the periodic  $H_1(t)$ , Eq (1.12.11) gives for the evolution propagator after one pulse train cycle:

$$U_{0,Av} = \exp(-iH_{0,1}t) \quad (1.12.5)$$

$$H_{0,1}^i = \frac{1}{t_c} \int_0^{t_c} dt \cdot H_0^i(t) \quad (1.12.6)$$

where  $H_0^i$  is the Hamiltonian in the interaction frame determined by Eq. (1.12.13)

$$H_0^i = U_1^{-1}(t) H_0 U_1(t) \quad (1.12.7)$$

This approach requires that the Hamiltonian fulfills the condition  $H_0 t_c \ll 1$ .

### 1.13 Basic solid state NMR techniques.

In this chapter, we give a qualitative overview of the pulse sequences which have been used extensively in the presented work and a general description of the most common pulse sequences.

Sample spinning under magic angle can not suppress to insignificant level all anisotropic interactions. Rf pulses are therefore widely used to remove residual couplings to increase the resolution of NMR spectra. Proton-proton dipolar decoupling techniques enable the use protons in ssNMR. For a static sample the spin Hamiltonian of a homonuclear dipolar interaction between two nuclei  $H_{D,zz}$  takes the form (Eq. (1.8.8)):

$$H_{D,zz} = \omega_{sk} [3S_z K_z - S \cdot K] \quad (1.13.1)$$

Application of a pulse train which would periodically permute in the interaction frame axis the Z, X, Y of the dipolar Hamiltonian resulting in an average Hamiltonian of zero:

$$\begin{aligned} H_{D,Av} &= \frac{1}{3} (H_{D,zz} + H_{D,xx} + H_{D,yy}) = \\ &= \frac{1}{3} \omega_{sk} \frac{1}{\sqrt{6}} [3S_z K_z - S \cdot K + 3S_x K_x - S \cdot K + 3S_y K_y - S \cdot K] = 0 \end{aligned} \quad (1.13.2)$$

The first pulse sequence, called WAHUHA-4 [20], suggested to remove homonuclear dipolar couplings at first order in average Hamiltonian theory is depicted in Figure 1.13.1:

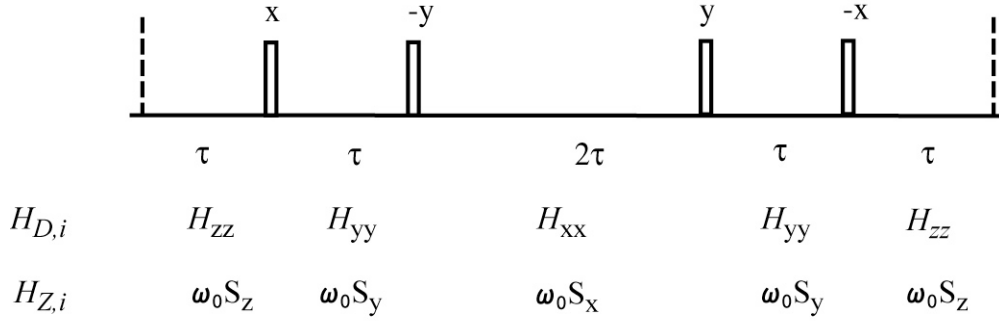


Figure 1.13.1. WAHUHA multiple-pulse sequence for homonuclear dipolar decoupling. Phases of  $90^\circ$  pulses, delays between them and dipolar Hamiltonian in the interaction frame for Zeeman interaction and dipolar coupling are shown on the plot.

The applied pulse sequences require short pulse duration  $\tau_p$ , and delays between the pulses must be shorter than the inverse dipolar couplings:

$$\tau_p \ll \tau \ll 1/\omega_{sk} \quad (1.13.3)$$

The average Zeeman Hamiltonian  $H_{Z,Av}$  corresponds to a new axis of quantization  $Z_{Av}=(1,1,1)$ . The Larmor frequency is scaled by a factor  $1/3^{1/2}$ .

$$\begin{aligned}
 H_{Z,Av} &= \frac{1}{3} (H_{Z,z} + H_{Z,x} + H_{Z,y}) = \\
 &= \frac{1}{3} \omega_0 [S_z + S_x + S_y] = \frac{1}{\sqrt{3}} \omega_0 S_{z,i} = 0
 \end{aligned} \quad (1.13.4)$$

where  $S_{z,i}$  is the projection of the spin  $S$  along the axis  $Z_{Av}$ .

The higher order terms in the average dipolar Hamiltonian, effect of rf pulses imperfections can be compensated by more elaborated pulse trains like MREV-8 and BR-24 [21,22].

In case of the sample spinning dipolar coupling become time dependent. The above mentioned pulse sequences work assuming quasi-static conditions, when the spinning frequency  $\omega_{rot}$  is much more slower than the periodicity of the pulse sequence  $\tau_{ps}$ :  $\omega_{rot} \ll 1/\tau_{ps}$ .

FSLG (frequency switched Lee-Goldburg) [23] and PMLG (phase modulated Lee-Goldburg) [24] have an advantage for homonuclear decoupling due to the short periodicity, when the dipolar coupling modulated by fast sample spinning is quasi-constant. Both pulse sequences use average rf fields oriented along the effective axis  $Z_{LG}$  directed along the vector (1,1,1) or (1,1,-1). The quantization axis  $Z_{LG}$  is to the same as in case of WAHUHA. The average spin Hamiltonian is calculated in the same interaction frame and yields the same results for dipolar and Zeeman interactions.

In case of sample rotation, the analysis is getting more complicated and average Hamiltonian theory is not applicable and efficient description can be provided by Floquet theory. Vega and coworkers performed deep analysis of the PMLG and a number of others homonuclear decoupling pulse sequences on the basis of the Floquet theory [25,26].

During the FSLG sequence, an efficient decoupling field is generated by the rf field of strength of  $\omega_1$  applied at a frequency shifted from Larmor frequency of protons by a value of  $\omega_1/2^{1/2}$ . Synchronous alternation of the phase of the rf field and the frequency offset makes the pulse sequence more robust. In case of the PMLG sequence, a rf field of the amplitude  $\omega_1$  is applied and its phase is stepwise swept with frequency  $\omega_1/2^{1/2}$  to emulate required frequency offset.

Heteronuclear dipolar decoupling pulse sequences suppress interactions between nuclei of different kind. The spin Hamiltonian of the nucleus S which is coupled to a system of N nuclei of type K can be written according Eq. (1.8.8, 1.8.9) in the form:

$$\begin{aligned}
H_D &= H_{het} + H_{homo} = \\
&= \omega_{sk} S_z K_{1,z} + \frac{1}{2} \sum_{i=1}^N \sum_{j \neq i}^N \omega_{ij} \left[ 2K_{i,z} K_{j,z} - \frac{1}{2} (K_{i,+} K_{i,-} + K_{i,-} K_{i,+}) \right] \\
H_{het} &= \omega_{sk} S_z K_{1,z} \\
H_{homo} &= \frac{1}{2} \sum_{i=1}^N \sum_{j \neq i}^N \omega_{ij} \left[ 2K_{i,z} K_{j,z} - \frac{1}{2} (K_{i,+} K_{i,-} + K_{i,-} K_{i,+}) \right] \tag{1.13.5}
\end{aligned}$$

where the heteronuclear dipolar coupling between spin S and  $K_1$  is given by  $H_{het}$  and the homonuclear interactions to the spin system  $K_i$  is represented by  $H_{homo}$ . If  $H_{homo}$  is equal to zero or much less than the spinning frequency, the total Hamiltonian is inhomogeneous in the sense of Maricq and Waugh [15] and there is no line broadening for the resonance of the spin S due to dipolar coupling to the spin  $K_1$ . Experimentally, this has been shown by

Reif and coworkers [27,28]. In spin systems with non zero  $H_{homo}$  a rf pulse sequence is required to increase resolution of the S resonances. For heteronuclear decoupling, a continuous wave (CW) rf irradiation can be applied. In the interaction frame determined by rf the Hamiltonian  $H_{rf} = \omega_1 K_{1,x}$  the heteronuclear interaction can be written in the form:

$$H_{het} = \omega_{sk} S_z (K_{1,z} \cos(\omega_1 t) + K_{1,y} \sin(\omega_1 t)) \quad (1.13.6)$$

According to average Hamiltonian theory,  $H_{het} = 0$  to first order approximation resulting in the elimination of line broadening for the S spin resonances. More efficient heteronuclear dipolar decoupling can be achieved by application of the two pulse phase modulation (TPPM) [29] pulse sequence, which consist of train of pairs of  $160^\circ$  pulses with small (appr.  $15^\circ$ ) phase shift.

Cross polarization (CP) [30,31] transfer between heteronuclei is an important element in the ssNMR experiments. It allows to correlate heteronuclei in multidimensional experiments, measure the size of heteronuclear dipolar coupling and allows to enhance the magnetization of low  $\gamma$  nuclei by polarization transfer from protons, making use of their high  $\gamma$  and fast longitudinal relaxation. The standard CP experiment starts with a  $90^\circ$   $^1\text{H}$  excitation pulse. The proton magnetization is then transferred from protons to the heteronucleus (e.g.  $^{13}\text{C}$ ) by applying rf fields on both channels, Figure 1.13.2:

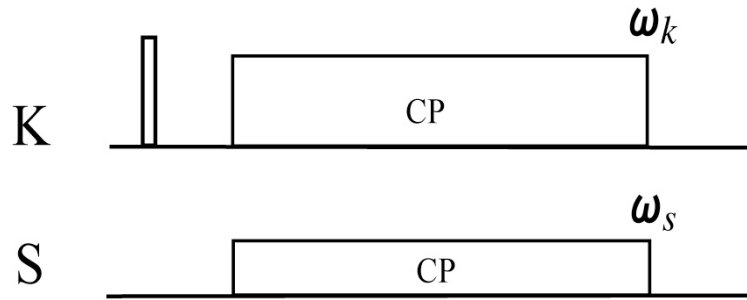


Figure 1.13.2. Schematic representation the cross polarization transfer experiment.

CP takes place when both nuclei are irradiated with a rf field difference equal to 0,  $\omega_k$ , or  $2\omega_k$ . Under this condition, dipolar couplings are recoupled in the rotating sample. In the laboratory frame the Hamiltonian for two dipolar coupled heteronuclear spins S and K irradiated with rf fields with strength of  $\omega_s$  and  $\omega_k$  respectively can be written in the form [32]:

$$\begin{aligned}
H_D &= \omega_{sk}(t) S_{z,L} K_{z,L} + \omega_k K_{x,L} + \omega_s S_{x,L} = \\
&= \frac{b_{sk}}{2} \left[ \sin^2(\beta) \cos(2\gamma + 2\omega_r t) - \sqrt{2} \sin(\beta) \cos(\gamma + \omega_r t) \right] S_{z,L} K_{z,L} + \\
&+ \omega_k K_{x,L} + \omega_s S_{x,L}
\end{aligned} \tag{1.13.7}$$

where the Euler angles  $\beta$  and  $\gamma$  relate the PAS system associated with the dipolar tensor and the rotor fixed frame. In the doubly rotating frame determined by the rf fields applied along the axis  $X$  to nuclei  $S$  and  $K$ , the Hamiltonian takes form:

$$\begin{aligned}
H_{D,i} &= \frac{b_{sk}}{2} \left[ \sin^2(\beta) \cos(2\gamma + 2\omega_r t) - \sqrt{2} \sin(\beta) \cos(\gamma + \omega_r t) \right] \times \\
&\times (S_x \cos(\omega_s t) + S_y \sin(\omega_s t)) (K_x \cos(\omega_k t) + K_y \sin(\omega_k t)) = \\
&= \frac{b_{sk}}{4} \left[ \sin^2(\beta) (e^{i(2\gamma + 2\omega_r t)} + e^{-i(2\gamma + 2\omega_r t)}) - \sqrt{2} \sin(\beta) (e^{i(\gamma + \omega_r t)} + e^{-i(\gamma + \omega_r t)}) \right] \times \\
&\times (S_+ e^{i\omega_s t} + S_- e^{-i\omega_s t}) (K_+ e^{i\omega_k t} + K_- e^{-i\omega_k t}) = \\
&= \frac{b_{sk}}{4} \left[ \sin^2(\beta) (e^{i(2\gamma + 2\omega_r t)} + e^{-i(2\gamma + 2\omega_r t)}) - \sqrt{2} \sin(\beta) (e^{i(\gamma + \omega_r t)} + e^{-i(\gamma + \omega_r t)}) \right] \times \\
&\times (S_+ K_+ e^{i(\omega_s + \omega_k)t} + S_- K_- e^{-i(\omega_s + \omega_k)t} + S_+ K_- e^{i(\omega_s - \omega_k)t} + S_- K_+ e^{-i(\omega_s - \omega_k)t})
\end{aligned} \tag{1.13.8}$$

The average over rotor period dipolar coupling is non zero when  $(\omega_s + \omega_k) = \omega_r$ ,  $2\omega_r$  or  $(\omega_s - \omega_k) = \omega_r$ ,  $2\omega_r$ . In the second case the Hamiltonian is proportional to the flip-flop term  $(S_+ K_- + S_- K_+)$ . If in the initial state only the nuclei  $K$  are polarized, the density operator can be written in the form:

$$\begin{aligned}
\rho(t=0) &= K_z = \rho_\Sigma(t=0) + \rho_\Delta(t=0) = \frac{K_z + S_z}{2} + \frac{K_z - S_z}{2} \\
\text{where } \rho_\Sigma(t=0) &= \frac{K_z + S_z}{2} \quad \text{and} \quad \rho_\Delta(t=0) = \frac{K_z - S_z}{2}
\end{aligned} \tag{1.13.9}$$

According to Eq. 1.7.6, commutators for both density operators with the Hamiltonian are:

$$\begin{aligned}
\left[ S_+ K_- + S_- K_+, \frac{K_z - S_z}{2} \right] &= \frac{1}{2} (S_+ K_- - S_- K_+ + S_+ K_- - S_- K_+) = (S_+ K_- - S_- K_+) \\
\left[ S_+ K_- + S_- K_+, \frac{K_z + S_z}{2} \right] &= \frac{1}{2} (S_+ K_- - S_- K_+ - S_+ K_- + S_- K_+) = 0
\end{aligned} \tag{1.13.10}$$

The evolution of the density operator can be calculated using Eq. (1.13.8-1.13.10 and 1.11.9):

$$\begin{aligned}\rho(t) &= \rho_{\Sigma}(t) + \rho_{\Delta}(t) = \frac{K_z + S_z}{2} + \frac{K_z - S_z}{2} \cos(\omega t) + (S_+ K_- - S_- K_+) \sin(\omega t) = \\ &= K_z \frac{(1 + \cos(\omega t))}{2} + S_z \frac{(1 - \cos(\omega t))}{2} + (S_+ K_- - S_- K_+) \sin(\omega t) \\ \text{where } \omega &= \begin{cases} b_{sk} \sin^2(\beta)/4 & \text{if } \omega_s - \omega_k = \pm 2\omega_r \\ -\sqrt{2} b_{sk} \sin(\beta)/4 & \text{if } \omega_s - \omega_k = \pm \omega_r \end{cases} \quad (1.13.11)\end{aligned}$$

In the spin system, the polarization oscillates between the nuclei K and S. In powder samples, the orientation for different dipolar coupled spin pairs is different, which requires averaging over all possible orientations.

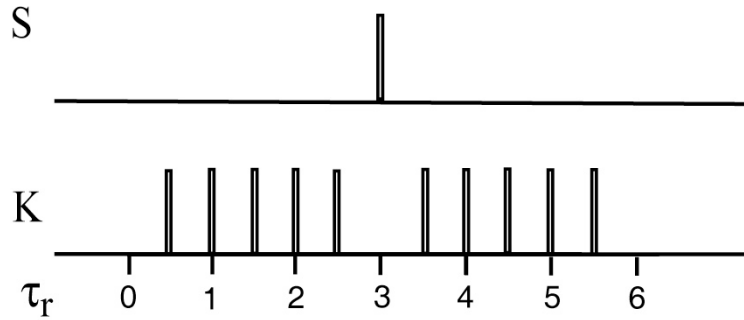


Figure 1.13.3. REDOR pulse sequence. All open bars represent  $180^\circ$  pulses applied synchronously with the rotation period  $\tau_r$ .

Other techniques that measure dipolar couplings between unlike spins are for example rotational-echo double resonance REDOR [33] and transferred echo double resonance TEDOR [34]. Figure 1.13.3 depicts one version (of many possible) REDOR sequences. Rotor synchronized  $180^\circ$  pulses are applied every half rotor period to recouple the heteronuclei dipolar interaction.

The spin Hamiltonian for two nuclei S and K is given by:

$$\begin{aligned}H_D &= \omega_{sk}(t) S_z K_z = \\ &= \frac{b_{sk}}{2} \left[ \sin^2(\beta) \cos(2\gamma + 2\omega_r t) - \sqrt{2} \sin(\beta) \cos(\gamma + \omega_r t) \right] S_z K_z \quad (1.13.12)\end{aligned}$$

where the Euler angles  $\beta$  and  $\gamma$  relate the PAS system associated with the dipolar tensor to the rotor fixed frame.  $180^\circ$  pulses applied each half rotor period invert the sign of the dipolar evolution and thus prevent refocusing of the dipolar coupling interaction. The

effective dipolar Hamiltonian  $H_{D,Av}$ , averaged over one rotor period  $\tau_r$  for a single crystallite is obtained by summation of the integrals over  $H_D(t)$ :

$$\begin{aligned} H_{D,Av} &= \frac{1}{\tau_r} \left[ \int_0^{\tau_r/2} H_D(t) dt - \int_{\tau_r/2}^{\tau_r} H_D(t) dt \right] \\ &= \frac{2\sqrt{2}}{\pi} b_{sk} \sin(\beta) \cos(\beta) \sin(\gamma) S_z K_z \end{aligned} \quad (1.13.13)$$

All basic recoupling techniques for unlike spin are viewed by Dusold and Sebald [32].

General approach to design re- and decoupling pulse sequences using symmetry principles for rotor synchronized pulses was developed by Levitt and coworkers [35,36,37].

#### 1.14 Overview of the thesis.

The major part of this thesis covers investigations on the potential use of deuteration in protein by ssNMR for proton detection and resolution enhancement, monitoring backbone motion, detection of dynamic water molecules. Furthermore pulse sequence is developed to achieve  $^{13}\text{C}$ - $^{13}\text{C}$   $J$  decoupling to increase the carbon spectral resolution.

In Chapter 2, proton detected experiments in MAS ssNMR of protein are represented. While proton detection in solution state NMR is a routinely used technique to increase sensitivity, application to ssNMR is hampered by broad  $^1\text{H}$  lines due to large proton-proton dipolar couplings. We show that deuteration of  $^{15}\text{N}$  labeled protein  $\alpha$ -SH3 allows proton detection without homonuclear decoupling at moderate spinning frequency of 10 kHz [38]. Further increase of the level of deuteration in the protein results in ultrahigh resolution of  $^1\text{H}$  and  $^{15}\text{N}$  resonances which can be obtained in 2D experiments without any homo- and heteronuclei decoupling [28].

In Chapter 3, TROSY effects [39] in ssNMR are analyzed. This effect can be exploited to study dynamic effects in the solid state to relate their effect on line width. A strong temperature dependence of the differential line width was observed. This study



might have significant impact for the improvement of resolution for solid state studies of large biomolecules. Resolution enhancement pulse schemes based on spin-state-selection schemes were implemented. Efficiency of different  $^1\text{H}$  and  $^{15}\text{N}$  polarization transfer techniques like CP and INEPT were analyzed.

In Chapter 4, the dynamics of the protein backbone of  $\alpha$ -SH3 domain is investigated by measurements of  $^{15}\text{N}$   $T_1$  and  $T_2$ . High resolution allows establish a correlation between  $T_1$ ,  $T_2$  values and the secondary structure elements of the protein. Slow and fast correlation times as well as order parameters might be obtained in course of these experiments and can be correlated to the secondary structure. Proton-nitrogen dipolar couplings have been measured to calculate order parameters.

Detection of water molecules and their dynamics in deuterated proteins was studied in Chapter 5. We present two experiments to measure the effective  $T_2$  decay rate of individual amide protons and the magnetization buildup rates between water and amide protons using spin diffusion as mixing element [40]. The obtained NMR experimental data are correlated with the dipolar couplings calculated from the  $\text{H}_2\text{O}-\text{H}^{\text{N}}$  distances as extracted from the X-ray structure of the protein. The experiments allow the site specific detection of water molecules in the solid state.

In Chapter 6, we show that decoupling of the  $^{13}\text{C}$ - $^{13}\text{C}$  homonuclear scalar couplings during stroboscopic detection can be successfully applied in order to increase the spectral resolution up to a factor of 2-2.5 and sensitivity up to a factor of 1.2. We expect that this approach will be useful for the study of larger biomolecular systems like membrane proteins and amyloidogenic peptides and proteins where spectral overlap is critical. The experiments are demonstrated on a uniformly  $^{13}\text{C}$ ,  $^{15}\text{N}$  labelled sample of Nac-Val-Leu-OH and applied to an uniformly  $^{13}\text{C}$ ,  $^{15}\text{N}$  enriched sample of a hexameric amyloidogenic peptide [41].

## 2 Chapter. Proton detection in MAS solid state NMR of proteins.

### 2.1 Introduction.

Structure investigations of non-crystalline solids by high resolution ssNMR made rapid progress during the last few years. Successful spectral assignment and determination of structural constraints in isotopically enriched materials (mostly  $^{13}\text{C}$ ,  $^{15}\text{N}$ ) is still limited by resolution and sensitivity. These limitations hamper application of current solid-state NMR techniques to larger important biological systems beyond 8kDa, like membrane proteins. In the past, many methods have been developed to suppress strong anisotropic interactions and improve line width in ssNMR, like sample preparation [42], fast and ultra fast MAS [43,44,45], development of hetero- and homonuclear dipole-dipole and  $J$  decoupling sequences [23,24,29,41,46]. Many ssNMR experiments involve protons as active nuclei in the pulse sequences for assignment [47] and proton-proton distances evaluations[40,48,49]. Sensitivity gain in these experiments could be achieved via direct proton detection, making use of their high gyromagnetic ratio  $\gamma$  which is a routine technique in solution state NMR. The indirect-to-direct relative signal to noise ratio for HETCOR experiments according to [50,51] is :

$$\frac{\left(\frac{S}{N}\right)_H}{\left(\frac{S}{N}\right)_X} = f \cdot \frac{\gamma_H^{3/2} \cdot Q_H^{1/2} \cdot A_H}{\gamma_X^{3/2} \cdot Q_X^{1/2} \cdot A_X} \cdot \sqrt{\frac{(\Delta\nu)_X \left(\nu_{1/2}\right)_X}{(\Delta\nu)_H \left(\nu_{1/2}\right)_H}} \quad (2.1.1)$$

where  $f$  is the efficiency of an additional magnetization transfer step from the  $X$  nucleus back to  $^1\text{H}$ ,  $\Delta\nu$  is the bandwidth of the nucleus detected in indirect dimension.  $Q$  is the quality factor of the RF coil for  $^1\text{H}$  and  $X$  nuclei.  $A$  describes geometrical factors, which might be different for  $^1\text{H}$  and  $X$  nuclei. The enhancement is inversely proportional to the ratio of the square root of the line widths  $(\nu_{1/2})_H$ . Except of the sensitivity enhancement, line narrowing in the proton dimension is very important for the improvement of resolution, since proton detection in ssNMR is hampered by large proton

line widths induced mostly by  $^1\text{H}$ - $^1\text{H}$  dipolar interactions. That is why the reduction of  $^1\text{H}$  line width is key to successful proton detection in ssNMR.

Several different approaches have been used to achieve  $^1\text{H}$  line narrowing for rotating solids. A number of windowed homonuclear decoupling schemes [52,53,54] were successfully employed for resolution and sensitivity enhancement in ssNMR. These approaches yield a  $^1\text{H}$  line width of 100-200 Hz, but suffer from the requirement of large receiver bandwidths, which allow audio frequency noise to fold into the spectral region and compromise overall sensitivity. The applied pulse sequences scale down  $^1\text{H}$  chemical shift dispersion, making them best suited for samples for which resolution is not critical.

In recent years, high speed ( $>30\text{kHz}$ ) MAS instrumentation became available [43,44,45], but unfortunately even at high spinning rates ( $>30\text{kHz}$ ), fully protonated samples still have broad ( $>500\text{Hz}$ ) homogenous lines. So fast spinning alone does not seem to provide a reasonable solution.

Alternatively,  $^1\text{H}$  line narrowing in solids could be achieved by combination of isotropic spin dilution and moderate (10-20 kHz) MAS which has been applied to peptides [55,56]. Dilution was achieved by perdeuteration of the sample with subsequent back-exchange of amide protons. In such samples the total proton density, which is a major determinant of the  $^1\text{H}$  line width, is usually well below  $1.0\text{ }^1\text{H}/100\text{\AA}^3$  [57,58]. It has been shown by Reif and Griffin [55] that perdeuteration yields significant improvement in sensitivity for  $^1\text{H}$  vs  $^{15}\text{N}$  detection by a factor of 5 and 9 at 13 KHz and 33 kHz, respectively.

A relevant problem in proton detected experiments of biological samples consists, however, in suppression of the magnetization of the residual solvent, necessary to keep samples hydrated.

In this chapter we demonstrate the use of moderate and high proton density dilution for  $^1\text{H}$  line narrowing. Dilution was achieved in a perdeuterated  $^{15}\text{N}$  enriched sample of the SH3 domain from chicken  $\alpha$ -spectrin via back-exchange of amide protons using 100%  $\text{H}_2\text{O}$  and a 10:90  $\text{H}_2\text{O}$ - $\text{D}_2\text{O}$  mixture for moderate and high proton density dilution. The sample dissolved in a 10:90  $\text{H}_2\text{O}$ - $\text{D}_2\text{O}$  mixture is dubbed as “dilute sample” and the one resolved in 100%  $\text{H}_2\text{O}$  is dubbed “deuterated”.

## 2.2 Sample preparation and NMR spectroscopy.

Sample preparation was done by Kristina Rehbein and Dr. Anne Diehl. A pET3d derivative coding for  $\alpha$ -spectrin SH3 domain from chicken brain was a gift of M. Saraste. The SH3 was expressed in *E. coli* BL21 (DE3) on M9 minimal medium in 100% D<sub>2</sub>O with 4 g/l d8-glycerol as the sole C-source and 1 g/l 15N NH<sub>4</sub>Cl. The cells grew at 37°C up to an optical density (OD<sub>600nm</sub>) of 0.6, then the temperature was dropped down to 22°C and the induction was started with 1 mM IPTG over night. The purification was done in H<sub>2</sub>O-buffered systems (anion exchange on Q-Sepharose FF and gelfiltration on Superdex75) as reported earlier [42] and resulted in an amide protonated, carbon deuterated preparation (reference sample). 15 mg of that sample were lyophilized and resolved in 10:90 H<sub>2</sub>O-D<sub>2</sub>O mixture to obtain a so called “dilute sample” with respect to protons.

From both samples microcrystalline precipitates were produced by mixing the protein solution (10 mg/ml) 1:1 with 200 mM (NH<sub>4</sub>)<sub>2</sub>SO<sub>4</sub> in H<sub>2</sub>O or 90% D<sub>2</sub>O, respectively, and adjusting the pH to 7.

NMR spectroscopy was carried out on Bruker-Avance wide bore instruments operating at 400MHz, 500MHz and 600MHz proton Larmor frequency. For experiments at 600MHz, a 4 mm and a 3.2 mm triple resonance probe were used to carry out experiments at MAS frequencies in the range of 8-13 kHz and 18-24 kHz respectively. Experiments at 500MHz and 400MHz were conducted using 2.5mm and 4mm probe respectively. In all experiments the sample temperature was kept constant at 275K.

## 2.3 <sup>1</sup>H Detection in MAS ssNMR spectroscopy of proteins employing Pulsed Field Gradients for residual solvent suppression.

The proton detected ssNMR experiments were carried out on a deuterated uniformly <sup>15</sup>N enriched sample of  $\alpha$ -SH3. Pulsed field gradients (PFG) were used for water signal suppression. In contrast to solution state, where water molecules tumble freely, they are tightly bound to the protein microcrystals in the solid state. Conventional water suppression pulse sequence like presaturation and binomial excitation schemes [59]

are impossible due to saturation transfer and the broad  $^1\text{H}$  water resonance line. Figure 2.3.1 shows the pulse sequences that are employed for the  $^{15}\text{N}$  and  $^1\text{H}$  detected  $^1\text{H}$ - $^{15}\text{N}$  correlation experiments:

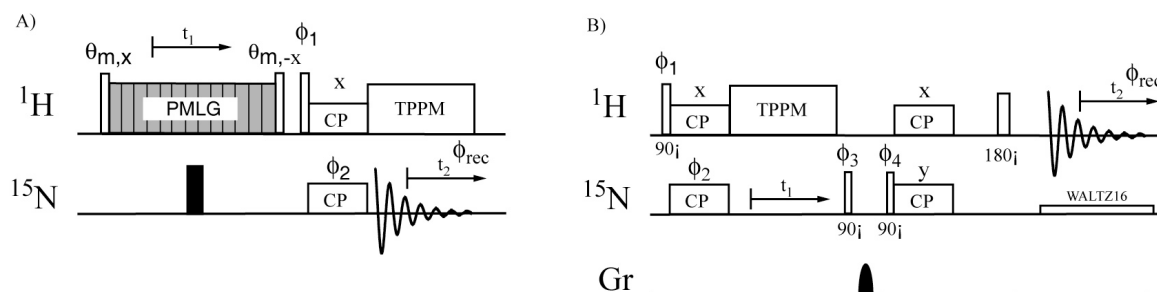


Figure 2.3.1. A)  $^{15}\text{N}$  detected  $^1\text{H}$ - $^{15}\text{N}$  correlation experiment employing PMLG [24] for proton-proton dipolar decoupling in the indirect dimension. Conventional 4 step phase cycle has been used:  $\phi_1=x,-x$ ;  $\phi_2=y, y, -y, -y$  and  $\phi_{\text{rec}}=x, -x, -x, x$ . B)  $^1\text{H}$  detected  $^1\text{H}$ - $^{15}\text{N}$  correlation experiment using PFG for  $\text{H}_2\text{O}$  suppression. A 16 step phase cycle is employed for optimum water suppression:  $\phi_1=y,-y$ ;  $\phi_2=2(y), 2(-y)$ ;  $\phi_3=4(x), 4(-x)$ ;  $\phi_4=8(x), 8(-x)$ ;  $\phi_{\text{rec}}=\phi_1+\phi_2+\phi_3+\phi_4$ . All  $90^\circ$  and  $180^\circ$  pulses are represented by open and black bars respectively. Gradient pulse is represented by shaped bar.

Both experiments were recorded at a spinning frequency of 10 kHz and a temperature of 275K. Conventional  $^{15}\text{N}$  detected experiment was recorded using PMLG [24] in the indirect evolution period to suppress residual proton-proton dipolar couplings which can not be fully removed by moderate spinning and deuteration. The CP [30] transfer time from  $^1\text{H}$  to  $^{15}\text{N}$  was set to 160  $\mu\text{s}$  using a typical field of 60 kHz and 50 kHz on the proton and the nitrogen channel, respectively. After CP, TPPM [29] decoupling is applied with rf power of 80kHz for efficient decoupling of protons. In the  $^1\text{H}$  detected version of the experiment,  $^{15}\text{N}$  magnetization is stored along Z axis after the the indirect evolution period for water suppression. A purge gradient is applied to dephase residual transverse water magnetization. Typically, sine-shaped gradients are employed of 5 ms duration and 30 G/cm of maximum strength. After back-transfer to  $^1\text{H}$ , a Hahn-echo, comprising two rotor periods, was implemented to eliminate baseline rolling due to probe ring down. WALTZ-16 was applied on the  $^{15}\text{N}$  channel during detection to achieve heteronuclear scalar decoupling, which is about 94 Hz. Recorded 2D spectra are represented on the figure 2.3.2:

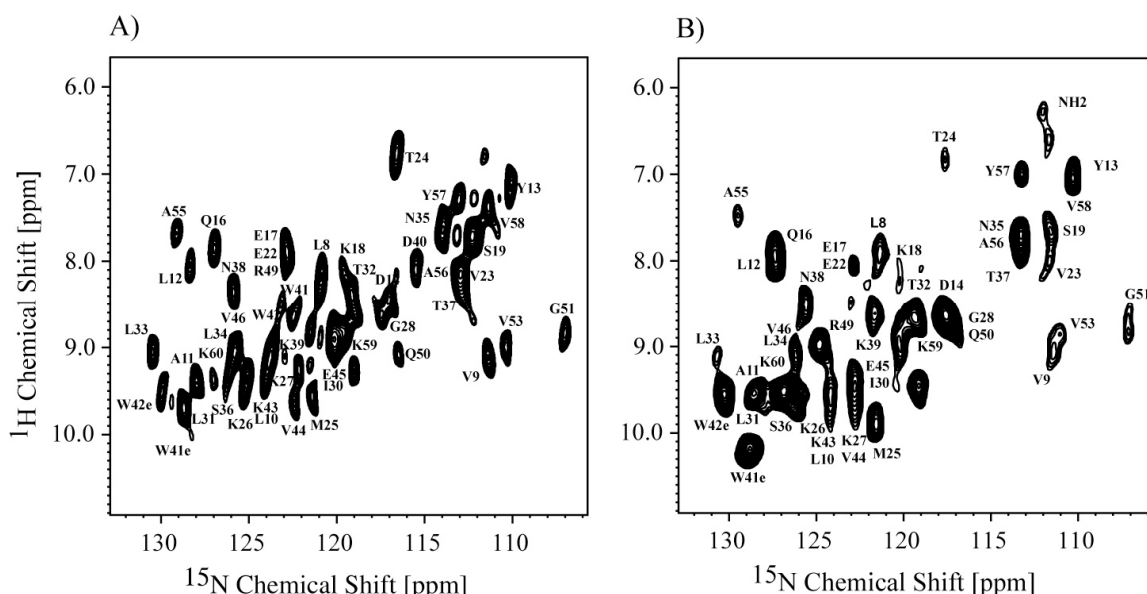


Figure 2.3.2. Experimental  $^{15}\text{N}$  A) and  $^1\text{H}$  B) detected  $^1\text{H}$ ,  $^{15}\text{N}$  correlation spectra using the pulse sequence displayed in Figure 2.3.1. For clarity, the  $^1\text{H}$  detected spectrum is displayed mirror imaged. Spectra have been recorded at  $B_0=500$  MHz of proton frequency, using a commercial 2.5mm double resonance probe which has been equipped with a gradient coil. The assignment is based on ref. [47].

The 1D single excitation pulse experiment shows that the water magnetization is approximately a factor of 1000 larger with respect to the protein  $\text{H}^{\text{N}}$  resonances as it is shown in figure 2.3.3 A and B. Figure 2.3.3 C shows a proton spectrum after a  $x$ -filter employing a double CP transfer without PFG pulses. A phase cycle of 128 scans results in water signal suppression by a factor of 500. However, still  $\text{RG}=32$  has to be employed. Combination of a  $x$ -filter and PFG allows to suppress the water signal to insignificant levels and remove artifacts at  $\pm 1.5$  kHz from the water signal as it is shown in figure 2.3.3 D. The receiver gain is increased to 1024.

Application of PMLG to achieve  $^1\text{H}$ ,  $^1\text{H}$  decoupling yields only moderate increase in resolution. For example residue G51 has a line width of 171 Hz and 268 Hz with and without employing PMLG, respectively. The loss in sensitivity associated with the windowed proton-proton decoupling pulse sequence [52,53] during detection therefore outweighs the possible improvement in resolution. The apparent resolution in the  $^1\text{H}$  dimension in the  $^1\text{H}$  detected experiment is approximately a factor 1.5 times smaller compared to the resolution that is achievable in the  $^{15}\text{N}$  detected version using PMLG for  $^1\text{H}$ ,  $^1\text{H}$  homonuclear decoupling in the indirect  $^1\text{H}$  dimension. Different intensities of

certain cross-peaks can be attributed to tightly bound water molecules in the protein structure which lead to a differential dipolar broadening of the individual  $^1\text{H}$  amid resonances in the  $^1\text{H}$ -detected experiment.

The influence of PFG on the water signal suppression is shown in the figure 2.3.3:

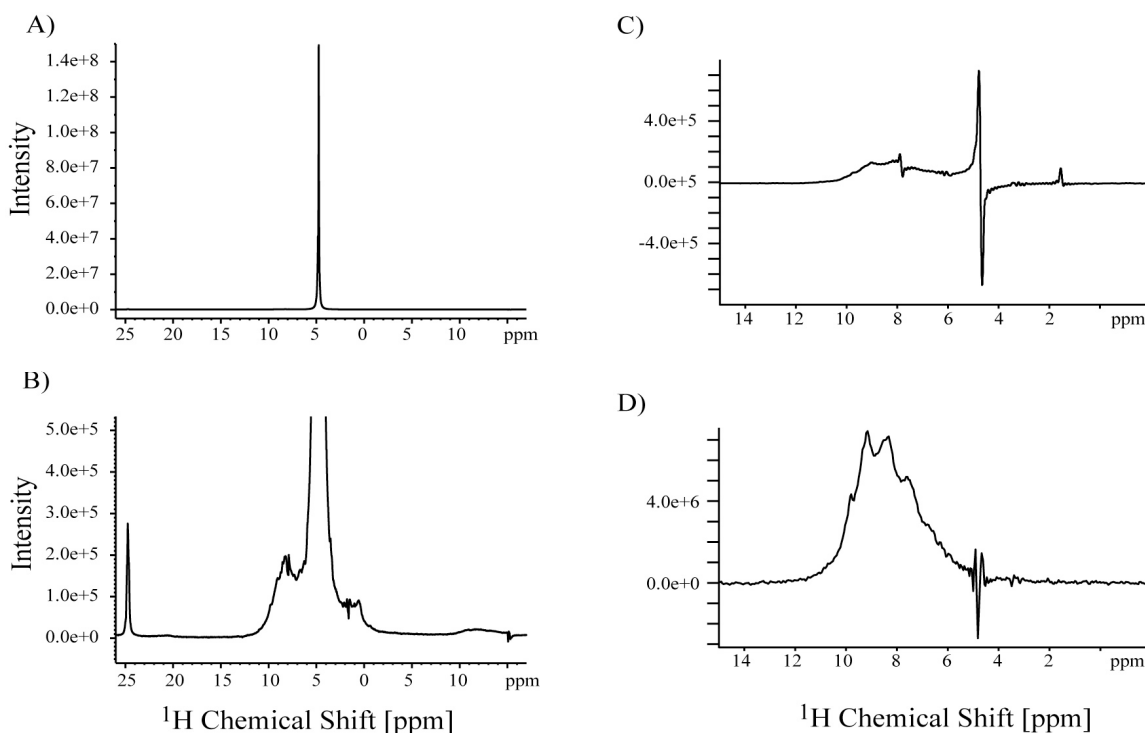


Figure 2.3.3.  $^1\text{H}$ -1D spectra for a deuterated  $^{15}\text{N}$  labeled  $\alpha$ -SH3 domain. A) and B) represent single excitation pulse experiment at different scaling factor. The water magnetization is approximately a factor of 1000 larger with respect to the HN resonances of the protein. The receiver gain (RG) has to be set to 32. C) x-filter experiment. The 1D version of the experiment is represented in figure 2.3.1 B recorded without the PFG pulses. The water signal is suppressed by a factor 500 only after 128 step phase cycling. However, still RG=32 has to be employed. D) Combination of a x-filter and PFG allows to suppress the water signal to an insignificant level and remove artifacts at  $\pm 1.5$  kHz from the water signal. The receiver gain is increased to 1024. For each experiment 128 scans have been accumulated at a spinning frequency of 10 kHz.

This approach allows to obtain high resolution proton detected  $^1\text{H}$ - $^{15}\text{N}$  correlation spectra, which have been reported for two small proteins [38,48,51], where the  $^1\text{H}$  line width of most resonances is typically on the order 150-250 Hz. The limits of resolution that can be obtained in  $^1\text{H}$ - $^{15}\text{N}$  2D NMR spectroscopy of isotopically enriched nanocrystalline proteins were explored by Zilm and coworkers [60]. Combinations of frequency switched Lee-Goldburg (FSLG) decoupling, fast magic angle sample spinning,

and isotopic dilution via deuteration are investigated as methods for narrowing the amide  $^1\text{H}$  resonances. The combination of these techniques results in  $^1\text{H}$  lines width on the order of 120-240 Hz at optimal conditions.

As it has been shown by others the resolution in the proton dimension at direct proton detection can be increased by application of higher spinning frequency, stronger external magnetic fields [48,51] and lower proton density [27,28,61] in proteins and peptides. The most promising results in resolution have been obtained by using high levels of proton density dilution, which are described in the next section.

## **2.4 Ultra-high resolution in proton solid-state NMR at high levels of deuteration.**

Using high proton density dilution allows to get extremely narrow proton lines on the order of 17-35 Hz at moderate spinning frequencies without homonuclear decoupling [28]. A high degree of dilution was achieved in perdeuterated  $^{15}\text{N}$  enriched sample of the SH3 domain from chicken  $\alpha$ -spectrin via backexchange of amide protons using a 10:90  $\text{H}_2\text{O}:\text{D}_2\text{O}$  mixture.

The employed 2D pulse scheme using proton detection is illustrated in figure 2.4.1 A. Effective suppression of the dominant water resonance was achieved by modification of the constant time (CT) experiment suggested by Zilm and coworkers [51]. The experiment starts with a  $90^\circ$   $^1\text{H}$  excitation pulse, followed by a ramped CP magnetization transfer of 800  $\mu\text{sec}$  duration from protons to nitrogen. The desired component of  $^{15}\text{N}$  polarization is stored along the Z axis during a variable delay ( $\tau-t_1/2$ ), which precedes and follows the  $^{15}\text{N}$  evolution period  $t_1$ . Two delays ( $\tau-t_1/2$ ) are required to introduce a  $180^\circ$  proton pulse for  $J$  decoupling in the indirect dimension keeping the experiment in a CT fashion for efficient water suppression. The total duration  $2\tau=t_{1\text{max}}$  is kept constant. We did not apply any heteronuclear decoupling schemes like TPPM or XiX in the indirect dimension, since high proton density dilution completely removes proton-proton dipolar couplings and makes the spin system inhomogeneous in the sense of Maricq and Waugh [20]. In this system,  $^{15}\text{N}$ - $^1\text{H}$  heteronuclear dipolar couplings have a minor influence on the  $^{15}\text{N}$  line width if the spinning rate is comparable or higher than the size of the interaction. The fixed delay  $\tau_w$ , following the  $t_{1\text{max}}$  period, is optimized for  $^1\text{H}$  water signal dephasing.



During  $\tau_w$ ,  $^{15}\text{N}$  magnetization is stored along the Z axis. Typical values for  $t_{1\text{max}}$  and  $\tau_w$  in our experiments are on the order of 30-50msec and 60-120 msec, respectively. As it was shown by Emsley and coworkers [8], the longitudinal relaxation time  $T_1$  of  $^{15}\text{N}$  is on the order of 7-20s, which allows to store  $^{15}\text{N}$  magnetization along the Z axis without significant losses within 170 msec. The back polarization transfer from  $^{15}\text{N}$  to  $^1\text{H}$  is accomplished using a second 800  $\mu\text{sec}$  ramped CP.  $^1\text{H}$  magnetization is finally acquired using the WALTZ-16  $^{15}\text{N}$  decoupling scheme [51], which was found to be more efficient in comparison to GARP and CW irradiation. The employed field strength on the  $^{15}\text{N}$  channel was set to 1.6 kHz.

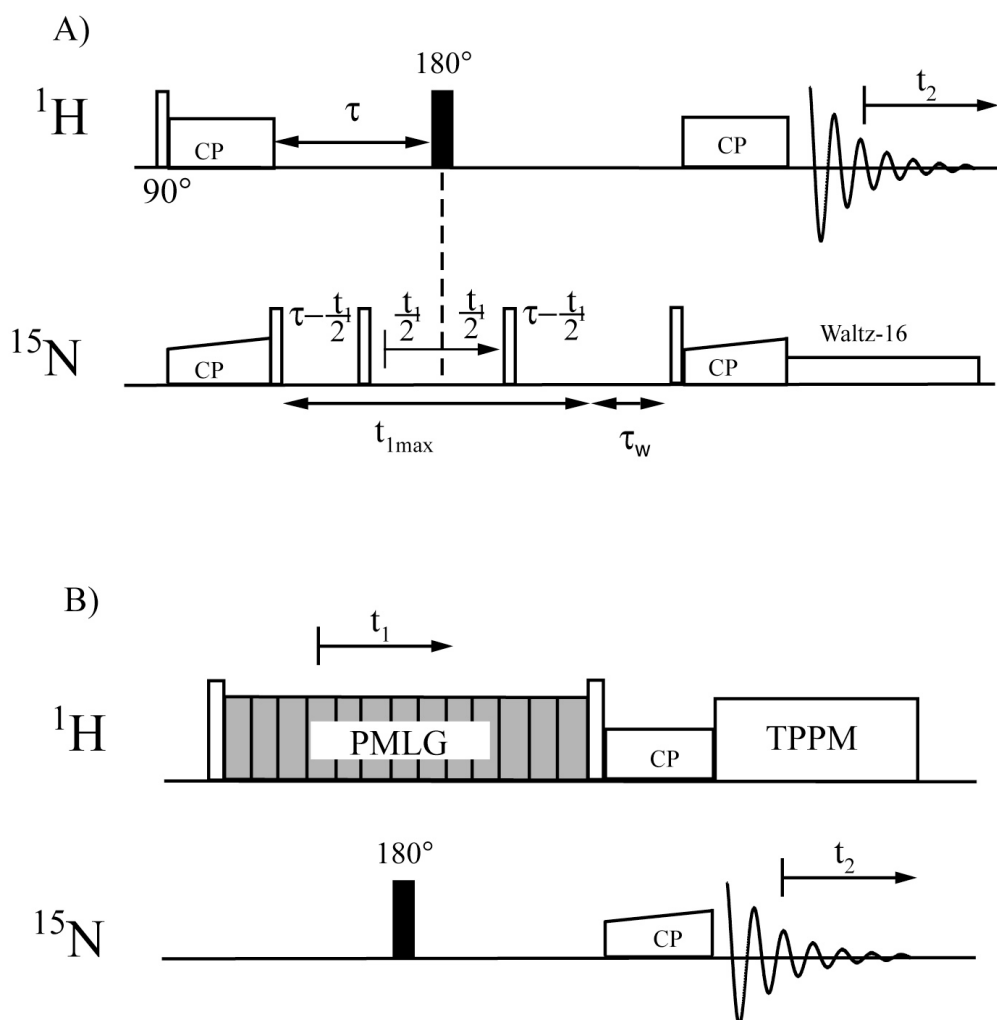


Figure 2.4.1. A) Pulse sequences employed for  $^1\text{H}$  and detected  $^{15}\text{N}$ - $^1\text{H}$  correlation experiments. B) Pulse sequence employed for  $^{15}\text{N}$  detected  $^{15}\text{N}$ - $^1\text{H}$  correlation experiments using PMLG-9 for  $^1\text{H}$ - $^1\text{H}$  decoupling.

Figure 2.4.1 B represents the pulse sequence which is employed for the  $^{15}\text{N}$  detected  $^1\text{H}$ - $^{15}\text{N}$  HSQC spectra. PMLG-9 [24] for  $^1\text{H}$ - $^1\text{H}$  decoupling in the indirect dimension was employed with an  $180^\circ$  pulse on the  $^{15}\text{N}$  channel for  $J$  decoupling in the middle of  $t_1$ . Homonuclear  $^1\text{H}$ - $^1\text{H}$  decoupling was performed using a proton RF fields of 81 kHz. During  $^{15}\text{N}$  detection, TPPM [29] proton decoupling was applied using a RF field of 90 kHz.

$^1\text{H}$  resolution improvement in case of a highly proton dilute protein sample has been examined. The  $^1\text{H}$ - $^{15}\text{N}$  HSQC spectra were recorded using  $^1\text{H}$  detection for sensitivity enhancement. As a reference to compare proton resolution, we recorded a  $^{15}\text{N}$  detected  $^1\text{H}$ - $^{15}\text{N}$  HSQC spectrum of perdeuterated  $\alpha$ -SH3 employing PMLG in the indirect dimension, which provides the best proton resolution at a magnetic field strength of 400-600MHz and at a spinning frequencies of 8-13kHz.

Figure 2.4.2 shows the comparison of the  $^{15}\text{N}$  and  $^1\text{H}$  detected  $^1\text{H}$ - $^{15}\text{N}$  HSQC experiments for the normal ( Fig. 2.4.2 B, D) and the dilute ( Fig. 2.4.2 A, C )  $\alpha$ -SH3 sample. The  $^1\text{H}$  detected experiments were acquired using the NMR pulse sequence shown in figure 2.4.1 A. The  $^{15}\text{N}$  detected experiments were acquired using the pulse scheme represented in figure 2.4.1 B. Figures 2.4.2 A and 2.4.2 C show the  $^1\text{H}$  detected experiments for the dilute sample at 400MHz and 600MHz proton Larmor frequency, respectively. The spinning frequency was set to 13kHz which is the maximum available for a commercially available 4mm rotor. For comparison, the  $^{15}\text{N}$  detected spectra for the normal sample are represented as well, in figure 2.4.2 B and figure 2.4.2 D. For clarity figure 2.4.2 B and 2.4.2 D are represented mirror imaged. In these experiments the spinning frequency was adjusted to 10kHz. It was shown previously that the proton line width is not sensitive to moderate changes in the spinning rate under homonuclear decoupling sequences [25,62], if broadening conditions due to interference between MAS and the periodicity of the decoupling sequence are avoided [25]. All spectra are apodized with 5 Hz lorentzian line broadening in both dimensions. Obviously, the resolution in the proton dimension is clearly improved yielding a fully resolved  $^{15}\text{N}$ - $^1\text{H}$  HSQC spectrum of the SH3 domain even at 400MHz external field. The experiments demonstrate the advantages of high degrees of proton spin density dilution, leading to an ultimate  $^1\text{H}$  resolution enhancement, which was not available so far despite many attempts to achieve

$^1\text{H}$  line narrowing, such like homonuclear decoupling and the development of ultra high speed MAS technology.

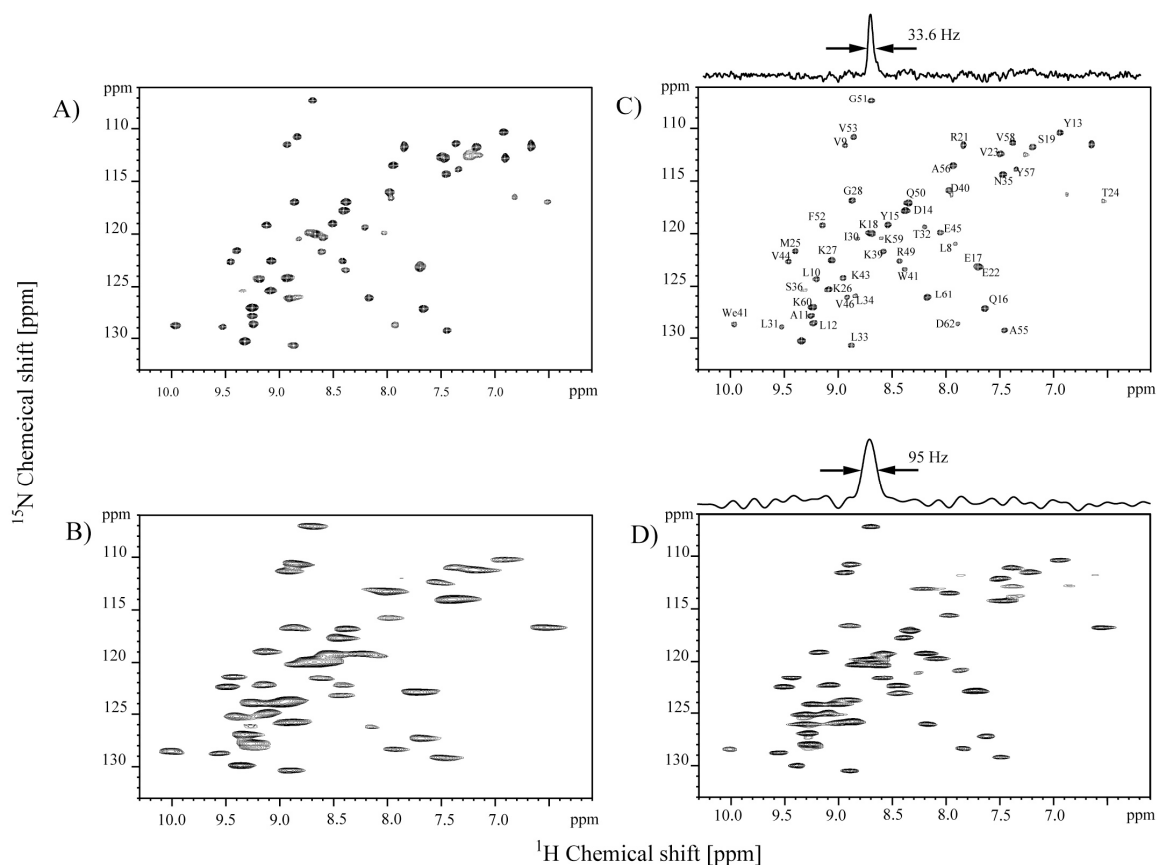


Figure 2.4.2. A) and C)  $^1\text{H}$  detected 2D  $^{15}\text{N}$ - $^1\text{H}$  correlation experiments of the dilute sample recorded at 400 MHz and 600 MHz instruments respectively, according to pulse scheme represented on Fig. 2.3.1 A). Figure B) and D)  $^{15}\text{N}$  detected 2D  $^{15}\text{N}$ - $^1\text{H}$  correlation experiments for the normal sample recorded at 400 MHz and 600 MHz instruments respectively, according to the pulse scheme represented in figure 2.3.1 B). All spectra were apodized using 5 Hz Lorentzian broadening in both dimensions. The row on the top of spectrum acquired on 600 MHz spectrometer represents a trace in the  $^1\text{H}$  dimension through the residue G51 with corresponding line width.

Figure 2.4.3 represents the  $^1\text{H}$  line width as a function of the rotor period for selected residues:

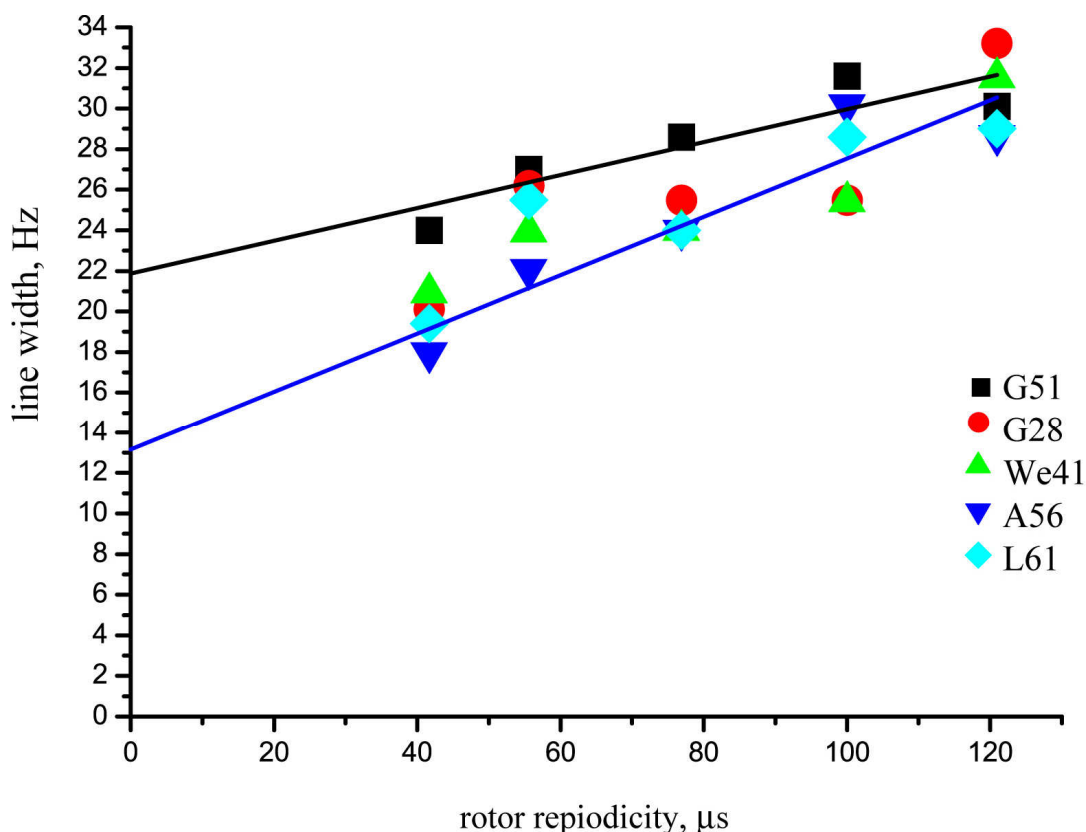


Figure 2.4.3.  $^1\text{H}$  line width as a function of inverse spinning rate for selected residues. Linear fit is made for G51 and A56.

The line width was measured at half height for each of the peaks. At first approximation, the line width is proportional to the inverse spinning rate. Similar results were obtained for adamantane [63] and polycarbonate [64]. Of particular interest is an investigation of protonated alanine which was studied embedded in a deuterated alanine matrix [61]. All these results show that in the fast spinning regime the residual dipolar line width is inversely proportional to the rotational frequency. Rienstra and coworkers [61] studied the slope of the line widths dependence on the spinning rate on the concentration of unexchangeable protons in the sample. The slope strongly depends on the proton density and varies from 6728 Hz/ms to 970 Hz/ms from the highest to the lowest degree of protonation. We found that the line widths is inversely proportional to the spinning rate as well. The fitted lines for residues G51 and A56 have slopes of 80.8 Hz/ms and 144 Hz/ms, respectively, what indicates that the achieved proton density in our dilute sample is much lower. In inhomogeneous spin systems, the line width does not depend on the rotational frequency if the later is comparable or higher than the size of the interactions, that is why

non-zero slopes of the fitted lines manifest that spin Hamiltonian of the studied system has a homogeneous nature [15] despite high proton density dilution, which can not totally suppress  $^1\text{H}$ - $^1\text{H}$  dipolar couplings. The fitted lines in figure 2.3.3 have not vanishing y-intercepts, implying that even infinite MAS rates can not remove all line broadening. This could be explained by the inherent relaxation time  $T_2$ , the sample heterogeneity, static field inhomogeneities (ca. 7 Hz, based on the  $^1\text{H}$  line width of the water sample, used for shimming of the probes). We attribute differences in the line widths, y-intercepts and slopes for the fitted lines to site to site variation in  $T_2$  relaxation time, local proton density, sample inhomogeneity. While the  $^1\text{H}$  line width for the dilute sample is on the order of 25-40 Hz, the line width of the normal sample under PMLG amounts to 80-150 Hz, after rescaling. The resolution in the proton dimension is therefore improved by a factor of 3-4 times. The  $^{15}\text{N}$  line width in both experiments is on the order of 20-30 Hz. In case of the  $^{15}\text{N}$  detected experiment PMLG and TPPM decoupling pulse sequences are applied for a total duration of 40-50 msec during each scan. This irradiation results in significant sample heating, which can reduce the life time of the sample even under good cooling conditions in case of short repetition delays [65]. In addition, application of decoupling pulse sequences decreases the achievable signal to noise ratio.  $^1\text{H}$  detected NMR experiments for the dilute sample do not require any decoupling irradiation, making this approach free of these disadvantages and reducing experimental set up time. The experimental scheme does not require rescaling of the proton chemical shift dimension, which is a problem associated with application of homonuclear decoupling sequences.

$^1\text{H}$  line width improvement is achieved by dilution of the proton density by a factor of 10. This results in a decrease of the Boltzman magnetization in the same proportion and increase the longitudinal relaxation time  $T_1$ . These factors are partially compromised by using  $^1\text{H}$  detection for sensitivity enhancement and the 4 fold  $^1\text{H}$  line narrowing, which makes experiments reasonably short. To record a 2D  $^1\text{H}$  detected spectrum we used 64 scans per FID with 3.8 hours of total experimental time, acquisition time in the proton and the nitrogen dimension was 120 ms and 26.4, ms respectively. The  $^{15}\text{N}$  detected experiments for the normal sample require 0.6 hour of experimental time, 8 scans per FID were used, acquisition time in the proton and the nitrogen dimension was 17.2 ms and 40 ms, respectively. In both experiments we obtained approximately the same signal-to-noise ratio, which is 10.4 and 12.3 for G51 projection in the proton dimension for  $^{15}\text{N}$  and  $^1\text{H}$

detected experiment respectively, while the amount of the dilute material packed in the rotor was ca. 2 times less. Taking into account that experimental time is proportional to the amount of material in second power, we can estimate that our experimental approach requires approximately 1.5 fold more time resulting in exclusive proton resolution. The relaxation rate  $T_1$  for the bulk  $^1\text{H}$  signal was found to be equal to 0.98 s and 1.76 s for the normal and the dilute sample, respectively.

Figure 2.4.4 represents the experimental data for the  $^1\text{H}$   $T_1$  measurements:

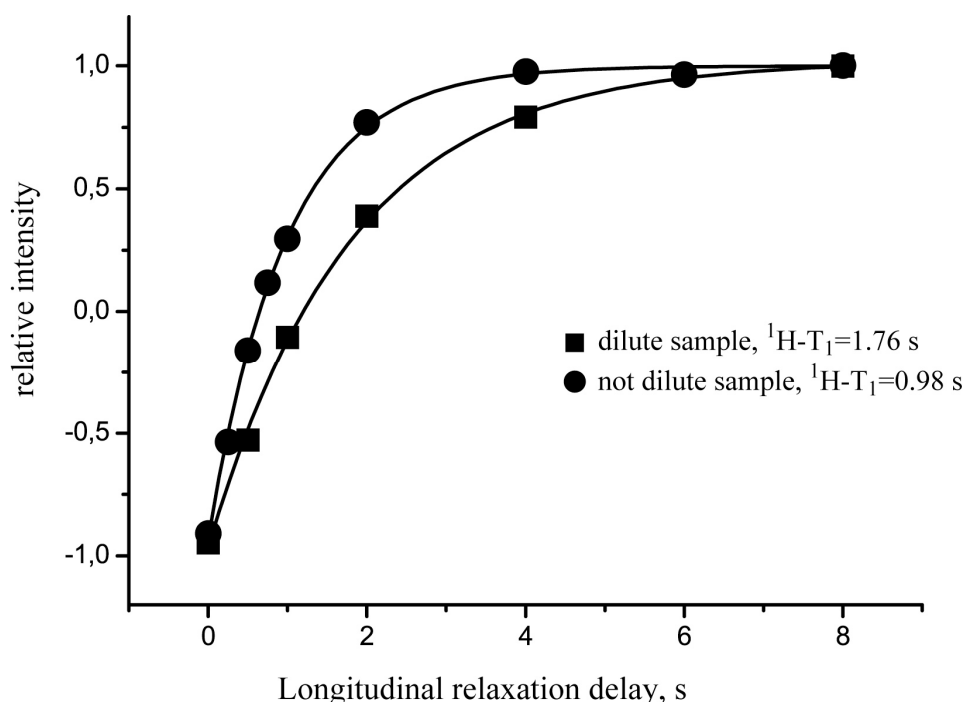


Figure 2.4.4. Inversion recovery data for  $^1\text{H}$  bulk signal of the dilute and non dilute sample. The data were fit using the function  $M(t)=M(\infty)+(M(0)-M(\infty))\cdot\exp(-t/T_1)$ .

The diluted sample has an unexpectedly short relaxation time  $T_1$ , allowing a recycle delay of 2.2 s, while for the normal sample a repetition delay of 2.3 s was used for dissipation of heat and to avoid sample degradation.

A systematic study of the proton line width in rigid solids as a function of spinning speed and proton density, with the latter controlled by the ratio of protonated and perdeuterated model compounds was carried out by Rienstra and coworkers [61]. The obtained line width for the lowest proton concentration of 5% in their model compound was on the order on 80 Hz, which is higher than in the presented experiments.

## 2.5 Conclusion.

It was demonstrated that moderate and high dilution of the proton spin density allows inverse  $^1\text{H}$  detection in ssNMR of proteins without any windowed proton-proton dipolar decoupling sequences. High degree of deuteration in a small protein allows to achieve extremely narrow proton resonance lines in the range of 17-35 Hz at moderate spinning frequencies. To our knowledge, this is the most narrow proton line width which has been reported for ssNMR experiments so far. Narrow proton lines allow high resolution  $^1\text{H}$  detected experiments at moderate magnetic fields to enhance sensitivity. The short longitudinal relaxation rate of amide protons allow a fast repetition rate in the experiments and therefore reasonably short experimental time. The labeling scheme opens perspectives in high resolution  $^1\text{H}$  detected spectroscopy for larger biological systems.

### 3 Chapter. *Transverse relaxation optimized spectroscopy in MAS solid-state NMR of proteins.*

#### 3.1 Introduction.

Differential line broadening [39,66] of  $^{15}\text{N}$ ,  $^{13}\text{C}$ ,  $^1\text{H}$  lines in doublets, determined by scalar couplings, is originated from interference of chemical shift anisotropy (CSA) and heteronuclear dipole-dipolar coupling at relaxation in proteins. Solution state NMR of biological macromolecules, after introducing transverse relaxation-optimized spectroscopy (TOSY) by Wüthrich and coworkers in 1991 [39], made a great progress towards studies of very larger proteins due to dramatically resolution improvements. As it has been shown in the original work spherical protein of 150 kDa size at external magnetic field corresponding to 750 MHz of  $^1\text{H}$  Larmor frequency has 5 and 60 Hz line widths for doublet peaks of  $^{15}\text{N}$  scalar coupled to  $^1\text{H}$ . This difference is due to the fact, that relaxation of sharp multiplet component is determined by mutually canceled CSA and heteronuclear dipole-dipolar coupling, while broad line is relaxing due to the sum of these two interactions. Conventional  $J$  decoupling techniques average out  $\text{H}^\alpha/\text{H}^\beta$  spin states and result in 33 Hz line width, while TROSY type technique selects only sharp component and benefits about 7 times in resolution in  $^{15}\text{N}$  dimension.

Characterization of dynamic processes in biological macromolecules is still mostly a domain of solution state NMR spectroscopy. However, also the solid state bears a great potential for the study of these processes [7,8,67]. So far, it is not very well understood why the spectra of a few amyloidogenic peptides or membrane proteins are characterized by very broad resonance lines [68,69,70], whereas others display a very favorable spectral quality [41,71,72,73]. The assumption that dynamic processes are the origin of these detrimental properties is corroborated by studies which demonstrate that molecules in an amyloid fibril can undergo chemical exchange between a conformation associated with an amyloid fibril and a soluble molecule [74,75]. Similar as in solution-state NMR spectroscopy, dynamic processes result in averaging of the  $\text{H}^\alpha/\text{H}^\beta$  proton spin-state in



standard  $^1\text{H}$  decoupled solid-state NMR experiments, with all the detrimental consequences to the spectra that are observed in solution-state NMR for very large proteins. On the other hand, interference between different relaxation mechanisms can be employed to manipulate the relaxation properties of a certain spin. These effects were explored with great success by Wüthrich and co-workers and resulted in the development of the TROSY technique [39,76,77,78,79].

Study of dynamic processes in the solid state found a lot of attention recently [7,8,80], as the measured experimental parameter (e.g.  $^{15}\text{N}$   $T_1$ ,  $T_2$ ,  $^2\text{H}$  quadrupolar coupling) is only dependent on local motional parameters and is not coupled to the global reorientation time  $\tau_c$  of the molecule as in solution state NMR. In order to investigate which influence protein dynamics have on the resolution in MAS solid state NMR spectral line shapes, we perform experiments on a microcrystalline sample of the chicken  $\alpha$ -spectrin SH3 domain. The X-ray structural model of the SH3 domain of chicken  $\alpha$ -spectrin at room temperature shows the high flexibility of D62, resulting in a larger variation of the spatial angle  $\Omega$  that the N-H bond vector adopts with respect to the external magnetic field [81]. This motion generates time dependent fluctuations of the local magnetic field induced by variations of the chemical shift anisotropy (CSA) of the nitrogen nucleus and the  $^{15}\text{N}$ - $^1\text{H}$  dipole-dipolar coupling (DD), which would result in differential transversal relaxation of the nitrogen magnetization due to CSA/DD cross correlated relaxation, which we focus on in our studies presented in this chapter.

Recent developments in sample preparation, allows full resolution of  $^1\text{H}$ - $^{15}\text{N}$  scalar coupling for proton and nitrogen lines by MAS solid state NMR spectroscopy [28]. These high resolution spectra were used to elucidate differential line broadening in  $^{15}\text{N}$  doublets. Due to long transversal relaxation times of  $^1\text{H}$  and  $^{15}\text{N}$ , INEPT (insensitive nuclei enhanced by polarization transfer), which is widespread solution state NMR technique, was employed to record HSQC and HMQC correlation spectra to compare with CP magnetization transfer, which is the base for heteronuclear correlation experiments in modern solid state NMR. Spin state selection, based on INEPT polarization transfer step, was applied to select narrow component of the  $^{15}\text{N}$  spectrum in order to increase apparent resolution.

### 3.2 Experimental section.

All solid state MAS NMR spectra have been obtained on SH3 domain from chicken  $\alpha$ -spectrin at extremely high level of deuteration [28]. Detailed description of the sample preparation is given in Chapter 2 and Ref. [28]. The prepared protein has been packed into 3.2 mm rotor in amounts ca. 10 mg.

The sample preparation was done by Kristina Rehbein and Dr. Anne Diehl.

NMR spectroscopy was carried out on Bruker-Avance instrument operating at 600MHz proton Larmor frequency equipped with commercial 3.2 mm double resonance probes. Typical line width for  $^1\text{H}$  and  $^{15}\text{N}$  signals obtained in such experiments are 20-30 Hz and 8-16 Hz respectively at spinning frequency of 13 kHz and 24 kHz. No rf power is needed for hetero- and homonuclear decoupling of anisotropical dipolar couplings. Proton detection schemes [28,38,51] were employed to achieve high sensitivity.

Experimental pulse sequences to study resolution and sensitivity aspects of two dimensional  $^1\text{H}$ - $^{15}\text{N}$  correlations at different  $^1\text{H}$ - $^{15}\text{N}$  polarization transfer methods are plotted in Figure 3.2.1. Figure 3.2.1 A represents  $^1\text{H}$ - $^{15}\text{N}$  correlation experiment, when CP is employed to correlate proton and nitrogen nuclear. The pulse sequence was described in details in Chapter 2 and Ref [28]. HSQC (heteronuclear single quantum coherence) and HMQC (heteronuclear multiple quantum coherence )  $^1\text{H}$ - $^{15}\text{N}$  correlation experiments employing scalar coupling for heteronuclear magnetization transfer are depicted in Figure 3.2.1 B and C respectively. These experiments were directly adopted from solution state NMR, where they play key role for heteronuclear correlation spectroscopy. In these schemes open and black bars represent  $90^\circ$  and  $180^\circ$  pulses respectively. RF fields strength of the pulses were 60 kHz for proton and 50 kHz for nitrogen channel in all represented experiments. Typical RF field strength for CP are 55 kHz for the  $^1\text{H}$  channel, while  $^{15}\text{N}$  channel was adopting values lower by spinning frequency than on proton channel. In the experiments represented in Figure 3.2.1. B and C, for optimal  $^1\text{H}$ - $^{15}\text{N}$  coherence transfer time  $t_{\text{in}}$  was optimized experimentally, and proved to be close to the theoretical optimum equal to  $1/4J_{\text{HN}}$ . For scalar  $^1\text{H}$ - $^{15}\text{N}$  decoupling  $^1\text{H}$   $180^\circ$  pulse was used in the indirect dimension, while in the direct dimension  $^1\text{H}$  magnetization was acquired using the WALTZ-16  $^{15}\text{N}$  decoupling scheme, with applied field strength of 2 kHz on the

$^{15}\text{N}$  channel. For optimal water suppression constant time experiment was used in HSQC experiment based on CP and INEPT polarization transfer.

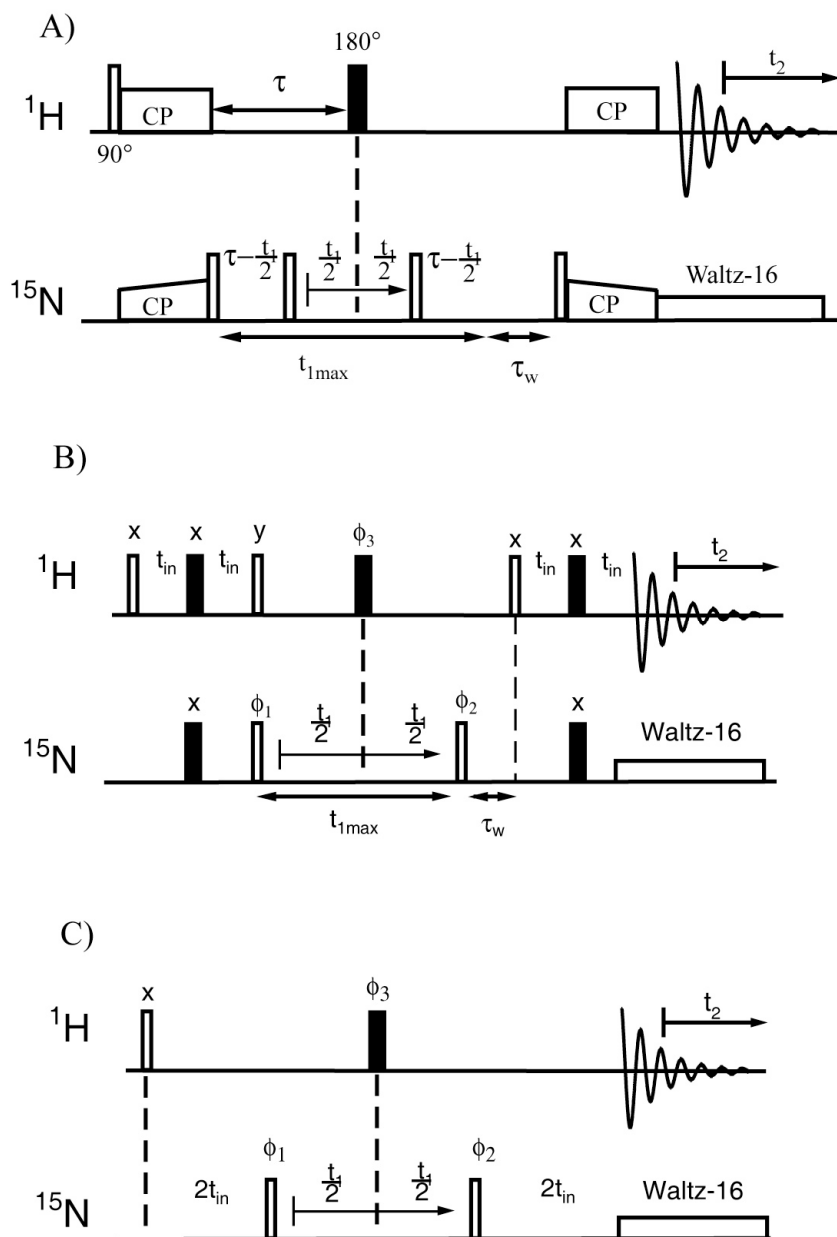


Figure 3.2.1.  $^1\text{H}$ ,  $^{15}\text{N}$  correlation pulse sequences. A) Heteronuclear polarization transfer is achieved by CP step. B) INEPT technique is employed to correlate proton and nitrogen nuclear. phase cycling is  $\phi_1=x, -x$ ;  $\phi_2=2(x), 2(-x)$ ;  $\phi_3=4(y)$  and  $\phi_{\text{receiver}}=2(x, -x, -x, x)$ . C) HMQC  $^1\text{H}$ ,  $^{15}\text{N}$  correlation spectra, using INEPT for heteronuclear magnetization transfer with employed phase cycling is  $\phi_1=x, -x$ ;  $\phi_2=8(x), 8(-x)$ ;  $\phi_3=2(x), 2(y), 2(-x), 2(-y)$  and  $\phi_{\text{receiver}}=2(x, -x, -x, x), 2(-x, x, x, -x)$ .

Narrow component of  $^{15}\text{N}$  doublet can be selected to increase apparent resolution in the indirect dimension by employing spin state selective excitation (S3E)

techniques[82]. Pulse sequence, based on an IPAP (in-phase anti-phase) [83,84] approach is illustrated in Figure 3.2.2:

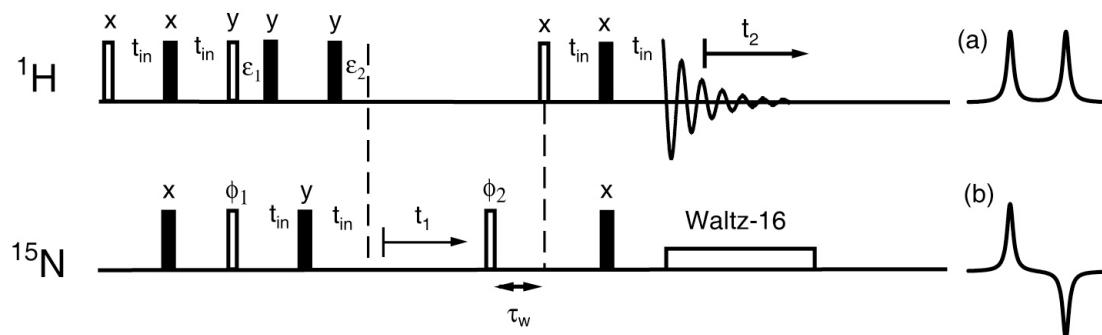


Figure 3.2.2. IPAP pulse sequence for  $^{15}\text{NH}^\alpha$  and  $^{15}\text{NH}^\beta$  spin-state-selection. Open and black bars represent  $90^\circ$  and  $180^\circ$  with 60 and 50 kHz strength on proton and nitrogen channel respectively. The in-phase spectrum is obtained adjusting the delays in filter  $\varepsilon_1 = t_{\text{in}}$  and  $\varepsilon_2 = 0$ , while phase cycling was  $\phi_1 = x, -x$ ;  $\phi_2 = 2(x), 2(-x)$  and  $\phi_{\text{receiver}} = (x, -x, -x, x)$ . The spectrum of the anti-phase spin state was recorded using delays in filter  $\varepsilon_1 = t_{\text{in}}/2$  and  $\varepsilon_2 = t_{\text{in}}/2$ , while phase cycling was  $\phi_1 = x, -x$ ;  $\phi_2 = 2(-y), 2(y)$  and  $\phi_{\text{receiver}} = (-x, x, x, -x)$ . The resulting spectra are schematically given next to pulse sequence denoted as (a) and (b) for in- and anti-phase spin state correspondingly. Their sum and difference yield the down- and upfield component of the  $^{15}\text{N}$  doublet, respectively.

### 3.3 Experimental results.

High deuteration degree of the protein allows to obtain ultra-high resolution  $^1\text{H}$ - $^{15}\text{N}$  correlation spectra in MAS solid-state NMR [27,28]. The achieved  $^1\text{H}$  and  $^{15}\text{N}$  line width is, respectively, on the order of 17-35 Hz and 8-20 Hz for MAS spinning frequencies in the range of 8-24 kHz. This approach enables  $^1\text{H}$  detected 2D  $^1\text{H}$ ,  $^{15}\text{N}$  correlation spectroscopy without homo- and heteronuclear dipolar decoupling. At the same time,  $^1\text{H}$ ,  $^{15}\text{N}$  scalar couplings can be easily base line resolved in either the direct or indirect evolution period of a multidimensional NMR experiment.

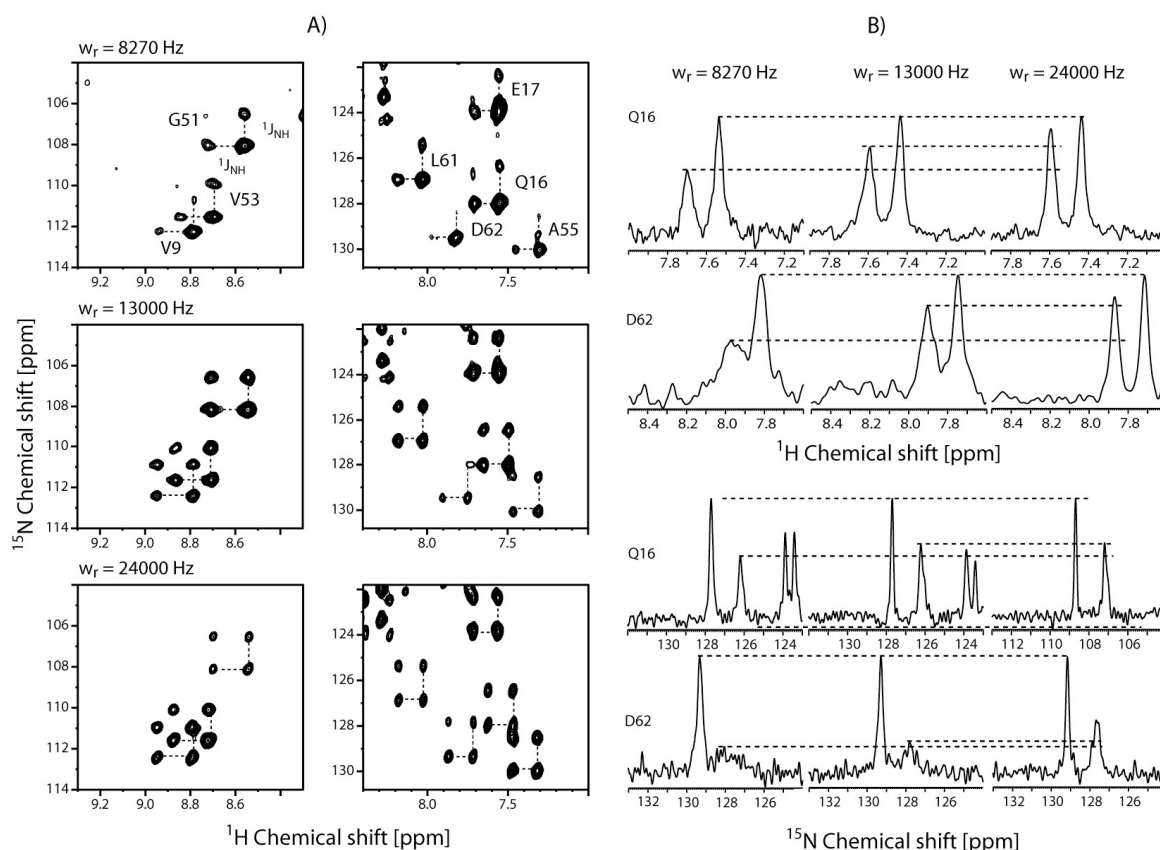


Figure 3.3.1. A) 2D  $^1\text{H}$ ,  $^{15}\text{N}$  correlation spectra recorded at different MAS rotation frequencies. All spectra were recorded at an external magnetic field strength of 14.1 T (corresponding to a  $^1\text{H}$  Larmor frequency of 600 MHz). Each signal is split into a doublet due to the  $^1J_{\text{NH}}$  scalar coupling. B) 1D traces through selected correlation signals along the  $^1\text{H}$  (top) and the  $^{15}\text{N}$  dimension (bottom).

Acquisition of  $^1\text{H}$ ,  $^{15}\text{N}$  correlation spectra without application of heteronuclear scalar decoupling results in TROSY type spectra as represented in Figure 3.3.1. Each correlation peak is split into a doublet in either the  $^1\text{H}$  as well as in the  $^{15}\text{N}$  dimension due to evolution of the  $^1J_{\text{HN}}$  scalar coupling. As in TROSY, the intensities of the individual components of the multiplet pattern are not equal. In contrast to solution-state NMR, however, where the size of effect is determined only by the reorientation time  $\tau_c$  of the molecule in solution, two effects are superimposed in the case of solid-state NMR samples:

- 1) Static interference of the  $^{15}\text{N}$  CSA and  $^1\text{H}$ - $^{15}\text{N}$  dipolar tensors. Both interactions act simultaneously on the  $^{15}\text{N}$  nucleus.
- 2) Dynamic interference due to  $^{15}\text{N}/^1\text{H}$ - $^{15}\text{N}$  cross-correlated relaxation. The presence of backbone dynamics in the solid-state has been observed in a number of studies [8,67,85].

Static interference effects are well documented in solid-state NMR experiments [86,87,88,89,90,91]. If scalar couplings are resolved in the solid-state, the two resonances originating from the  $H^\alpha$  and  $H^\beta$  spin state in the  $^{15}\text{N}$  spectrum are associated with different anisotropies: The upfield and downfield component in the nitrogen dimension are related to approximately the sum and difference anisotropy of the  $^{15}\text{N}$  CSA and  $^{15}\text{N}$ - $^1\text{H}$  dipolar interaction, respectively. As the interaction Hamiltonian of the  $^{15}\text{N}$  spin can be considered to be purely inhomogeneous in the sense of Maricq and Waugh [15], no MAS frequency dependence of the line widths is expected for the static case. The intensities of the  $\text{N-H}^{\alpha\beta}$  multiplet components are therefore only dependent on the MAS rotation frequency, as at larger MAS frequencies the total signal intensity is not distributed any longer over multiple rotational spinning side bands. A more thorough consideration is given in Figure 3.3.2 in order to outline the physical basis of the effect. It is obvious that variations in the size and orientation of the  $^{15}\text{N}$  CSA as well as the  $^{15}\text{N}$ - $^1\text{H}$  dipolar tensor will change the relative  $^{15}\text{N-H}^{\alpha\beta}$  multiplet intensity ratio at a given MAS rotation frequency. This effect is, however, negligible assuming the variation of tensor parameters which have been experimentally determined so far.  $^{15}\text{N}$  CSA value are well documented by a number of solution and solid state NMR works [92,93,94] and give for  $\Delta\sigma=\sigma_{\parallel}-\sigma_{\perp}=170\pm 8$  ppm,  $\sigma_z=100\pm 5$  ppm.  $^{15}\text{N}$ - $^1\text{H}$  bond which collinear with  $^{15}\text{N}$ - $^1\text{H}$  heteronuclear dipolar coupling tensor has 20-25° tilting angle relatively principal axis Z of the CSA tensor. In addition to the static effect which is based on the chemical properties of an individual amino acid, only dynamics can then contribute to a differential line width for  $\text{N-H}^{\alpha\beta}$  multiplet components. We simulated, using SIMPSON package [95] (input files are given in Appendix 1.1), the ratio between up- and downfield components of  $^{15}\text{N}$  multiplet as a function of the principal values  $\sigma_z$  and asymmetry parameter  $\eta$  of the  $^{15}\text{N}$  CSA tensor as well as its orientation relatively  $^{15}\text{N}$ - $^1\text{H}$  dipolar tensor. Isolated  $^{15}\text{N}$ - $^1\text{H}$  spin pair was considered in the simulations. The results are represented as contour plots in Figure 3.3.2:

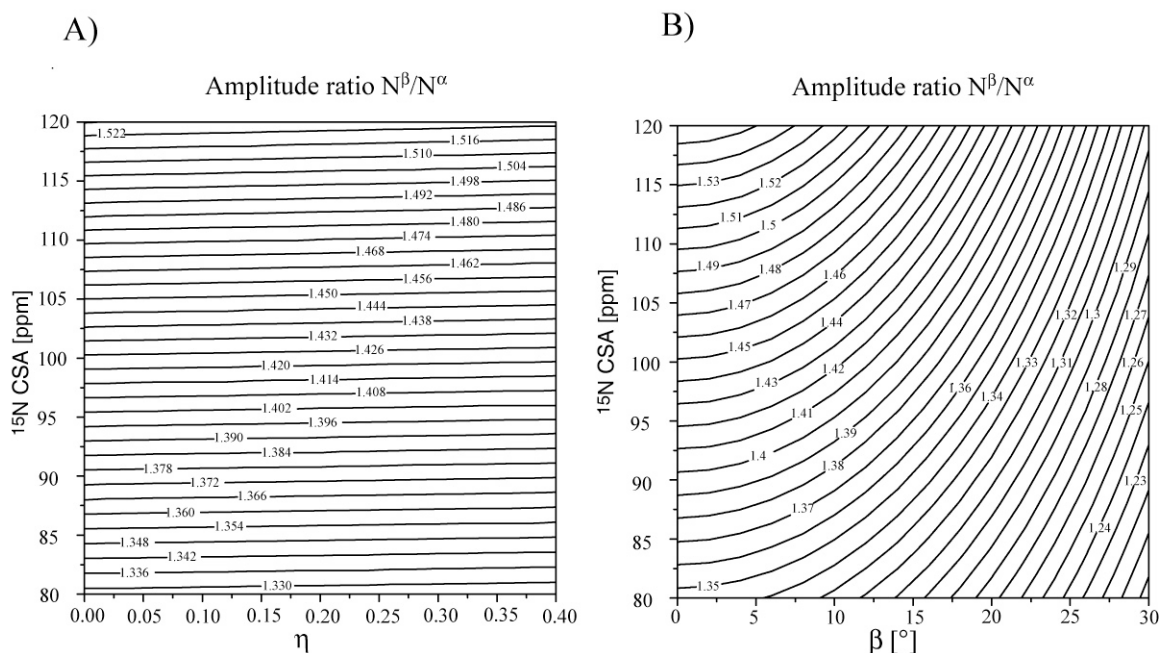


Figure 3.3.2. A) Simulation of the  $NH^\alpha/NH^\beta$  intensity ratio of the nitrogen signal as a function of the reduced anisotropy  $\sigma_z$  and the asymmetry parameter  $\eta$  at a MAS frequency of 10 kHz (the angle is kept constant at  $\beta = 90$  ppm). In both simulation, an external magnetic field of 14.1 T is assumed, corresponding to a  $^1\text{H}$  Larmor frequency of 600 MHz and  $^{15}\text{N}$ - $^1\text{H}$  dipolar coupling is 10828 Hz. B) Simulation of the  $NH^\alpha/NH^\beta$  intensity ratio of the nitrogen signal as function of the reduced anisotropy  $\sigma_z$  and the Euler angle  $\beta$  at a MAS frequency of 10 kHz (the asymmetry is kept constant at  $\eta=0.2$ ).

The simulations show that the line width of both  $^{15}\text{N}$  lines in the doublet are equal and the presented ratio is valid for amplitude and integral values of the peaks. These simulations allows to extract the principal value  $\sigma_z$  of  $^{15}\text{N}$  CSA tensor and the angle  $b$  between it and HN bond utilizing experiments at different external magnetic fields. This approach can be good alternative to single crystal's measurements, recoupling pulse sequences [96] and sideband analysis at slow spinning [97]. The asymmetry parameter  $\eta$  does not influence the ratio, and practically not accessible, as well as by ROCSA and sideband analysis. In order to extract these parameters accurately, high precision measurements have to be carried out.

A major concern in the experiments is the proper adjustment of the magic angle. Missetting of this angle reintroduces anisotropic interactions and yields a dramatic deterioration of the line shape and width, especially of the broad component of the spectrum. This effect is illustrated in the Figure 3.3.3:

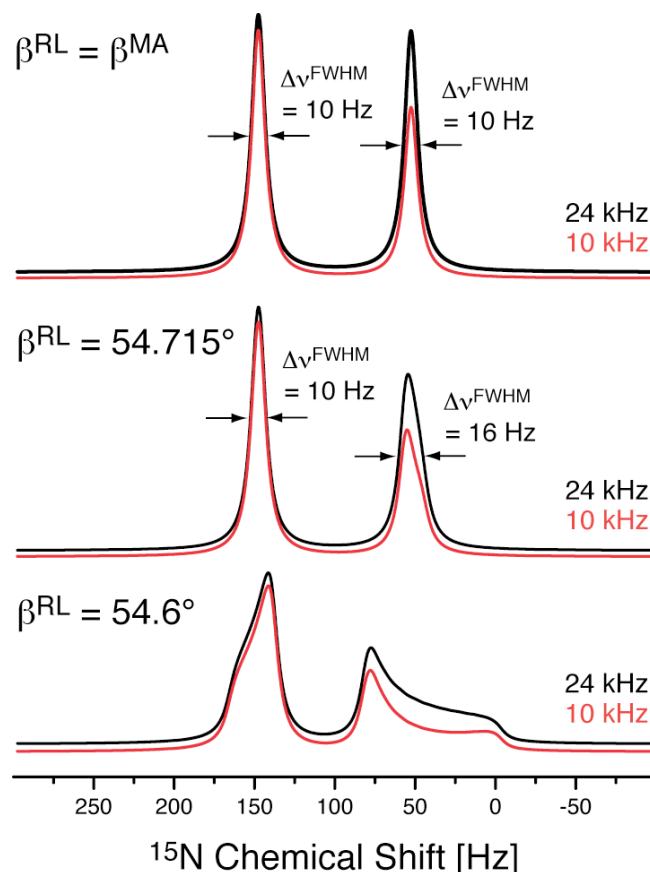


Figure 3.3.3. Theoretical  $^{15}\text{N}$  spectrum assuming a chemical shift anisotropy of 100 ppm and a dipolar and scalar coupling to a directly bonded proton of 10 kHz and -95 Hz, respectively, and an external magnetic field of 600 MHz. Simulations are shown for a MAS rotation frequency of 10 kHz (red) and 24 kHz (black). The simulation is carried out for three different values for the Euler angle  $\beta^{\text{RL}}$  which describes the angle between the principal axes of the rotor fixed frame and the laboratory coordinate system. Missetting of the "magic angle" ( $\beta^{\text{MA}} = \beta^{\text{RL}} = \arctan(\sqrt{2}) \approx 54.73561^\circ$ ) reintroduces the sum and difference anisotropy for the upfield and downfield component in the spectrum, respectively.

The influence on the magic angle missettings in the presented simulations are largely exaggerated compared to the achieved accuracy in the experimental setup. A magic angle missettings of  $0.0206^\circ$  and  $0.011^\circ$  result in a differential line width of 6 and 1.5 Hz respectively. The minimum differential line width observed in our experiments amounts to 1 Hz which would be highest possible line broadening due to magic angle miscalibration.

Static interference effects are usually not observed in solution-state NMR, since they are averaged to zero due to the tumbling of the molecule in solution. However, a



second order dynamic interference effect which is based on dipolar and chemical shift anisotropy relaxation interference still influences the spectra. This effect is the physical basis of TROSY [39] and cross-correlated relaxation experiments [98,99]. The size of the  $^{15}\text{N}$ ,  $^{15}\text{N}$ - $^1\text{H}$  cross-correlated relaxation rate  $\Gamma^{\text{CSA/DD}}$  be expressed as [66]:

$$\begin{aligned}\Gamma^{\text{CSA/DD}} &= \frac{1}{15} d \cdot c [4J_0(0) + 3J_1(\omega_N)] P_2(\cos \theta) \\ d &= \left( \frac{\gamma_N \gamma_H h}{2\pi r_{\text{HN}}^3} \right) \equiv \omega_{\text{HN}} \\ c &= (\gamma_N B_0 (\sigma_{\parallel} - \sigma_{\perp})) \equiv \omega_N \cdot (\Delta\sigma)\end{aligned}\tag{3.3.1}$$

where gyromagnetic ratios of  $^{15}\text{N}$  and  $^1\text{H}$  are denoted as  $\gamma_N$  and  $\gamma_H$  respectively,  $h$  is Planck's constant and  $r_{\text{HN}}$  is the effective  $^{15}\text{N}$ - $^1\text{H}$  distance. The Larmor frequency of  $^{15}\text{N}$  and  $^1\text{H}$  is represented by  $\omega_N$  and  $\omega_H$  respectively. The frequency of dipole-dipolar proton-nitrogen coupling is denoted by  $\omega_{\text{HN}}$ . The principal values of  $^{15}\text{N}$  CSA tensor are given by  $\sigma_{\parallel} = \sigma_z$  and  $\sigma_{\perp} = \sigma_x = \sigma_y$ . The tensor can be assumed axially symmetric [99].

It is found experimentally that  $\theta$  adopts values on the order of 20-25° [92,93]. For an isotropic motional model without internal motion, the spectral density function  $J(\omega)$  is given as  $J(\omega) = \tau_c / (1 + \omega^2 \tau_c^2)$ . In addition to the size and relative orientation of the CSA and dipolar tensors, the cross-correlated relaxation rate is therefore directly proportional to the size of the molecular correlation time  $\tau_c$ . Assuming that there is significant dynamics of the protein backbone in the solid-state, the ratio of the  $^{15}\text{N}$ - $\text{H}^{\alpha}/\text{H}^{\beta}$  multiplet intensities will be affected. In the solid-state, the exact size of the expected effect for an individual amide site is governed by the corresponding spectral density function implicated in the underlying motional model. Importantly, motions occurring on time scales which are fast compared to the rotor revolution will not depend on the MAS rotation frequency.

In general, we observe larger effects for  $^{15}\text{N}$  compared to  $^1\text{H}$ . We speculate that the limited resolution in the  $^1\text{H}$  dimension is due to residual  $^1\text{H}$ ,  $^1\text{H}$  dipolar couplings even at these very high degrees of deuteration employed in this study. This is corroborated by the MAS spinning frequency dependence of the  $^1\text{H}$  line width as reported earlier [28]. In the following, we focus therefore on the analysis of cross-correlated relaxation in the  $^{15}\text{N}$  dimension. We expect, however, that similar effects as described now for  $^{15}\text{N}$  will be

observable for  $^1\text{H}$  as higher MAS rotation frequencies ( $> 30\text{ kHz}$ ) become available in the future.

In order to identify motional properties as the source of the effect, we recorded temperature dependent  $^1\text{H}$ ,  $^{15}\text{N}$  correlation spectra without  $^1\text{H}$  decoupling in the indirect  $^{15}\text{N}$  dimension. The  $^{15}\text{N}$  dimension of a  $^1\text{H}$  coupled  $^1\text{H}$ ,  $^{15}\text{N}$  correlation experiment for correlation signals resulting from the amid moiety of L61 and D62 recorded at different temperatures is represented in Figure 3.3.4:

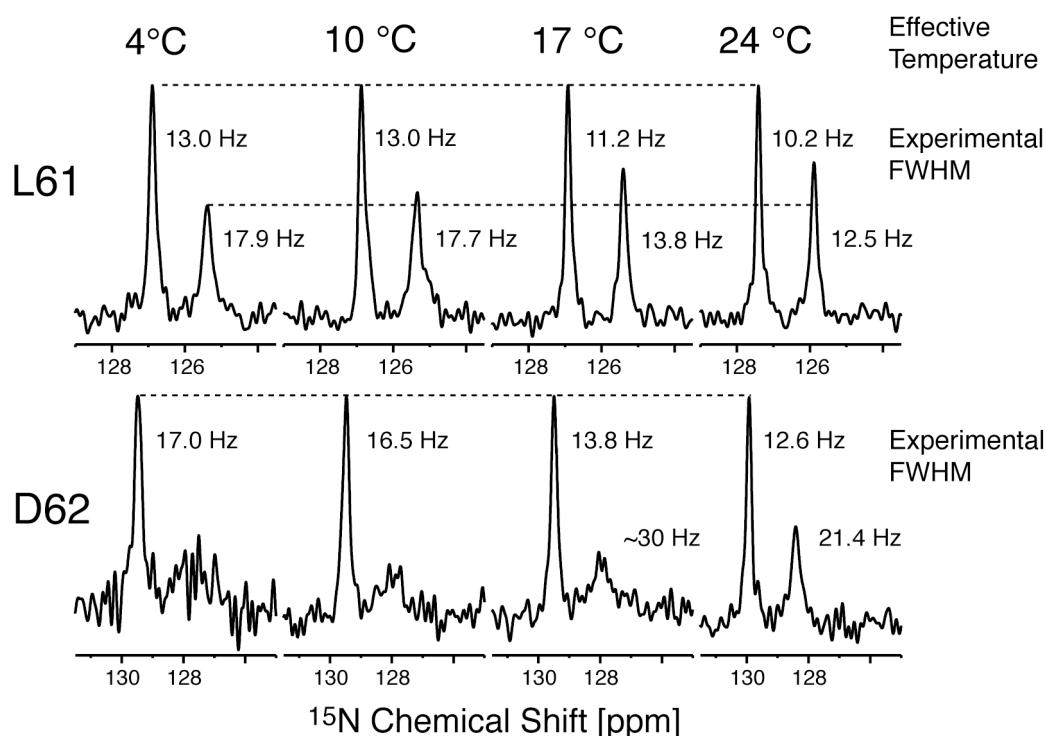


Figure 3.3.4. 1D columns along the  $^{15}\text{N}$  dimension in a  $^1\text{H}$  coupled  $^1\text{H}$ ,  $^{15}\text{N}$  correlation experiment in the solid-state for different temperatures. The MAS frequency was set to 13 kHz. The effective temperature, as well as the line width (FWHM) of each resonance is indicated in the figure. Only at increased temperatures, the upfield component for the correlation signal of the amid of D62 is visible in the spectrum. Spectra recorded at all temperature are reproduced after multiple heating and cooling cycles. Pulse sequence depicted in Figure 3.2.1 A was used to record these correlations.

Clearly, the experimental differential  $\text{N-H}^\alpha/\text{H}^\beta$  intensity is temperature dependent, and must therefore be due to local dynamics as all experimental parameters which influence the static properties of the effect (like e.g. the MAS frequency and angle) are

kept constant. In addition, we observe variations in the relaxation behaviour for different residues in the protein [81] indicating that indeed local motional effects are detected.

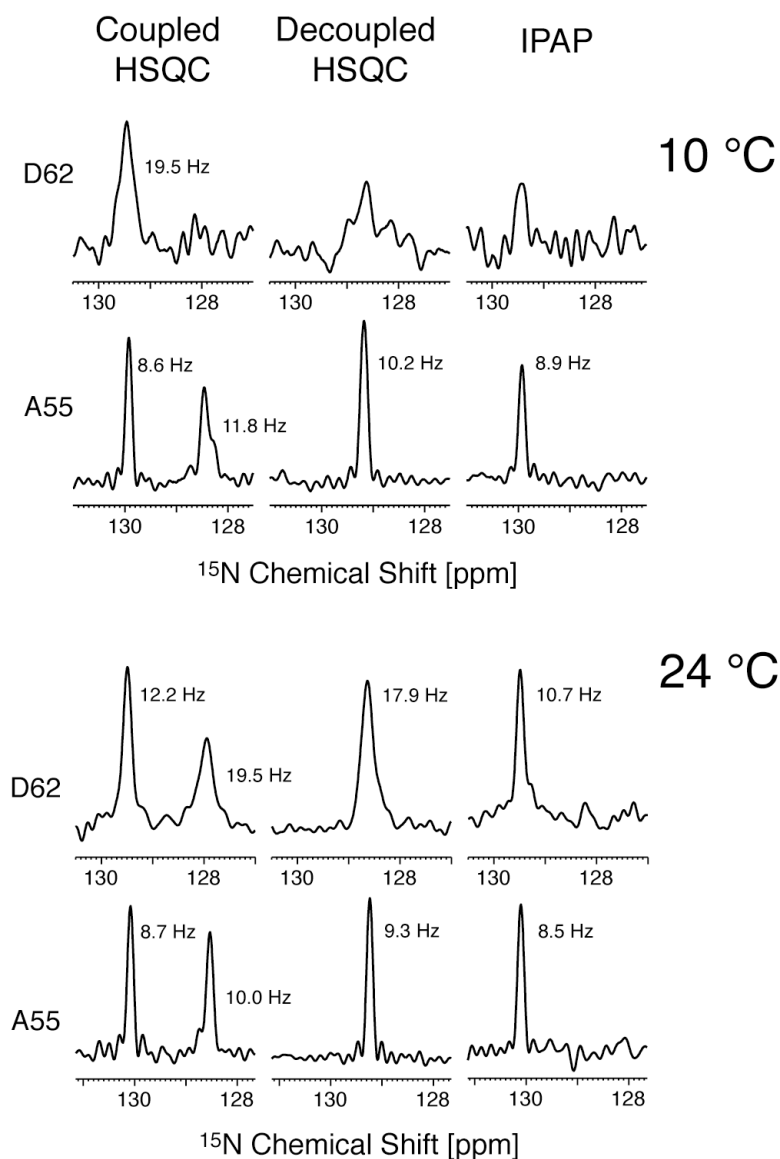


Figure 3.3.5. 1D columns along the  $^{15}\text{N}$  dimension in  $^1\text{H}$ ,  $^{15}\text{N}$  correlation experiments (HSQC: Heteronuclear Single Quantum Correlation; IPAP: In-Phase Anti-Phase) in the solid-state. For the spectra shown at the top and the bottom of the figure, the effective temperature was set to 10°C and 24°C, respectively. The MAS frequency was adjusted to 24 kHz in both cases. The line width (FWHM) of each resonance is indicated in the figure. Experimental details on the employed pulse sequences are provided as part of the supporting information.

The upfield component of D62 is broadened beyond detection in the  $^{15}\text{N}$  dimension for temperatures below 17°C. This residue therefore constitutes a typical case for which TROSY type techniques should be beneficial in order to increase the resolution

and sensitivity in the NMR spectra. The size of the line width of the  $^1\text{H}$  scalar decoupled  $^1\text{H}$ ,  $^{15}\text{N}$  correlation spectrum adopts approximately the average value of the line width of the upfield and downfield component. The apparent resolution in the  $^{15}\text{N}$  dimension can be increased, if we select only the narrow component of the spectrum. This can be achieved by application of spin state selective excitation (S3E) techniques [82]. Spin-state selective experiments have recently been successfully applied in the solid-state in order to achieve homonuclear scalar decoupling in uniformly  $^{13}\text{C}$  enriched peptides and proteins [91,100]. In particular, we recorded an IPAP  $^1\text{H}$ ,  $^{15}\text{N}$  correlation experiment [83,84] in which in-phase and anti-phase correlation signals are added and subtracted in order to yield only the upfield or downfield component of the doublet. The results of these experiments for residues D62 and A55 as 1D columns of  $^{15}\text{N}$  dimension are represented in Figure 3.3.5.

The pulse scheme for the IPAP experiment is illustrated in Figure 3.2.2 and details on the experimental setup and NMR parameters are given in the Experimental section. For comparison, results of HSQC measurements with and without  $^1\text{H}$ - $^{15}\text{N}$  scalar decoupling in the indirect dimension are represented in the figure as well. These experiments were performed according to pulse sequence depicted in Figure 3.2.1 B. Two effective sample temperature of 10 °C and 24 °C were studied to elucidate efficiency of introduced technique at different motional regimes, controlled by temperature variations.

Smaller, but still significant effects are observed, if the temperature of the sample is raised to 24°C. Our experiments show that the line width of  $^{15}\text{N}$  can be strongly affected by backbone motion, induced only by moderate temperature changes. The dynamic properties of other biomolecules like and membrane proteins and fibrillar aggregates are likely to be different, but might result in undetectable broadening of the  $^{15}\text{N}$  resonances if standard solid state NMR experiments are employed. The effective resolution can then only be increased by application of TROSY type techniques highly deuterated biomolecules.

In order to quantitate the motional contribution to the intensities, we determined the differential  $^{15}\text{NH}^{\alpha/\beta}$  multiplet intensities as an empirical function of the MAS rotor periodicity  $\tau_r$ . Summarize all above mentioned effects which contribute to the ratio of the  $^{15}\text{NH}^{\alpha/\beta}$  multiplet intensities we express the function in Equation 3.3.2:

$$\frac{I(NH^\beta)}{I(NH^\alpha)} = A \left( \sigma_N, \beta^{N,NH} \right) \frac{1}{\tau_r^X} + B \left( \beta^{RL} \right) \frac{1}{\tau_r^Y} + C \left( \tau_C \right) \quad (3.3.2)$$

The pre-factor  $A$  comprises all terms related to the static values of the anisotropy  $\sigma$  as well as, the  $^1\text{H}$ - $^{15}\text{N}$  dipole and the angle  $\beta$  between the principal axes of the two anisotropies. It has been shown that the differential intensity is independent of the asymmetry parameter  $\eta$  of the  $^{15}\text{N}$  CSA (see Figure 3.3.9 ).  $B$  is a correction term which takes into account a possible misadjustment of the magic angle.  $C$  describes the dynamic contribution and is independent of the MAS rotation frequency. We can fit  $X = 2.4$ , and  $A = 4.0$  and  $4.8$  for a  $^{15}\text{N}$  chemical shift anisotropy of 80 and 120 ppm, respectively. By simulation, we find that magic angle miscalibration induces an offset to the ratio of the  $^{15}\text{NH}^{\alpha\beta}$  multiplet intensities (with  $Y \approx 0$ ). This constant offset is on the order of 5% assuming a magic angle misadjustment of  $0.009^\circ$ . At the same time, this particular missetting results in a differential line width of the  $^{15}\text{NH}^{\alpha\beta}$  multiplet component of 1 Hz. This is the approximate minimum differential line width that we observe at high temperatures and fast spinning (24 kHz). We can therefore exclude miscalibration of the magic angle as a potential source of the observed effect. In addition, magic angle missetting would yield the same effect on the multiplet intensities for all residues in the protein. We observe, however, large variations for different amino acids in the protein.

Figure 3.3.6 summarizes simulations and experimental data for selected residues. Care was taken in order to compensate for heating effects which are caused by friction due to sample spinning [81]. Simulations in which the angle between the rotor spinning axis and the external magnetic field is systematically varied (exact magic angle and mis-setting of  $0.009^\circ$ ) are represented as black and red lines, respectively. Even at this relatively large deviation from the ideal condition, the experimental data are not reproduced very well. A MAS frequency independent offset can only be explained taking motional effects into account.

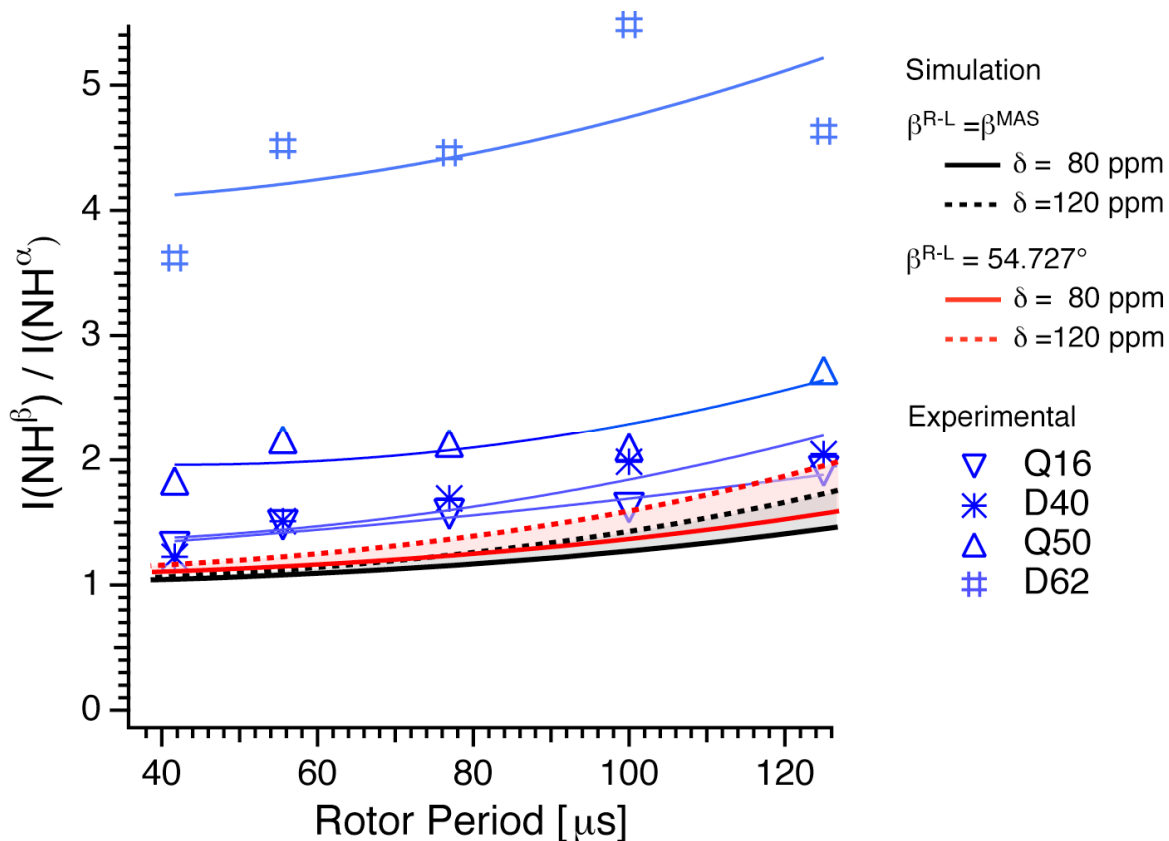


Figure 3.3.6. Experimental and simulated ratio of the  $^{15}\text{NH}^{\alpha/\beta}$  multiplet intensities as a function of the MAS frequency. The experimental data is compensated for heating effects due to friction induced by MAS. The effective temperature in all experiments was adjusted to 10 °C. Spectra were recorded at an external magnetic field strength  $B_0 = 14.1$  T. Variation of the reduced anisotropy  $\delta_z$  is indicated grey. In the simulation, the angle between the principal axes of the dipolar and the CSA interaction tensors was set to 20°. Missetting of the magic angle (resulting in a differential line width of 1 Hz) is indicated in red.  $\beta^{\text{MA}} = \arctan(\sqrt{2}) \approx 54.73561$ . Motional effects result in a constant offset of the  $\text{NH}^{\alpha/\beta}$  intensity ratio independent of the MAS rotation frequency (represented as blue line e.g. for the residue D62).

Line width for up- and downfield  $^{15}\text{N}$  multiplets has been studied for different type of  $^1\text{H}$ - $^{15}\text{N}$  correlation experiments at different experimental conditions to explore achievable limits of resolution for the introduced sample preparation. This information is also important to estimate gain in resolution at application of TROSY technique in comparison with experiments employing  $^1\text{H}$ - $^{15}\text{N}$  scalar decoupling. Three 2D  $^1\text{H}$ - $^{15}\text{N}$  correlation spectra were recorded with acquisition time of 92 msec in  $^{15}\text{N}$  dimension. Two experiments at spinning frequency of 24 kHz and 13 kHz and sample respective effective temperature of 24 °C and 10 °C were obtained using CP according to the pulse sequence

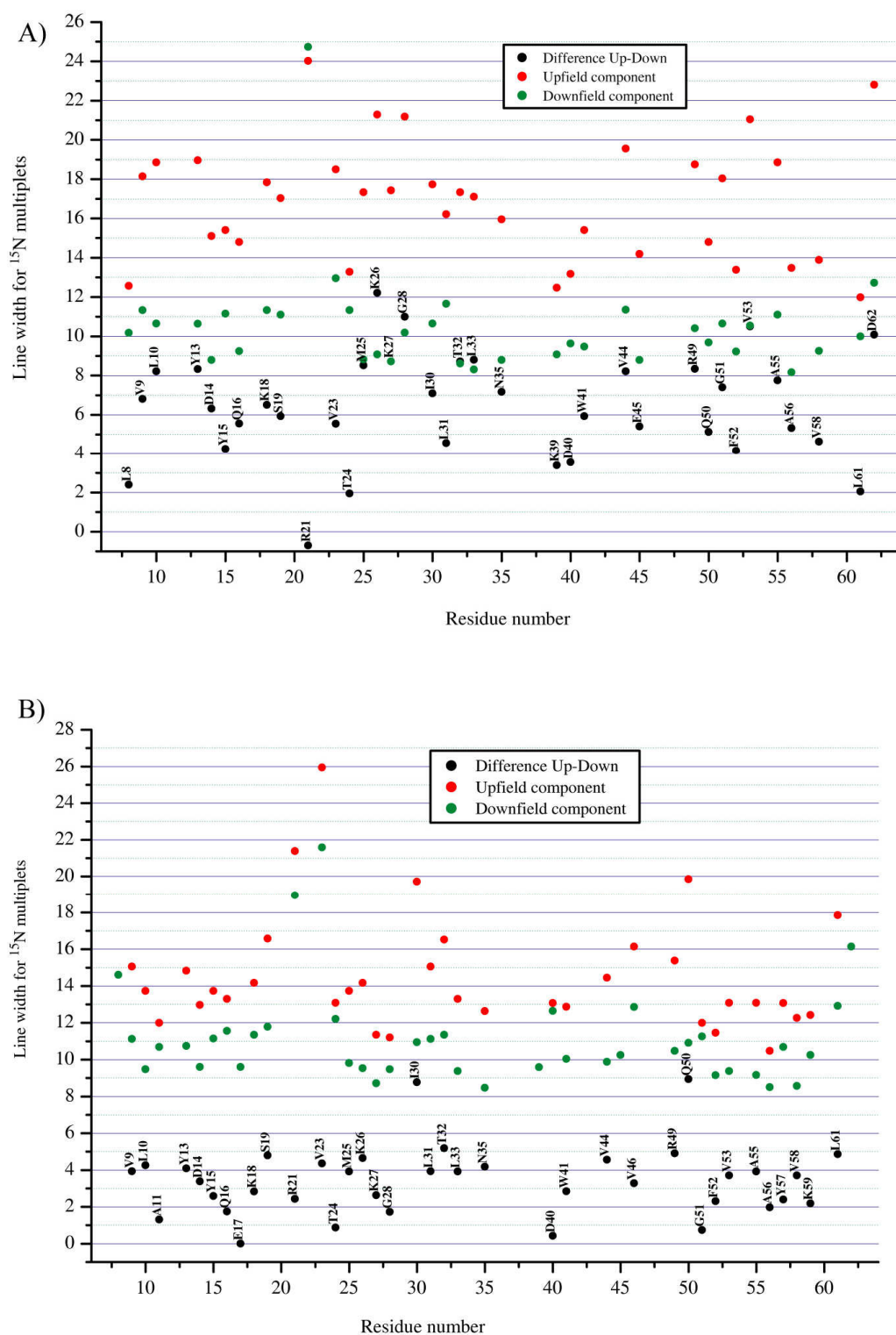


Figure 3.3.7. Line widths for up- and downfield components of highly deuterated SH3. Pulse scheme of the experiments employ CP magnetization transfer and its illustrated in details in Figure 3.2.1 A. A) Spinning frequency is 24 kHz and sample temperature is 24 °C. B) Spinning frequency is 13 kHz and sample temperature is 10 °C.

depicted in Figure 3.2.1 A. In this experiment initial value of the density matrix is represented by operator  $N_x$ . Extracted line widths are given in Figure 3.3.7.

Another experiment was recorded employing the pulse scheme, based on INEPT and which is depicted in Figure 3.2.2 B. Spinning frequency was 24 kHz and sample temperature was 24 °C. In the indirect evolution period density matrix at initial point is given by operator  $H_z N_x$ . Line width obtained in this experiment are represented in Figure 3.3.8:

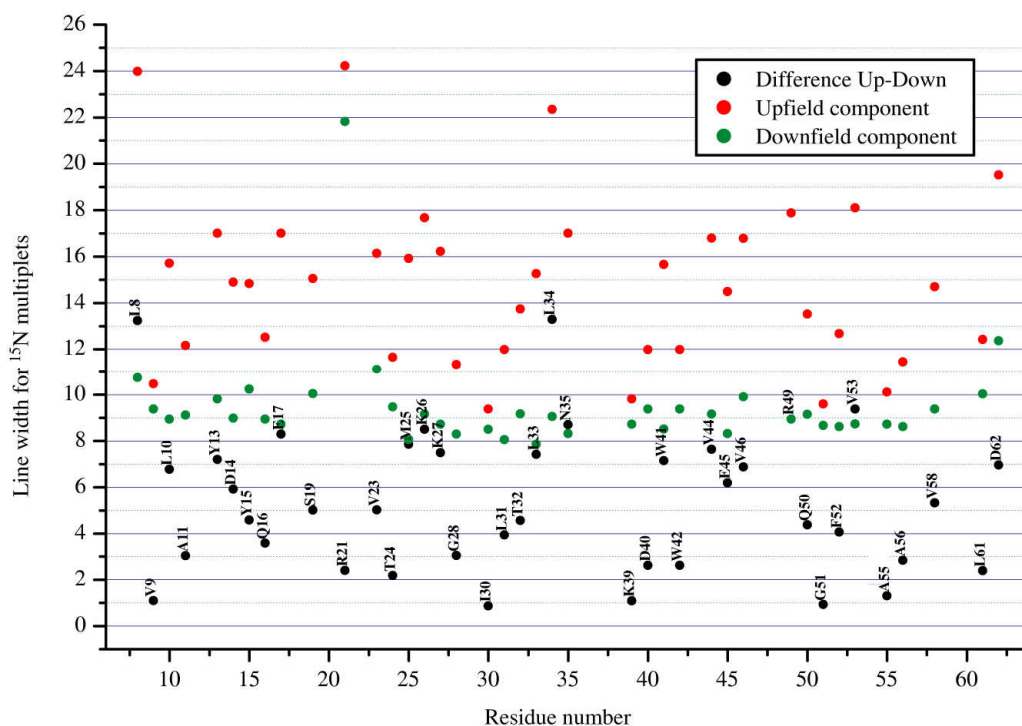


Figure 3.3.8. Line widths for up- and downfield components of highly deuterated SH3. Pulse scheme of the experiments employ CP magnetization transfer and its illustrated in details in Figure 3.2.1 B. Spinning frequency is 24 kHz and sample temperature is 24 °C.

All the experiments show the same range of the line widths, which states that spinning frequency, sample temperature and evolving density matrix operator do not have principal influence on obtained resolution, except of highly mobile residues like L8 and D62. Small variations could originate not only from considered reasons, but also from temperature unstability of the sample for experiments employing two CP transfer step of 0.8 ms each. Isotropic chemical shift of protein signals in a  $^1\text{H}$ - $^{15}\text{N}$  2D correlation experiment depends, in general, on sample temperature. We recorded a series 2D spectra



at 13 kHz spinning frequency, employing pulse scheme depicted in Figure 3.2.1 A at 4 °C, 10 °C, 17 °C and 24 °C. Superposition of two 2D spectra recorded at 4 °C and 24 °C is presented in Figure 3.3.9:

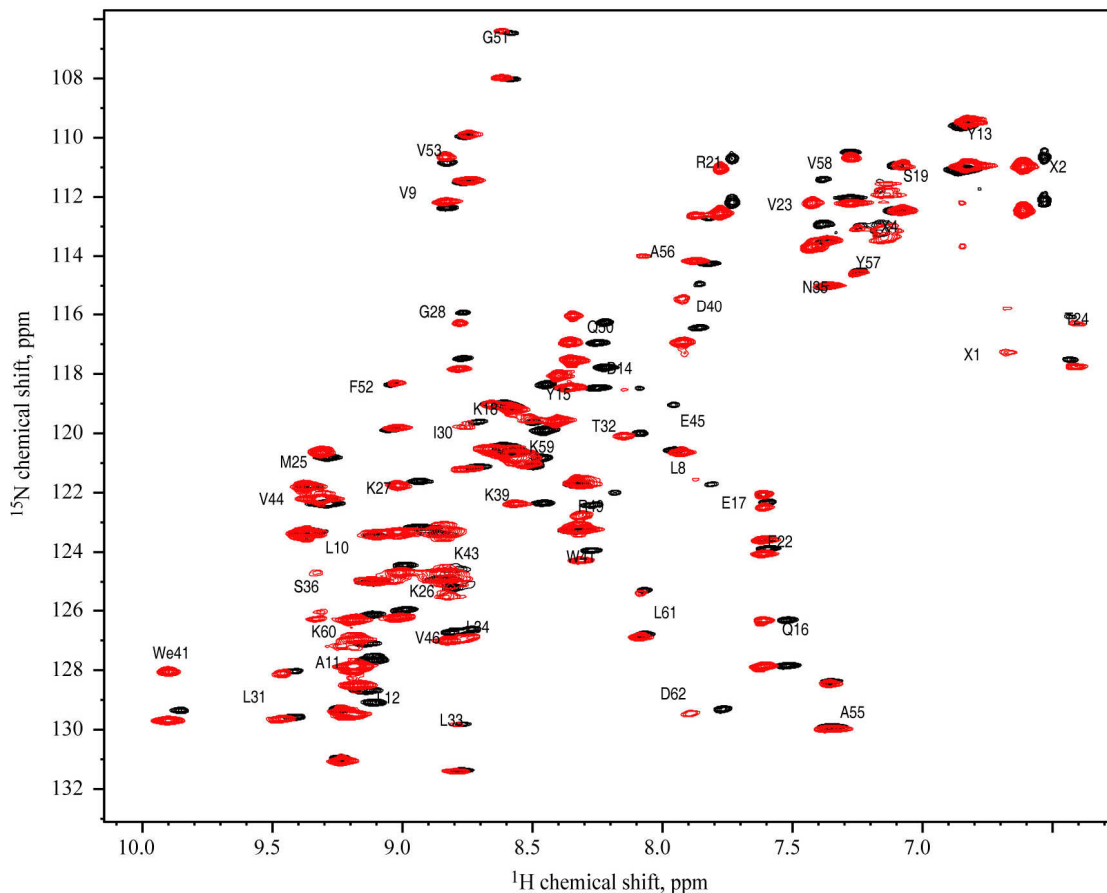


Figure 3.3.9.  $^1\text{H}$ - $^{15}\text{N}$  correlation of SH3 recorded at 24 °C (black) and 4 °C (red).

Spectra recorded at 10 °C and 17 °C show intermediate chemical shifts between presented two correlations and not shown. We can see that many residues show chemical shift changes, comparable with line width, in both dimensions. These effect originates from temperature dependent processes like water-protein proton exchange, conformational exchange as well as changing of nuclear chemical environment due to different motional character of backbone. All high power pulses, (e.g. CP, homo- and heteronuclear decoupling sequences) heat up the sample and temperature's increase can achieve 40 °C [65,101]. In course of these experiments protein temperature is not stable and adopts large range of values resulting in detection of the chemical shift averaged over all temperatures.



These spectra directly manifest additional advantage of high deuteration scheme to achieve optimal resolution.

We also performed comparative studies of all pulse sequences illustrated in Figure 3.2.1 to find optimum of sensitivity in these experiments. Scalar decoupled spectra were recorded at spinning frequency of 24 kHz and effective sample temperature 24 °C. The ratio of the peaks' intensity is given by Figure 3.3.10.

Studies of efficiency of INEPT as heteronuclear polarization transfer element, made on  $^1\text{H}$  bulk signal, shows that its efficiency strongly increases at increasing spinning frequency and sample's temperature. For these reference experiments we took maximum available for commercial equipment rotation frequency and highest possible temperature of the protein to keep it stable. Inspection of the results in Figure 3.3.10 shows that  $^1\text{H}$ - $^{15}\text{N}$  scalar coupling is significantly more efficient than heteronuclear dipolar interaction for polarization transfer. These experiments also give qualitative information about the degree of residue mobility [7]. Peaks which have low "Ratio CP/INEPT" belong to atoms located in highly mobile regions.

In conclusion, we have shown that dynamics in the ns- $\mu\text{s}$  timescale can indeed induce significant line broadening of  $^{15}\text{N}$  resonances in solid-state NMR experiments in solid-state samples. Averaging of  $^{15}\text{N}$ - $\text{H}^{\alpha/\beta}$  multiplet components due to  $^1\text{H}$  decoupling induces an effective relaxation of the  $^{15}\text{N}$  coherence. In the absence of static conformational heterogeneity, high resolution solid-state NMR spectra can only be recorded by application of TROSY type techniques which select the narrow component of the multiplet pattern. We speculate that this effect prevented so far the NMR spectroscopic characterization of many membrane proteins and fibrillar aggregates. Only in very favorable cases in which dynamics are either of very small amplitude or very fast (ps), high resolution spectra can be obtained. We expect that this approach which requires high levels of deuteration will have a significant impact on the rate and quality by which NMR spectroscopic investigations will emerge in the future.

We found as well that these labeling scheme gives perspectives not only in resolution improvement, but in sensitivity enhancement.

## 4 Chapter. Quantitative analysis of backbone dynamics in microcrystalline sample of the SH3 domain of $\alpha$ -spectrin by MAS solid-state NMR.

### 4.1 Introduction.

Biological functionality of proteins is determined by structure-dynamics relationship. The internal protein motions are responsible for such processes as ligand binding, catalysis, folding, ions and water transfer etc. [102,103 Massi, 2005 #132,104,105,106]. Liquid state NMR has been proved to be well suited technique to probe the internal and overall proteins dynamics [107]. For last decades it has collected enormous body of information about motion at different time scales and amplitude ranges [108,109,110]. Many protocols have been established to challenge this key properties of proteins.

Solid state NMR has advantages in studding of molecular flexibility, since the overall tumbling in solid state is absent and does not contribute to relaxation processes. In such systems internal motion can directly manifest itself not being hidden by global molecular reorientation. Solid state NMR enables to study amorphous and unsoluble systems and probe their motional properties.

For motional studies in solid state systems many approaches have been developed in the past, like line shape analysis of CSA and quadrupolar couplings of deuterium, as well as relaxation measurements have been done [14,111,112,113]. Several experiments in the past have been performed on solid state proteins employing these techniques and  $^{15}\text{N}$  longitudinal relaxation experiments [114,115]. These experiments, however, due to limited resolution and signal-to-noise ratio do not provide widespread multiple site-specific picture of dynamics information, which would show variation of correlation time and motional amplitude from one part of the molecule to another, and give only rough estimation of motional character in solid state proteins.

Rapid progress in ssNMR methods like microcrystalline sample preparation [42] and decoupling pulse sequences [29], made possible complete assignment of proteins in

solid state [42,116,117,118,119,120,121]. These techniques provide with perspectives to obtain knowledge about many site-specific motional parameters. A number of works have been made recently to characterize dynamical properties in solid proteins. Extensive studies of  $^{15}\text{N}$  longitudinal relaxation have been used to determine motional properties of backbone in Chr protein by Emsley and coworkers, using explicit average sum (EAS) formalism [8,85,122]. Deuterium quadrupolar couplings and relaxation properties have been used by Reif and coworkers to characterize side chain dynamics [7,80,123]. Motional averaging of  $^1\text{H}$ - $^{15}\text{N}$  and  $^1\text{H}$ - $^{13}\text{C}$  dipolar couplings have been measured [94,124,125] to determine order parameters in solid state proteins. Recently, differential transversal relaxation times have been employed to obtain motional information about backbone in SH3 [67].

In this chapter we present studies of backbone dynamical properties of microcrystalline sample of the SH3 domain of  $\alpha$ -spectrin by MAS solid-state NMR. Extremely high level of deuteration of the  $^{15}\text{N}$  labeled protein [28] was used to obtain a variety of high quality experimental data. The dynamics were probed by measurement of the  $^{15}\text{N}$  longitudinal [67] and transversal relaxation [67] rates at different external magnetic fields. Motional averaged  $^{15}\text{N}$ - $^1\text{H}$  dipolar couplings have been obtained in studies of  $^{15}\text{N}$ - $^1\text{H}$  cross-polarization (CP) dynamics [31] to quantify general order parameter of motion. A vast set of the experimental data allows to employ many parametrical model-free approach introduced by Lipari and Szabo [110] and extended by Croneberg and coworkers [126] for the data interpretation. Obtained fast and slow correlation times as well as fast and slow order parameters show high variation of backbone flexibility, as it has been shown earlier [8,85].

## 4.2 Experimental section.

Longitudinal and transversal relaxation data as well as reduced dipolar couplings have been obtained on SH3 domain from chicken  $\alpha$ -spectrin at extremely high level of deuteration [28].  $^{15}\text{N}$  labeled perdeuterated SH3 protein has been resolved in 10:90  $\text{H}_2\text{O}$ - $\text{D}_2\text{O}$  mixture to reduce proton density to very low level resulting in ultrahigh resolution in 2D  $^{15}\text{N}$ - $^1\text{H}$  correlation spectra. Detailed description of the sample preparation is given in

Chapter 2 and Ref. [28]. The prepared protein has been packed into 3.2 mm and 4 mm rotors in amounts ca. 10 mg each. Only experimental data obtained on high deuterated samples were used for the motional analysis.

Fully protonated  $\alpha$ -SH3 protein has been prepared according to the protocol described in Ref. [42]. The longitudinal relaxation experiments conducted on this sample were used to elucidate influence of  $^{15}\text{N}$ - $^{15}\text{N}$  proton driven spin diffusion (PDSF) on apparent  $^{15}\text{N}$  longitudinal relaxation times [122]. These data were not considered in theoretical analysis of dynamical properties of the protein backbone.

The samples preparation was done by Kristina Rehbein and Dr. Anne Diehl.

NMR spectroscopy was carried out on Bruker-Avance instruments operating at 600MHz and 900MHz proton Larmor frequency equipped with 4 mm and 3.2 mm double resonance probes. All experimental pulse sequences are based on proton detected 2D  $^1\text{H}$ - $^{15}\text{N}$  correlation experiments introduced in Chapter 2, Figure 2.4.1 A, with incorporated elements to measure physical property of interest. Typical line width for  $^1\text{H}$  and  $^{15}\text{N}$  signals obtained in such experiments are 20-30 Hz and 8-16 Hz respectively at spinning frequency of 13 kHz and 24 kHz. No rf power is needed for hetero- and homonuclear decoupling of anisotropical dipolar couplings. Proton detection scheme [28,38,51] was employed to achieve high sensitivity.

Longitudinal relaxation time ( $T_1$ ) has been measured at two external magnetic fields, corresponding to 600 MHz and 900 MHz proton Larmor frequency, using the 4 mm probe. In both experiments the probe temperature was set to 275.0 K, which corresponds to an effective sample temperature of 285.0 K. Spinning frequency was adjusted to 13 kHz to avoid the sample degradation in course of long term experiments. The employed experimental pulse sequence is given in Figure 4.2.1.

Effective suppression of the dominant water resonance was achieved by modification of the constant time (CT) experiment suggested by Zilm and coworkers [51]. The experiment starts with a  $90^\circ$   $^1\text{H}$  excitation pulse, followed by a ramped CP magnetization transfer of 800  $\mu\text{sec}$  duration from protons to nitrogen. After the  $90^\circ$  pulse, the  $^{15}\text{N}$  polarization is stored along the Z-axis during a variable delay  $\Delta T$ , when longitudinal  $^{15}\text{N}$  polarization is allowed to relax. A variable delay ( $\tau-t_1/2$ ) precedes and follows the  $^{15}\text{N}$  evolution period  $t_1$ . Two delays ( $\tau-t_1/2$ ) are required to introduce a  $180^\circ$

proton pulse for  $J$  decoupling in the indirect dimension keeping the experiment constant time with respect to the water magnetization. The fixed delay  $\tau_w$ , following the CT period, is optimized for water signal suppression. Typical values for  $t_{1\max}$  and  $\tau_w$  in our experiments are on the order of 30 ms and 60-120 ms, respectively. Since the longitudinal

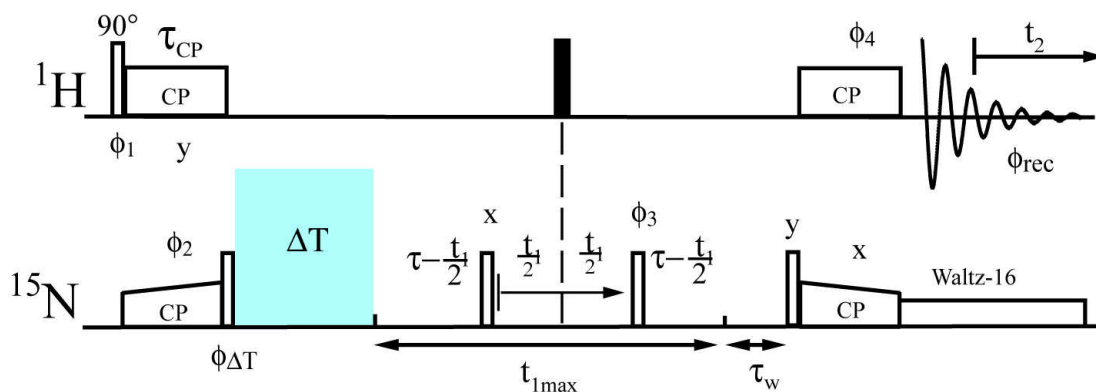


Figure 4.2.1. Pulse sequence to measure  $^{15}\text{N}$   $T_1$ . Open and filled bars represent  $90^\circ$  and  $180^\circ$  pulses, respectively.

relaxation time  $T_1$  of  $^{15}\text{N}$  is on the order of 7-20 s [8,67], the  $^{15}\text{N}$  magnetization can be stored along the Z-axis without significant losses in our experiment. The back-transfer of polarization to  $^1\text{H}$  is accomplished using a second 800  $\mu\text{sec}$  ramped CP step. Typical values for rf power during CP applied to proton and nitrogen channels are 45 and 54 kHz respectively.  $^1\text{H}$  magnetization is finally acquired using WALTZ-16 heteronuclear scalar decoupling. The employed field strength on the  $^{15}\text{N}$  channel was set to 2 kHz. The acquisition time was set to 26 ms and 100 ms for indirect and direct dimensions for experiments at both external magnetic fields. All hard pulses had 50 kHz and 60 kHz strength on nitrogen and proton channels respectively. In total, five  $^1\text{H}$ - $^{15}\text{N}$  correlation experiments were recorded at two external magnetic fields with different delays  $\Delta T$ . At 600 MHz instrument relaxation delays were set to 0, 2, 4, 8 and 15 seconds, while at 900 MHz spectrometer they adopted 0, 2, 4, 7 and 13 seconds. Additional reference spectra with  $\Delta T=0$  were recorded in the middle of each experimental series. Phase cycle  $\phi_{DT}=(x, -x)$  and  $\phi_{\text{rec}}=(y, -y)$  has been implemented for the spin temperature filter. Data were processed with an exponential line broadening of 5 Hz in both dimensions.

The pulse scheme to measure differential transversal relaxation rates of  $^{15}\text{N}$  is given by figure 4.2.2:

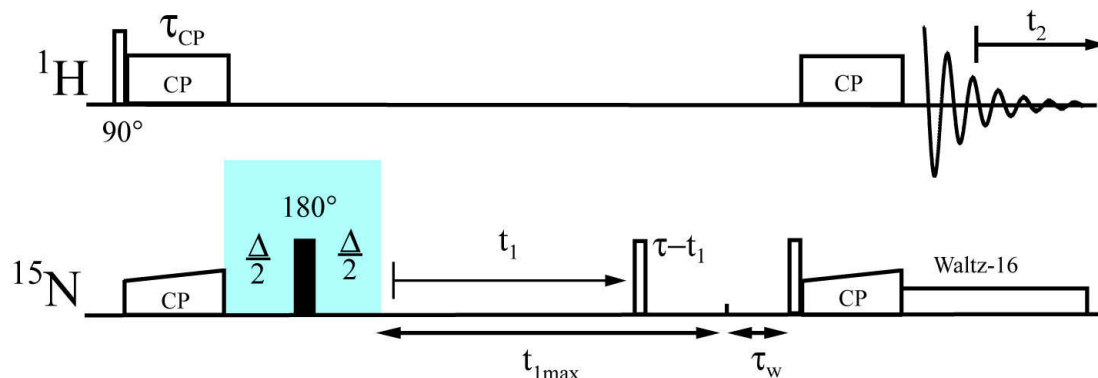


Figure 4.2.2. Pulse sequence employed for the measurements of  $^{15}\text{NH}^{\alpha}/^{15}\text{NH}^{\beta}$  differential  $T_2$  decay rates. Open and filled bars represent  $90^\circ$  and  $180^\circ$  pulses, respectively.

The transversal relaxation experiments were conducted on an instrument at external magnetic field corresponding to 600 MHz proton Larmor frequency, using a 3.2 mm probe. Differential transversal relaxation rates have been measured at spinning frequency of 16 kHz and 24 kHz to elucidate influence of residual homonuclear dipolar couplings in the proton net. The probe temperature was set to 259.0 K and 275.2 K for 24 kHz and 16 kHz MAS frequency, respectively. Effective protein temperature at these conditions corresponds to 285.3 K.

The transversal relaxation experiments are similar to described earlier the longitudinal relaxation experiment. After a first CP step follows a variable delay  $\Delta$ , when  $^{15}\text{N}$  transversal magnetization is allowed to relax. In the center of  $\Delta$ , a  $180^\circ$  nitrogen pulse is applied in order to refocus the  $^{15}\text{N}$  chemical shift,  $^1\text{H}$ - $^{15}\text{N}$  scalar coupling and the external magnetic field inhomogeneities. During CP a rf field of 55 kHz has been applied for the proton channel, while strength on the nitrogen channel was 35 kHz and 43 kHz at 24 kHz and 16 kHz MAS frequency respectively. The acquisition time was set to 50 ms and 100 ms for the indirect and the direct dimensions. In total, eight  $^1\text{H}$ - $^{15}\text{N}$  correlation experiments were recorded with different delays  $\Delta$  of 0, 4, 9, 17, 28, 42, 65 and 100 milliseconds. Two additional reference spectra with  $\Delta=0$  were recorded in the course of each experimental series. All spectra were apodized used 7 and 5 Hz lorentzian broadening



in the proton and nitrogen dimension respectively. All other experimental parameters are the same as has been used in the longitudinal relaxation experiment.

The pulse sequence to measure  $^1\text{H}$ - $^{15}\text{N}$  heteronuclear dipolar couplings is given in Figure 4.2.3:

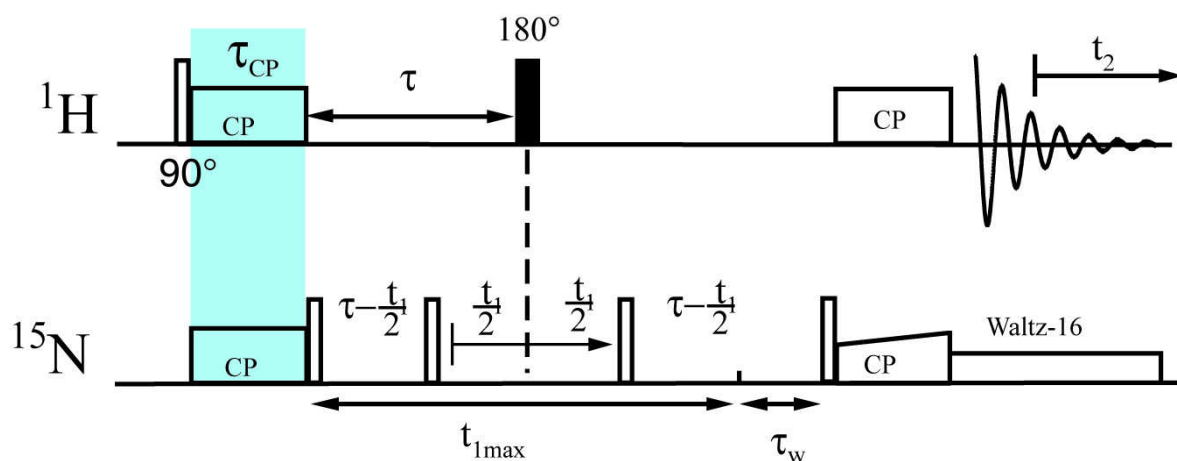


Figure 4.2.3. Pulse sequence employed for the measurements of  $^{15}\text{N}$ - $^1\text{H}$  heteronuclear dipolar couplings. Open and filled bars represent  $90^\circ$  and  $180^\circ$  pulses, respectively.

The experiment was conducted on an instrument at external magnetic field corresponding to 600 MHz proton Larmor frequency, using a 3.2 mm probe. The spinning frequency has been set to 24 kHz to reduce proton-proton dipolar coupling as much as possible. The probe temperature was set to 259.0 K, which corresponds to an effective sample temperature of 285.3 K. After  $^1\text{H}$   $90^\circ$  excitation pulse CP of variable duration  $\tau_{\text{CP}}$  was applied to monitor oscillating dynamics of  $^{15}\text{N}$  magnetization, which directly depends on  $^1\text{H}$ - $^{15}\text{N}$  dipolar coupling. RF fields of  $^1\text{H}$  and  $^{15}\text{N}$  channels were set at 64 kHz and 40 kHz respectively. In total, 68 experiments were recorded with uniform increment of  $\tau_{\text{CP}}$  equal to 12  $\mu\text{s}$ , resulting in evolution time of 804  $\mu\text{s}$ . The acquisition time was set to 26 ms and 100 ms for the indirect and the direct dimension respectively. Data were processed with an exponential line broadening of 7 Hz in both dimensions.

All other experimental details are the same as in the experiments described earlier.

Longitudinal relaxation rates of  $^{15}\text{N}$  in fully protonated sample have been measured according to the pulse sequence represented in figure 4.2.4:

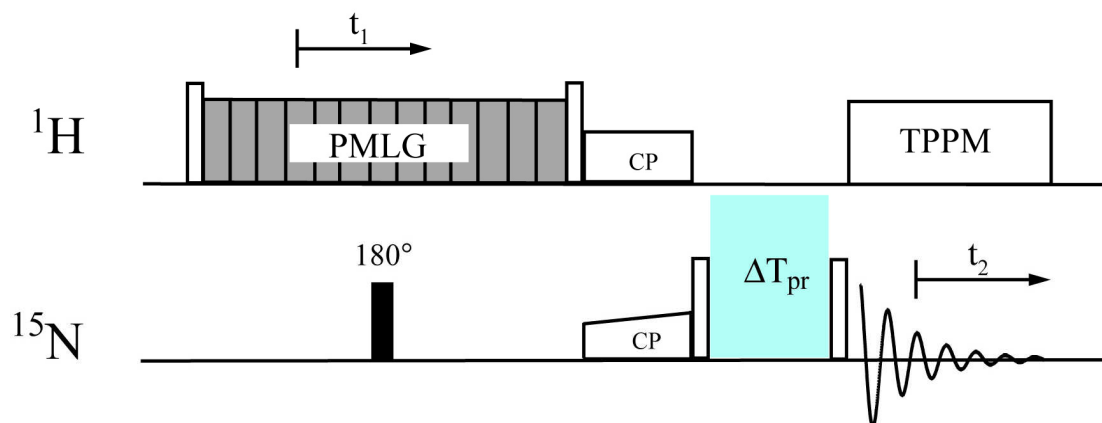


Figure 4.2.4. Pulse sequence to measure  $^{15}\text{N}$   $T_1$  in the protonated sample. Proton-proton dipolar interactions are suppressed by PMLG-9 in the indirect dimension, while  $^{15}\text{N}$  detection was employed. Open and filled bars represent  $90^\circ$  and  $180^\circ$  pulses, respectively.

$^1\text{H}$ - $^1\text{H}$  dipolar decoupling in the indirect proton evolution period was achieved by applying of PMLG-9 decoupling sequence [24] with proton field strength of 81 kHz. A  $180^\circ$  pulse on the  $^{15}\text{N}$  channel is applied in the center of  $t_1$  for heteronuclear  $J$  decoupling. After CP transfer,  $^{15}\text{N}$  magnetization is stored along the Z axis allowing to relax during variable delay  $\Delta T_{\text{pr}}$ . At  $^{15}\text{N}$  detection, TPPM [29] proton decoupling was applied using a RF field of 90 kHz. The acquisition time was set to 10 ms and 27 ms for indirect and direct dimensions. Five 2D  $^1\text{H}$ - $^{15}\text{N}$  correlations were recorded with delays  $\Delta T_{\text{pr}}$  0, 2, 4, 6.5 and 12 seconds. One additional reference experiment with  $\Delta T_{\text{pr}}=0$  was recorded in course of the experimental series. At Fourier transformation data were apodized with an exponential line broadening of 10 Hz and 15 Hz in the nitrogen and proton dimension respectively.

### 4.3 Theoretical background.

In the following, we consider relaxation of  $^{15}\text{N}$  spin of amide group in the protein backbone. Motional modulation of  $^{15}\text{N}$ - $^1\text{H}$  dipole-dipole coupling and anisotropy of the  $^{15}\text{N}$  chemical shift results in incoherent effects, like transversal and longitudinal magnetization relaxations, which bring the spin system into Boltzman equilibrium state.

The fast regime of internal motion keeps the theoretical considerations within the limits of Redfield's relaxation theory [127] as it has been confirmed by previous NMR studies in solids [7,8,114,115]. In general, the dynamics of longitudinal and transversal magnetization decays are different and have different functional dependence on the interaction parameters and motional regimes, characterizing the system. Combined analysis of these relaxation data allows to obtain reliable amplitudes and frequencies of the internal motion in range of validity of the employed theory.

The longitudinal relaxation rate  $R_1=1/T_1$  is given by [66]:

$$R_1 = \frac{d^2}{10} [J_0(\omega_H - \omega_N) + 3J_1(\omega_N) + 6J_2(\omega_H + \omega_N)] + \frac{2}{15} c^2 J_1(\omega_N)$$

$$d^2 = \left( \frac{\gamma_N \gamma_H h}{2\pi r_{HN}^3} \right)^2 \equiv \omega_{HN}^2 \quad (4.3.1)$$

$$c^2 = (\gamma_N B_0 (\sigma_{\parallel} - \sigma_{\perp}))^2 \equiv \omega_N^2 \cdot (\Delta\sigma)^2$$

where gyromagnetic ratios of  $^{15}\text{N}$  and  $^1\text{H}$  are denoted as  $\gamma_N$  and  $\gamma_H$  respectively,  $h$  is Planck's constant and  $r_{HN}$  is the effective  $^{15}\text{N}$ - $^1\text{H}$  distance. The Larmor frequency of  $^{15}\text{N}$  and  $^1\text{H}$  is represented by  $\omega_N$  and  $\omega_H$  respectively. The frequency of dipole-dipolar proton-nitrogen coupling is denoted by  $\omega_{HN}$ . The principal values of  $^{15}\text{N}$  CSA tensor are given by  $\sigma_{\parallel} = \sigma_z$  and  $\sigma_{\perp} = \sigma_x = \sigma_y$ . The tensor can be assumed axially symmetric for our considerations [93,99].

In solid state NMR a spin Hamiltonian of an isolated  $^{15}\text{N}$ - $^1\text{H}$  pair is heterogeneous in the sense of Maricq and Waugh [15] and the  $^{15}\text{N}$  line width is determined by relaxation only if the spinning rate is comparable or higher than the size of the CSA and dipole-dipolar interaction. In a system where the proton of  $^{15}\text{N}$ - $^1\text{H}$  pair is coupled by homonuclear dipole-dipolar interaction with a proton net, the spin Hamiltonian is not homogeneous anymore and the dephase of transversal magnetization of  $^{15}\text{N}$  spin is determined not only by relaxation, but influenced also by heteronuclear dipolar coupling with the directly bound proton. In this system the  $^{15}\text{N}$   $T_2$  relaxation dynamics can not be used to probe motional properties of proteins. In a proton dilute SH3 sample proton line widths depend on the spinning frequency, manifesting the inhomogeneous nature of the spin Hamiltonian [28]. In such a system,  $T_2$  measurements are perturbed by heteronuclear dipolar couplings and do not provide directly information about the relaxation. In a system

of 4 protons with weak mutual dipolar interactions of 800-1200 Hz, additional line broadening of both multiplet components of  $^{15}\text{N}$  scalar coupled to  $^1\text{H}$  is uniform and is about 4 Hz, according to the simulations, which results are given in Figure 4.3.1:

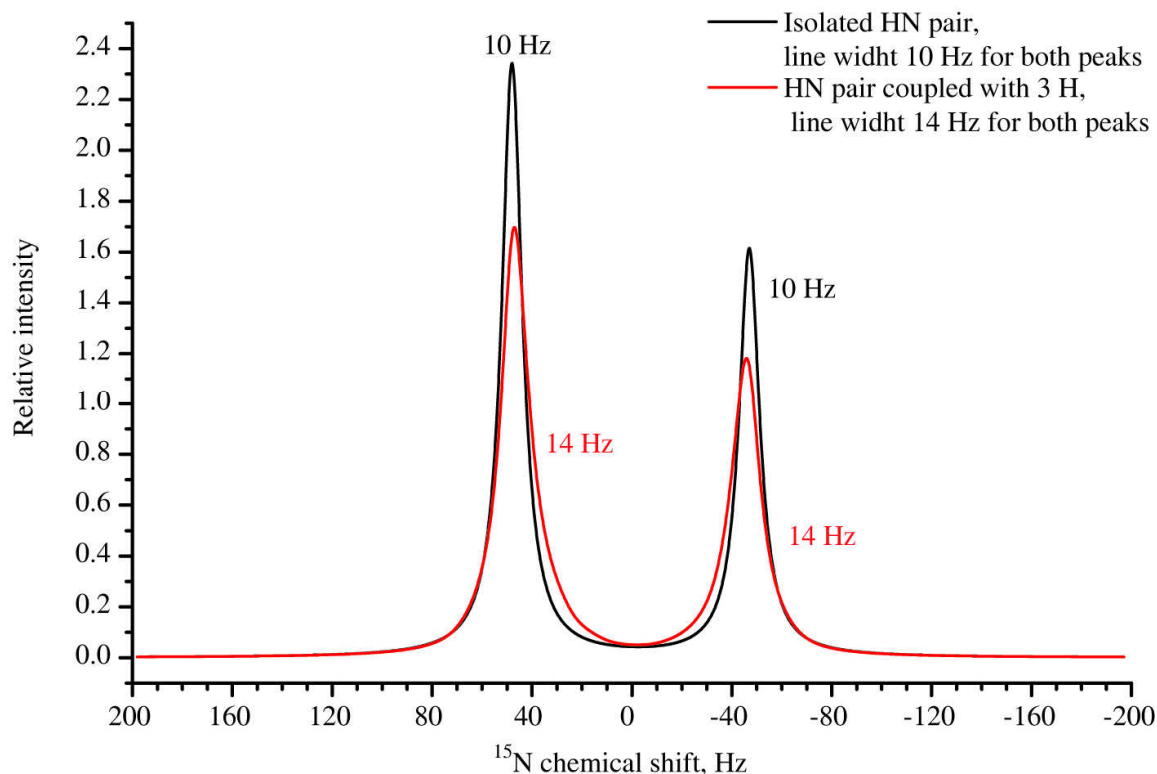


Figure 4.3.1. SIMPSON simulations for line width of  $^{15}\text{N}$  spin coupled to isolated  $^1\text{H}$  (black) or  $^1\text{H}$  dipolar interacting with proton net of 3 spins (red). Line widths at half high are given in the plot.

The simulations have been made using Simpson package [95] and input files are given in Appendix 2.1. The size of homonuclear dipole-dipolar coupling of two protons at a distance of 5 Å is 0.97 kHz. In perdeuterated proteins the proton density is well below  $1.0 \text{ } ^1\text{H}/100\text{Å}^3$  [57,58], for dilute SH3, the proton density is about 10 folds less, since back-exchange of amide protons was made in a 10:90  $\text{H}_2\text{O}$ - $\text{D}_2\text{O}$  mixture. In such protein, the average proton-proton distance is 10 Å resulting in dipole-dipolar coupling of 0.12 kHz, which is well below the values used in the simulations. The asymmetry in the line width of the  $^1\text{H}$ - $^{15}\text{N}$  scalar coupled multiplets is still determined by a cross-correlation relaxation between  $^{15}\text{N}$  CSA tensor and  $^1\text{H}$ - $^{15}\text{N}$  dipolar coupling. The theoretical expression for the cross-correlation rate  $\eta$  is [66]:

$$\begin{aligned}
\eta &= \frac{1}{15} d \cdot c [4J_0(0) + 3J_1(\omega_N)] P_2(\cos \theta) \\
d &= \omega_{HN} \\
c &= \omega_N \cdot (\sigma_{\parallel} - \sigma_{\perp})
\end{aligned} \tag{4.3.2}$$

where  $P_2(x)=(3x^2-1)/2$  is a second Legendre polynomial and  $\theta$  is an angle between the principal axis of HN dipolar tensor and the  $\sigma_z$  axis of  $^{15}\text{N}$  CSA. Other constants are determined in Eq. (4.3.1).  $J_m(\omega)$  is the spectral density function, which depends on the nature of the motion of the HN vector. Direct calculation of the spectral density function for MAS solid state NMR has been made in a number of works [85,128]. Our interpretation of the experimental data is based on the model free approach (MFA) introduced by Lipari and Szabo [110] and extended by Gronenborn and coworkers [126]. In this approach the density function is given by:

$$J(\omega) = \frac{S^2 \cdot \tau_R}{1 + \omega^2 \tau_R^2} + (1 - S_f^2) \frac{\tau_f}{1 + \omega^2 \tau_f^2} + S_f^2 (1 - S_s^2) \frac{\tau_s}{1 + \omega^2 \tau_s^2} \tag{4.3.3}$$

where overall rotational motion is described by the correlation time  $\tau_R$  and the generalized order parameter  $S$ , which is a measure of spatial restriction of the motion. Internal motion is considered to be consisting of superimposed fast and slow motions with fast  $\tau_f$  and slow  $\tau_s$  correlation times [126,128]. Generalized order parameters for fast and slow motion are given by  $S_f^2$  and  $S_s^2$ , respectively. Due to boundary conditions the generalized order parameter can be decomposed as:

$$S^2 = S_s^2 S_f^2 \tag{4.3.4}$$

if slow and fast motions are independent. For sake of physical reasonability fast and slow correlation times should be different at least by one order of magnitude. In the solid proteins rotational reorientation is absent, and the first term in the Eq. (4.3.3) should be omitted, resulting in simplification of motional analysis.

#### 4.4 Experimental results.

The longitudinal relaxation, as well as transverse cross-correlated relaxation rates were measured on a proton dilute  $^{15}\text{N}$  enriched sample of the SH3 domain from chicken  $\alpha$ -spectrin, which has been described in Experimental section. Representative plots of

longitudinal magnetization decay for selected residues collected at 600 MHz are shown in Figure 4.4.1:

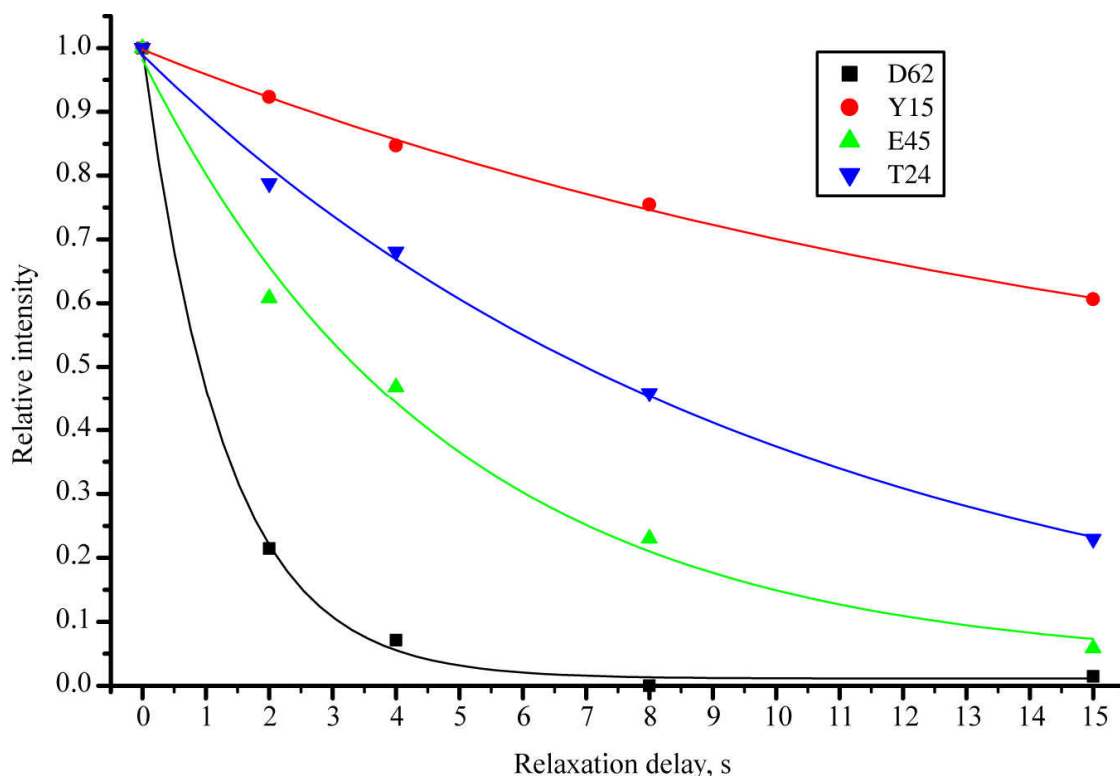


Figure 4.4.1. Relaxation decay for longitudinal  $^{15}\text{N}$  magnetization for D62, Y15, E45 and T24 measured at external magnetic field of 600 MHz proton Larmor frequency. The intensities were renormalized to have first point equal 1. A two parameters monoexponential decay function was used to fit the experimental data. Fitting curves are represented in the same colors as experimental data.

The  $T_1$  relaxation data were obtained according to the pulse scheme represented in Figure 4.2.1. High resolution allows to extract relaxation rates for 46 residues and make a map, covering almost completely backbone. Figure 4.4.2 shows the measured  $T_1$  values at 600 MHz and 900 MHz fields. Monoexponential fit was used to extract relaxation rates from the experimental results. Numerical values of  $T_1$ , as well as  $T_2$  and  $\eta$  are given in Appendix 2.2.

Inspection of Figure 4.4.2 shows strong site specific variations of  $T_1$ . Since the  $^{15}\text{N}$  CSA and  $^1\text{H}$ - $^{15}\text{N}$  dipolar couplings have minor variations for HN pairs in the backbone [93,94,129] it manifests strong difference in motional regime. The obtained  $T_1$  relaxation

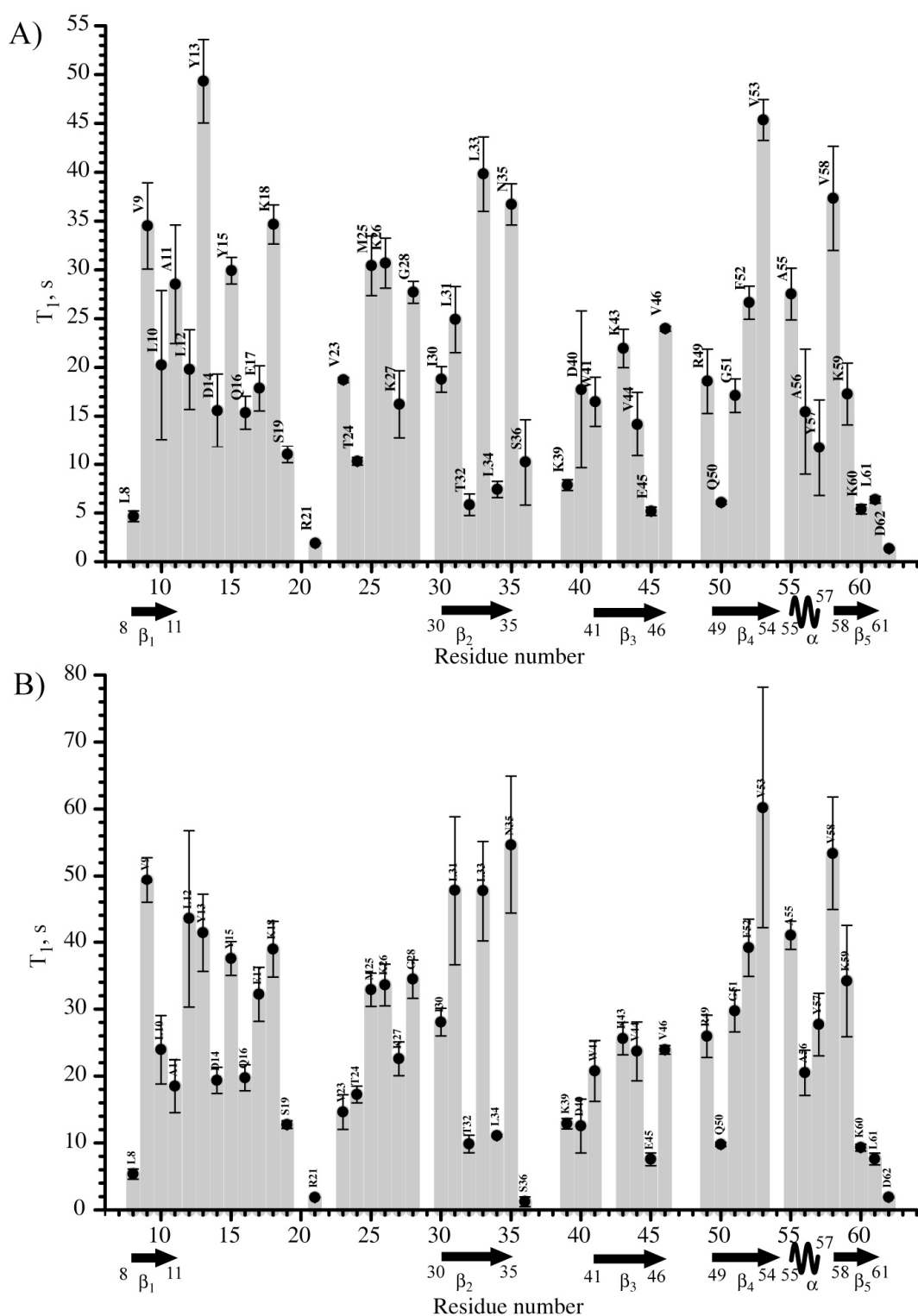


Figure 4.4.2.  $T_1$  relaxation time with respective error bar as a function of residue number. The data were obtained in the experiments performed according to the pulse sequence presented in Figure 4.2.1. A) and B) represent data collected at 600 MHz and 900 MHz respectively. The secondary structure elements are depicted below the X-axis.

data are in agreement with previous works [8,67]. Quantitative analysis shows that at higher magnetic field relaxation time for most residues is considerably longer, approximately 1.2-1.5 times. This reflects that the relaxation is determined mostly by slow motional regime, when  $\omega_N \cdot \tau_s \gg 1$ .

So far, transverse relaxation parameters were not accessible, since it was not understood what determines  $T_2$  relaxation in the solid-state. In protonated samples, residual hetero- and homonuclear dipolar interactions which are not suppressed by MAS or heteronuclear dipolar decoupling can induce significant line broadening which makes impossible the  $T_2$  measurements and analysis. In this chapter, we present an experiment which allows to indirectly access  $T_2$  by measurement of the dynamic interference of the  $^{15}\text{N}$  CSA and the  $^1\text{H}, ^{15}\text{N}$  dipolar coupling in a proton, nitrogen spin pair. These experiments are feasible due to the dramatically decreased proton density, described in Chapter 2 and in the experimental section. This approach in sample preparation yields  $^1\text{H}$  line widths on the order of 17-35 Hz and  $^{15}\text{N}$  line widths on the order of 8-17 Hz at spinning frequency of 8-24 kHz without any homo- and heteronuclear decoupling [28]. Completely resolved  $^1\text{H}-^{15}\text{N}$  scalar coupling allows to measure differential relaxation induced by interference between  $^1\text{H}-^{15}\text{N}$  dipolar coupling and  $^{15}\text{N}$  CSA.  $^{15}\text{N}-^1\text{H}$  2D correlation spectrum recorded according to the pulse sequence given by Figure 4.2.2 at delay  $\Delta=0$  is represented in Figure 4.4.3. High resolution allows to resolve most of the residues and obtain  $T_2$  relaxation parameters for 40 of them. Here and below all represented transversal relaxation experimental results were obtained at a spinning frequency of 24 kHz, except when it states different.





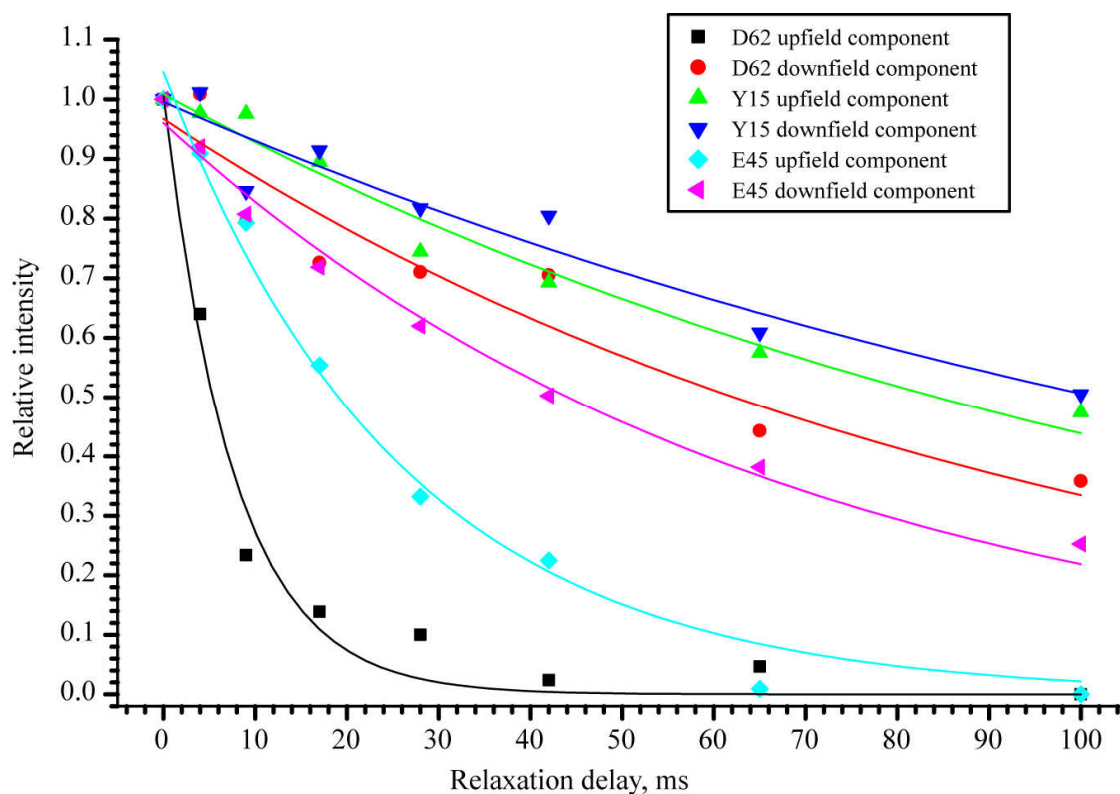


Figure 4.4.4. Relaxation decay of transversal  $^{15}\text{N}$  magnetization, measured at external magnetic field of 600 MHz proton Larmor frequency. Up- and downfield doublet component of D62, Y15 and E45 are plotted. Normalized intensities were fitted employing two parametrical monoexponential decay function. Fitting curves are represented in the same colors as corresponding experimental data.

The transversal relaxation rates for upfield and downfield  $^{15}\text{N}$  doublet components are represented in Figure 4.4.5. The experimental data were fitted with monoexponential decay curve. The upfield component relaxes faster for all residues. Such behavior is quantitatively consistent with the theoretical description given above and allows to employ transversal relaxation data to evaluate backbone motion. Residues G28, L33 and A11 show opposite behavior, which we explain by lack of resolution and sensitivity.

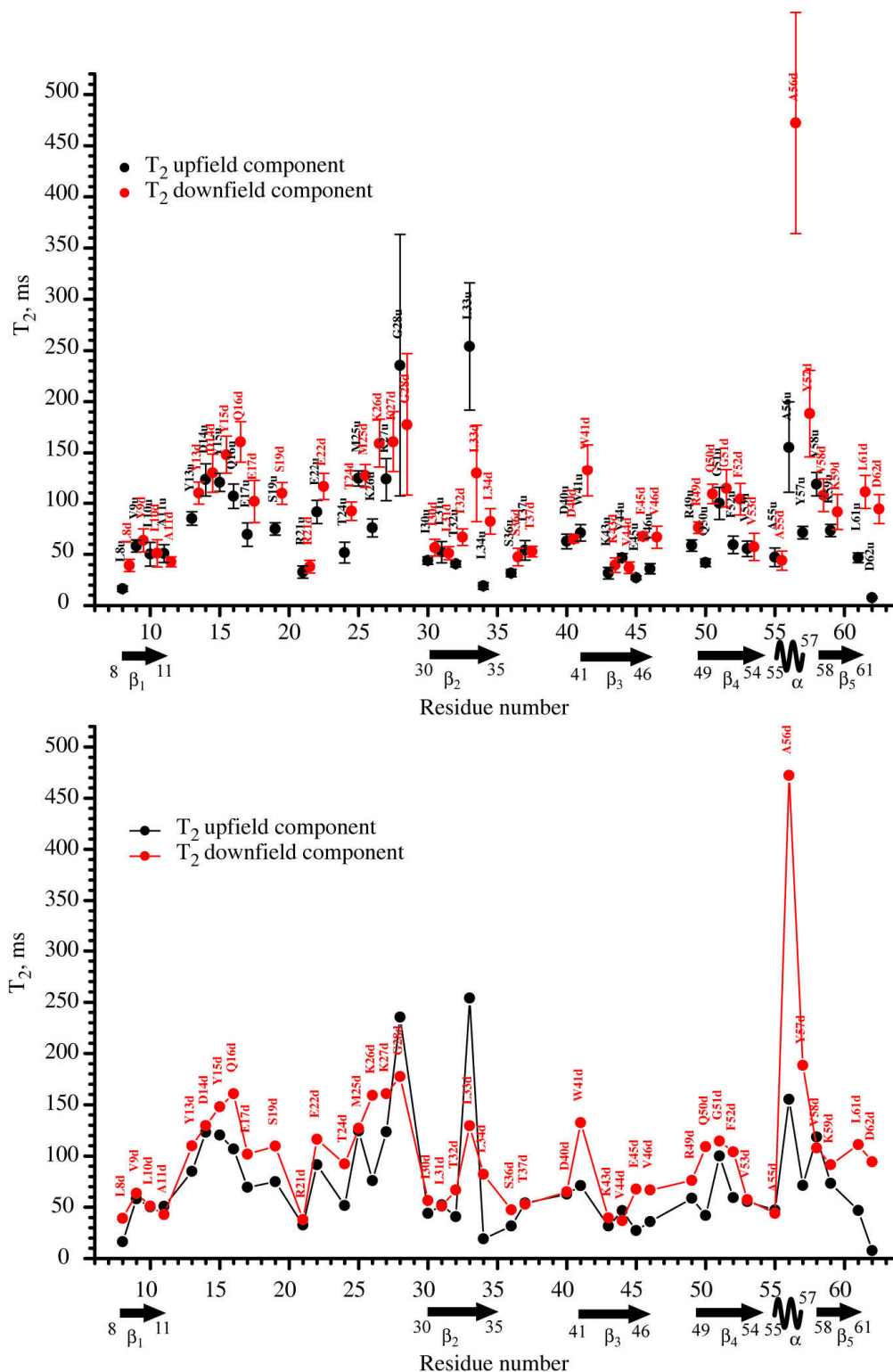


Figure 4.4.5. Experimental transversal relaxation rates of  $^{15}\text{N}$  magnetization. Data for up- and downfield doublet components are represented with and without experimental error bar.

Site specific variations in absolute values of  $T_2$  are well pronounced, but direct consideration of  $T_2$  in relaxation analysis in solid state NMR spectroscopy are not feasible

due to uncertain impact of the dipolar coupled proton net with nitrogen via heteronuclear dipolar interaction. Only difference between up- and downfield components might be accounted to obtain motional parameters. Differential relaxation rates defined as  $1/2(1/T_{2,\text{upfield}} - 1/T_{2,\text{downfield}})$  are represented in Figure 4.4.6:

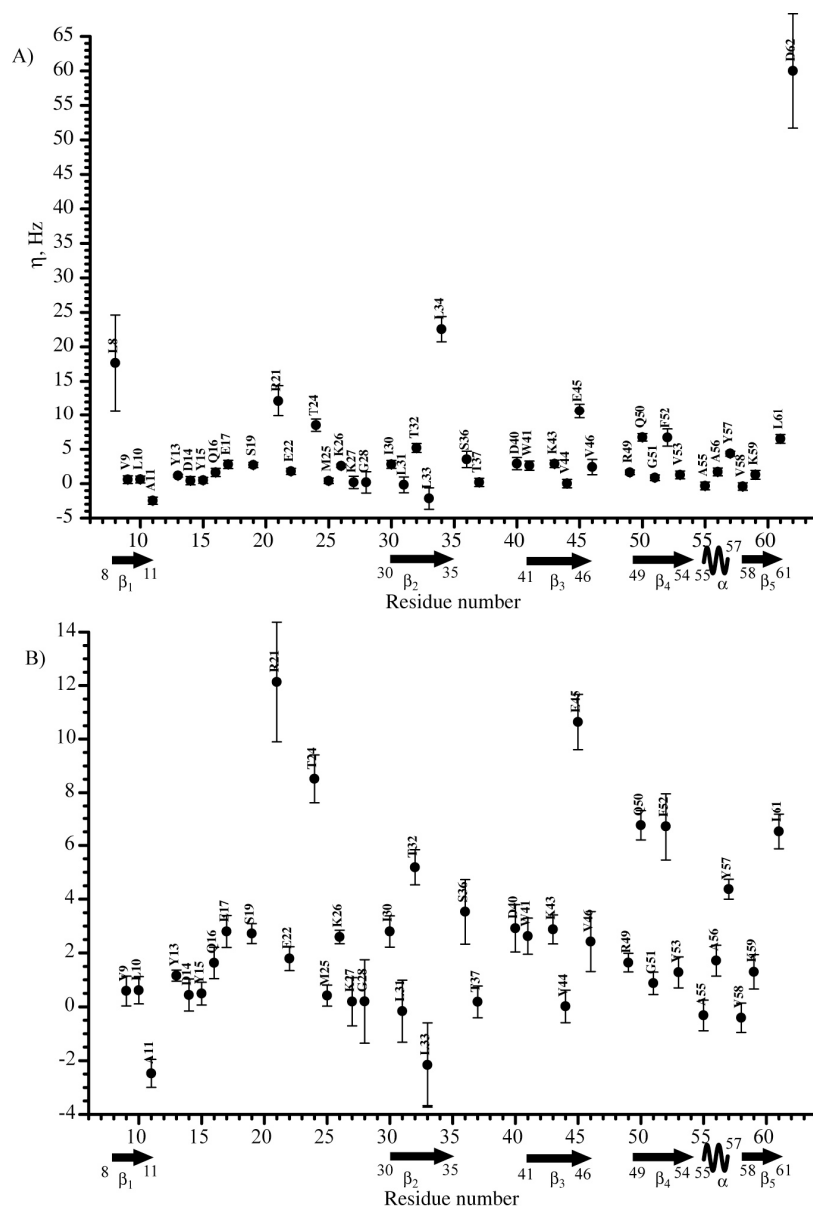


Figure 4.4.6. Experimental CSA/DD cross correlated relaxation rates with fitting error bar. A) and B) represent the experimental data at different scale.

In the experiments we observed non zero differential decay for a number of residues. Residues D62 and L8 located in the C and N terminus, as well as L34, E45, T24 and R21 show extremely high differential line broadening, comparable with proteins in

solution state. Even though high resolution X-ray structure of SH3 [40], (PDB entry 1u06) shows increase in B factor only for two of these residues D62 and L34.

Comparison for differential transversal relaxation rates measured at 16 kHz and 24 kHz are represented in Figure 4.4.7.

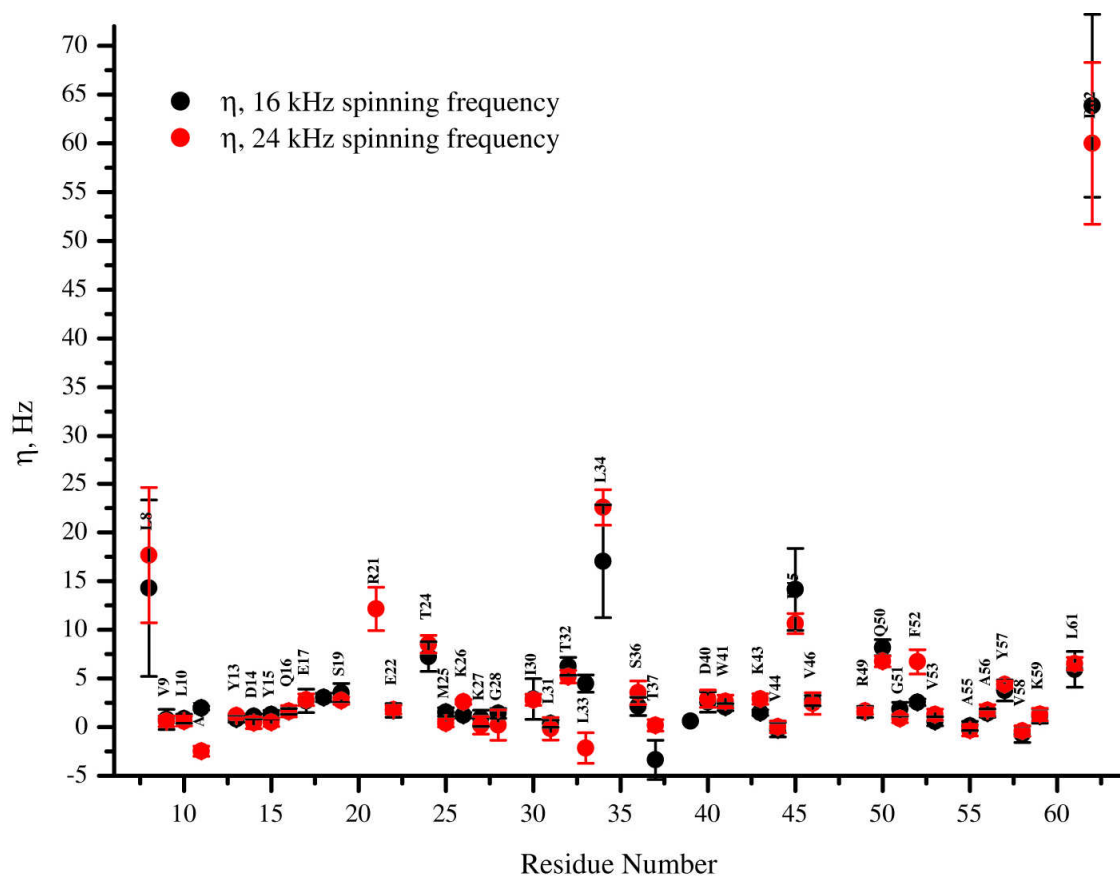


Figure 4.4.7. Experimental CSA/DD cross correlated relaxation rates recorded at 16 kHz and 24 kHz spinning frequency, represented by red and black circles respectively.

Correlation within the experimental error gives the experimental prove for validity of the introduced technique, as it has been predicted earlier by the simulations represented in Figure 4.3.1.

Protein-water hydrogen exchange has impact on measured cross-correlated

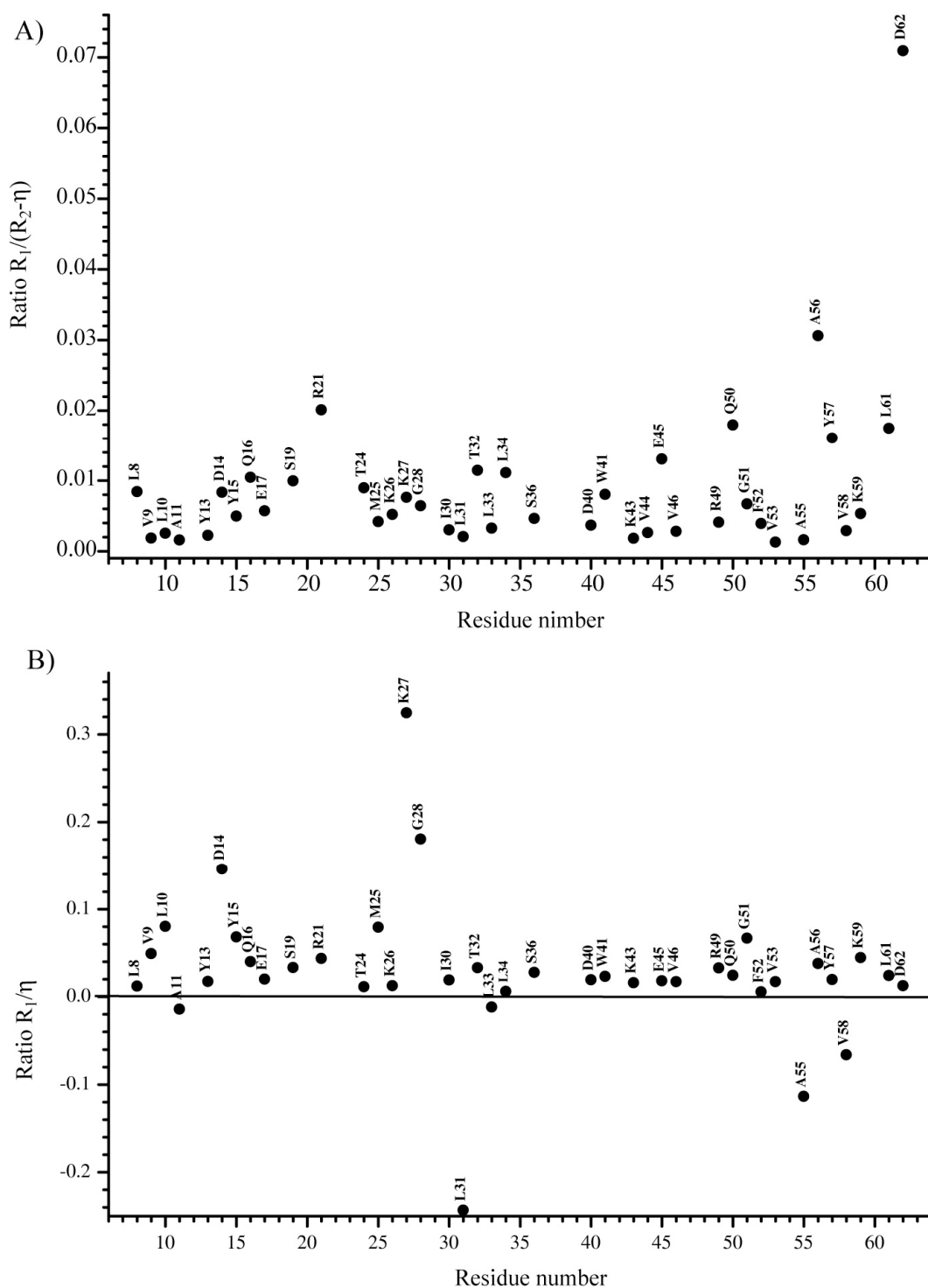


Figure 4.4.8. A) Ratio of transversal relaxation rate of TROSY-component and longitudinal rate for  $^{15}\text{N}$ . B) Ratio of differential transversal relaxation rate and longitudinal rate for  $^{15}\text{N}$ .

relaxation rates, as it has been revealed by a number of works [130,131,132], since  $^1\text{H}$  spin changes quantum state between  $+1/2$  and  $-1/2$ . This results in mixing up- and downfield

$^{15}\text{N}$  components and observable relaxation rates are mixture of both rates, corresponding to TRSOSY and anti-TROSY component. In our experiments the upper limit of the exchange can be approximated by the apparent decay rates in  $^{15}\text{N}$ - $T_1$  measurements. Proton exchange, and thus, replacement of  $^1\text{H}$  by  $^2\text{H}$ , will directly result in a loss of signal intensity. Figure 4.4.8 illustrates the ratio of  $R_1$  and  $\eta$ , as well as the ratio of  $R_1$  and slow decaying multiplet component.

One can see that transversal decay time is much faster than the possible hydrogen exchange, and the measured  $\eta$  values represent the real differential transversal relaxation rates. Observed strong  $^{15}\text{N}$   $T_1$  field dependence manifests that the apparent longitudinal relaxation times are not determined by proton exchange, since this effect is field independent.

The generalized order parameter  $S$  in solid state NMR characterize the amplitude of internal motional and can be extracted by observation of averaged anisotropic interactions. Heteronuclear  $^{15}\text{N}$ - $^1\text{H}$  dipole-dipolar coupling is well suited to probe the order parameter [94,124,125], since it is almost independent on local structure conformations. To measure  $^1\text{H}$ - $^{15}\text{N}$  dipolar couplings, the pulse sequence depicted in Figure 4.2.3 was employed. The size of the dipolar couplings was extracted using fitting routine programmed in SIMPSON simulation package (SIMPSON input file is given in Appendix 2.3). It was assumed that weak proton homonuclear dipole-dipolar interactions in highly proton dilute sample is suppressed to insignificant level by MAS of 24 kHz. This is confirmed by narrow  $^1\text{H}$  line widths on the order of 25 Hz. In rotating frame, determined by spin locking  $^1\text{H}$  field, residual homonuclear dipolar couplings are reduced in twice [14], allowing completely neglect homonuclear dipolar coupling in proton bath. CP dynamics in an isolated  $^1\text{H}$ - $^{15}\text{N}$  was considered in course of the fitting procedure. Three variable parameters were included in the simulations:  $^1\text{H}$ - $^{15}\text{N}$  heteronuclear dipolar coupling, simple exponential damping of the time domain data as well as scaling factor. Dynamics of magnetization transfer from proton to nitrogen during CP for residues Y15, T24, E45 and D62 are given in Figure 4.4.9 with respective simulated curves.

The fitting results for 44 residues are represented in Figure 4.4.10 and given in numerical format in Appendix 2.4.

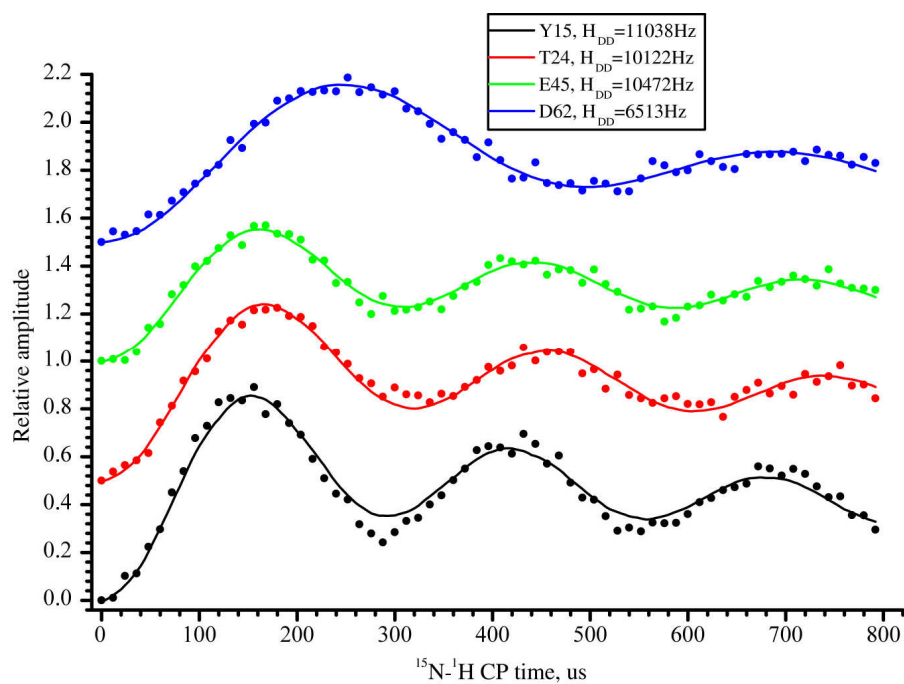


Figure 4.4.9. Evolution of  $^{15}\text{N}$  magnetization for selected residues in course of CP. Simulated curves are represented in corresponding color.

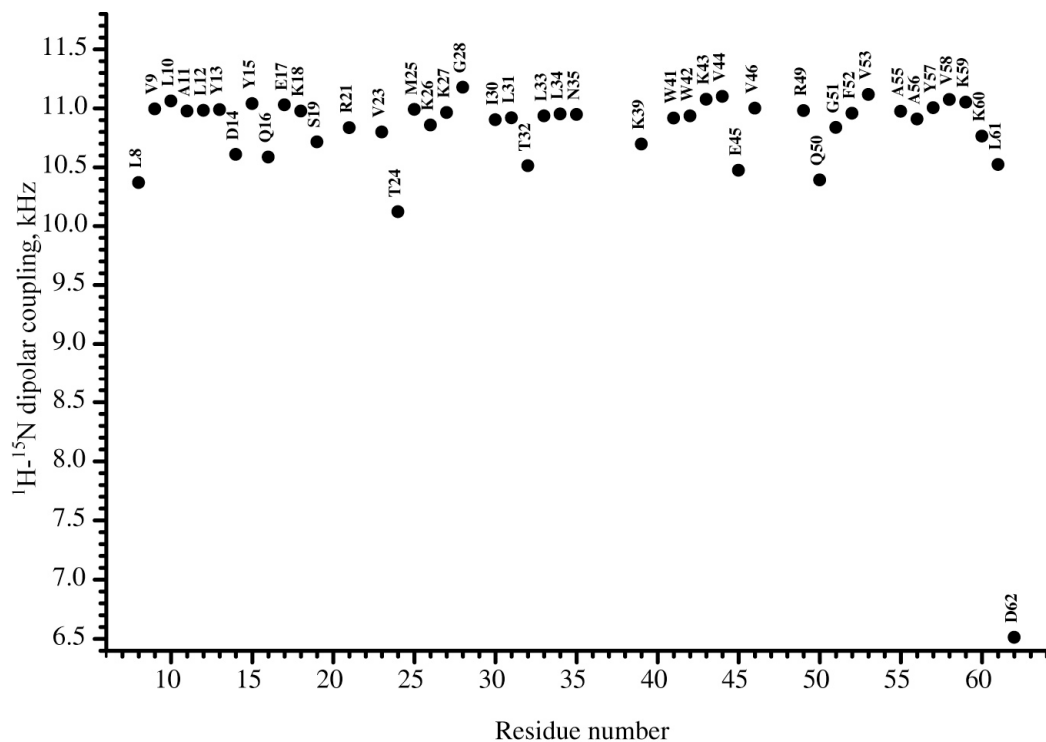


Figure 4.4.10. Measurements of  $^1\text{H}$ - $^{15}\text{N}$  backbone heteronuclear dipolar couplings of SH3 according to pulse sequence given in Figure 4.2.3.



Most of dipolar couplings between proton and nitrogen are close to coupling in static  $^1\text{H}$ - $^{15}\text{N}$  pair with a bond length of 1.02 Å, which corresponds to 11478 Hz in frequency units. These results demonstrate that HN bonds are subjected to very restricted motion in terms of extended MFA. Similar results for HN and HC bonds in backbone of solid state proteins were found in other works [94,124,125]. The relaxation rates for  $^{15}\text{N}$  magnetization in course of the experiment are in the range of 130-800 Hz, which shows slow decay of antiphase coherence, involving  $^{15}\text{N}$  and  $^1\text{H}$  spins.

In solid state NMR the generalized order parameter is a ratio of motional averaged dipolar coupling to it is value at static limit. Trajectory of motion related to dynamic model. If HN bond diffuses in a cone with semiangle  $\alpha$  than general order parameter  $S$  may be expressed as [110]:

$$S = \cos(\alpha)(1 + \cos(\alpha))/2 \quad (4.4.1)$$

For  $\alpha = 21.3^\circ$  it gives order parameter of 0.9. A relationship between order parameter and parameters of motional trajectory have been studied for a number of models by different authors [128,133,134,135].

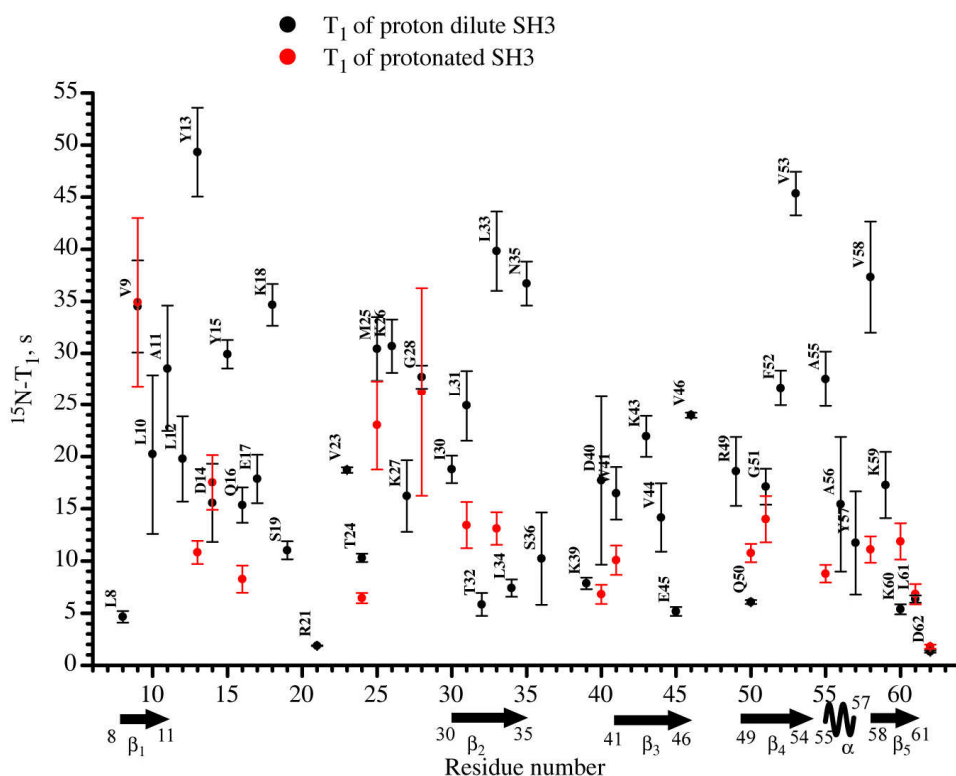


Figure 4.4.11. A comparison of longitudinal relaxation rates measured on protonated (red) and dilute (black) sample of SH3 vs. residue number.

Potential influence of protonation on observable  $^{15}\text{N}$   $T_1$  values was studied by comparison of longitudinal relaxation rates measured on fully protonated and proton dilute samples, which are presented in Figure 4.4.11.

Although many residues show the same relaxation times in both experiments, in general relaxation is considerably longer for the highly deuterated sample, which can be explained in view of the following effects. As it has been shown previously [5,122], in a protonated proteins  $^{15}\text{N}$ - $^{15}\text{N}$  diffusion takes place on second time scale and can equalize observable longitudinal relaxation rates which are in the range of 0.02-0.2 Hz. Strong dependence on the MAS speed of  $^{15}\text{N}$ - $^{15}\text{N}$  PDSD and observable longitudinal relaxation rates have been studied in other works [136,137] which strongly confirm this source of uncertainty in  $^{15}\text{N}$   $T_1$  observations. Another possible source of interference in  $^{15}\text{N}$  motional analysis could be a relaxation induced by neighboring protons in protonated sample. These  $^{15}\text{N}$   $T_1$  relaxation interactions are suppressed to insignificant level at the protein preparation, used for our experiments.

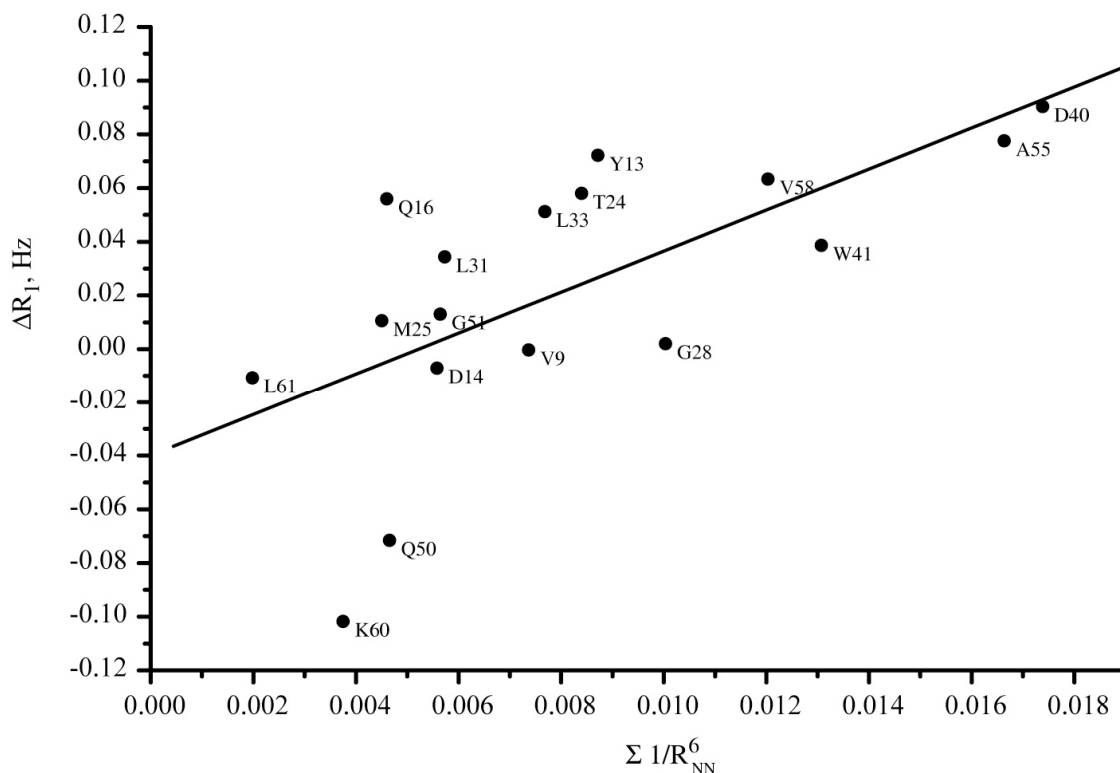


Figure 4.4.12. Differences of longitudinal relaxation rates measured in protonated and proton dilute sample of SH3 as a function of sixth power of inverse distance between nitrogen neighboring. Linear fit represented as continuous line.

Correlation of difference in  $^{15}\text{N}$  relaxation rates for protonated and highly deuterated samples  $\Delta R_1 = R_{1,\text{protonated}} - R_{1,\text{deuterated}}$  to local nitrogen density within 6Å vicinity is plotted in Figure 4.4.12.

The sum of  $^{15}\text{N}$ - $^{15}\text{N}$  inverted distances in sixth power, calculated according to crystallographic structure (PDB entry 1u06 and 2NUZ), at first approximation proportional to  $^{15}\text{N}$ - $^{15}\text{N}$  PDSD. The correlation is loosely represented by linear fit  $\Delta R_1 = -0.04 + 7.64 \cdot (\Sigma 1/R_{\text{NN}}^6)$ , with standard deviation of 0.021 and 2.27 for the y-intercept and the slope respectively. From this experiments we see no straight correlations for changes in  $R_1$  and possible  $^{15}\text{N}$ - $^{15}\text{N}$  PDSD, which shows that the observable  $R_1$  rates in protonated samples can not be reliable corrected using simple empirical model based only on local nitrogen density. We can conclude that high deuteration degree in proteins is required to obtain relaxation information in isolated HN pairs to study backbone dynamics, since that evolution of quantum system of many interacting spins can not be described accurate for a protein.

#### 4.5 Simulated results and discussions.

Simulations to fit the experimental data were performed using the extended model free approach [110,126]. Theoretical interpretation of relaxation experiments based on extended MFA is very common in solution state NMR for decades, while limited works [67,80,115,128] employed it to analyze motion by solid state NMR. In solution there is fast isotropical overall molecule tumbling on nanosecond timescale resulting in isotropic relaxation rates.

In solid state, a powder sample consists of crystallites which are fixed in a rotor and have isotropic distribution of orientations which are modulated by rotor spinning and small amplitude internal motions. Under these conditions motional trajectory of each crystallite is very restricted and depends on the orientation in the rotor frame. In general, it leads to anisotropic relaxation rates, as it has been shown in number of works [85,128]. Thus, experimentally observed  $T_1$  and  $\eta$  rates are average values over a rotor period and crystallites ensemble.

Measured heteronuclear  $^{15}\text{N}$ - $^1\text{H}$  dipolar interactions allow to obtain directly the generalized order parameters as the ratio of motional averaged dipolar couplings to its value at static limit.

In order to extract the dynamic parameters  $\tau_f$ ,  $\tau_s$  and  $S_s^2$ , the difference between experimental and theoretical data were calculated according to the Equation 4.5.1:

$$RMSD = \left( \left[ \frac{1}{R_{1,600}^{ex}} (R_{1,600}^{theo} - R_{1,600}^{ex}) \right]^2 + \left[ \frac{1}{R_{1,900}^{ex}} (R_{1,900}^{theo} - R_{1,900}^{ex}) \right]^2 + \left[ \frac{1}{\eta^{ex}} (\eta^{theo} - \eta^{ex}) \right]^2 \right)^{1/2} \quad (4.5.1)$$

where  $RMSD$  is difference between experimental and theoretical data, which was minimized by a grid search on  $\tau_f$ ,  $\tau_s$  and  $S_s^2$ , superscripts *theo* and *ex* denote theoretical and experimental values for transversal relaxation rate  $\eta$ , longitudinal relaxation rates  $R_{1,600}$  and  $R_{1,900}$  obtained in 600 MHz and 900 MHz external magnetic fields respectively. The theoretical values for the relaxation rates were calculated according to the equations 4.3.1, 4.3.2, 4.3.3 and 4.3.4. Three experimental values can determine unambiguous three unknown dynamic variables  $\tau_f$ ,  $\tau_s$  and  $S_s^2$ , describing backbone motion.

Fast correlation times are determined by local librations and are on the order of 10 ps. At first approximation relaxation rates in solid state can be characterized by slow correlation times [67,85,115, Giraud, 2005 #159], while fast correlation times have a minor impact. It can be assumed that  $\tau_f = 15$  ps [115]. At these approximations we map  $RMSD$  surface in  $\tau_s$  and  $S_s^2$  coordinates to localize the minimum for each residue. For the simulation  $^{15}\text{N}$  CSA value  $\Delta\sigma = 170$  ppm and its angle  $\theta = 20^\circ$  were taken. Other numerical values for parameters are:  $^1\text{H}$ - $^{15}\text{N}$  dipolar coupling is 11478 Hz, proton frequency for spectrometers at nominal external magnetic field of 600 MHz and 900 MHz are 600.1275 MHz and 900.19 MHz respectively. Mapped  $RMSD$  for the residue T24 is presented below. In order to consider an impact of different relaxation data on convergence of  $RMSD$  two additional minimization fittings were made based only on longitudinal relaxation rates obtained at 600 MHz and 900 MHz external magnetic fields (difference noted  $RMSDT1$ ), and longitudinal relaxation rates and transversal cross correlated relaxation rates at 600 MHz magnetic field (difference noted  $RMSDT1\eta$ ). Expressions for calculated values are given below:

$$\begin{aligned}
RMSDT1 &= \left( \left[ \frac{1}{R_{1,600}^{ex}} (R_{1,600}^{theo} - R_{1,600}^{ex}) \right]^2 + \left[ \frac{1}{R_{1,900}^{ex}} (R_{1,900}^{theo} - R_{1,900}^{ex}) \right]^2 \right)^{1/2} \\
RMSDT1eta &= \left( \left[ \frac{1}{R_{1,600}^{ex}} (R_{1,600}^{theo} - R_{1,600}^{ex}) \right]^2 + \left[ \frac{1}{\eta^{ex}} (\eta^{theo} - \eta^{ex}) \right]^2 \right)^{1/2}
\end{aligned} \tag{4.5.2}$$

where all notations correspond to the ones introduced in Equations 4.5.1. The experimental (with standard deviation) and fitted values for T24 are given in the Table 4.5.1:

Table 4.5.1. Experimental and fitted values for T24.

	$\tau_s$ , ns	$S_s^2$	$T_1$ , s (600MHz)	$T_1$ , s (900MHz)	$\eta$ , Hz	Fitting error
Experiment			10.3±0.4	17.23±1.24	8.52±0.90	
RMSD fit	34.8	0.78	10.62	17.97	8.0	0.08
RMSDT1eta fit	35.2	0.78	10.74	---	8.08	0.065
RMSDT1 fit	32.4	0.79	10.28	17.24	---	0.003

where generalized order parameter  $S^2=0.78$ .

Figure 4.5.1 illustrates *RMSD*, *RMSDT1* and *RMSDT1eta* surfaces in coordinates  $\tau_s$  and  $S_s^2$ .

While fits based on differential transversal relaxation rate show well defined extreme, minimization routine based only on  $T_1$  data give a ‘valley’ of possible solutions for  $\tau_s$  and  $S_s^2$ , which demonstrates that this analysis effectively determines the ratio  $(1-S_s^2)/\tau_s$ . This is to be expected, when the data are limited to  $T_1$  times, and similar behavior has been observed in other studies [67,85].

Optimization procedure according to Equation 4.5.1 was applied to 33 residues, which have full set of experimental data, while  $\tau_f$  was assumed to be of 15 ps. *RMSD* values for 18 residues were within a range of error of 26%, which corresponds to the estimated experimental accuracy. Slow correlation times with the corresponding square of order parameters as well as the square of generalized order parameter are plotted in Figure 5.4.2.

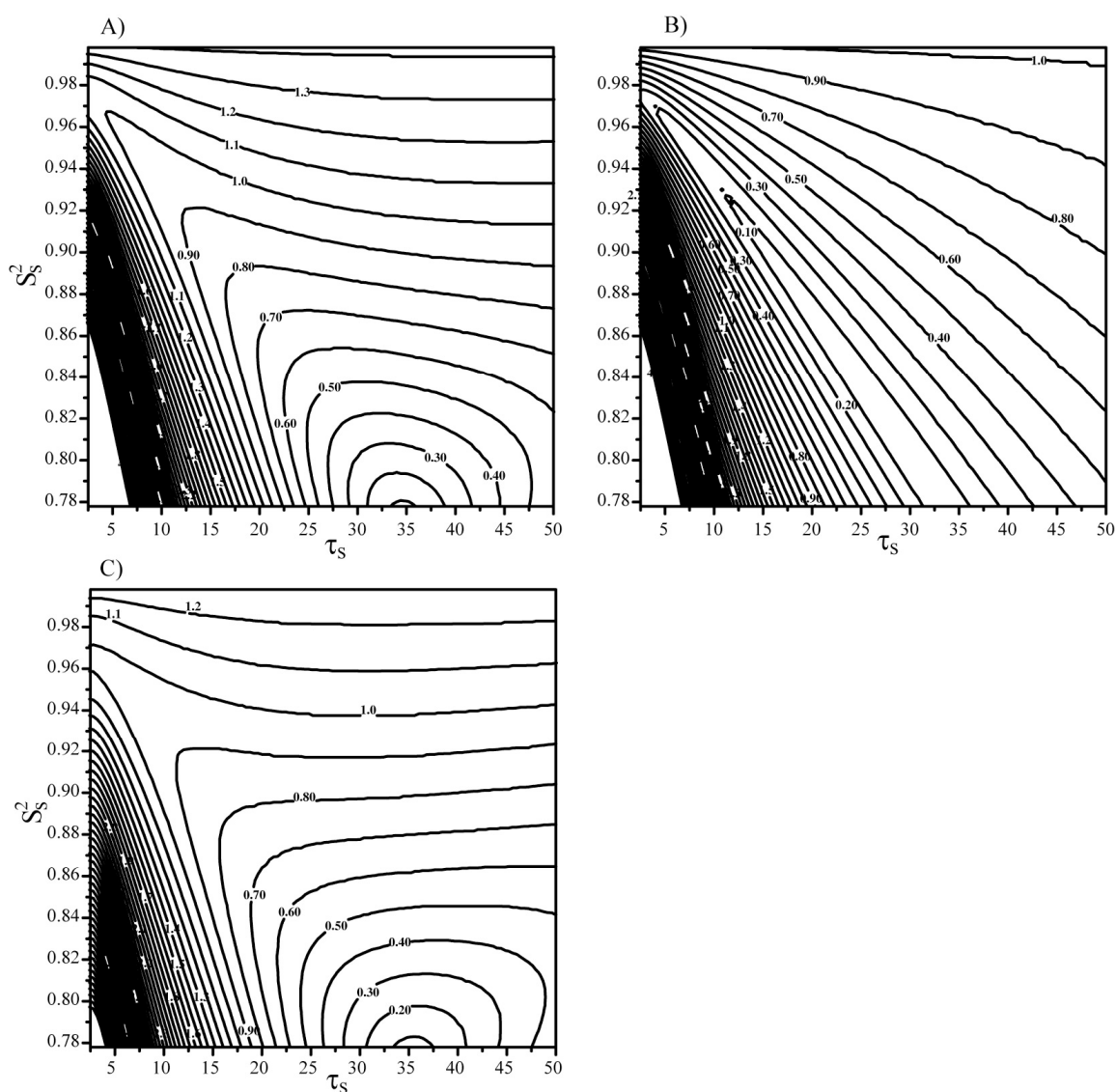


Figure 4.5.1. Difference between theoretical and experimental relaxation data for T24 as a function of  $\tau_s$  and  $S^2$ . Surfaces for RMSD, *RMSDT1* and *RMSDT1eta* are represented by A), B) and C) respectively.

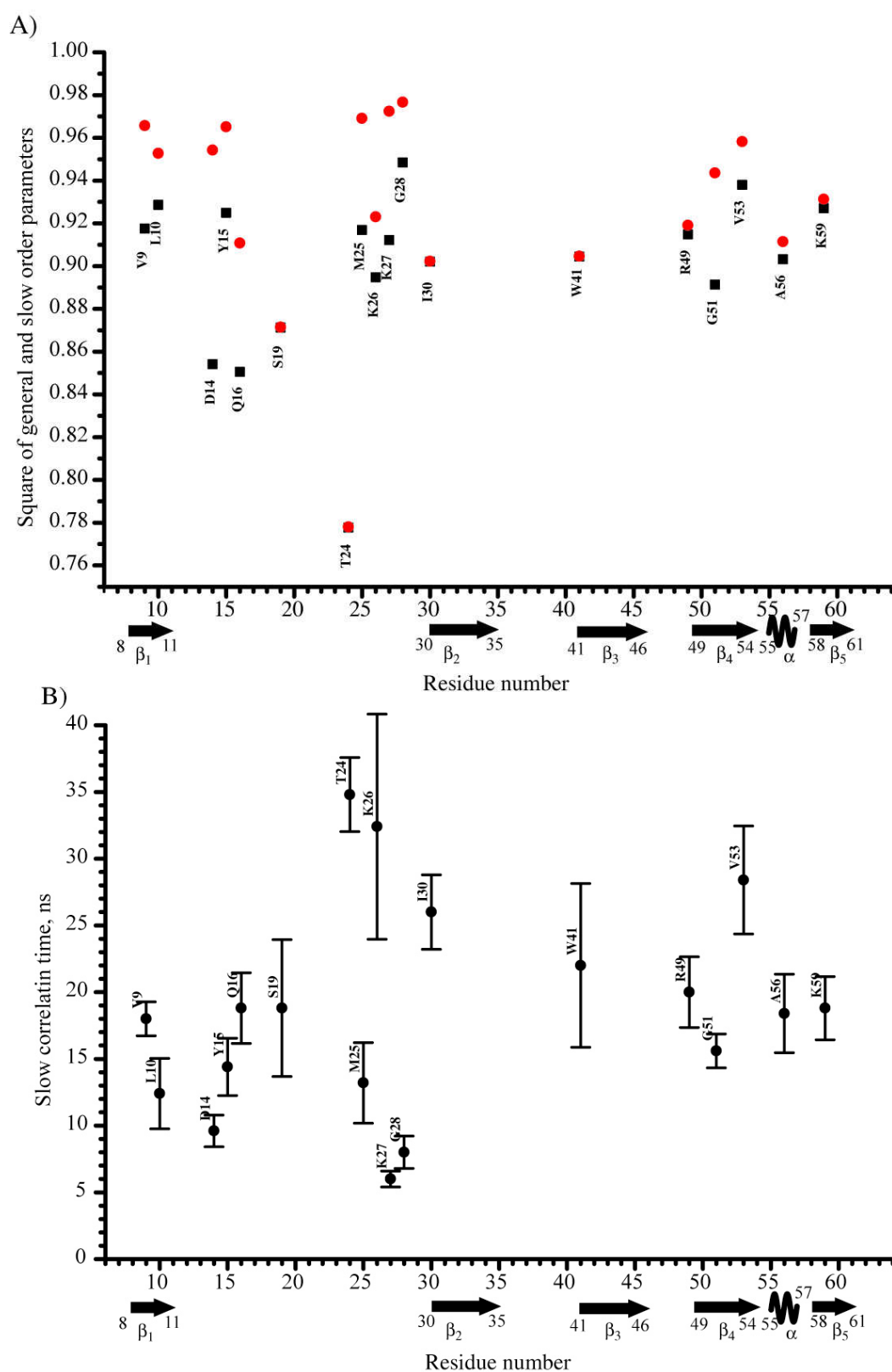


Figure 4.5.2. A) Square of generalized (black) and slow motion (red) order parameters. B) Slow correlation time. Error bars in figure B) represent total *RMSD* of the fit.

Values obtained for  $\tau_s$  and  $S_s^2$  are consistent with data obtained by Emsley and coworkers for Ch microcrystalline protein [85].

The presented results of the simulations demonstrate that fast correlation time might have significant impact on relaxation dynamics for a number of residues. In attempt to capture influence of this motion and its characteristics, we reanalyze all the data in a view of *RMSD* minimization determined by Equation 4.5.1 using for 3 dimensional (3D) grid search as variable parameters not only  $\tau_s$  and  $S_s^2$ , but  $\tau_f$  as well. Motional parameters were reconsidered for all residues. Home made C++ code employed to extract dynamical values is given in Appendix 2.5. Generalized order parameter as well as order parameter for slow motion are shown in Figure 4.5.3:

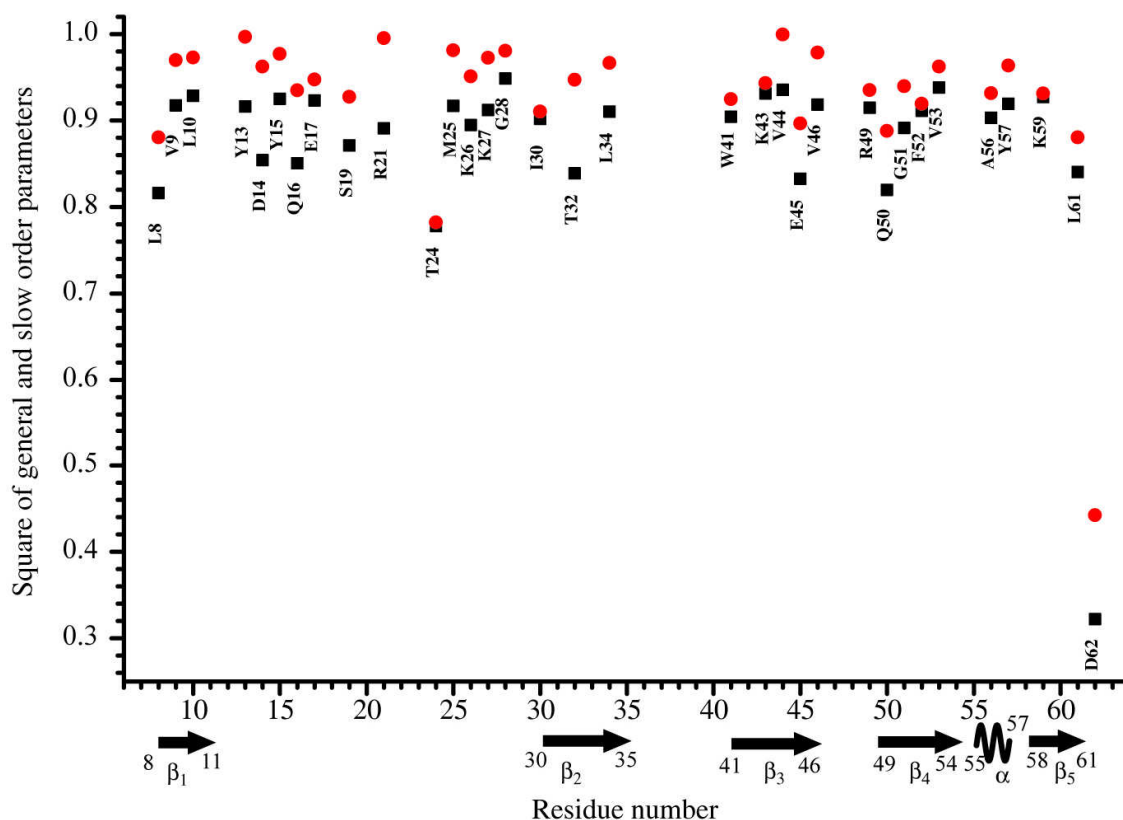


Figure 4.5.3. Square of generalized (black) and slow motion (red) order parameters obtained in 3D grid search for SH3 backbone.

Fast and slow correlation times are given in Figures 4.5.4 and 4.5.5 at different scales.



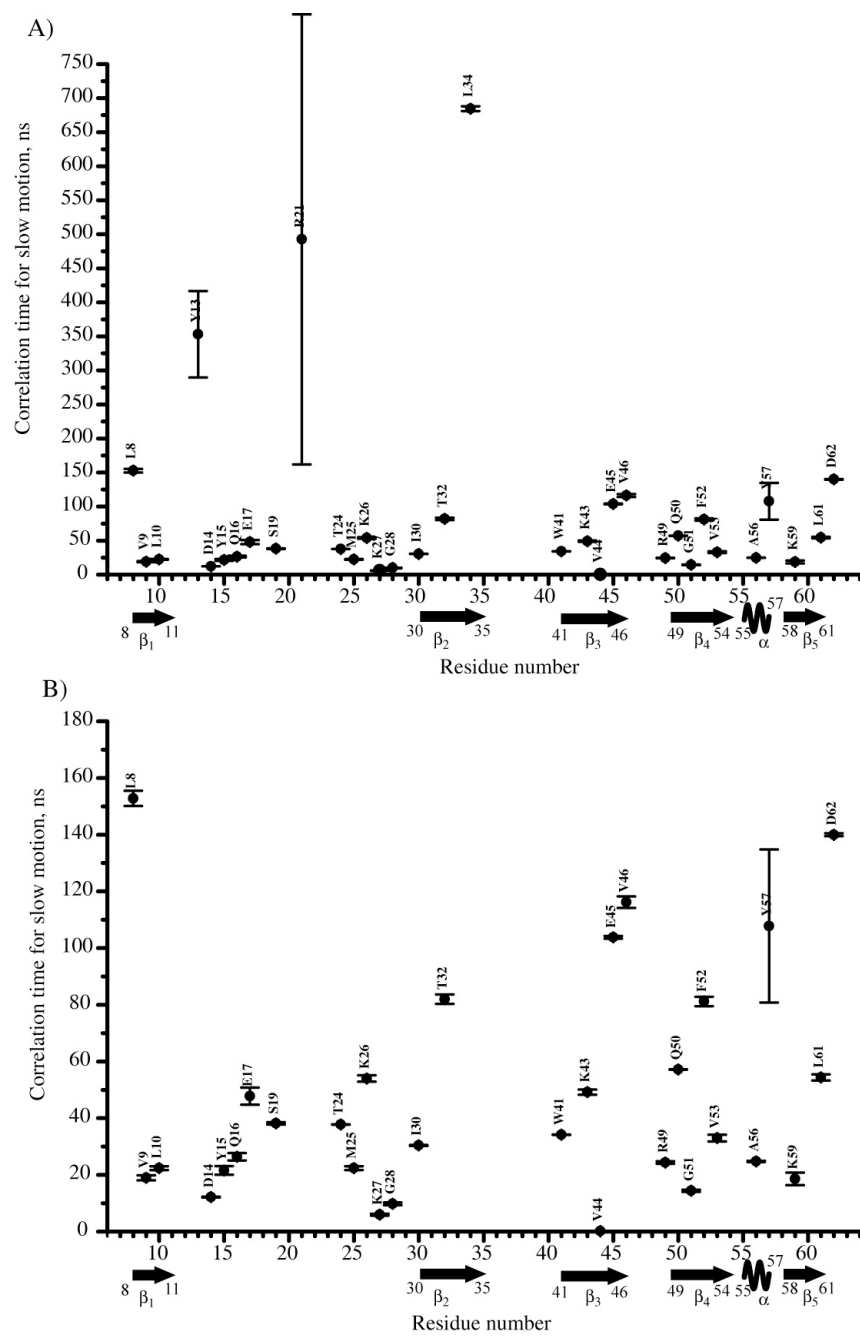


Figure 4.5.4. Slow correlation times for SH3 backbone from three parametrical relaxation data fitting. Error bars represent total *RMSD* of the fit. The data are represented at two scales.

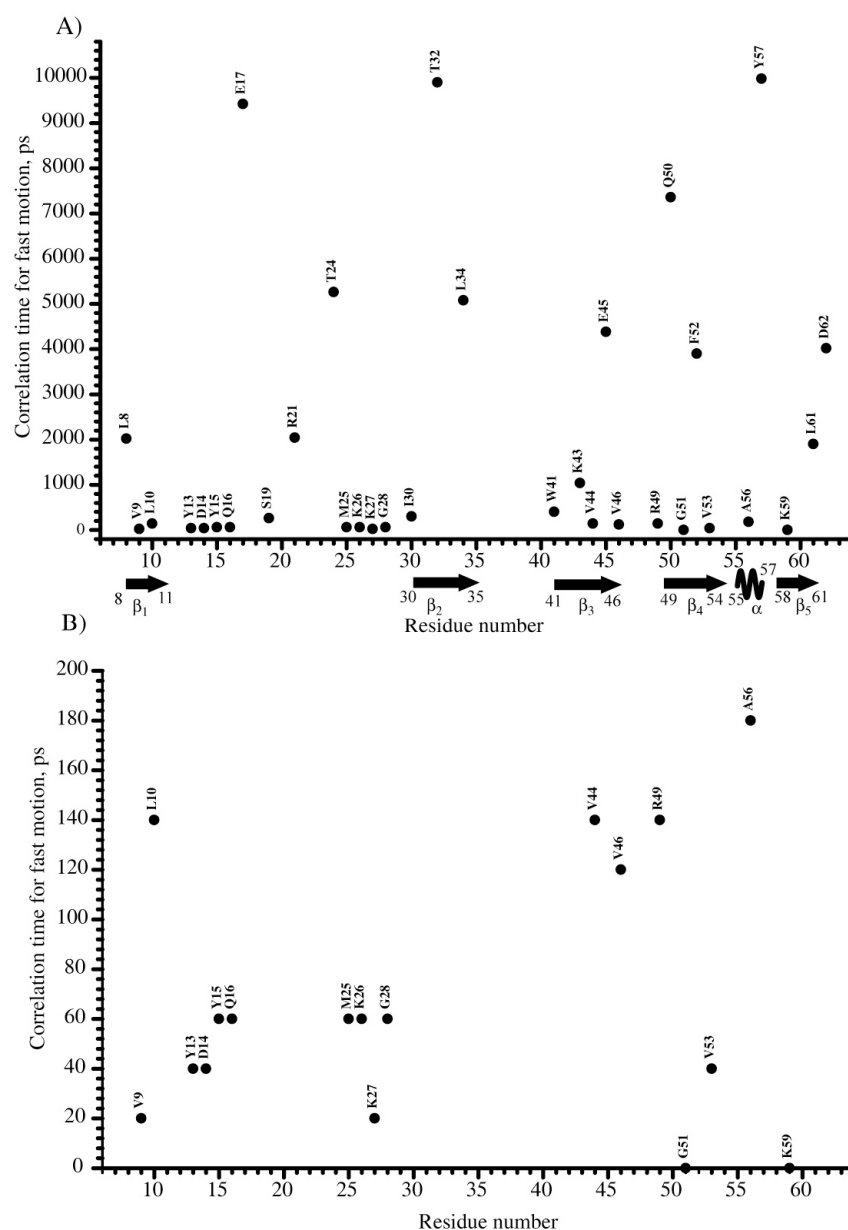


Figure 4.5.5. Fast correlation times for SH3 backbone from three parametrical relaxation data fitting. The data are represented at two scales.

Represented in Figure 4.5.4 error bars give minimum of total *RMSE*. Presence of a big error for Y13, R21 and Y57 are explained by low experimental data quality and are not consider in following analysis. As it follows from structural elements of SH3 depicted in all Figures there is no straightforward correlation of motional parameters and secondary elements of the protein. The same results were observed in the work of Emsley and coworkers [85]. For solution state NMR, relationship between motional parameters and secondary structure elements are well established and usually loops, N- and C- terminus

and other flexible regions have well pronounced low  $S^2$  and  $J(\omega_N)$  values [138,139]. Our experimental data for measured  $^{15}\text{N}$ - $^1\text{H}$  dipolar coupling and  $T_1$  show that there is no such strong dependence, but a tendency, that non structured elements have low  $S^2$  and, contrary to solution state,  $J(\omega_N)$  has higher values, e.g. D62 , L8, R21, T24. All the residues showing short  $T_1$  (L8, R21, T24, T32, L34, E45, Q50, Y57, L61 and D62) have  $\eta$  higher than 5 Hz. We also did not reveal any correlation between hydrogen bonding and motional parameters. Recent work in solution state NMR [140] shows the possibility of inter  $\beta$ -sheets long-range correlated motion, providing wave type spreading of slow motion and conformational changes across a protein. This idea can stimulate possible analysis approaches to connect secondary structure and slow motion in a solid protein as well. The summary of all simulation results is given in Appendix 2.6.

Inspection of Figures 4.5.4 and 4.5.5 show an outstanding class of residues, which have extremely long slow and fast correlation times of nanosecond and 50-200 ns range respectively. These values are much more higher than typical correlation times for proteins' backbone in solution state, which are on the order of 10 ps and 10 ns for fast and slow motion respectively. Recent combined studies of  $^{15}\text{N}$  relaxation data from solution and solid state NMR [67,80] suggest that internal dynamics of a globular protein in liquid and in crystalline solid are essentially identical, which has many other lines confirming this supposition. One physical rationale behind is the nature of forces determining fast and slow motion. Fast motion is actually due to local librations determined mostly by forces of chemical bonds. While a base for slow motion are long range forces, which have a higher variability and resulting in broader correlation time distribution. The major difference between backbone relaxation in solid and solution state is, so far, overall tumbling. Recent studies of backbone motion [141] by means of residual dipolar couplings revealed a presence of an additional motion on the order of 100 ns, which is consistent with our results for slow motion of a group of residues. In order to explain obtained long correlation time for a number of residues we can consider a presence of an additional slow motion regime with correlation time around 100 ns. Obtained for these residues "fast motion", according to physical consumptions, should be considered as another slow motional regime, which has a typical correlation time  $\sim 10$  ns, and which has been deeply studied before by liquid state NMR. Additionally a motion on the time scale of 10 ps must

be present. Due to limited set of experimental data it can not be quantitatively described and more relaxation experiments are required for detailed description of this motion.

In conclusion, we could show that due to large scale of deuteration transverse relaxation properties of  $^{15}\text{N}$  can be measured in solid state NMR, which have not been accessible before. Combined with high quality longitudinal relaxation experiments and heteronuclear  $^{15}\text{N}$ - $^1\text{H}$  dipolar couplings measurements these data provide reliable base for quantitative analysis of backbone motion in microcrystalline protein of SH3. Observed substantial difference in longitudinal and transversal differential rates manifest strong site dependent variability of backbone. Extended model free approach was employed to extract parameters like correlation time and order parameter of motions at different time scales. It has been shown that transversal relaxation experiments dramatically increase accuracy of obtained motional parameters. Additional relaxation processes on a time scale of 50-200 ns has been detected.

We expect that these experiments will find widespread application in the characterization of dynamics of biomolecules at high quality level.

## 5 Chapter. Detection of water molecules in a microcrystalline sample of the SH3 domain of $\alpha$ -spectrin by MAS solid-state NMR.

### 5.1 Introduction.

The interaction of water with proteins is a major determinant of protein stability. In protein crystal structures, many water molecules are found to be closely associated with polar surface groups and may confer correlated dynamical behavior of these groups. More importantly, water molecules adopt a very important role in function of many membrane proteins like e.g. proton pumps like bacteriorhodopsin and secondary transporters. The discovery and characterization of channels in cell membranes, for which the Nobel price for Chemistry in 2003 was awarded to Peter Agre and Roderic MacKinnon, has ongoing impact on the study of membrane proteins in general. Even though many structural aspects of water and ion channels could be clarified [142,143], questions concerning the details of the transport mechanism remain to be answered [144]. Solid state NMR is well suited to address these problems due to its sensitivity to the local environment of a given spin. Characterization of mobile water molecules in MAS ssNMR was pioneered by Griffin and co-workers [145], who detected water molecules in the vicinity of the Schiff-base nitrogen in bacteriorhodopsin.

Deuteration offers the unique possibility to study the dynamics of these water molecules in details. Deuteration is required in order to suppress strong intermolecular proton-proton dipolar interactions which would perturb weaker interactions between the protein and water molecules of interest.

It was demonstrated in solution state NMR that information about hydration dynamics can be obtained from nuclear Overhauser effects (NOEs) between water and protein protons [146,147,148]. Tightly bonded water molecules can be site-specifically localized. If their correlation time is long enough ( $\omega\tau_c > 1.13$ ), they give rise to a negative NOE which has the same sign as the diagonal peak. Complementary information on the dynamics of water molecules can be obtained from magnetic relaxation dispersion

measurements [149]. This method makes use of a differential rotational correlation time of water molecules which gives rise to a characteristic frequency dependence of the longitudinal relaxation rate  $R_1$  especially of quadrupolar nuclei like  $^2\text{H}$  and  $^{17}\text{O}$ , and allows the determination of the life time of water molecules bound in the interior of a protein. This life time is strongly temperature dependent and was estimated to be in the order of  $\mu\text{sec}$  at room temperature [150,151,152]. Water molecules exchange with external bulk water as a result of protein conformational fluctuations. Motion in this time regime ( $\tau_c \approx 1\mu\text{sec}$ ) should therefore induce relaxation in neighboring  $\text{H}^{\text{N}}$  resonances due to dipole dipole interactions.

In this chapter we present a qualitative description of the water dynamics in a protein in the solid state [40]. The dynamic characteristics are indirectly monitored by the efficiency of magnetization transfer between the water molecule and a reporter amide proton and by the  $T_2$  relaxation of the amide protons which we find to be altered due to the presence of mobile water. The conclusions are drawn from comparison of the ssNMR data with a X-ray structure. Available resolution of X-ray structure is  $1.49 \text{ \AA}$ , which allows the refinement of water molecules in the structure. The current study was motivated by the observation that certain cross peaks in the previously described  $^1\text{H}$  detected  $^1\text{H},^{15}\text{N}$  correlation experiment were absent, when homonuclear decoupling was omitted in the proton dimension [38]. Recently have reported studies about correlations between side chain carbon resonances carbons nearby labile protein protons and water protons. Mechanisms like water-protein hydrogen exchange [153,154], dipolar-mediated water-protein interaction [155] were considered. These correlations were predominantly observed for Tyr, Thr, Ser, Lys and His residues with labile hydroxyl, imidazole ring, or side-chain amine protons. Heteronuclear Overhauser effects was observed between  $^{15}\text{N}$  and  $^1\text{H}$  nuclei, confirming dipolar relaxation mechanism in a microcrystalline protein [156].

The presented experiments are sensitive to distance and dynamics of the detected water molecules with respect to the protein. We show here for the first time that information about localization and dynamics of water molecules can be obtained in the solid state by interpretation of the relaxation behaviour of a reporter amide proton.

## 5.2 Materials and solid state NMR methods.

The SH3 protein sample was expressed and purified according to the protocol described in [42]. The X-ray structure used for the complimentary analysis was determined by Dr. Katja Faelber. It was solved at 100 K. The structure was deposited in the PDB, entry 1U06. The detailed description is given elsewhere [40].

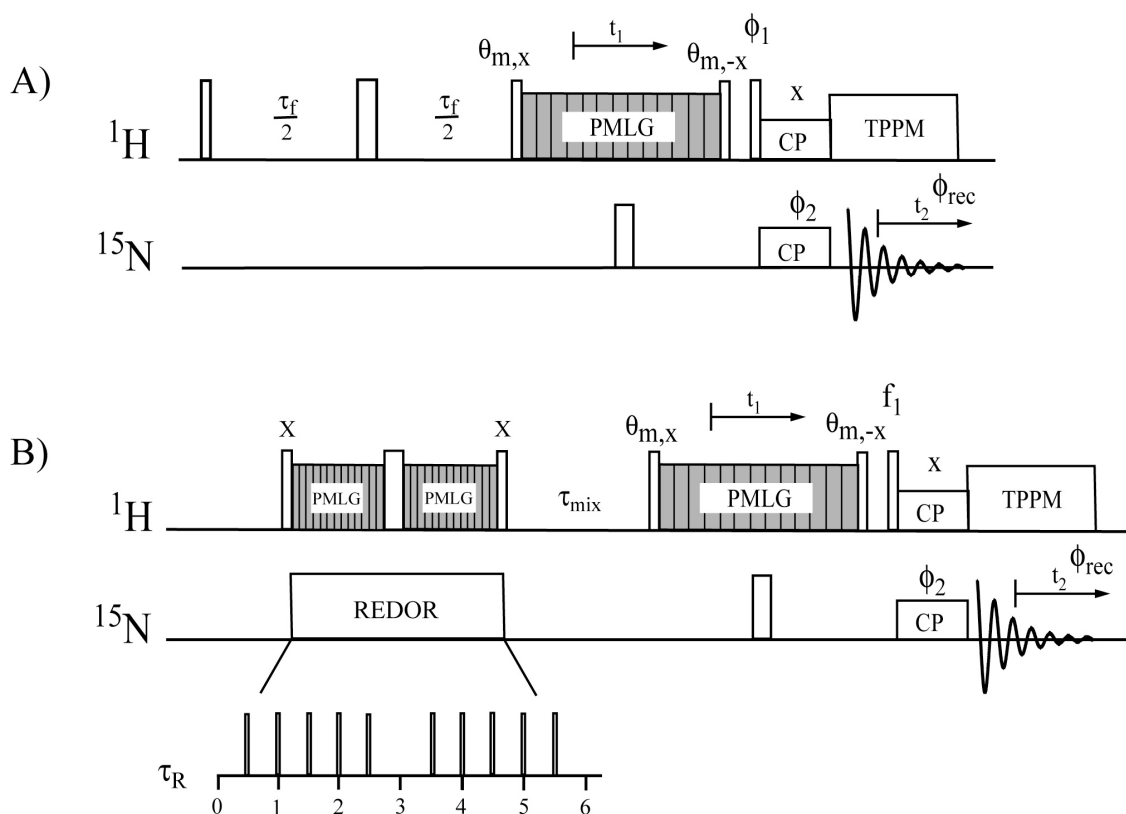


Figure 5.2.1. NMR pulse sequences for localization of water molecules bound to proteins by MAS solid state NMR. A)  $^{15}\text{N}$  detected  $^1\text{H}$ ,  $^{15}\text{N}$  PMLG correlation experiment including a  $^1\text{H}$   $T_2$  filter along a third dimension  $\tau_f$ . B)  $\text{H}_2\text{O}-\text{H}^{\text{N}}$  spin diffusion experiment.  $\text{H}^{\text{N}}$  magnetization is initially suppressed using a REDOR-filter element which dephases all proton magnetization of nuclei in spatial proximity of a  $^{15}\text{N}$  nucleus. Other, non  $^{15}\text{N}$  bonded protons are not affected by the filter. A REDOR filtering time of 6 rotor periods is employed. A variable spin diffusion mixing time  $\tau_{\text{mix}}$  allows for magnetization transfer from water protons and OH protons in the protein side chains to the amide proton which is detected in a  $^1\text{H}$ ,  $^{15}\text{N}$  PMLG correlation experiment. The CP contact time is set to 160  $\mu\text{s}$  to allow only for transfer between directly bonded proton and nitrogen nuclei.

NMR experiments to measure  $^1\text{H}$  dephase after  $T_2$  filter (Figure 5.2.1 A) were performed on a 600 MHz Bruker-Avance wide-bore spectrometer equipped with a 4 mm triple resonance probe. Experiments to measure  $\text{H}_2\text{O}-\text{H}^{\text{N}}$  spin diffusion (Figure 5.2.1 B) were recorded on a 400 MHz Bruker-Avance wide-bore spectrometer equipped with a 4 mm triple resonance probe. Approximately 9 mg of the protein was used. MAS frequency was set to 10 kHz and temperature was adjusted to 280 K. Both experiments are based on  $^{15}\text{N}$  detected  $^1\text{H}-^{15}\text{N}$  correlation experiment. During the proton evolution in the indirect dimension  $^1\text{H}-^1\text{H}$  homonuclear decoupling was achieved by PMLG-9 [24] using proton frequency of 81kHz and a  $t_1^{\text{max}}$  of 15 ms. The  $^1\text{H}-^{15}\text{N}$   $J$  coupling as well as possible residual dipolar broadening was removed by implementation of a  $^{15}\text{N}$   $180^\circ$  degree pulse applied in the middle of  $t_1$  [157]. After the indirect evolution polarization transferred via CP from  $^1\text{H}$  to  $^{15}\text{N}$ . The CP mixing time was set to 160  $\mu\text{s}$  to restrict polarisation transfer between directly bonded nuclei. During detection, TPPM [29] of 90kHz was applied on  $^1\text{H}$  channel for heteronuclear decoupling.

$T_2$  filter experiment (Figure 5.2.1 A) starts with excitation pulse on  $^1\text{H}$  channel, rotor synchronized  $180^\circ$  pulse was applied in the middle of evolution period to refocus all inhomogeneous interactions. The  $^1\text{H},^{15}\text{N}$  correlation experiment follows this element. In the  $\text{H}_2\text{O}-\text{H}^{\text{N}}$  spin diffusion experiment, a REDOR filtering element of six rotor periods duration is implemented to dephase magnetization of nitrogen-bonded protons. During REDOR PMLG is applied to protons to avoid any dipole-dipolar interactions of the proton network. Duration of the REDOR dephasing period was numerically optimized using SIMPSON [95] to suppress proton polarization after their dephasing in the tilted frame. A  $90^\circ$  pulse flips protons along Z and subsequent spin diffusion provides polarization transfer to  $\text{H}^{\text{N}}$  from water protons with following detection by a 2D  $^1\text{H},^{15}\text{N}$  correlation experiment.

### 5.3 Results.

We have observed previously that in the absence of homonuclear  $^1\text{H},^1\text{H}$  dipolar decoupling certain  $^1\text{H}^{\text{N}}$  resonances are broadened in a direct proton evolution period [38]. In the following, we describe two experiments that were carried out in order to



characterize the origin of this effect. Both experiments are based on a  $^{15}\text{N}$  detected PMLG  $^1\text{H}$ ,  $^{15}\text{N}$  correlation experiment.  $^{15}\text{N}$  instead of  $^1\text{H}$  detection was employed in order to unambiguously address the influence of water on the proton spectra.

In the first experiment, a  $^1\text{H}$   $T_2$  filter precedes the PMLG  $^1\text{H}$  evolution period (Figure 5.2.1 A). As a function of the filtering time  $\tau_f$ , we observe a differential decay of the  $^1\text{H}$ ,  $^{15}\text{N}$  correlation peaks (Figure 5.3.1). The intensity of different cross peaks as function of the mixing time is presented in Figure 5.3.2. The decaying intensities were fitted assuming mono-exponential decay according to the equation:

$$I^{T_2-f}(\tau_f) = I_0^{T_2-f} \exp(-\tau_f / T_2^{\text{eff}}) \quad (5.3.1)$$

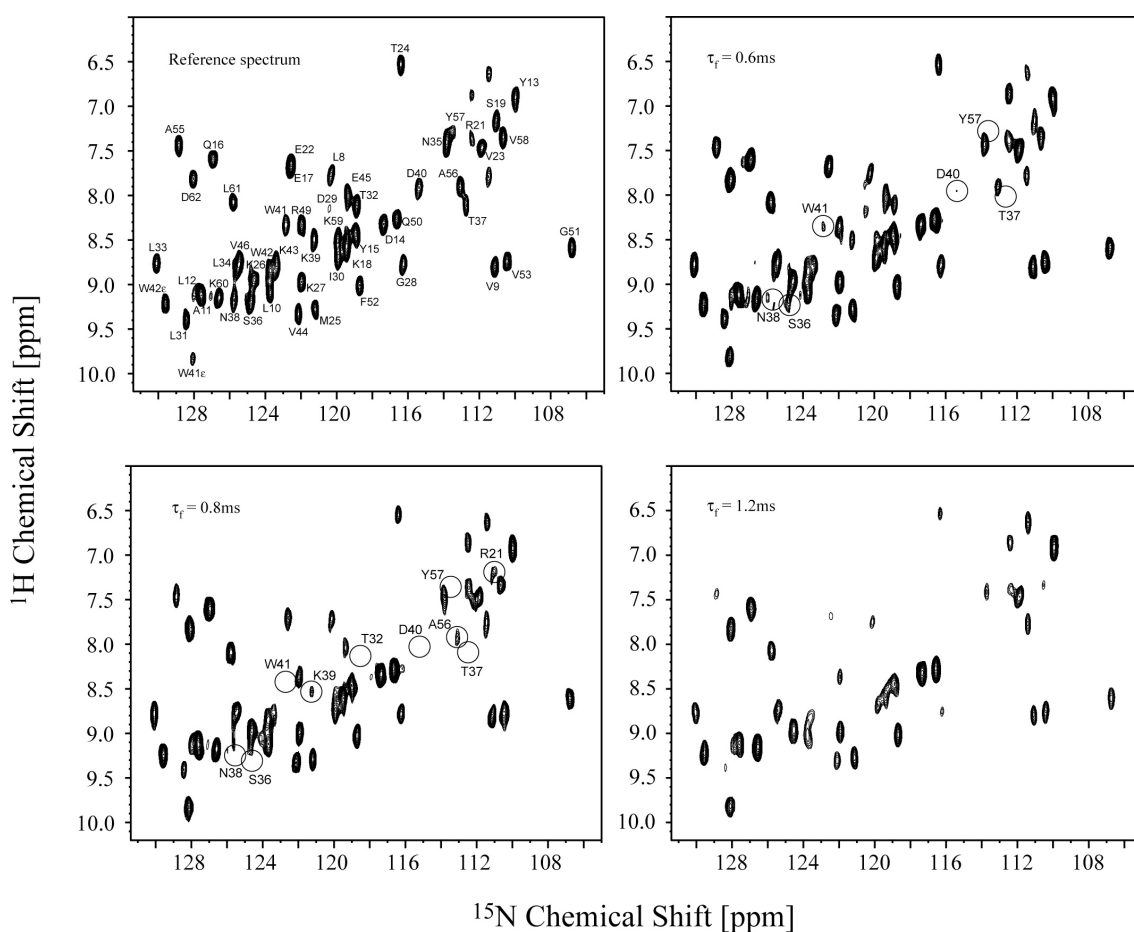


Figure 5.3.1. 2D  $T_2$  filtered  $^1\text{H}$ ,  $^{15}\text{N}$  correlation spectra obtained with the pulse sequence presented in Figure 5.2.1 A at various mixing times  $\tau_f$ .

Intensities were normalized to the intensity  $I_0$  of the respective cross peak at  $\tau_f = 0$  ms filtering time. The slowest decay rate is observed for residue D62 with an effective  $T_2$  time of 2.56 ms, whereas the fastest decay rate could reliably be assigned to residue D40

that decays with an effective  $T_2$  time of 0.17 ms. The  $T_2$  decay rates of the  $H^N$  protons of all amino acid residues are summarized in Table 5.3.1. Note that the decay rates differ by more than a factor of 10 from one another.

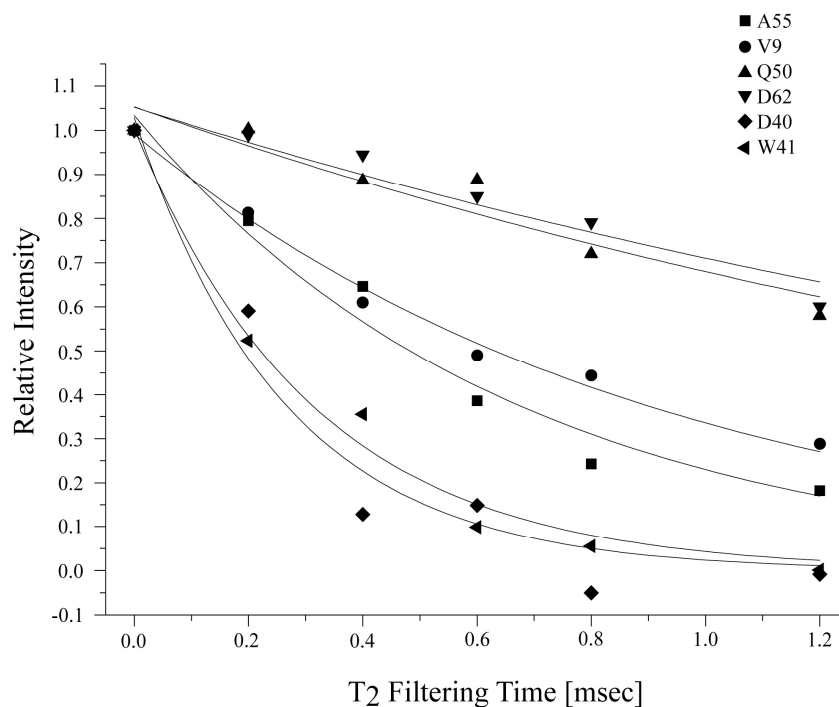


Figure 5.3.2.  $T_2$  decay rates for different residues as a function of the  $T_2$  filtering time  $\tau_f$ .

In the second experiment (Figure 5.2.1 B), a REDOR type filter element is employed in order to suppress all protons which are directly bonded to  $^{15}\text{N}$ . In a subsequent mixing period (spin diffusion), magnetization is transferred from  $\text{H}_2\text{O}$  and OH protons to  $H^N$  protons which are detected again in a  $^1\text{H}, ^{15}\text{N}$  correlation experiment (Figure 5.3.3). The experiment was carefully adjusted and no correlations were observed for a mixing time of  $\tau_{\text{mix}} = 0$  ms. Buildup curves for several correlations are shown as a function of mixing time in Figure 5.3.4.

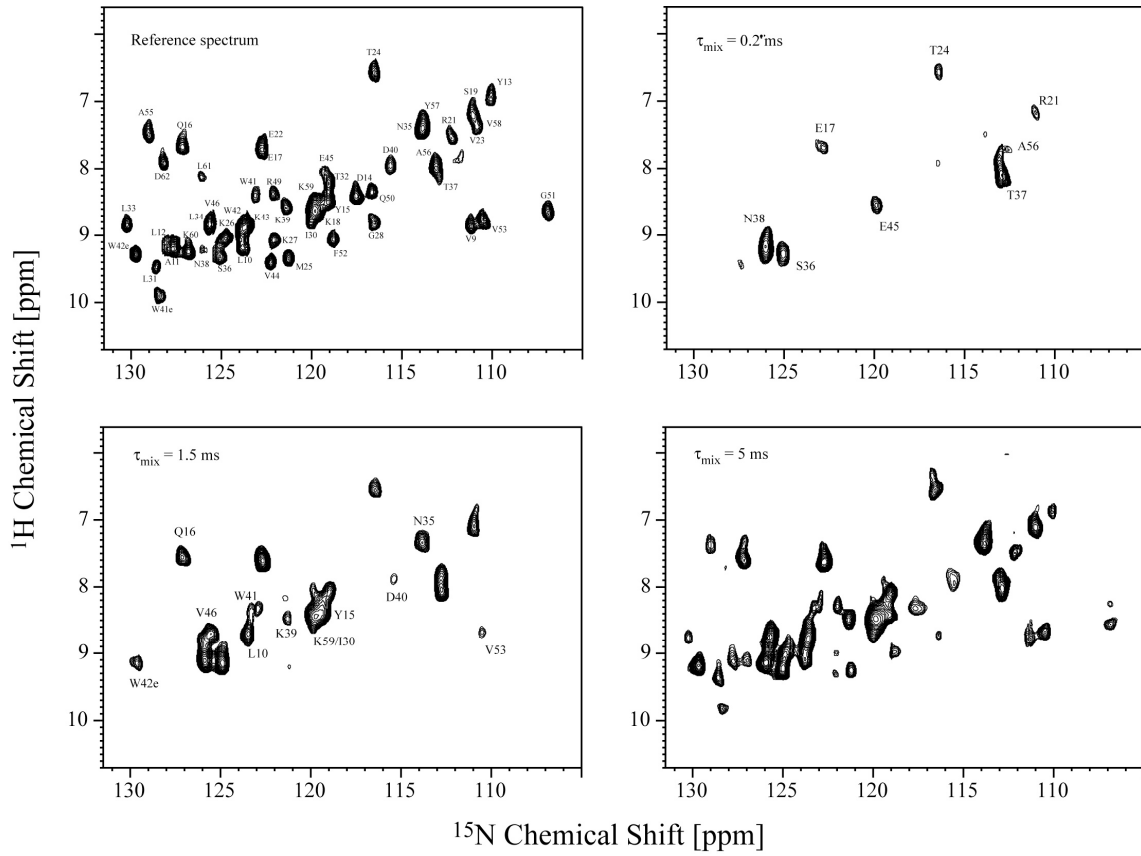


Figure 5.3.3. 2D  $\text{H}_2\text{O}-\text{H}^{\text{N}}$  spin diffusion  $^1\text{H}, ^{15}\text{N}$  correlation spectra obtained with the pulse sequence presented in Figure 5.3.2 B at various  $^1\text{H}, ^{15}\text{N}$  spin diffusion mixing times  $\tau_{\text{mix}}$ . Reference spectrum is represented by 2D  $^1\text{H}, ^{15}\text{N}$  correlation experiment without REDOR filter.

The characteristic time for  $\text{H}^{\text{N}}$  magnetization buildup in this experiment is represented for all amino acid residues in Table 5.3.1. The buildup rates given in Table 5.3.1 are obtained after fitting the experimental data to the empirical equation:

$$I^{\text{REDOR}-f}(\tau_{\text{mix}}) = I_0^{\text{REDOR}-f} r \left[ 1 - \exp(-\tau_{\text{mix}} / T^{\text{H}_2\text{O} \rightarrow \text{H}^{\text{N}}}) \right] \quad (5.3.2)$$

Intensities are normalized to the intensity  $I_0$  of the respective cross peak in a regular  $^{15}\text{N}$  detected PMLG  $^1\text{H}, ^{15}\text{N}$  correlation experiment.  $r$  corresponds to the ratio of cross peak volumes:

$$r = I_{\text{REDOR}-f}^0 / I_0 \quad (5.3.3)$$

obtained in the  $\text{H}_2\text{O} \rightarrow \text{H}^{\text{N}}$  spin diffusion experiment at infinite mixing time to the peak volume extracted from the reference PMLG experiment.  $I_{\text{REDOR}-f}^\infty$  is included as a variable

parameter in the fit, since efficiency of the spin diffusion transfer might depend on the number of protons in the vicinity of the respective  $H^N$ .

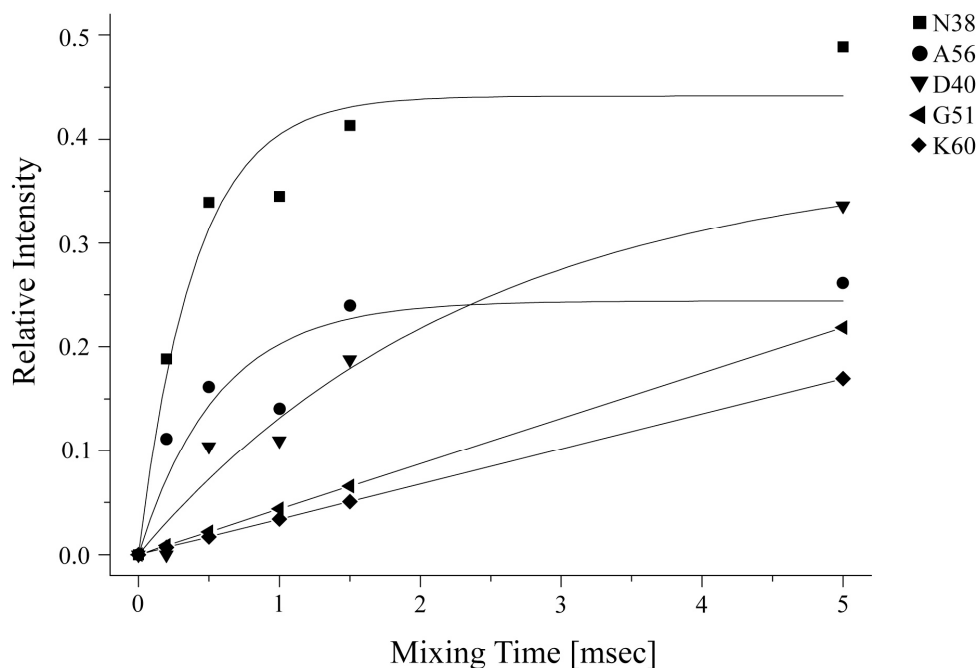


Figure 5.3.4. Magnetization buildup curves as a function of the  $^1H$ ,  $^1H$  spin diffusion mixing times  $\tau_{mix}$  for selected residues obtained from the pulse sequence shown in Figure 5.3.2 B.

The fastest buildup is observed for residue N38 with an apparent buildup time constant  $T^{H_2O \rightarrow H^N}$  of 0.4 ms. For this residues, a maximum intensity of  $I_{REDOR-f}^\infty$  of 0.44 is obtained. The slowest buildup can reliably be determined for K39 where a value of  $T^{H_2O \rightarrow H^N}$  of 5.5 ms is obtained. In this case,  $I_{REDOR-f}^\infty / I_{REDOR-f}^0$  reaches a value of 0.7. For approximately half of the residues, cross peaks in the  $H_2O \rightarrow H^N$  spin diffusion experiment are only obtained for mixing times  $\tau_{mix} \geq 5.0$  ms (i.e. V9, Y13, D14, Y15, V44, R49, Q50, G51, F52, A55, K60 and D62 etc.). For this class of residues, a linear fit was employed in order to extract the respective buildup time constant  $T^{H_2O \rightarrow H^N}$ . In this case, a value for  $I_{REDOR-f}^\infty$  of approximately 0.2 is obtained. For two residues, V58 and L61, a much larger value for  $T^{H_2O \rightarrow H^N}$  greater than 100 ms is extracted from the data. This is due to the fact that the cross peak intensity in the  $H_2O \rightarrow H^N$  spin diffusion experiment at  $\tau_{mix} = 5.0$  ms is very low. Longer values for  $\tau_{mix}$  would have to be acquired in order to

retrieve an accurate buildup time constant. Therefore, these two residues are omitted in the discussion.

In order to validate the NMR data, the NMR structural parameters have to be compared to a high resolution X-ray structure of the wild-type SH3 domain of chicken  $\alpha$ -spectrin, determined at a resolution of 1.49 Å (PDB entry: 1U06) [40].

Table 5.3.1.  $H^N$  isotropic chemical shift values,  $H^N$   $T_2$  decay rates and  $H_2O \rightarrow H^N$  spin diffusion buildup rates for the SH3 domain of  $\alpha$ -spectrin. Characteristic distances to other exchangeable protons in the protein and to water protons as extracted from the X-ray structure are indicated for each  $H^N$  proton.  $\bar{x}$  denotes the average value and  $\sigma$  the standard deviation for the respective fitted parameter.

		T <sub>2</sub> Decay		H <sub>2</sub> O-H <sup>N</sup> spin diffusion				
Res	δ <sup>iso</sup> <sup>1</sup> H <sup>N</sup> [ppm]	T <sub>2</sub> <sup>eff</sup> [μs]		r=I <sup>∞</sup> <sub>REDOR,t</sub> /I <sub>0</sub>		T <sup>H<sub>2</sub>O→HN</sup> [μs]		Interacting Protons
		$\overline{\chi}$	$\sigma$	$\overline{\chi}$	$\sigma$	$\overline{\chi}$	$\sigma$	
L8	8.0	912	102					
V9	8.8	923	51	0.327		15300		HN31/2.96;
L10	9.1							HN59/2.62;
A11	9.2							HN29/3.73+HN28/3.84
L12	9.1							HN13/2.39
Y13	7.0	1287	316	0.217		23000		HN12/2.39
D14	8.4	1776	85	0.217		23000		HN27/3.27+O10/2.01
Y15	8.5	999	150	0.250		20000		HN25/2.90+2HZ18/3.29+O30/3.31
Q16	7.6	1712	297	0.61	0.3	4643	3564	O26/3.95
E17	7.7			0.43	0.02	764	108	1HG24/2.55
K18	8.6	689	115					HN19/2.05
S19	7.1	473	34	0.42	0.05	1428	379	HN18/2.05+HN22/3.53+*O25/4.74
R21	8.1							HN22/2.52+HG19/3.40
E22	7.6	500	41	0.43	0.02	764	108	HN21/2.52+HN19/3.53+O25/3.79
V23	7.5	1408	198					HN52/3.34
T24	6.5	502	36	0.42	0.06	1421	430	12HH49/2.21+11HH49/2.81+1HG24/3.68+O20/3.07
M25	9.3	1187	445	0.244		20520		HN15/2.90
K26	9.0	911	172	0.27	0.04	1352	505	O16/3.27+O49/3.76
K27	9.2	1200	176	0.115		43336		HN14/3.23+O34/3.50+O31/3.96
G28	8.8	665	66	0.117		42581		HN29/2.64+HN11/3.84+O8/3.25
D29	8.4	584	78					HN28/2.64+HN11/3.73+O4/3.35
I30	8.7	593	86					*O6/4.32
L31	9.5							HN9/2.96
T32	8.2	360	39	0.48	0.03	954	153	HN45/3.14+1HG32/3.58+O5/4.04+*O6/4.44
L33	8.9	1121	69					HN7/3.37
L34	8.9			0.40	0.03	730	154	HN35/2.23
N35	7.4	533	78	0.45	0.04	2946	509	HN34/2.23+ HN43/3.12+HN36/3.93+*O44/4.92
S36	9.2	449	39	0.63	0.09	1768	524	HN37/2.59+HN35/3.93+HG36/3.46+O3/1.91+O24/2.91
T37	8.1	<b>171</b>	19	0.43	0.04	1184	282	HN36/2.59+HN38/2.65+1HG37/3.46+O1/3.00 +O3/3.60
N38	9.1	456	54	0.44	0.03	<b>403</b>	100	HN37/2.65+O1/1.98
K39	8.6	423	35	0.7	0.2	5468	2291	HN40/2.45+O7/2.00

D40	8.0	259	34	0.38	0.05	2390	652	HN41/2.26+HN39/2.45+O7/3.86
W41	8.4	316	28	0.44	0.11	2452	1268	HN40/2.26+*O1/4.84
W42	9.0							HN53/3.14+HN55/3.38
K43	8.9	541	115	0.51	0.06	1909	457	HN35/3.12+O1/3.54
V44	9.3	1121	125	0.206		24200		HN51/2.71
E45	8.1	409	87					HN32/3.14
V46	8.9							HN49/3.38+HN47/3.79
R49	8.4	585	37	0.313		16000		HN48/2.52+HN46/3.38+O53/3.83+O21/3.95
Q50	8.4	2281	384	0.192		26000		O23/1.97
G51	8.7	1027	87	0.219		22900		HN44/2.71
F52	9.0	1268	181	0.240		20800		HN23/3.34+O9/3.87
V53	8.8	1129	150	0.33	0.11	3439	1975	HN42/3.14
A55	7.4	665	69	0.246		20300		HN56/2.81+HN42/3.38+O2/3.01
A56	7.9	500	44	0.24	0.03	567	235	HN57/2.72+HN55/2.81+ O2/2.02+O33/3.52
Y57	7.3	372	71					HN58/2.48+HN56/2.72
V58	7.3	571	109	0.046				HN57/2.48
K59	8.6	245	56	0.39	0.02	499	82	HN10/2.62+*O8/5.3+*O31/5.48+*O13/5.63
K60	9.2	1493	257	0.169		<b>29500</b>		O11/1.95+O51/3.98
L61	8.1	423	49	0.032				HN62/2.36
D62	7.8	<b>2588</b>	342	0.189		26469		O/1.9+HN61/2.36 (PDB1QKX)

Residues for which build up rate was calculated using a linear approximation: V9, Y13, D14, Y15, M25, K27, G28, V44, R49, Q50, G51, F52, A55, K60, D62. Water molecules marked with asterisk adopting a distance longer than 4Å and not considered in the evaluation in Figures 5.4.1-5.4.5.

## 5.4 Discussion.

Inspection of Table 5.3.1 indicates that there is no easy correlation between the data of the  $T_2$ -Filter and the  $\text{H}_2\text{O}-\text{H}^{\text{N}}$  spin diffusion experiment. The  $\text{H}_2\text{O}-\text{H}^{\text{N}}$  spin diffusion experiment selects for protons which are not directly attached to  $^{15}\text{N}$ . Magnetization is then transferred to the amide proton using spin diffusion mixing. We were expecting therefore that a fast buildup rate in the  $\text{H}_2\text{O}-\text{H}^{\text{N}}$  spin diffusion experiment should also result in a rapid  $T_2$  decay of the respective  $\text{H}^{\text{N}}$  resonance. This is, however, not the case. Possible interactions for a given amide  $\text{H}^{\text{N}}$  are the contacts  $\text{H}^{\text{N}}-\text{H}^{\text{N}}$ ,  $\text{H}^{\text{N}}-\text{OH}$  (side chain) and  $\text{H}^{\text{N}}-\text{H}_2\text{O}$ . The buildup rate in the  $\text{H}_2\text{O}-\text{H}^{\text{N}}$  spin diffusion experiment should be sensitive to a cluster of water molecules around the water molecule which is close to the  $\text{H}^{\text{N}}$  resonance that we can detect. Dipolar truncation might reduce the buildup rate in this case. On the other hand, the  $T_2$ -filter experiment should be especially sensitive if more than one  $\text{H}^{\text{N}}$  proton is in close proximity to the detected amide proton. Taken together, the two experiments yield complimentary information about the respective spin system and its dynamic.

In order to better estimate the experimental data and the correlation to the X-ray structure, we represent the relative decay or buildup rates of the two experiments as a function of the inverse third power of the  $^1\text{H}$ - $^1\text{H}$  distances involved for the respective amide proton. The  $T_2$  decay is described semi-analytically using the equation:

$$(1/T_2)^{(i)} = A + B \sum_j 1/r_{ij}^3 \quad (5.4.1)$$

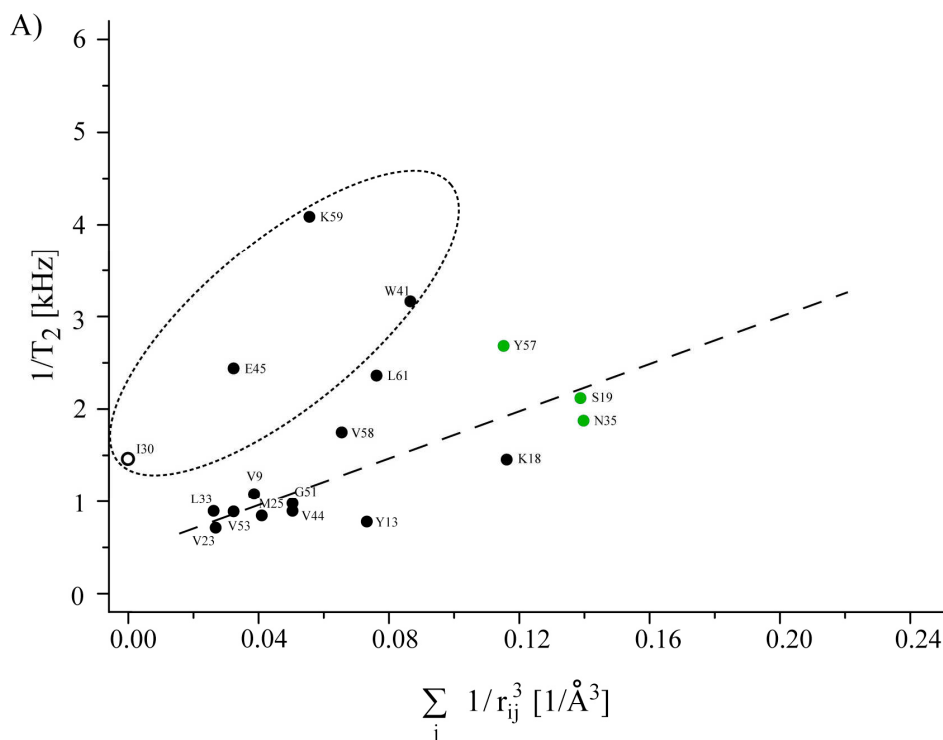


Figure 5.4.1. Effective  $1/T_2$  relaxation rate as a function of the dipolar interactions as expected from the X-ray structure. Only residues are represented for which no water molecule is found within 4.0 Å. Residues which have no, one and more than one dipolar interaction to another  $\text{H}^{\text{N}}$  proton in the protein structure are colored white, black and green, respectively.

Figure 5.4.1 represents only those amide protons for which no water molecule is found within 4 Å in the X-ray structure. Residues which have no, one and more than one dipolar interaction to another  $\text{H}^{\text{N}}$  proton in the protein structure are colored white, black and green, respectively. There is apparently no correlation between the  $1/T_2$  decay rate and the number of interacting protons. In order to fit the NMR experimental data, we assumed a linear relation between the  $1/T_2$  decay rate and the dipolar interactions calculated from the  $\text{H}^{\text{N}}$ -H distances (with H being  $\text{H}^{\text{N}}$ , OH and  $\text{H}_2\text{O}$ ) as extracted from the the X-ray structure. E45, T32, W41 and I30 are excluded from the fit, since they deviate

significantly from the average value. Additional residues which are in close proximity to water molecules are taken into account in Figure 5.4.2. Red and blue symbols indicate the theoretical dipolar coupling values assuming that one and two protons contribute to the interaction, respectively.

The distance between the amide proton and the water proton is calculated according to:

$$r_{ij} = \sqrt{d_{H^N,O}^2 + d_{O,H}^2 + 2d_{H^N,O}d_{O,H}\cos\phi} \quad (5.4.2)$$

where  $d_{HN,O}$  denotes the distance between  $H^N$  and water oxygen,  $d_{O,H}$  the bond length in the water molecule and  $\phi$  the angle between the  $N-H^N$  and  $O-H$  vector [158]. In order to calculate the H,H distances, we assumed that the water oxygen is hydrogen bonded to the amide proton. In addition, we have used a value of  $\phi = 52.52^\circ$  [158], assuming symmetrically bonded water molecules.

The experimental decay data taking water molecules into account fit the same empirical relation, with the exception of residues D14, Q50 and K60. For these  $H^N$  protons, a long effective  $T_2$  is observed, even though water molecules are found in close proximity.



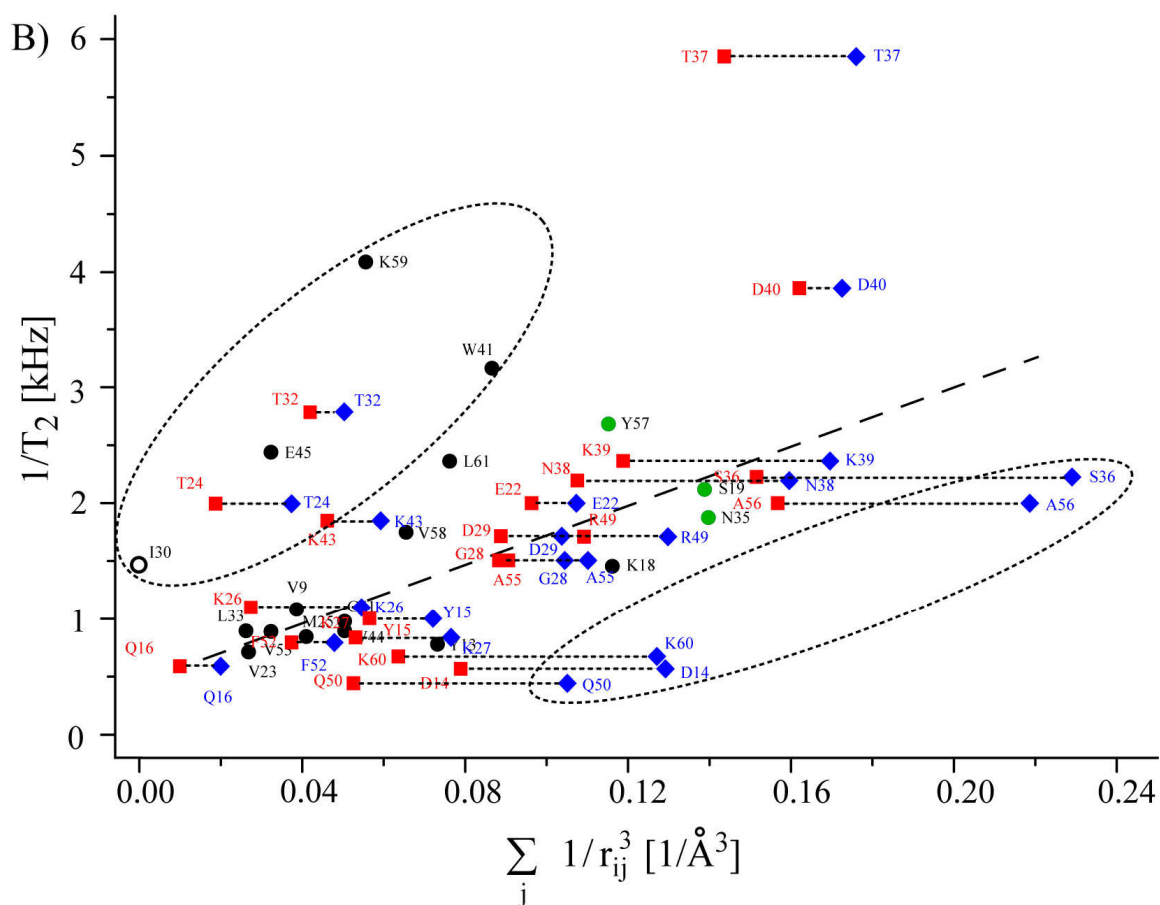


Figure 5.4.2. Effective  $1/T_2$  relaxation rate as a function of the dipolar interactions as expected from the X-ray structure. All residues are represented. Red and blue symbols indicate the theoretical dipolar coupling values assuming that one and two water protons contribute to the interaction, respectively.

So far, the isotropic and anisotropic  $H^N$  chemical shifts, as well as their orientations in the molecular frame are not taken into account in the analysis of the  $T_2$  decay rates. The observed deviations might be due to  $n=0$  rotational resonance effect [159]. Therefore, the  $1/T_2$  decay rate was analyzed as a function of the  $H^N, H^N$  chemical shift difference ( $\Delta\delta$ ) (Figure 5.4.3). The projection angle between the two  $H^N-N$  vectors which are in spatial proximity is represented in the Figure 5.4.3 as well which might be an approximation for the differential  $^1H$  chemical shift anisotropy (CSA). Residues for which the  $H^N$  atom is in contact with another  $H^N$  atom within 2.0 Å, 2.0-2.5Å, 2.5Å-3.0Å, 3.0Å-3.5Å and 3.5Å-4.0Å are colored in magenta, red, green, blue and yellow, respectively. In cases where a  $H^N$  proton is in vicinity of two amide protons, only the strongest interaction is taken into account. For small chemical shift differences, a slight increase in the rate is observed as expected (e.g. T32, Y57, E45). The range of the  $n=0$  rotational resonance

effect is defined by the line width of the respective  $H^N$  resonance which is on the order of 200 Hz ( $\equiv 0.3$  ppm). On the other hand, a large dispersion of  $1/T_2$  decay rates is observed for  $H^N$  protons for which only a small isotropic chemical shift difference between the dipolar coupled nuclei is observed (residues colored in green, corresponding to a  $H^N, H^N$  distance of 3.0-3.5 Å). We therefore conclude that other mechanisms than  $n=0$  rotational resonance must as well contribute to the  $1/T_2$  decay rate.

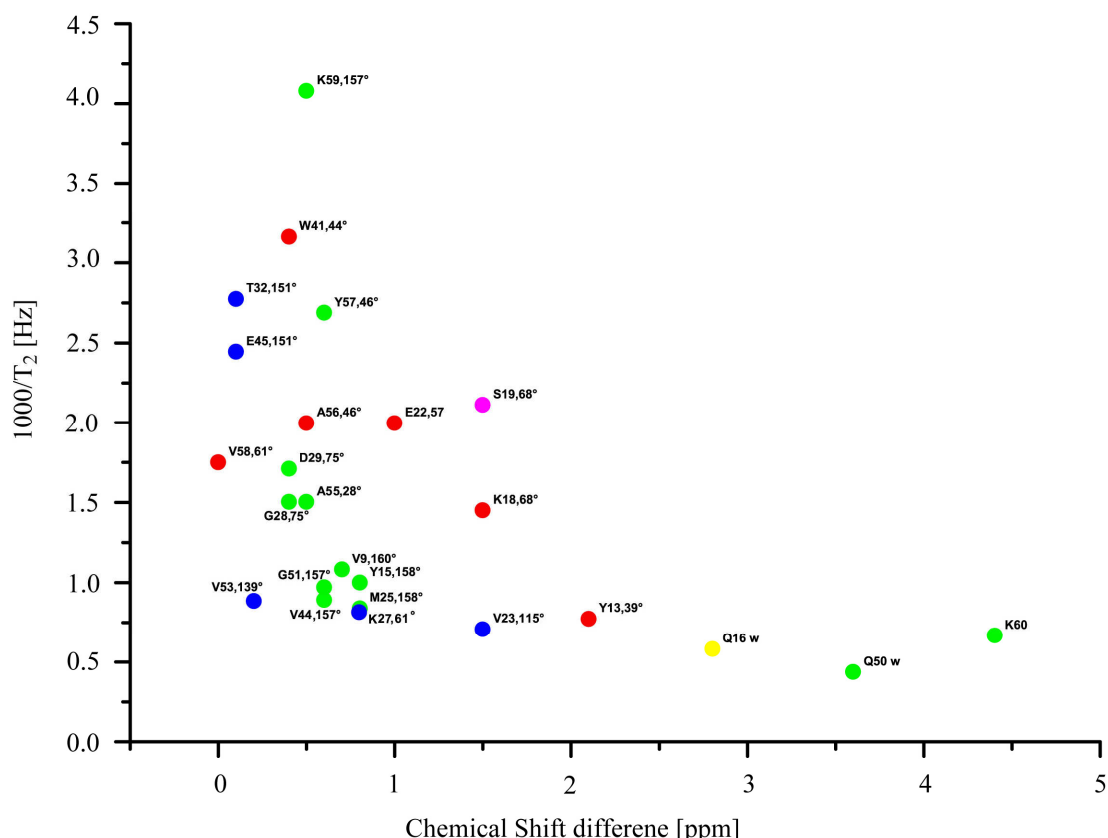


Figure 5.4.3.  $1/T_2$  relaxation rate as a function of the isotropic chemical shift difference between two  $H^N$  protons. Only the strongest interaction is taken into account in cases where a  $H^N$  proton is in close proximity to two  $H^N$  protons. Residues for which the  $H^N$  atom is in contact with another  $H^N$  atom within 2.0 Å, 2.0-2.5 Å, 2.5 Å-3.0 Å, 3.0 Å-3.5 Å and 3.5 Å-4.0 Å are colored in magenta, red, green, blue and yellow, respectively.

In Figure 5.4.4, the NMR experimental  $H_2O-H^N$  build up rate is correlated with the dipolar couplings calculated from the  $H_2O-H^N$  distances extracted from the X-ray structure. Total dipolar coupling for each residue is calculated according to Eq. 5.4.2. At first sight, the buildup rate does not seem to be related to the expected dipolar interactions.

However, taking into account that water molecules can be classified according to their binding properties with respect to the protein it allows to identify three distinct water molecules—in addition to bulk water: (I) Water molecules being in contact with bulk solvent; (II) Tightly bonded water within the core of the protein; (III) Dynamic water molecules located in flexible regions of the protein. These regions are indicated in Figure 5.4.4. A qualitative explanation for this interpretation is given below.

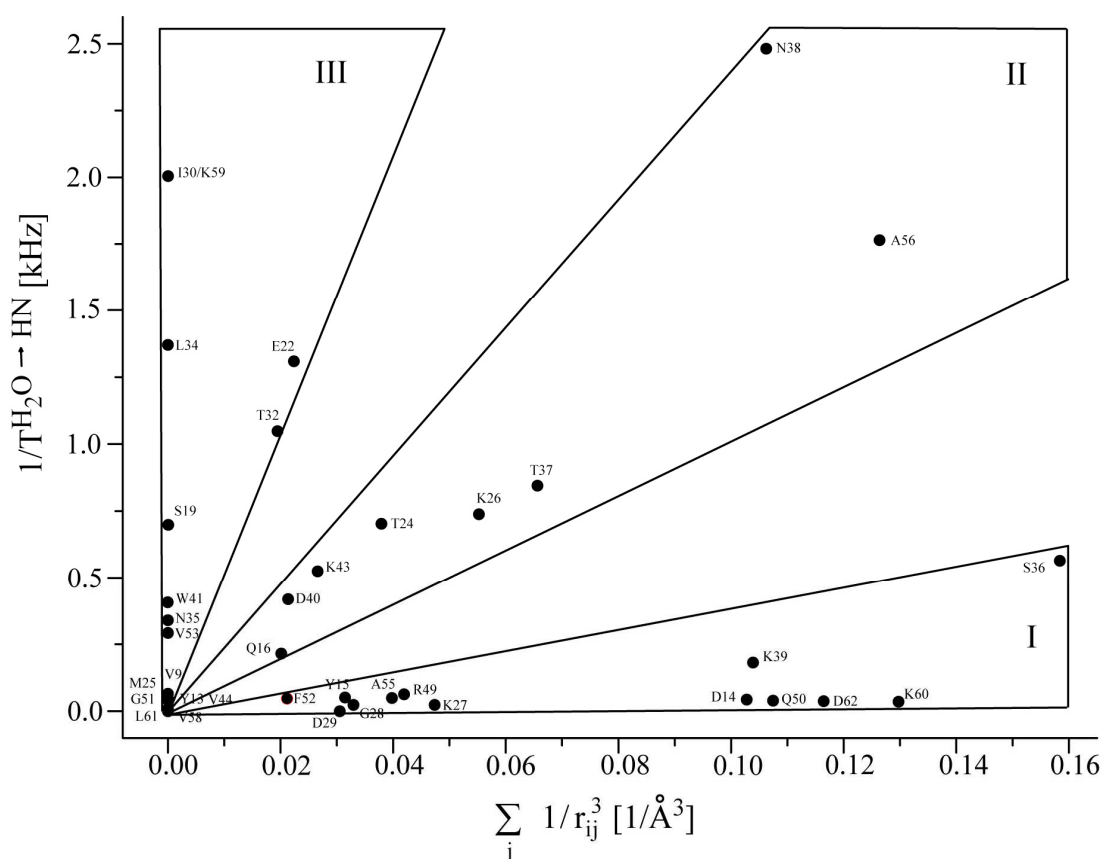


Figure 5.4.4.  $\text{H}_2\text{O}-\text{H}^{\text{N}}$  spin diffusion buildup rates as a function of the dipolar interactions expected from the X-ray structure. Amide protons which are in contact with bulk water, tightly bound water and flexible regions of the protein are labeled with I, II and III, respectively.

For completeness, Figure 5.4.5 represents the maximum intensity  $I_{\text{REDOR-f}}^{\infty}$  that can be achieved for each  $^1\text{H}, ^{15}\text{N}$  correlation peak as a function of the  $1/T^{(\text{H}_2\text{O} \rightarrow \text{HN})}$  buildup rate. For very long mixing times, this ratio should give informations about the number of water protons in the vicinity of the respective  $\text{H}^{\text{N}}$  proton. (For 1 protons, a value of 0.5 would be expected; for 2 protons 0.67 etc.).

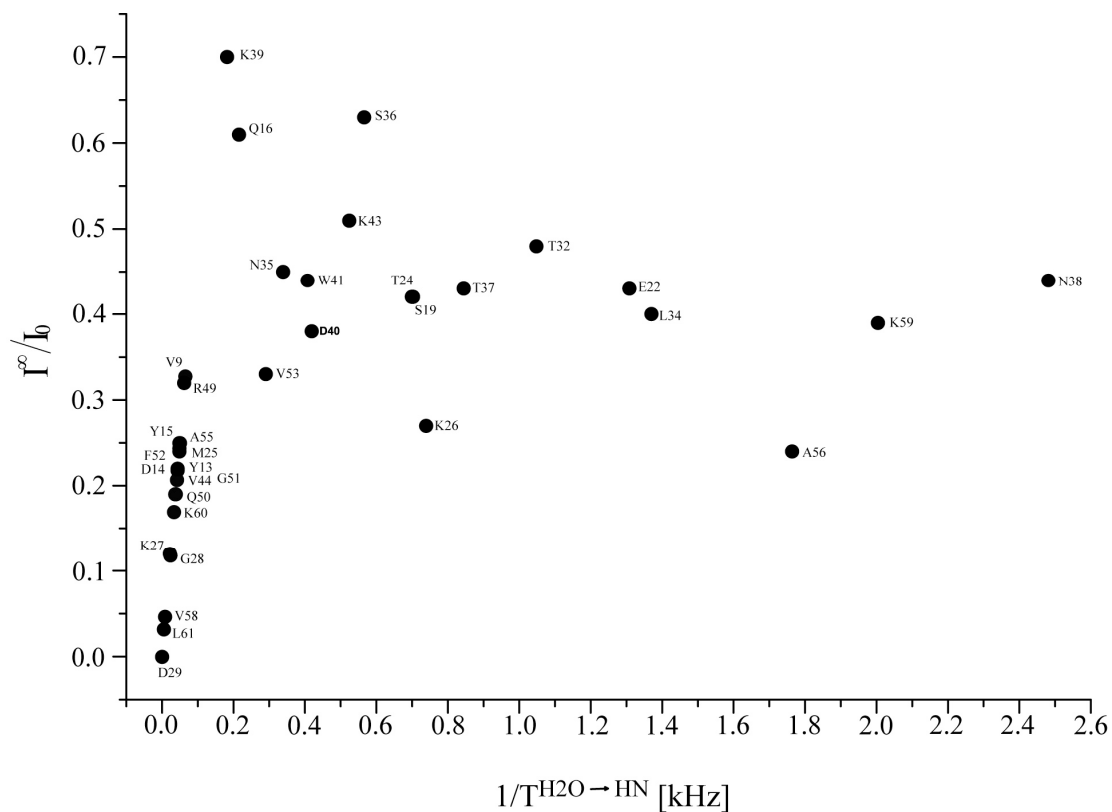


Figure 5.4.5. Ratio  $r$  between cross peak volumes extracted from the  $^1\text{H}$ ,  $^{15}\text{N}$  PMLG correlation reference experiment and the equilibration intensity  $I_{\text{REDOR-f}}^\infty$  extracted from the  $\text{H}_2\text{O}-\text{H}^{\text{N}}$  spin diffusion experiment, as a function of the experimental  $1/T_2$  decay rate.

(I) For residues D14, Q50, and K60, we observe a very small buildup rate  $1/T^{(\text{H}_2\text{O} \rightarrow \text{HN})}$ . At the same time,  $1/T_2$  adopts a smaller value as what would be expected from the distances extracted from the X-ray structure (Figure 5.4.2). The crystal structure displays a very dense network of water molecules around these residues which is located on the surface of the protein and is in contact with bulk water. We explain this finding that water protons near residues located in region I are in very fast exchange with bulk solvent water molecules. This would result in a reduction of dipolar interactions. Therefore, these water molecules do not contribute to a magnetization buildup in the  $\text{H}_2\text{O}-\text{H}^{\text{N}}$  spin diffusion experiment nor to the  $\text{H}^{\text{N}}$   $T_2$  decay, and are not detectable by MAS solid-state NMR.

(II) Tightly bounded water within the core of the protein (region II). Residues located in region II (N38, A56, T37 etc.), follow an empirical relation between the  $1/T^{(\text{H}_2\text{O} \rightarrow \text{HN})}$  buildup rate and the dipolar interaction expected from the X-ray structure. These

water molecules behave solid-like. Most of them have contacts to a symmetry-related molecule in the crystal. They can therefore be considered as being located in a pseudo-core of the protein.

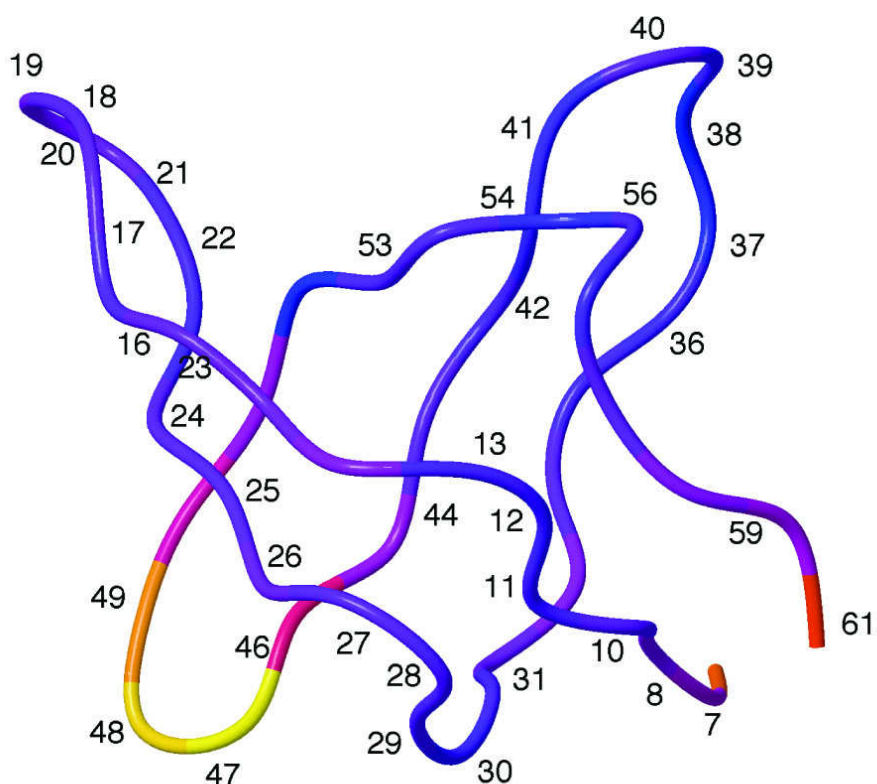


Figure 5.4.6. MOLMOL representation of the chicken  $\alpha$ -spectrin SH3 domain. Colour coding is according to the X-ray B-factor. B-factors of around 10, 20 and 30  $\text{\AA}^2$  are represented in blue, red and yellow, respectively.

(III) Dynamic water molecules (region III). For residues which are located in region III (V46, E22 etc.), we find a very rapid magnetization buildup in the  $\text{H}_2\text{O} \rightarrow \text{H}^{\text{N}}$  spin diffusion experiment, whereas no interaction partner ( $\text{H}^{\text{N}}$ , OH or  $\text{H}_2\text{O}$ ) is found in the respective region of the X-ray structure. V46 is located in a loop region which connects  $\beta$ -strands 3 and 4. For this loop, a higher B-factor of 21.3  $\text{\AA}^2$  is found compared to the average B-factor of the structure of 14.2  $\text{\AA}^2$ . Interestingly,  $^1\text{H}$ ,  $^{15}\text{N}$  correlations for N47 (B-factor = 31.17  $\text{\AA}^2$ ) and D48 (B-factor = 31.71  $\text{\AA}^2$ ) cannot be assigned in the MAS solid-

state NMR spectra. Figure 5.4.6 displays the SH3 structure color coded according to the B-factor of X-ray data refinement.

In the current electron density refinement, only water molecules are taken into account that have an occupancy of 100%. Water molecules which undergo chemical exchange between two or more sites have an occupancy of less than 100% and cannot be detected in the X-ray structure at the current resolution. In addition to dipole–dipole interactions, which are expected for protons in the solid-state yielding a  $1/r^3$  dependence, fluctuations of dipolar interactions inducing relaxation might have to be taken into account for these mobile water molecules. Magnetic relaxation dispersion allows for the determination of the correlation time of water molecules in the core of a protein [151]. The correlation time could be estimated to be on the order of  $\tau_c \approx 1\mu\text{s}$ . Motion of water molecules on this time scale should induce relaxation in neighbouring  $\text{H}^{\text{N}}$  resonances due to fluctuations of dipole dipole interactions. Such motion would be in agreement with the observation of disordered regions in the protein crystal in which the electron densities are not very well defined indicating small conformational heterogeneities. We cannot totally rule out the possibility that differences observed between the solid-state NMR data and the X-ray crystal structure are due to the different temperatures which are used in the X-ray (100 K) and NMR studies (280 K), respectively. In order to unambiguously address this question, a room temperature X-ray structure would be required. We expect, however, that for a X-ray structure determined at 280 K, the discrepancies in region III between the NMR and the X-ray data would be even more striking, since the number of well defined water molecules would be lower due to increased thermal motion.

For four residues (E17, R21, T32 and S36), the fast  $\text{H}_2\text{O}-\text{H}^{\text{N}}$  cross peak buildup rate can only be explained taking into account the presence of short contacts between exchangeable protons residing in the backbone and in side chain chemical groups: E17 ( $\text{E17H}^{\text{N}}-\text{T24OH}$ , 1.1 Å), R21 ( $\text{R21H}^{\text{N}}-\text{S19OH}$ , 2.7 Å), T32 ( $\text{T32H}^{\text{N}}-\text{T32OH}$ , 3.4 Å) and S36 ( $\text{S36H}^{\text{N}}-\text{S36OH}$ , 2.3 Å). It was not possible to detect the corresponding side chain protons in a direct or indirect fashion. Suppression of exchange relayed transfers ( $\text{H}_2\text{O} \rightarrow \text{OH} \rightarrow \text{H}^{\text{N}}$ ) is theoretically possible, but requires the application of periodic band-selective decoupling pulses covering the entire  $^1\text{H}$  chemical shift range from 12 to 6 ppm [160]. This is not possible, since this pulse would as well affect the water- $\text{H}^{\text{N}}$  correlations.

In the long run, however, applications to deuterated protein samples with selective methyl group protonation [161] are possible to suppress these unwanted correlations.

Previously,  $^1\text{H}$ ,  $^{13}\text{C}$  correlations were observed between side chains containing labile protons and water [153,154,155]. We can exclude that chemical exchange during cross-polarization contributes significantly to the  $\text{H}_2\text{O}-\text{H}^{\text{N}}$  buildup rate. Exchange rates between amide protons and the solvent are typically on the order of  $<10$  Hz [162]. No cross peaks between water and amide nitrogens are detected using a CP contact time between 150  $\mu\text{s}$  and 2 ms in a  $^1\text{H}$ ,  $^{15}\text{N}$  PMLG correlation experiment. In addition, broadening of the  $\text{H}^{\text{N}}$  resonances due to chemical exchange between the  $\text{H}^{\text{N}}$  proton and the solvent can be ruled out, since homonuclear  $^1\text{H}$ ,  $^1\text{H}$  dipolar decoupling yields line narrowing of the  $\text{H}^{\text{N}}$  resonance lines. The opposite behaviour would be expected, if chemical exchange is the major contribution to line broadening. Therefore one can conclude that the effects that are observed are due to  $^1\text{H}$ ,  $^1\text{H}$  homonuclear coupling.

In conclusion, it has been shown that MAS solid state NMR can provide information about water molecules in a protein structure undergoing dynamics on a ns to  $\mu\text{s}$  timescale. Upon comparison with the X-ray structure of the SH3 domain, three regions could be identified which are assigned to water involved in a hydrogen network close to bulk water, to water buried in the interior of the protein and to flexible regions of the molecule. Analysis of the  $\text{H}_2\text{O}-\text{H}^{\text{N}}$  spin diffusion buildup experiment allows the assignment of these dynamic water molecules, whereas water molecules which are located on the surface of the protein and which exchange rapidly with the bulk solvent are not detected. The  $T_2$  decay experiment is sensitive both to  $\text{H}^{\text{N}},\text{H}^{\text{N}}$  and  $\text{H}^{\text{N}},\text{H}_2\text{O}$  interactions. In cases where the X-ray structure is not known, short  $\text{H}^{\text{N}},\text{H}^{\text{N}}$  distances are readily identified as described earlier [163]. This should allow a differentiation of  $\text{H}^{\text{N}},\text{H}^{\text{N}}$  and  $\text{H}^{\text{N}},\text{H}_2\text{O}$  interactions. These experiments will find use in order to better understand the role of water in stabilizing protein structures.

## 6 Chapter. Resolution enhancement in MAS solid-state NMR by application of $^{13}\text{C}$ homonuclear scalar decoupling during acquisition.

### 6.1 Introduction.

In the past, many methods have been developed to suppress strong anisotropic interactions and improve line width in solid state NMR, like sample preparation [28,42], fast and ultra fast MAS [44,45], development of hetero- and homonuclear dipole-dipole decoupling sequences [23,24,29]. These developments resulted in significant line narrowing making scalar homonuclear couplings the major determinants of the  $^{13}\text{C}$  line width in uniformly enriched samples.

The achievable line width of  $^{13}\text{C}$  without  $J$  decoupling is on the order of 100-150 Hz [164], while typical one bond  $J$ -coupling constants in amino acids are 55 Hz for  $\text{C}_\alpha\text{-C}'$  and 35Hz for  $\text{C}_\alpha\text{-C}_\beta$  [165,166]. In addition,  $^3J_{\text{cc}}$  couplings between backbone and side chain carbons yield an additional contribution to the observed line width. Removal of these couplings is getting more important in ssNMR as higher quality spectra are obtained.

$^{13}\text{C}$ ,  $^{13}\text{C}$  homonuclear decoupling can be achieved either by application of selective radiofrequency pulse schemes or biosynthetically by using a labelling strategy in which each  $^{13}\text{C}$  is only directly bonded to  $^{12}\text{C}$  nuclei. A number of approaches to achieve  $J$  decoupling which were originally developed in solution state NMR have successfully been implemented in solid-state NMR. Selective  $^{13}\text{C}$  labelling schemes [5,167,168] remove  $J$  couplings and also reduce dipolar truncation effects, facilitating long range distances determination. On the other hand, uniform  $^{13}\text{C}$  labelling of backbone is required for sequential assignments. Application of selective pulses for refocusing homonuclear  $J$  coupling in the indirect dimension was used in solution NMR [169]. This idea was implemented in solid state NMR by Strauss et al [170] and later reconsidered by Igumenova et al [88] to decouple  $^{13}\text{C}$ . These approaches were limited so far to the indirect dimension, while the direct dimension would be more efficient in terms of experimental



time expenses. Combination of decoupling in both the direct and indirect dimension should yield, however, the best resolution.

Recently Emsley and co-workers [91,100] applied spin-state selective excitation schemes in solid state NMR, which were originally developed by Sørensen and co-workers [82] for solution state NMR. Single and double IPAP selection filters were used for 1D experiments to separate a single multiplet component by recording and superposition of in- and anti-phase doublet and quartet spectra [91]. In the 2D  $^{13}\text{C}$ ,  $^{13}\text{C}$  correlation experiment a quite elegant scheme was employed [100] where spin state selection in the indirect dimension was achieved using an IPAP sequence within a constant time  $^{13}\text{C}$  evolution period, while PDSO is used as a zero-quantum mixing sequence to obtain spin-state selective  $\text{C}'\text{-C}_\alpha$  polarization transfer, yielding line narrowing in the direct dimension after combination of interleaved recorded data sets with one another. The major prerequisite are relatively long filtering time periods on the order of  $J/2$  often resulting in significant polarization losses at moderate MAS frequencies. The experiment demonstrates a remarkable improvement in resolution in the direct dimension by as much as 44%, while the line width in the indirect dimension was enhanced by 17%. The last value was achieved due to a relatively short  $t_1^{\text{max}}$ , which was a compromise between loss of polarization (ca. 35%) and line width. An empirical scaling factor is used for combination of different data sets to extract the single spin component [100] and it is linked to the PDSO mixing time, which does not transfer the same way an in- and anti-phase signal. The way to define the scaling factor is not obvious and is based on an empirical approach.

Carbon-carbon scalar couplings can also be removed by selective irradiation of one or several spectral regions of interacting nuclei. In this case, the respective multiplet collapses into a single resonance line. Such decoupling techniques are used for decoupling in the indirect dimension in solution state NMR, employing wide band selective adiabatic pulses [171,172]. Band selective homonuclear carbon-carbon decoupling can be applied during  $^{13}\text{C}$  acquisition. This approach has recently been successfully implemented for  $^{13}\text{C}$  detection of paramagnetic proteins [173] in solution state NMR.

In this chapter, we implement a mono and double band selective homonuclear  $J$  decoupling sequence based on selective irradiation in the direct dimension to increase the effective resolution for solid-state NMR applications. We show that the application of a

weak RF field does not interfere with sample rotation if care is taken to avoid HORROR ( $\omega_{\text{rf}} = \omega_{\text{rot}}/2$ ) [174] or R3 ( $\omega_{\text{rf}} = n \cdot \omega_{\text{rot}}$ ) [175] conditions. The method was tested first using an uniformly  $^{15}\text{N}$ - $^{13}\text{C}$  enriched peptide sample, Nac-Val-Leu-OH, and was then applied to an amyloidogenic hexameric peptide (STVIIIE), where severe overlap in the  $\text{C}_\alpha$  and  $\text{C}'$  spectral region prevented the assignment of these resonances.

## 6.2 Experimental.

All experiments were carried out on a 600 MHz Bruker-Avance spectrometer, equipped with a 4mm triple resonance probe. The employed 1D and 2D pulse schemes are illustrated in figure 6.2.1. We assume that all anisotropic interactions as well as  $^{13}\text{C}$ - $^1\text{H}$  scalar couplings were reduced to an insignificant level by MAS (ca. 11-12.5 kHz) and application of the TPPM proton decoupling scheme, using a RF field strength of ca. 90 kHz. All experiments start with a  $90^\circ$   $^1\text{H}$  excitation pulse followed by a ramped CP magnetization transfer from protons to carbon. In the 2D experiment,  $\text{C}'$  is selectively irradiated during the evolution in the indirect dimension to suppress the scalar coupling to  $\text{C}_\alpha$ . Proton driven spin diffusion is used to yield magnetization transfer between different carbon sites. In all experiments band-selective homonuclear  $^{13}\text{C}$ ,  $^{13}\text{C}$  scalar decoupling was achieved during stroboscopic detection by application of band-selective adiabatic RF pulses. In order to avoid misunderstanding hereafter we use the term “stroboscopic/windowed detection” to designate detection having RF power irradiation applied on the detected nucleus during the acquisition. This scheme requires to lock/open the preamplifier gate after/before each sampling point. This results in increase in the noise level. On the other hand, the expression “standard detection” is used to denote detection, when the preamplifier gate is kept locked during the whole acquisition time.

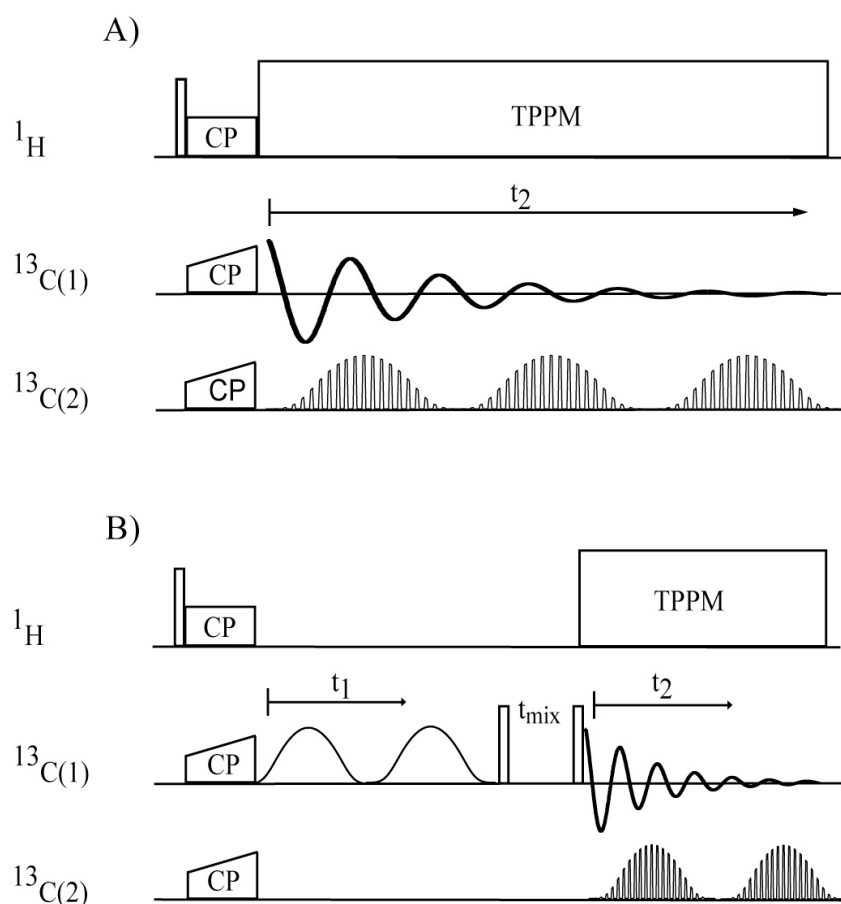


Figure 6.2.1. A) Pulse sequence employed for  $^{13}\text{C}$ - $^{13}\text{C}$  homonuclear scalar decoupling during detection. Selective pulses with windows for data sampling are represented as shapes with gaps and  $90^\circ$  pulses are indicated by open bars. B) 2D  $^{13}\text{C}$ - $^{13}\text{C}$  PDS pulse scheme with  $^{13}\text{C}$ - $^{13}\text{C}$  homonuclear decoupling during detection. Selective irradiation in the indirect dimension is represented as a shape.

The window duration for irradiation (HDDUTY) was set to 37% of the dwell time, as a compromise between decrease of the signal-to-noise ratio due to probe ring down and efficiency of the decoupling performance. In the experiments, a dwell time of  $14.7\ \mu\text{s}$  was employed. A supercycled adiabatic SEDUCE-1 (digitized into 1000 points) pulse [70,176] was used to irradiate the selected frequency band(s), generating a “DANTE-like” [177] train facilitating the selectivity of the shaped pulse. In the stroboscopic regime at low power the signal-to-noise ratio depends on HDDUTY according to [173]:

$$\frac{S}{N} = \frac{S}{N}_0 \cdot \sqrt{1 - \frac{\text{HDDUTY}}{100}} \quad (6.2.1)$$

yielding 0.79 for a HDDUTY value of 37%. Experimentally, we observe however a smaller value: the signal-to-noise ratio measured at HDDUTY of 37% and zero power is

reduced to 0.65 compared to conventional detection. However, collapse of multiplets into singlets still yields a sensitivity improvement.

### 6.3 Results and discussion.

For a quantitative characterization of band-selective homodecoupling the uniformly  $^{15}\text{N}$ - $^{13}\text{C}$  labelled dipeptide Nac-Val-Leu-OH was used as a test sample. The MAS frequency was set to 12.5 kHz. All experiments were carried out at 280 K. Figure 6.3.1 shows several experimental  $^{13}\text{C}$ -1D spectra, in which no decoupling was applied (A, D, F),  $\text{C}_\alpha$  was decoupled from  $\text{C}'$  (B),  $\text{C}_\alpha$  was simultaneously decoupled from  $\text{C}'$  and  $\text{C}_\beta$  (C) and  $\text{C}'$  was decoupled from  $\text{C}_\alpha$  (E). MLEV16 [178] and P9 [179,180] supercycling of the selective pulses was used in experiments B), E) and C), respectively.

All shaped pulses were generated using the STDISP utility in XWINNMR 3.5. The experimental results are summarized in Table 1. Stroboscopic detection was used for the reference experiments represented in (A) and (D), to allow for direct comparison with the homonuclear decoupling experiments, shown in (B), (C) and (E).  $\text{C}'$  region of a spectrum recorded with standard detection is represented in (F) to allow comparison with stroboscopic detection (D) which was used for reference experiment. Noise levels were equalized for both experiments.

Observed line width of not decoupled  $\text{C}'$  and  $\text{C}_\alpha$  resonances are between 101 and 125 Hz, while  $J$  coupling is clearly resolved only for Leu  $\text{C}'$ . Homonuclear  $J$  couplings are comparable with the line widths what makes the decoupling efficient. Except of  $^{13}\text{C}$ ,  $^{13}\text{C}$  and  $^{13}\text{C}$ ,  $^{15}\text{N}$   $J$  couplings (ca. 50-90Hz) and homogeneous broadening (ca. 30Hz [88]) not completely suppressed interactions like CSA,  $^1\text{H}$ ,  $^{13}\text{C}$  and  $^{13}\text{C}$ ,  $^{13}\text{C}$  dipolar couplings contribute to the line width. The last interaction broadens lines due to the second-order dipolar shift. For low magnetic fields at  $\omega_r$  between  $n=1$  and  $n=2$  rotational resonance conditions the broadening is comparable with  $^{13}\text{C}$ ,  $^{13}\text{C}$   $J$  coupling and it's influence on the line width was carefully studied in [88]. At higher magnetic fields this effect is reduced due to truncation of “flip-flop” term in homo-nuclear dipolar spin Hamiltonian by the

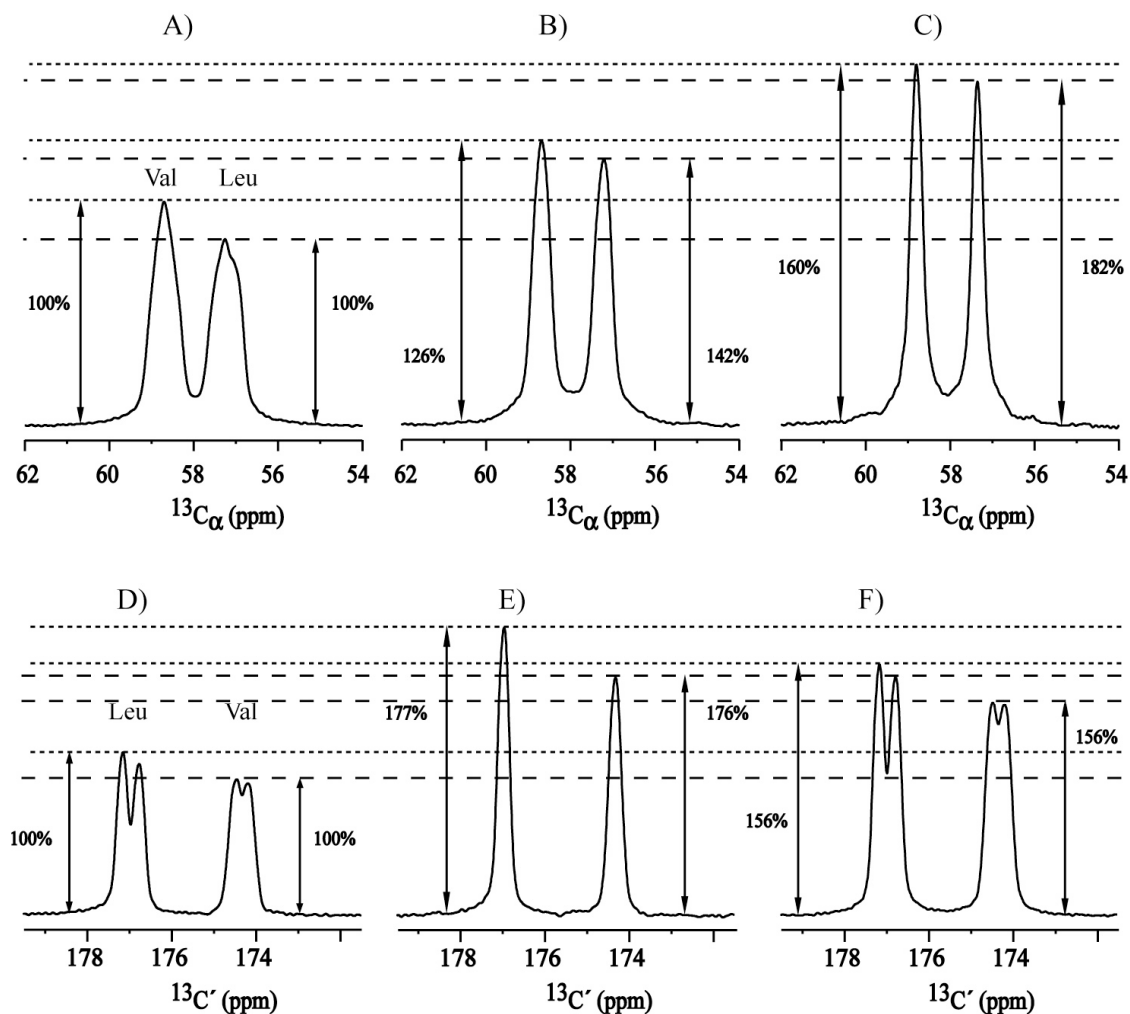


Figure 6.3.1.  $^{13}\text{C}$ -1D spectra of u- $^{13}\text{C}$ - $^{15}\text{N}$  Nac-Val-Leu-OH, displaying the  $^{13}\text{C}'$  and  $^{13}\text{C}_\alpha$  spectral regions. The MAS frequency was adjusted to 12.5 kHz. The acquisition time was set to 50 ms. The signal was processed without any apodization. The same experimental conditions were used in all experiments in order to allow for direct comparison of resolution and the signal-to-noise ratio. Stroboscopic detection was used in all cases except of F) to allow a direct comparison.

- A)  $\text{C}_\alpha$  without decoupling.
- B)  $\text{C}_\alpha$  with  $\text{C}'$  decoupling.
- C)  $\text{C}_\alpha$  with simultaneous decoupling from  $\text{C}'$  and  $\text{C}_\beta$  regions.
- D)  $\text{C}'$  without decoupling.
- E)  $\text{C}'$  with  $\text{C}_\alpha$  decoupling.
- F)  $\text{C}'$  without decoupling, no stroboscopic detection.

large chemical shift difference term. The influence of the truncation we clearly observed in spectra of Nac-Val-Leu-OH at 400 MHz spectrometer, where  $J$  coupling splitting of Leu C' is not well resolved any more and line width for carbonyl resonances roughly 10 Hz more (data not shown). This fact points that external magnetic field directly results in decoupling performance.

We observe a reduction in line width for Leu and Val C' in the case of decoupling from  $C_\alpha$  by 59 and 49 Hz, respectively, which is in the order of the C'- $C_\alpha$  scalar coupling, indicating good performance. In the case of decoupling  $C_\alpha$  from C', a line narrowing of 50.5 Hz and 36 Hz is observed for Leu and Val  $C_\alpha$ , respectively. Simultaneous decoupling of C' and  $C_\beta$  while observing  $C_\alpha$  results in a line narrowing of 74 and 58 Hz for Leu and Val, respectively. Previously, a line narrowing in the direct dimension in case of decoupling  $C_\alpha$  from C' using the spin-state selective scheme of 40-42 Hz [91], and in the indirect dimension in case of simultaneous decoupling of  $C_\alpha$  from C' and  $C_\beta$  of ca. 55 Hz [88] could be achieved at moderate spinning frequencies.

Sensitivity gain obtained by the decoupling experiments comparatively to the reference experiments are given on figure 6.3.1. Taking into account factor 0.65 for sensitivity decreasing in case of stroboscopic detection one can obtain that gain achieves 116% for Leu  $C_\alpha$ .

Despite the advantage of higher sensitivity and resolution, homodecoupling can cause significant Bloch-Siegert shift (BSS) of the resonances of interest [181]. In the case of decoupling  $C_\alpha$  from C' and C' from  $C_\alpha$ , no induced shifts were observed due to the large chemical shift difference between these nuclei. Double band selective decoupling causes an induced shift of the  $C_\alpha$  and  $C_\gamma$  resonance frequency due to irradiation of  $C_\beta$ . The BSS value in this experiment for both Val and Leu  $C_\alpha$  is 19 Hz. This value is on the order of 0.13 ppm and therefore much smaller than the line width and close to the digital resolution one obtains in multi-dimensional experiments. BSS can be compensated by using an additional symmetric pulse of the same shape having the opposite frequency offset from the signal of interest which can easily be implemented in the indirect dimension. The major limitation of this approach in the direct dimension is the short time available for RF irradiation during detection. Using a compensatory pulse significantly decreases the decoupling performance in the direct dimension (results not shown). Also, calculation of

the BSS based on numerical simulations is possible [171] and can be performed for any elaborative adiabatic pulse.

Table 6.3.1. Full linewidth at half height ( $\Delta$ ) in Hz for Nac-Val-Leu for decoupling of different spectral regions.

	$\Delta$ Leu C'	$\Delta$ Val C'	$\Delta$ Val C $_{\alpha}$	$\Delta$ Leu C $_{\alpha}$	RF Power (Hz)	Refocusing pulse duration (ms)	Supercycle	BSS (Hz)
A			111.5	125				
B			75.5	74.5	4400	12.7	Mlev16	0 Hz
C			53.5	51	8300	10.640	P9	19 Hz
D	107	101.5						
E	48	52.5			4400	12.7	Mlev16	0 Hz

Abbreviations in the table for different spectra correspond to ones used in capture of Fig. 6.3.2.

A) C $_{\alpha}$  without decoupling.

B) C $_{\alpha}$  with C' decoupling .

C) C $_{\alpha}$  with simultaneous decoupling from C' and C $_{\beta}$  regions.

D) C' without decoupling.

C' with C $_{\alpha}$  decoupling.

The homonuclear decoupling sequence was applied to an amyloidogenic hexameric peptide (STVIIIE) [182].  $^{13}\text{C}$ -1D spectra of  $^{13}\text{C}$ - $^{15}\text{N}$  uniformly labelled STVIIIE with and without decoupling are presented on figure 6.3.2 B and A respectively. The spectrum without decoupling was acquired in standard detection mode. The natural abundance spectrum of the peptide is shown in figure 6.3.2 C. Comparison of the decoupled spectrum with the natural abundance and not decoupled spectra demonstrates the high efficiency of the decoupling scheme.

Single band  $^{13}\text{C}'$ - $^{13}\text{C}_{\alpha}$   $J$  decoupling was achieved by selective irradiation of the  $^{13}\text{C}_{\alpha}$  region. Parameters of the employed pulse are similar to those used in the previous experiments applied to the dipeptide. An adiabatic SEDUCE-1 pulse with a MLEV-16 supercycle was applied with an on-resonance frequency of 59 ppm (see figure 6.3.2 D ) employing a RF field amplitude of 5 kHz and a duration of 11.5 ms. In case of continuous irradiation it has excitation band width of 4kHz, while windows for detection make it more selective. RF power and duration of the pulse were experimentally adjusted for the optimal performance.

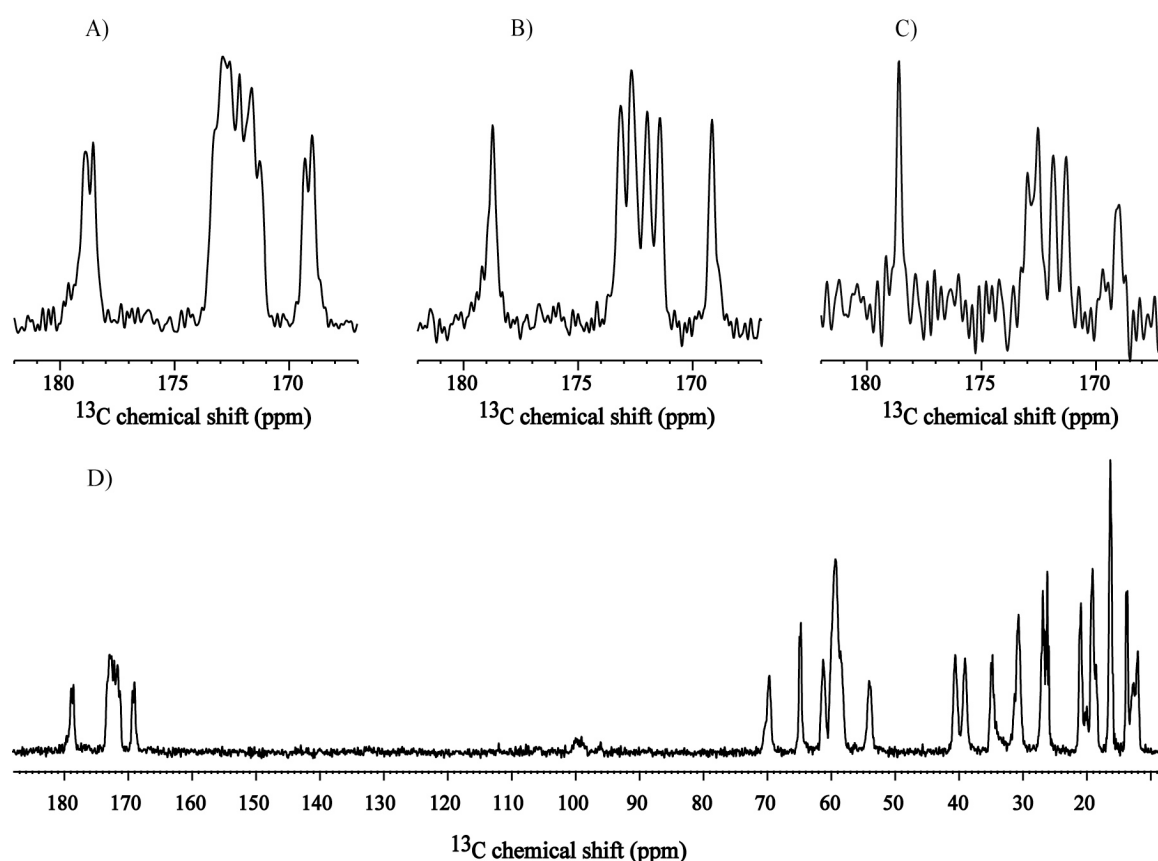


Figure 6.3.2.  $^{13}\text{C}$ -1D spectra of fibrillized STVIIIE demonstrating the performance of  $^{13}\text{C}$ - $^{13}\text{C}$  homonuclear scalar decoupling. Spectra were acquired with a MAS frequency of 11 kHz, temperature of 273 K and application of a 90 kHz RF field strength for TPPM decoupling.

A) C' region of  $^{13}\text{C}$ - $^{15}\text{N}$  uniformly labelled sample without homonuclear scalar decoupling, standard detection is used, ns=256.

B) C' region of  $^{13}\text{C}$ - $^{15}\text{N}$  uniformly labelled sample with homonuclear scalar decoupling applied to the  $\text{C}_\alpha$  region, ns=256.

(C) Natural abundance spectrum, ns=22000.

(D) Full spectrum of  $^{13}\text{C}$ - $^{15}\text{N}$  uniformly labelled sample, ns=256.

Spectra (A), (B) and (D) were recorded at the same conditions. The acquisition time in the experiments was 35ms. The experimental time for each experiment was 8 min. The spectrum (C) was recorded using an acquisition time of 30 ms, and was recorded within 22 hours. No apodization was applied for all spectra.

Signal-to-noise ratio for the highest peak in not decoupled spectrum is 31.1, while decoupled spectrum yields S/N 27.5. Such ratio for C' region is lower than in the experiments for Nac-Val-Leu-OH, which can be explained by the spectral overlap and broader line width. For our experience decoupling performance decreases while irradiated



bandwidth increases. It is also a case for STVIE which has broader  $C_\alpha$  region. Higher RF decoupling power can improve decoupling performance, but it results in unwanted spikes and artefacts.

This approach was utilized to improve the resolution of the 2D experiment.  $C^{\text{aliphatic}}-C'$  spectral regions of the PDSD  $^{13}\text{C}-^{13}\text{C}$  correlation experiment performed with and without homonuclear decoupling are presented in Fig. 6.3.3 B and A respectively. The former spectrum was recorded using the pulse sequence shown in Figure 6.2.1 B. Homonuclear  $J$  decoupling in the direct dimension was analogous to the 1D experiments. For the indirect dimension, the same pulse shape was employed, while the amplitude of the applied RF field was set to 1600 Hz due to continuity of the irradiation. The resolution achieved in the decoupling experiment allows unambiguous assignment of all resonances, especially  $C_\alpha-C'$  correlations, which was not possible before. The standard PDSD experiment demonstrates for most peaks resolved  $J$  couplings, making the spectrum more confusing for interpretation, especially for the regions with spectral overlap. In the decoupled spectrum, we count only six  $C_\alpha-C'$  correlations, while seven would be expected. The missing  $C'$  resonance is broadened due to chemical exchange between different conformations (data not shown). Analysis of the chemical shifts of the cross peaks indicates that the missing resonance belongs to side chain glutamic acid carboxyl.

This 2D experiment also contains  $C_\alpha-C_\beta$  correlation (data not shown) with  $^{13}\text{C}, ^{13}\text{C}$   $J$  decoupling only in the direct dimension, while there is no decoupling in the indirect dimension. Due to strong spikes between 45 and 80 ppm caused by selective irradiation, cross peaks for serine and threonine are not observable, while valine, isoleucine and glutamic acid have sharper lines in the direct dimension. Spikes could be reduced to not significant level by decreasing irradiation power, but it also would reduce the decoupling performance.

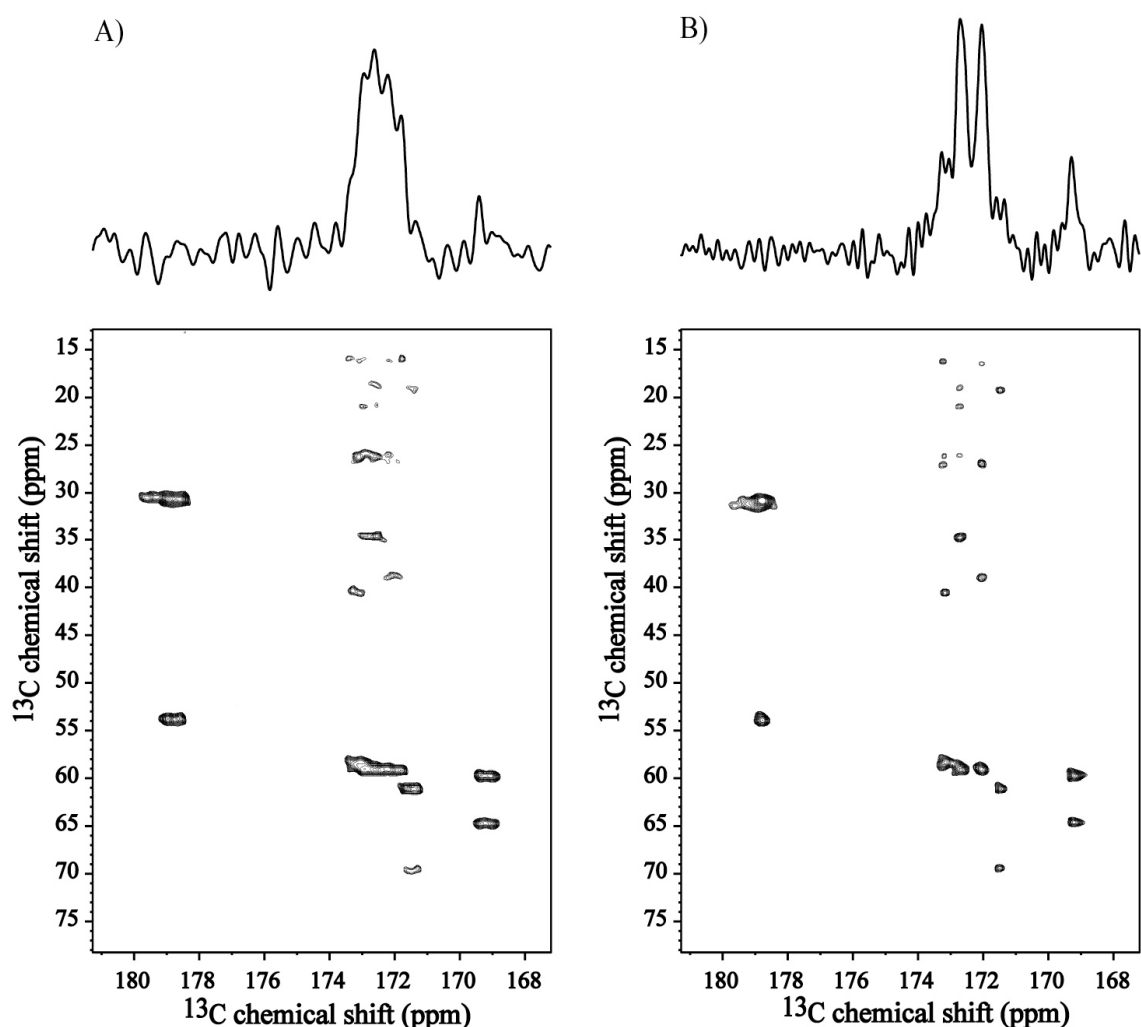


Figure 6.3.3.  $C^{\text{aliphatic}}-C'$  regions of two PDSD spectra of fibrillized  $u-[^{13}\text{C}-^{15}\text{N}]$  STVIIIE using a mixing time of 15ms.

A) Reference experiment, without homonuclear  $J$  decoupling.

B) Experiment recorded with homonuclear  $J$  decoupling in both dimensions according to the pulse sequence represented in figure 6.2.1 B.

All spectra were recorded at the same experimental conditions. The MAS frequency was set to 11kHz, temperature was adjusted to 273 K and TPPM of 90 kHz was used for heteronuclear decoupling in both dimensions. An acquisition time of  $t_1^{\text{max}}=10\text{ms}$  and  $t_2^{\text{max}}=30\text{ms}$  was used for the indirect and direct dimension, respectively, with TPPI [12] for phase sensitive detection. Both spectra were processed by applying a sine-bell function phase shifted by  $\pi/3$  and by  $\pi/3.5$  in  $t_1$  and in  $t_2$  respectively. Total experimental time for both spectra was 12 hours. Plot levels in both spectra are chosen to be slightly above than noise level. Spectra on the top are row projection at 59.3 ppm in the indirect dimension.

The experiments obviously show that decoupling during acquisition is useful for improving the spectral resolution in the direct dimension.  $J$  decoupling is highly efficient

when  $J$  is comparable or larger than the natural line width. In cases where the  $J$  scalar coupling is resolved, decoupling results in reducing the number of peaks by a factor of  $2^n$ , where  $n$  corresponds to the number of decoupled spins. This can dramatically enhance the resolution in complicated spectra. If the sum of scalar couplings  $\Sigma J_i$  is not less than natural line width, ideal decoupling decreases the line width by  $\Sigma J_i$ . In this case, presented experimental approach gives the theoretical value for a signal-to-noise ratio enhancement in case of full decoupling of spectra as:

$$\frac{S}{N} = k \cdot \left. \frac{S}{N} \right|_0 \cdot 2^n \quad (6.3.1)$$

where  $\left. \frac{S}{N} \right|_0$  denotes the signal-to-noise ratio of the spectrum without decoupling.

The factor  $k$  describes the signal-to-noise ratio decrease due to employing of stroboscopic detection and  $n$  corresponds to the number of decoupled spins. While spin-state-selective schemes yield a signal-to-noise ratio:

$$\frac{S}{N} = h \cdot \left. \frac{S}{N} \right|_0 \cdot \sqrt{2^n} \quad (6.3.2)$$

where  $\left. \frac{S}{N} \right|_0$  denotes the signal-to-noise ratio of the spectrum without decoupling.

The factor  $h$  reflects the signal decrease during the preparation period, which for moderate MAS frequencies of 10-15 kHz is on the order of 0.4-0.85, depending on the nucleus [91],  $n$  refers to the number of decoupled spins 1/2.

In conclusion, it has been shown that application of homonuclear decoupling is feasible during detection. This decoupling schemes increases the resolution of the carbon resonances up to a factor of 2-2.5. At the same time, sensitivity can be moderately increased (up to factor 1.2). We assume that this strategy turns out to be useful for larger biomolecules like e.g. membrane proteins, where spectral overlap is critical.

## References:

- [1] Snyder, D.A.; Chen, Y.; Denissova, N.G.; Acton, T.; Aramini, J.M.; Ciano, M.; Karlin, R.; Liu, J.F.; Manor, P.; Rajan, P.A.; Rossi, P.; Swapna, G.V.T.; Xiao, R.; Rost, B.; Hunt, J. and Montelione, G.T. (2005): Comparisons of NMR spectral quality and success in crystallization demonstrate that NMR and X-ray crystallography are complementary methods for small protein structure determination, *J. Am. Chem. Soc.* (vol. 127), pp. 16505-16511.
- [2] Yee, A.A.; Savchenko, A.; Ignachenko, A.; Lukin, J.; Xu, X.H.; Skarina, T.; Evdokimova, E.; Liu, C.S.; Semesi, A.; Guido, V.; Edwards, A.M. and Arrowsmith, C.H. (2005): NMR and X-ray crystallography, complementary tools in structural proteomics of small proteins, *J. Am. Chem. Soc.* (vol. 127), pp. 16512-16517.
- [3] Lange, A.; Becker, S.; Seidel, K.; Giller, K.; Pongs, O. and Baldus, M. (2005): A concept for rapid protein-structure determination by solid-state NMR spectroscopy, *Angewandte Chemie-International Edition* (vol. 44), No. 14, pp. 2089-2092.
- [4] Lange, A.; Giller, K.; Hornig, S.; Martin-Eaucclair, M. F.; Pongs, O.; Becker, S. and Baldus, M. (2006): Toxin-induced conformational changes in a potassium channel revealed by solid-state NMR, *Nature* (vol. 440), No. 7086, pp. 959-962.
- [5] Castellani, F.; Rossum, B.J. van; Diehl, A.; Rehbein, K. and Oschkinat, H. (2002): Structure of a protein determined by solid-state magic-angle spinning NMR spectroscopy, *Nature* (vol. 420), pp. 98-102.
- [6] Rienstra, C.M.; Tucker-Kellogg, L.; Jaroniec, C.P.; Hohwy, M.; Reif, B.; Lozano-Peres, T.; B.Tidor and Griffin, R.G. (2002): De Novo Structure Determination of Peptides and Proteins with High Resolution Solid State MAS NMR, *Proc. Nat. Acad. Sci. USA* (vol. 99), pp. 10260-10265.
- [7] Hologne, M.; Faelber, K.; Diehl, A. and Reif, B. (2005): Characterization of dynamics of perdeuterated proteins by MAS solid-state NMR, *J. Am. Chem. Soc.* (vol. 127), pp. 11208-11209.

- [8] Giraud, N.; Bockmann, A.; Lesage, A.; Penin, F.; Blackledge, M. and Emsley, L. (2004): Site-specific backbone dynamics from a crystalline protein by solid-state NMR spectroscopy, *J. Am. Chem. Soc.* (vol. 126), pp. 11422-11423.
- [9] Castellani, F. (2003): Structure determination of immobilized proteins by solid-state NMR spectroscopy., Ph.D. Thesis, Berlin.
- [10] Blum, K. (1981): Density matrix theory and applications., Plenum Press, New York.
- [11] Weissbluth, M. (1978): Atoms and molecules., Springer, New York.
- [12] Ernst, R.R.; Bodenhausen, G. and Wokaun, A. (1987): Principles of nuclear magnetic resonance in one and two dimensions, Clarendon, Oxford.
- [13] Slichter, C.P. (1978): Principles of magnetic resonance, Springer, Berlin.
- [14] Schmidt-Rohr, K. and Spiess, H.W. (1994): Multidimensional Solid-State NMR and Polymers, Academic Press, San Diego 1994.
- [15] Maricq, M.M. and Waugh, J.S. (1979): NMR in rotating solids, *J. Chem. Phys.* (vol. 70), pp. 3300-3316.
- [16] Harris, R.K. (1996): Nuclear spin properties and notation., *Encyclopedia of Nuclear Magnetic Resonance*, editors D.M. Grant and R.K. Harris (1996) (vol. 5), pp. 3301-3314.
- [17] Lifshitz, E.M. and Landau, L.D. (1981): Quantum Mechanics: Non-Relativistic Theory, Volume 3, Butterworth-Heinemann.
- [18] Abraham, R.J.; Loftus, P. and Fisher, J. Patrick (1988): Introduction to NMR Spectroscopy, John Wiley and Sons.
- [19] Magnus, W. (1954): On the Exponential Solution of Differential Equations for a Linear Operator, *Communications on Pure and Applied Mathematics* (vol. 7), No. 4, pp. 649-673.
- [20] Waugh, J. S.; Huber, L. M. and Haeberle, U. (1968): Approach to High-Resolution Nmr in Solids, *Physical Review Letters* (vol. 20), No. 5, pp. 180-&.
- [21] Rhim, W. K.; Elleman, D. D. and Vaughan, R. W. (1973): Analysis of Multiple Pulse Nmr in Solids, *Journal of Chemical Physics* (vol. 59), No. 7, pp. 3740-3749.
- [22] Burum, D. P. and Rhim, W. K. (1979): Analysis of Multiple Pulse NMR in Solids .3, *Journal of Chemical Physics* (vol. 71), No. 2, pp. 944-956.

[23] Bielecki, A.; Kolbert, A.C. and Levitt, M.H. (1989): Frequency-switched pulse sequence - homonuclear decoupling and dilute spin NMR in solids, *Chem. Phys. Lett.* (vol. 155), pp. 341-346.

[24] Vinogradov, E.; Madhu, P.K. and Vega, S. (1999): High-resolution proton solid-state NMR spectroscopy by phase-modulated Lee-Goldburg experiment, *Chem. Phys. Lett.* (vol. 314), pp. 443-450.

[25] Vinogradov, E.; Madhu, P.K. and Vega, S. (2000): A bimodal Floquet analysis of phase modulated Lee-Goldburg high resolution proton magic angle spinning NMR experiments, *Chem. Phys. Lett.* (vol. 329), pp. 207-214.

[26] Vinogradov, E.; Madhu, P. K. and Vega, S. (2005): Strategies for high-resolution proton spectroscopy in solid-state NMR, *New Techniques in Solid-State Nmr* (vol. 246) pp. 33-90.

[27] Agarwal, V.; Diehl, A.; Skrynnikov, N. and Reif, B. (2006): High resolution H-1 detected H-1,C-13 correlation spectra in MAS solid-state NMR using deuterated proteins with selective H-1,H-2 isotopic labeling of methyl groups, *Journal of the American Chemical Society* (vol. 128), No. 39, pp. 12620-12621.

[28] Chevelkov, V.; Rehbein, K.; Diehl, A. and Reif, B. (2006): Ultrahigh resolution in proton solid-state NMR spectroscopy at high levels of deuteration, *Angewandte Chemie-International Edition* (vol. 45), No. 23, pp. 3878-3881.

[29] Bennett, A.E.; Rienstra, C.M.; Auger, M.; Lakshmi, K.V. and R.G.Griffin (1995): Heteronuclear decoupling in rotating solids, *J. Chem. Phys. Lett.* (vol. 103), pp. 6951-6958.

[30] Pines, A.; Gibby, M. G. and Waugh, J. S. (1973): Proton-Enhanced NMR of Dilute Spins in Solids, *Journal of Chemical Physics* (vol. 59), No. 2, pp. 569-590.

[31] Pines, A.; Waugh, J. S. and Gibby, M. G. (1972): Proton-Enhanced Nuclear Induction Spectroscopy - Method for High-Resolution NMR of Dilute Spins in Solids, *Journal of Chemical Physics* (vol. 56), No. 4, pp. 1776-&.

[32] Dusold, S. and Sebald, A. (2000): Dipolar recoupling under magic-angle spinning conditions, *Annual Reports on Nmr Spectroscopy*, Vol 41 (vol. 41) pp. 185-264.

[33] Gullion, T. and Schaefer, J. (1989): Rotational-Echo Double-Resonance NMR, *Journal of Magnetic Resonance* (vol. 81), No. 1, pp. 196-200.

[34] Hing, A. W.; Vega, S. and Schaefer, J. (1992): Transferred-Echo Double-Resonance NMR, *Journal of Magnetic Resonance* (vol. 96), No. 1, pp. 205-209.

[35] Lee, Y. K.; Kurur, N. D.; Helmle, M.; Johannessen, O. G.; Nielsen, N. C. and Levitt, M. H. (1995): Efficient Dipolar Recoupling in the NMR of Rotating Solids - a Sevenfold Symmetrical Radiofrequency Pulse Sequence, *Chemical Physics Letters* (vol. 242), No. 3, pp. 304-309.

[36] Carravetta, M.; Eden, M.; Zhao, X.; Brinkmann, A. and Levitt, M. H. (2000): Symmetry principles for the design of radiofrequency pulse sequences in the nuclear magnetic resonance of rotating solids, *Chemical Physics Letters* (vol. 321), No. 3-4, pp. 205-215.

[37] Levitt, M. H. (2002): Symmetry-based pulse sequences in magic-angle spinning solid-state NMR, *Encyclopedia of Nuclear Magnetic Resonance: Supplementary Volume* edited by D. M. Grant and R. K. Harris.

[38] Chevelkov, V.; Rossum, B.J. van; Castellani, F.; Rehbein, K.; Diehl, A.; Hohwy, M.; Steuernagel, S.; Engelke, F.; Oschkinat, H. and Reif, B. (2003): H-1 detection in MAS solid-state NMR Spectroscopy of biomacromolecules employing pulsed field gradients for residual solvent suppression, *Journal of the American Chemical Society* (vol. 125), pp. 7788-7789.

[39] Pervushin, K.; Riek, R.; Wider, G. and Wuthrich, K. (1997): Attenuated T-2 relaxation by mutual cancellation of dipole-dipole coupling and chemical shift anisotropy indicates an avenue to NMR structures of very large biological macromolecules in solution, *Proceedings of the National Academy of Sciences of the United States of America* (vol. 94), No. 23, pp. 12366-12371.

[40] Chevelkov, V.; Faelber, K.; Diehl, A.; Heinemann, U.; Oschkinat, H. and Reif, B. (2005): Detection of Water Molecules in a polycrystalline sample of a chicken a-spectrin SH3 domain, *Journal of Biomolecular NMR* (vol. 31), pp. 295-310.

[41] Chevelkov, V.; Chen, Z.J.; Bermel, W. and Reif, B. (2005): Resolution enhancement in MAS solid-state NMR by application of C-13 homonuclear scalar decoupling during acquisition, *Journal of Magnetic resonance* (vol. 172), pp. 56-62.

[42] Pauli, J.; Rossum, B.J. van; Forster, H.; Groot, H.J.M. de and Oschkinat, H. (2000): Sample optimization and identification of signal patterns of amino acid side chains

in 2D RFDR spectra of the alpha-spectrin SH3 domain, *J. Magn. Reson.* (vol. 143), pp. 411-416.

[43] Samoson, A.; Tuhern, T. and Gan, Z. (2001): High-field high-speed MAS resolution enhancement in H-1 NMR spectroscopy of solids, *Solid state nuclear magnetic resonance* (vol. 20 (3-4):), pp. 130-136.

[44] Ernst, M.; Meier, M.A.; Tuhern, T.; Samoson, A. and Meier, B.H. (2004): Low-power high-resolution solid-state NMR of peptides and proteins, *J. Am. Chem. Soc.* (vol. 126), pp. 4764-4765.

[45] Ernst, M.; Samoson, A. and Meier, B.H. (2003): Low-power XiX decoupling in MAS NMR experiments, *J. Magn. Reson.* (vol. 163), pp. 332-339.

[46] Madhu, P.K.; Zhao, X. and Levitt, M.H. (2001): High-resolution H-1 NMR in the solid state using symmetry-based pulse sequences, *Chem. Phys. Lett.* (vol. 346), pp. 1142-1148.

[47] Rossum, B.J. van; Castellani, F.; Pauli, J.; Rehbein, K.; Hollander, J.; Groot, H.J.M. de and Oschkinat, H. (2003): Assignment of amide proton signals by combined evaluation of HN, NN and HNCA MAS-NMR correlation spectra, *J. Biomol. NMR* (vol. 25), pp. 217-223.

[48] Paulson, E.K.; Morcombe, C.R.; Gaponenko, V.; Dancheck, B.; Byrd, R.A. and Zilm, K.W. (2003): High-sensitivity observation of dipolar exchange and NOEs between exchangeable protons in proteins by 3D solid-state NMR spectroscopy, *J. Am. Chem. Soc.* (vol. 125), pp. 14222-14223.

[49] Reif, B.; Jaroniec, C.P.; Rienstra, C.M.; Hohwy, M. and Griffin, R.G. (2001): H-1-H-1 MAS correlation spectroscopy and distance measurements in a deuterated peptide, *J. Magn. Reson.* (vol. 151), pp. 320-327.

[50] Ishii, Y.; Yesinowski, J.P. and Tycko, R. (2001): Sensitivity enhancement in solid-state C-13 NMR of synthetic polymers and biopolymers by H-1 NMR detection with high-speed magic angle spinning, *J. Am. Chem. Soc.* (vol. 123), pp. 2921-2922.

[51] Paulson, E.K.; Morcombe, C.R.; Gaponenko, V.; Dancheck, B.; Byrd, R.A. and Zilm, K.W. (2003): Sensitive high resolution inverse detection NMR spectroscopy of proteins in the solid state, *J. Am. Chem. Soc.* (vol. 125), pp. 15831-15836.



[52] Vinogradov, E.; Madhu, P.K. and Vega, S. (2002): Proton spectroscopy in solid state nuclear magnetic resonance with windowed phase modulated Lee-Goldburg decoupling sequences, *Chem. Phys. Lett.* (vol. 354), pp. 193-202.

[53] Brown, S.P.; Lesage, A.; Elena, B. and Emsley, L. (2004): Probing proton-proton proximities in the solid state: High-resolution two-dimensional H-1-H-1 double-quantum CRAMPS NMR spectroscopy, *J. Am. Chem. Soc.* (vol. 126), pp. 13230-13231.

[54] Levitt, M.H.; Kolbert, A.C.; Bielecki, A. and Ruben, D.J. (1993): High-resolution <sup>1</sup>H NMR in solids with frequency-switched multiple-pulse sequences, *Solid state nuclear magnetic resonance* (vol. 2), pp. 151-163.

[55] Reif, B. and Griffin, R.G. (2003): H-1 detected H-1, N-15 correlation spectroscopy in rotating solids, *J. Magn. Reson.* (vol. 160), pp. 78-83.

[56] McDermott, A.E.; Creuzet, F.J.; Kolbert, A.C. and Griffin, R.G. (1992): High-resolution magic-angle-spinning NMR spectra of protons in deuterated solids, *J. Magn. Reson.* (vol. 98), pp. 408-413.

[57] Musacchio, A.; Noble, M.; Pauptit, R.; Wierenga, R. and Saraste, M. (1992): Crystal-Structure of a Scr-Homology-3 (SH3) domain, *Nature* (vol. 359), pp. 851-855.

[58] Gallagher, T.; Alexander, P.; Bryan, P. and Gilliland, G.L. (1994): Two crystal-structures of the B1 immunoglobulin-binding domain of streptococcal protein-G and comparison with NMR, *Biochemistry* (vol. 33), pp. 4721-4729.

[59] Gueron, M.; Plateau, P. and Decors, M. (1991): Solvent Signal Suppression in Nmr, *Progress in Nuclear Magnetic Resonance Spectroscopy* (vol. 23), pp. 135-209.

[60] Morcombe, C.R.; Paulson, E.K.; Gaponenko, V.; Byrd, R.A. and Zilm, K.W. (2005): H-1-N-15 correlation spectroscopy of nanocrystalline proteins, *J. Biomol. NMR* (vol. 31), pp. 217-230.

[61] Zhou, D.H.; Graesser, D.T.; Franks, W.T. and Rienstra, C.M. (2006): Sensitivity and resolution in proton solid-state NMR at intermediate deuteration levels: quantitative line width analysis and applications to correlation spectroscopy, *J. Magn. Reson.* (vol. 178), pp. 297-307.

[62] Lesage, A.; Sakellariou, D.; Hediger, S.; Elena, B.; Charmont, P.; Steuernagel, S. and Emsley, L. (2003): Experimental aspects of proton NMR spectroscopy in solids using phase-modulated homonuclear dipolar decoupling, *J. Magn. Reson.* (vol. 163), pp. 105-113.

[63] Hafner, S. and Spiess, H.W. (1998): Advanced solid state NMR spectroscopy of strongly dipolar coupled spins under fast magic angle spinning, Concepts in magnetic resonance Part A (vol. 10), pp. 99-128.

[64] Filip, C.; Hafner, S.; Schnell, I.; Demco, D.E. and Spiess, H.W. (1999): Solid-state nuclear magnetic resonance spectra of dipolar-coupled multi-spin systems under fast magic angle spinning, J. Chem. Phys. (vol. 110), pp. 423-440.

[65] Stringer, J.A.; Bronnimann, C.E.; Mullen, C.G.; Zhou, D.H.H.; Stellfox, S.A.; Li, Y.; Williams, E.H. and Rienstra, C.M. (2005): Reduction of RF-induced sample heating with a scroll coil resonator structure for solid-state NMR probes, J. Magn. Reson. (vol. 173), pp. 40-48.

[66] Goldman, M. (1984): Interference Effects in the Relaxation of a Pair of Unlike Spin-1/2 Nuclei, Journal of Magnetic Resonance (vol. 60), No. 3, pp. 437-452.

[67] Chevelkov, V.; Diehl, A. and Reif, B. (2007): Quantitative measurement of differential N-15-H-alpha/beta T-2 relaxation rates in a perdeuterated protein by MAS solid-state NMR spectroscopy, Magnetic Resonance in Chemistry (vol. 45), pp. S156-S160.

[68] Petkova, A. T.; Ishii, Y.; Balbach, J. J.; Antzutkin, O. N.; Leapman, R. D.; Delaglio, F. and Tycko, R. (2002): A structural model for Alzheimer's beta-amyloid fibrils based on experimental constraints from solid state NMR, Proceedings of the National Academy of Sciences of the United States of America (vol. 99), No. 26, pp. 16742-16747.

[69] Ventura, S.; Zurdo, J.; Narayanan, S.; Parreno, M.; Manges, R.; Reif, B.; Chiti, F.; Giannoni, E.; Dobson, C. M.; Aviles, F. X. and Serrano, L. (2004): Short amino acid stretches can mediate amyloid formation in globular proteins: The Src homology 3 (SH3) case, Proceedings of the National Academy of Sciences of the United States of America (vol. 101), No. 19, pp. 7258-7263.

[70] McCoy, M.A. and Mueller, L. (1993): Selective decoupling, J. Magn. Reson. Ser. A (vol. 101), pp. 122-130.

[71] Siemer, A. B.; Ritter, C.; Ernst, M.; Riek, R. and Meier, B. H. (2005): High-resolution solid-state NMR spectroscopy of the prion protein HET-s in its amyloid conformation, Angewandte Chemie-International Edition (vol. 44), No. 16, pp. 2441-2444.

[72] Jaroniec, C. P.; MacPhee, C. E.; Bajaj, V. S.; McMahon, M. T.; Dobson, C. M. and Griffin, R. G. (2004): High-resolution molecular structure of a peptide in an amyloid fibril determined by magic angle spinning NMR spectroscopy, *Proceedings of the National Academy of Sciences of the United States of America* (vol. 101), No. 3, pp. 711-716.

[73] Heise, H.; Hoyer, W.; Becker, S.; Andronesi, O. C.; Riedel, D. and Baldus, M. (2005): Molecular-level secondary structure, polymorphism, and dynamics of full-length alpha-synuclein fibrils studied by solid-state NMR, *Proceedings of the National Academy of Sciences of the United States of America* (vol. 102), No. 44, pp. 15871-15876.

[74] Carulla, N.; Caddy, G. L.; Hall, D. R.; Zurdo, J.; Gairi, M.; Feliz, M.; Giralt, E.; Robinson, C. V. and Dobson, C. M. (2005): Molecular recycling within amyloid fibrils, *Nature* (vol. 436), No. 7050, pp. 554-558.

[75] Narayanan, S. and Reif, B. (2005): Characterization of chemical exchange between soluble and aggregated states of beta-amyloid by solution-state NMR upon variation of salt conditions, *Biochemistry* (vol. 44), No. 5, pp. 1444-1452.

[76] Wider, G. and Wuthrich, K. (1999): NMR spectroscopy of large molecules and multimolecular assemblies in solution, *Current Opinion in Structural Biology* (vol. 9), No. 5, pp. 594-601.

[77] Pervushin, K. (2000): Impact of Transverse Relaxation Optimized Spectroscopy (TROSY) on NMR as a technique in structural biology, *Quarterly Reviews of Biophysics* (vol. 33), No. 2, pp. 161-197.

[78] Riek, R.; Fiaux, J.; Bertelsen, E. B.; Horwich, A. L. and Wuthrich, K. (2002): Solution NMR techniques for large molecular and supramolecular structures, *Journal of the American Chemical Society* (vol. 124), No. 41, pp. 12144-12153.

[79] Fiaux, J.; Bertelsen, E. B.; Horwich, A. L. and Wuthrich, K. (2002): NMR analysis of a 900K GroEL-GroES complex, *Nature* (vol. 418), No. 6894, pp. 207-211.

[80] Reif, B.; Xue, Y.; Agarwal, V.; Pavlova, M. S.; Hologne, M.; Diehl, A.; Ryabov, Y. E. and Skrynnikov, N. R. (2006): Protein side-chain dynamics observed by solution- and solid-state NMR: Comparative analysis of methyl H-2 relaxation data, *Journal of the American Chemical Society* (vol. 128), No. 38, pp. 12354-12355.

- [81] Chevelkov, V.; Faelber, K.; Schrey, A.; Rehbein, K.; Diehl, A. and Reif, B. (2007): Differential line broadening in MAS solid-state NMR due to dynamic interference, *Journal of the American Chemical Society* (vol. 129), pp. 10195-10200.
- [82] Sørensen, M.D.; Meissner, A. and O.W.Sørensen (1999): C-13 natural abundance (SE)-E-3 and (SCT)-C-3 experiments for measurement of J coupling constants between C-13(alpha) or H-1(alpha) and other protons in a protein, *J. Magn. Reson.* (vol. 137), pp. 237-242.
- [83] Andersson, P.; Weigelt, J. and Otting, G. (1998): Spin-state selection filters for the measurement of heteronuclear one-bond coupling constants, *Journal of Biomolecular Nmr* (vol. 12), No. 3, pp. 435-441.
- [84] Ottiger, M.; Delaglio, F. and Bax, A. (1998): Measurement of J and dipolar couplings from simplified two-dimensional NMR spectra, *Journal of Magnetic Resonance* (vol. 131), No. 2, pp. 373-378.
- [85] Giraud, N.; Blackledge, M.; Goldman, M.; Bockmann, A.; Lesage, A.; Penin, F. and Emsley, L. (2005): Quantitative analysis of backbone dynamics in a crystalline protein from nitrogen-15 spin-lattice relaxation, *Journal of the American Chemical Society* (vol. 127), No. 51, pp. 18190-18201.
- [86] Zilm, K. W. and Grant, D. M. (1981): C-13 Dipolar Spectroscopy of Small Organic-Molecules in Argon Matrices, *Journal of the American Chemical Society* (vol. 103), No. 11, pp. 2913-2922.
- [87] Wu, G.; Sun, B. Q.; Wasylishen, R. E. and Griffin, R. G. (1997): Spinning sidebands in slow-magic-angle-spinning NMR spectra arising from tightly J-coupled spin pairs, *Journal of Magnetic Resonance* (vol. 124), No. 2, pp. 366-371.
- [88] Igumenova, T.I. and McDermott, A.E. (2003): Improvement of resolution in solid state NMR spectra with J-decoupling: an analysis of lineshape contribution in uniformly 13-C enriched amino acids and proteins, *J. Magn. Reson.* (vol. 164), pp. 270-285.
- [89] Griffey, R. H. and Redfield, A. G. (1987): Proton-Detected Heteronuclear Edited and Correlated Nuclear-Magnetic-Resonance and Nuclear Overhauser Effect in Solution, *Quarterly Reviews of Biophysics* (vol. 19), No. 1-2, pp. 51-82.
- [90] Harris, R. K.; Packer, K. J. and Thayer, A. M. (1985): Slow Magic-Angle Rotation C-13 Nmr-Studies of Solid Phosphonium Iodides - the Interplay of Dipolar,

Shielding, and Indirect Coupling Tensors, *Journal of Magnetic Resonance* (vol. 62), No. 2, pp. 284-297.

[91] Duma, L.; Hediger, S.; Lesage, A. and Emsley, L. (2003): Spin-state selection in solid-state NMR, *J. Magn. Reson.* (vol. 164), pp. 187-195.

[92] Hall, J. B. and Fushman, D. (2006): Variability of the N-15 chemical shielding tensors in the B3 domain of protein G from N-15 relaxation measurements at several fields. Implications for backbone order parameters, *Journal of the American Chemical Society* (vol. 128), No. 24, pp. 7855-7870.

[93] Chekmenev, E. Y.; Zhang, Q. W.; Waddell, K. W.; Mashuta, M. S. and Wittebort, R. J. (2004): N-15 chemical shielding in glycyl tripeptides: Measurement by solid-state NMR and correlation with x-ray structure, *Journal of the American Chemical Society* (vol. 126), No. 1, pp. 379-384.

[94] Franks, W. T.; Zhou, D. H.; Wylie, B. J.; Money, B. G.; Graesser, D. T.; Frericks, H. L.; Sahota, G. and Rienstra, C. M. (2005): Magic-angle spinning solid-state NMR spectroscopy of the beta 1 immunoglobulin binding domain of protein G (GB1): N-15 and C-13 chemical shift assignments and conformational analysis, *Journal of the American Chemical Society* (vol. 127), No. 35, pp. 12291-12305.

[95] Bak, M.; Rasmussen, J. T. and Nielsen, N. C. (2000): SIMPSON: A general simulation program for solid-state NMR spectroscopy, *Journal of Magnetic Resonance* (vol. 147), No. 2, pp. 296-330.

[96] Chan, J. C. C. and Tycko, R. (2003): Recoupling of chemical shift anisotropies in solid-state NMR under high-speed magic-angle spinning and in uniformly C-13-labeled systems, *Journal of Chemical Physics* (vol. 118), No. 18, pp. 8378-8389.

[97] Herzfeld, J. and Berger, A. E. (1980): Sideband Intensities in Nmr-Spectra of Samples Spinning at the Magic Angle, *Journal of Chemical Physics* (vol. 73), No. 12, pp. 6021-6030.

[98] Reif, B.; Hennig, M. and Griesinger, C. (1997): Direct measurement of angles between bond vectors in high-resolution NMR, *Science* (vol. 276), No. 5316, pp. 1230-1233.

[99] Tjandra, N.; Szabo, A. and Bax, A. (1996): Protein backbone dynamics and N-15 chemical shift anisotropy from quantitative measurement of relaxation interference effects, *Journal of the American Chemical Society* (vol. 118), No. 29, pp. 6986-6991.

[100] Duma, L.; Hediger, S.; Brutscher, B.; Boekmann, A. and Emsley, L. (2003): Resolution enhancement in multidimensional solid-state NMR spectroscopy of proteins using spin-state selection, *J. Am. Chem. Soc.* (vol. 125), pp. 11816-11817.

[101] Dvinskikh, S. V.; Yamamoto, K.; Durr, U. H. N. and Ramamoorthy, A. (2007): Sensitivity and resolution enhancement in solid-state NMR spectroscopy of bicelles, *Journal of Magnetic Resonance* (vol. 184), No. 2, pp. 228-235.

[102] Palmer, A. G. (2004): NMR characterization of the dynamics of biomacromolecules, *Chemical Reviews* (vol. 104), No. 8, pp. 3623-3640.

[103] Palmer, A. G.; Kroenke, C. D. and Loria, J. P. (2001): Nuclear magnetic resonance methods for quantifying microsecond-to-millisecond motions in biological macromolecules, *Nuclear Magnetic Resonance of Biological Macromolecules, Pt B* (vol. 339) pp. 204-238.

[104] Clore, G. M. and Schwieters, C. D. (2004): How much backbone motion in ubiquitin is required to account for dipolar coupling data measured in multiple alignment media as assessed by independent cross-validation?, *Journal of the American Chemical Society* (vol. 126), No. 9, pp. 2923-2938.

[105] Atkinson, R. A. and Kieffer, B. (2004): The role of protein motions in molecular recognition: insights from heteronuclear NMR relaxation measurements, *Progress in Nuclear Magnetic Resonance Spectroscopy* (vol. 44), No. 3-4, pp. 141-187.

[106] Massi, F.; Grey, M. J. and Palmer, A. G. (2005): Microsecond timescale backbone conformational dynamics in ubiquitin studied with NMR R-1 $\rho$  relaxation experiments, *Protein Science* (vol. 14), No. 3, pp. 735-742.

[107] Bruschweiler, R. (2003): New approaches to the dynamic interpretation and prediction of NMR relaxation data from proteins, *Current Opinion in Structural Biology* (vol. 13), No. 2, pp. 175-183.

[108] Pellecchia, M.; Sem, D. S. and Wuthrich, K. (2002): NMR in drug discovery, *Nature Reviews Drug Discovery* (vol. 1), No. 3, pp. 211-219.

[109] Akke, M. and Palmer, A. G. (1996): Monitoring macromolecular motions on microsecond to millisecond time scales by R(1) $\rho$ -R(1) constant relaxation time NMR spectroscopy, *Journal of the American Chemical Society* (vol. 118), No. 4, pp. 911-912.

[110] Lipari, G. and Szabo, A. (1982): Model-Free Approach to the Interpretation of Nuclear Magnetic-Resonance Relaxation in Macromolecules .1. Theory and Range of Validity, *Journal of the American Chemical Society* (vol. 104), No. 17, pp. 4546-4559.

[111] Williams, J. C. and McDermott, A. E. (1993): Cis-Trans Energetics in Urea and Acetamide Studied by Deuterium Nmr, *Journal of Physical Chemistry* (vol. 97), No. 47, pp. 12393-12398.

[112] Wittebort, R. J.; Olejniczak, E. T. and Griffin, R. G. (1987): Analysis of Deuterium Nuclear-Magnetic-Resonance Line-Shapes in Anisotropic Media, *Journal of Chemical Physics* (vol. 86), No. 10, pp. 5411-5420.

[113] Spiess, H. W. (1980): Deuteron Spin Alignment - a Probe for Studying Ultraslow Motions in Solids and Solid Polymers, *Journal of Chemical Physics* (vol. 72), No. 12, pp. 6755-6762.

[114] Cole, H. B. R. and Torchia, D. A. (1991): An Nmr-Study of the Backbone Dynamics of Staphylococcal Nuclease in the Crystalline State, *Chemical Physics* (vol. 158), No. 2-3, pp. 271-281.

[115] Mack, J. W.; Usha, M. G.; Long, J.; Griffin, R. G. and Wittebort, R. J. (2000): Backbone motions in a crystalline protein from field-dependent H-2-NMR relaxation and line-shape analysis, *Biopolymers* (vol. 53), No. 1, pp. 9-18.

[116] Igumenova, T. I.; McDermott, A. E.; Zilm, K. W.; Martin, R. W.; Paulson, E. K. and Wand, A. J. (2004): Assignments of carbon NMR resonances for microcrystalline ubiquitin, *Journal of the American Chemical Society* (vol. 126), No. 21, pp. 6720-6727.

[117] Igumenova, T. I.; Wand, A. J. and McDermott, A. E. (2004): Assignment of the backbone resonances for microcrystalline ubiquitin, *Journal of the American Chemical Society* (vol. 126), No. 16, pp. 5323-5331.

[118] Bockmann, A.; Lange, A.; Galinier, A.; Luca, S.; Giraud, N.; Juy, M.; Heise, H.; Montserret, R.; Penin, F. and Baldus, M. (2003): Solid state NMR sequential resonance assignments and conformational analysis of the 2 x 10.4 kDa dimeric form of the *Bacillus subtilis* protein Crh, *Journal of Biomolecular Nmr* (vol. 27), No. 4, pp. 323-339.

[119] van Rossum, B. J.; Castellani, F.; Rehbein, K.; Pauli, J. and Oschkinat, H. (2001): Assignment of the nonexchanging protons of the alpha-spectrin SH3 domain by two- and three-dimensional H-1-C-13 solid-state magic-angle spinning NMR and

comparison of solution and solid-state proton chemical shifts, *Chembiochem* (vol. 2), No. 12, pp. 906-914.

[120] Pauli, J.; Baldus, M.; van Rossum, B.; de Groot, H. and Oschkinat, H. (2001): Backbone and side-chain C-13 and N-15 signal assignments of the alpha-spectrin SH3 domain by magic angle spinning solid-state NMR at 17.6 tesla, *Chembiochem* (vol. 2), No. 4, pp. 272-281.

[121] McDermott, A.; Polenova, T.; Bockmann, A.; Zilm, K. W.; Paulsen, E. K.; Martin, R. W. and Montelione, G. T. (2000): Partial NMR assignments for uniformly (C-13, N-15)-enriched BPTI in the solid state, *Journal of Biomolecular Nmr* (vol. 16), No. 3, pp. 209-219.

[122] Giraud, N.; Blackledge, M.; Bockmann, A. and Emsley, L. (2007): The influence of nitrogen-15 proton-driven spin diffusion on the measurement of nitrogen-15 longitudinal relaxation times, *Journal of Magnetic Resonance* (vol. 184), No. 1, pp. 51-61.

[123] Hologne, M.; Chen, Z. J. and Reif, B. (2006): Characterization of dynamic processes using deuterium in uniformly H-2, C-13, N-15 enriched peptides by MAS solid-state NMR, *Journal of Magnetic Resonance* (vol. 179), No. 1, pp. 20-28.

[124] Lorieau, J. L. and McDermott, A. E. (2006): Conformational flexibility of a microcrystalline globular protein: Order parameters by solid-state NMR spectroscopy, *Journal of the American Chemical Society* (vol. 128), No. 35, pp. 11505-11512.

[125] Lorieau, J. and McDermott, A. E. (2006): Order parameters based on (CH)-C-13-H-1, (CH2)-C-13-H-1 and (CH3)-C-13-H-1 heteronuclear dipolar powder patterns: a comparison of MAS-based solid-state NMR sequences, *Magnetic Resonance in Chemistry* (vol. 44), No. 3, pp. 334-347.

[126] Clore, G. M.; Szabo, A.; Bax, A.; Kay, L. E.; Driscoll, P. C. and Gronenborn, A. M. (1990): Deviations from the Simple 2-Parameter Model-Free Approach to the Interpretation of N-15 Nuclear Magnetic-Relaxation of Proteins, *Journal of the American Chemical Society* (vol. 112), No. 12, pp. 4989-4991.

[127] Redfield, A. G. (1957): On the Theory of Relaxation Processes, *Ibm Journal of Research and Development* (vol. 1), No. 1, pp. 19-31.

[128] Torchia, D. A. and Szabo, A. (1982): Spin-Lattice Relaxation in Solids, *Journal of Magnetic Resonance* (vol. 49), No. 1, pp. 107-121.



[129] Wylie, B. J.; Franks, W. T. and Rienstra, C. M. (2006): Determinations of N-15 chemical shift anisotropy magnitudes in a uniformly N-15, C-13-labeled microcrystalline protein by three-dimensional magic-angle spinning nuclear magnetic resonance spectroscopy, *Journal of Physical Chemistry B* (vol. 110), No. 22, pp. 10926-10936.

[130] Grzesiek, S. and Bax, A. (1993): Measurement of Amide Proton-Exchange Rates and Noes with Water in C-13/N-15-Enriched Calcineurin-B, *Journal of Biomolecular Nmr* (vol. 3), No. 6, pp. 627-638.

[131] Skrynnikov, N. R. and Ernst, R. R. (1999): Detection of intermolecular chemical exchange through decorrelation of two-spin order, *Journal of Magnetic Resonance* (vol. 137), No. 1, pp. 276-280.

[132] Iwahara, J.; Jung, Y. S. and Clore, G. M. (2007): Heteronuclear NMR spectroscopy for lysine NH<sub>3</sub> groups in proteins: Unique effect of water exchange on N-15 transverse relaxation, *Journal of the American Chemical Society* (vol. 129), No. 10, pp. 2971-2980.

[133] Bruschweiler, R. and Wright, P. E. (1994): Nmr Order Parameters of Biomolecules - a New Analytical Representation and Application to the Gaussian Axial Fluctuation Model, *Journal of the American Chemical Society* (vol. 116), No. 18, pp. 8426-8427.

[134] Woessner, D. E. (1962): Nuclear Spin Relaxation in Ellipsoids Undergoing Rotational Brownian Motion, *Journal of Chemical Physics* (vol. 37), No. 3, pp. 647-&.

[135] Woessner, D. E. (1962): Spin Relaxation Processes in a 2-Prton System Undergoing Anisotropic Reorientation, *Journal of Chemical Physics* (vol. 36), No. 1, pp. 1-&.

[136] Phan, V.C.; Fry, E. A.; Crum, L. A.; Paulson, E. K.; Morcombe, C.R.; Hans, J.; Byrd, R. A. and Zilm, K. W. (2007): Spin Exchange and Cross Relaxation in the Solid State NMR of Proteins, ENC proceedings.

[137] Krushelnitsky, A.; Brauniger, T. and Reichert, D. (2006): N-15 spin diffusion rate in solid-state NMR of totally enriched proteins: The magic angle spinning frequency effect, *Journal of Magnetic Resonance* (vol. 182), No. 2, pp. 339-342.

[138] Palmer, A. G.; Williams, J. and McDermott, A. (1996): Nuclear magnetic resonance studies of biopolymer dynamics, *Journal of Physical Chemistry* (vol. 100), No. 31, pp. 13293-13310.

[139] Fushman, D.; Tjandra, N. and Cowburn, D. (1999): An approach to direct determination of protein dynamics from N-15 NMR relaxation at multiple fields, independent of variable N-15 chemical shift anisotropy and chemical exchange contributions, *Journal of the American Chemical Society* (vol. 121), No. 37, pp. 8577-8582.

[140] Bouvignies, G.; Bernado, P.; Meier, S.; Cho, K.; Grzesiek, S.; Bruschweiler, R. and Blackledge, M. (2005): Identification of slow correlated motions in proteins using residual dipolar and hydrogen-bond scalar couplings, *Proceedings of the National Academy of Sciences of the United States of America* (vol. 102), No. 39, pp. 13885-13890.

[141] Lakomek, N.A.; Fares, C.; Walter, K.; Becker, S.; Gulich, R.; Egger, D.; Carlomagno, T.; Meiler, J.; Lunkenheimer, P. and Griesinger, C. (2007): Are there concerted backbone motions in ubiquitin at 110 ns?, *ENC proceedings*.

[142] Zhou, Y. F.; Morais-Cabral, J. H.; Kaufman, A. and MacKinnon, R. (2001): Chemistry of ion coordination and hydration revealed by a K<sup>+</sup> channel-Fab complex at 2.0 angstrom resolution, *Nature* (vol. 414), No. 6859, pp. 43-48.

[143] Murata, K.; Mitsuoka, K.; Hirai, T.; Walz, T.; Agre, P.; Heymann, J. B.; Engel, A. and Fujiyoshi, Y. (2000): Structural determinants of water permeation through aquaporin-1, *Nature* (vol. 407), No. 6804, pp. 599-605.

[144] Saparov, S. M. and Pohl, P. (2004): Beyond the diffusion limit: Water flow through the empty bacterial potassium channel, *Proceedings of the National Academy of Sciences of the United States of America* (vol. 101), No. 14, pp. 4805-4809.

[145] Harbison, G. S.; Roberts, J. E.; Herzfeld, J. and Griffin, R. G. (1988): Solid-State Nmr Detection of Proton-Exchange between the Bacteriorhodopsin Schiff-Base and Bulk Water, *Journal of the American Chemical Society* (vol. 110), No. 21, pp. 7221-7223.

[146] Clore, G. M.; Bax, A.; Wingfield, P. T. and Gronenborn, A. M. (1990): Identification and Localization of Bound Internal Water in the Solution Structure of Interleukin-1-Beta by Heteronuclear 3-Dimensional H-1 Rotating-Frame Overhauser N-

15-H-1 Multiple Quantum Coherence Nmr-Spectroscopy, *Biochemistry* (vol. 29), No. 24, pp. 5671-5676.

[147] Otting, G. (1997): NMR studies of water bound to biological molecules, *Progress in Nuclear Magnetic Resonance Spectroscopy* (vol. 31), pp. 259-285.

[148] Otting, G. and Wuthrich, K. (1989): Studies of Protein Hydration in Aqueous-Solution by Direct Nmr Observation of Individual Protein-Bound Water-Molecules, *Journal of the American Chemical Society* (vol. 111), No. 5, pp. 1871-1875.

[149] Noack, F. (1986): Nmr Field-Cycling Spectroscopy - Principles and Applications, *Progress in Nuclear Magnetic Resonance Spectroscopy* (vol. 18), pp. 171-276.

[150] Gottschalk, M.; Dencher, N. A. and Halle, B. (2001): Microsecond exchange of internal water molecules in bacteriorhodopsin, *Journal of Molecular Biology* (vol. 311), No. 3, pp. 605-621.

[151] Halle, B. and Denisov, V. P. (2001): Magnetic relaxation dispersion studies of biomolecular solutions, *Nuclear Magnetic Resonance of Biological Macromolecules, Pt A* (vol. 338) pp. 178-201.

[152] Denisov, V. P.; Peters, J.; Horlein, H. D. and Halle, B. (1996): Using buried water molecules to explore the energy landscape of proteins, *Nature Structural Biology* (vol. 3), No. 6, pp. 505-509.

[153] Bockmann, A.; Juy, M.; Bettler, E.; Emsley, L.; Galinier, A.; Penin, F. and Lesage, A. (2005): Water-protein hydrogen exchange in the micro-crystalline protein Crh as observed by solid state NMR spectroscopy, *Journal of Biomolecular Nmr* (vol. 32), No. 3, pp. 195-207.

[154] Lesage, A. and Bockmann, A. (2003): Water-protein interactions in microcrystalline Crh measured by H-1-C-13 solid-state NMR spectroscopy, *Journal of the American Chemical Society* (vol. 125), No. 44, pp. 13336-13337.

[155] Lesage, A.; Emsley, L.; Penin, F. and Bockmann, A. (2006): Investigation of dipolar-mediated water-protein interactions in microcrystalline Crh by solid-state NMR spectroscopy, *Journal of the American Chemical Society* (vol. 128), No. 25, pp. 8246-8255.

[156] Giraud, N.; Sein, J.; Pintacuda, G.; Bockmann, A.; Lesage, A.; Blackledge, M. and Emsley, L. (2006): Observation of heteronuclear overhauser effects confirms the

N-15-H-1 dipolar relaxation mechanism in a crystalline protein, *Journal of the American Chemical Society* (vol. 128), No. 38, pp. 12398-12399.

[157] Lesage, A. and Emsley, L. (2001): Through-bond heteronuclear single-quantum correlation spectroscopy in solid-state NMR, and comparison to other through-bond and through-space experiments, *Journal of Magnetic Resonance* (vol. 148), No. 2, pp. 449-454.

[158] Voet, D. and Voet, J.G. (1995): *Biochemistry*, 2nd edition, John Wiley and Sons, New York.

[159] Levitt, M. H.; Raleigh, D. P.; Creuzet, F. and Griffin, R. G. (1990): Theory and Simulations of Homonuclear Spin Pair Systems in Rotating Solids, *Journal of Chemical Physics* (vol. 92), No. 11, pp. 6347-6364.

[160] Cai, S.; Stevens, S. Y.; Budor, A. P. and Zuiderweg, E. R. P. (2003): Solvent interaction of a Hsp70 chaperone substrate-binding domain investigated with water-NOE NMR experiments, *Biochemistry* (vol. 42), No. 38, pp. 11100-11108.

[161] Rosen, M. K.; Gardner, K. H.; Willis, R. C.; Parris, W. E.; Pawson, T. and Kay, L. E. (1996): Selective methyl group protonation of perdeuterated proteins, *Journal of Molecular Biology* (vol. 263), No. 5, pp. 627-636.

[162] Gemmecker, G.; Jahnke, W. and Kessler, H. (1993): Measurement of Fast Proton-Exchange Rates in Isotopically Labeled Compounds, *Journal of the American Chemical Society* (vol. 115), No. 24, pp. 11620-11621.

[163] Reif, B.; van, B.J. Rossum; Castellani, F.; Rehbein, K.; Diehl, A. and Oeschkinat, H. (2003): Characterization of H-1-H-1 distances in a uniformly H-2,N-15-labeled SH3 domain by MAS solid-state NMR spectroscopy, *J. Am. Chem. Soc.* (vol. 125), pp. 1488-1489.

[164] McDermott, A.; Polenova, T.; Bockmann, A.; Zilm, K.W.; Paulsen, E.K.; R.W.Martin and Montelione, G.T. (2000): Partial NMR assignments for uniformly (C-13, N-15)-enriched BPTI in the solid state, *J. Biomol. NMR* (vol. 16), pp. 209-219.

[165] Cavanagh, J.; Fairbrother, W.; Palmer, A.G. and Skelton, N.J. (1996): *Protein NMR Spectroscopy: Principles and Practice*, Academic Press, New York, pp. 480-481.

[166] Sattler, M.; Schleucher, J. and Griesinger, C. (1999): Heteronuclear multidimensional NMR experiments for the structure determination of proteins in solution employing pulsed field gradients, *Prog. NMR Spect.* (vol. 34), pp. 93-158.

[167] LeMaster, D.M. and Kushlan, D. M. (1996): Dynamical mapping of E-coli thioredoxin via C-13 NMR relaxation analysis, *J. Am. Chem. Soc.* (vol. 139), pp. 9255-9264.

[168] Hong, M. and Jakes, K. (1999): Selective and extensive C-13 labeling of a membrane protein for solid-state NMR investigations, *J. Biomol. NMR* (vol. 14), pp. 71-74.

[169] Brüschweiler, R.; Griesinger, C.; Sorensen, O.W. and Ernst, R.R. (1988): Combined use of hard and soft pulses for omega-1 decoupling in two-dimensional NMR-spectroscopy, *J. Magn. Reson.* (vol. 78), pp. 178-185.

[170] Straus, S.K.; Brems, T. and Ernst, R.R. (1996): Resolution enhancement by homonuclear J decoupling in solid-state MAS NMR, *Chem. Phys. Lett.* (vol. 262), pp. 709-715.

[171] Matsuo, H.; Kupce, E.; Li, H.J. and Wagner, G. (1996): Increased sensitivity in HNCA and HN(CO)CA experiments by selective C-beta decoupling, *J. Magn. Reson. Ser. B* (vol. 113), pp. 91-96.

[172] Matsuo, H.; Kupce, E. and Wagner, G. (1996): Resolution and sensitivity gain in HCCH-TOCSY experiments by homonuclear C-beta decoupling, *J. Magn. Reson. Ser. B* (vol. 113), pp. 190-194.

[173] Bermel, W.; Bertini, I.; Felli, I.C.; Kummerle, R. and Pierattelli, R. (2003): C-13 direct detection experiments on the paramagnetic oxidized monomeric copper, zinc superoxide dismutase, *J. Am. Chem. Soc.* (vol. 125), pp. 16423-16429.

[174] Nielsen, N.C.; Bildsoe, H.; Jakobsen, H.J. and Levitt, M.H. (1994): Double-quantum homonuclear rotary resonance: Efficient dipolar recovery in magic-angle spinning nuclear magnetic resonance, *J. Chem. Phys.* (vol. 101), pp. 1805-1812.

[175] Oas, T.G.; R.G.Griffin and Levitt, M.H. (1988): Rotary resonance recoupling of dipolar interactions in solid-state nuclear magnetic resonance spectroscopy, *J. Chem. Phys.* (vol. 89), pp. 692-695.

[176] McCoy, M.A. and Mueller, L. (1992): Selective shaped pulse decoupling in NMR - homonuclear [C-13] carbonyl decoupling, *J. Am. Chem. Soc.* (vol. 114), pp. 2108-2112.

[177] Morris, G.A. and Freeman, R. (1978): Selective excitation in fourier-transform nuclear magnetic resonance, *J. Magn. Reson.* (vol. 29), pp. 433-462.

[178] Levitt, M.H. and Freeman, R. (1981): Composite pulse decoupling, *J. Magn. Reson.* (vol. 43), pp. 502-507.

[179] Cho, H.; Baum, J. and Pines, A. (1987): Iterative maps with multiple fixed-points for excitation of 2 level systems, *J. Chem. Phys.* (vol. 86), pp. 3089-3106.

[180] Cho, H.M.; Tycko, R.; Pines, A. and Guckenheimer, J. (1986): Iterative maps for bistable excitation of 2-level systems, *Phys. Rev. Letters* (vol. 56), pp. 1905-1908.

[181] Bloch, F. and Siegert, A. (1940): Magnetic Resonance for Nonrotating Fields, *Phys. Rev.* (vol. 57), pp. 522-527.

[182] Paz, M.L. de la; Goldie, K.; Zurdo, J.; Lacroix, E.; Dobson, C.M.; Hoenger, A. and Serrano, L. (2002), *Proc. Nat. Acad. Sci. USA* (vol. 99), pp. 16052-16057.

### *Appendix 1.1. Simulation of $^{15}\text{N}$ peaks ratio.*

SIMPSON input file to simulate of the  $\text{NH}^\alpha/\text{NH}^\beta$  intensity ratio of the nitrogen signal as function of the reduced anisotropy  $\sigma_z$  and the Euler angle  $\beta$  at a MAS frequency of 10 kHz (the asymmetry is kept constant at  $\eta=0.2$ ). In the simulation, an external magnetic field of 14.1 T is assumed, corresponding to a  $^1\text{H}$  Larmor frequency of 600 MHz and  $^{15}\text{N}$ - $^1\text{H}$  dipolar coupling is 10828 Hz. Results are presented in Figure 3.3.3 A.

```
spinsys {
channels 15N 1H
nuclei 15N 1H
dipole 1 2 10828.1 0 0 0
jcoupling 1 2 -95 0 0 0 0 0
shift 2 1p 7.7p 0.65 40 0 0
shift 1 100 90p 0.2 0 0 0
}
par {
spin_rate 10000
gamma_angles 80
sw 100000
crystal_file zcw986
np 40000
start_operator I1x+I2x
detect_operator I1p
proton_frequency 600e6
method gcompute
}
proc pulseseq {} {
global par
maxdt 1
delay 100000
}
proc main {} {
global par
set i 0
set outfile1 [open HNJbeta-CSA10-600-90p.dat w]
puts $outfile1 "here integral inntensity of 15N multiplets at 10kHz spinning frequency
HNJbeta-CSA10-600.in "
puts $outfile1 " beta changes from 0 to 30, step 2 "
puts $outfile1 "CSA changes from 80 to 120, step 2 "
puts $outfile1 "integration 100-297.5 and -97.5-100 full left and right"
puts $outfile1 "integration 147.5-297.5 and -97.5-52.5 half left and right"
```

```
puts $outfile1 "ratio fullleft/fullright, ratio halfleft/halfright, check ratiofull/ratiohalf"
puts $outfile1 "beta CSA fullleft fullright halfleft halfright ratiofullleft/right
ratiohalfleft/right checkfull/half "
```

```
set outfile2 [open HNbeta-CSA10-600s-90p.dat w]
puts $outfile2 "here integral inntensity of 15N multiplets at 10kHz spinning frequency
HNbeta-CSA10-600.in "
puts $outfile2 " beta changes from 0 to 30, step 2 "
puts $outfile2 "CSA changes from 80 to 120, step 2 "
puts $outfile2 "integration 100-297.5 and -97.5-100 full left and right"
puts $outfile2 "integration 147.5-297.5 and -97.5-52.5 half left and right"
puts $outfile2 "ratio halfleft/halfright "
puts $outfile2 "CSA beta"
```

```
set name [ list HNbeta-CSA000-80 HNbeta-CSA002-80 HNbeta-CSA004-80 HNbeta-
CSA006-80 HNbeta-CSA008-80 HNbeta-CSA010-80 HNbeta-CSA012-80 \ HNbeta-
CSA014-80 HNbeta-CSA016-80 HNbeta-CSA018-80 HNbeta-CSA020-80 HNbeta-
CSA022-80 HNbeta-CSA024-80 HNbeta-CSA026-80 \ HNbeta-CSA028-80 HNbeta-
CSA030-80 \HNbeta-CSA000-82 HNbeta-CSA002-82 \
```

```
/* cycled names for output files */
```

```
HNbeta-CSA000-118 HNbeta-CSA002-118 HNbeta-CSA004-118 HNbeta-CSA006-118
HNbeta-CSA008-118 HNbeta-CSA010-118 HNbeta-CSA012-118 \ HNbeta-CSA014-118
HNbeta-CSA016-118 HNbeta-CSA018-118 HNbeta-CSA020-118 HNbeta-CSA022-118
HNbeta-CSA024-118 HNbeta-CSA026-118 \ HNbeta-CSA028-118 HNbeta-CSA030-118
\ HNbeta-CSA000-120 HNbeta-CSA002-120 HNbeta-CSA004-120 HNbeta-CSA006-120
HNbeta-CSA008-120 HNbeta-CSA010-120 HNbeta-CSA012-120 \HNbeta-CSA014-120
HNbeta-CSA016-120 HNbeta-CSA018-120 HNbeta-CSA020-120 HNbeta-CSA022-120
HNbeta-CSA024-120 HNbeta-CSA026-120 \ HNbeta-CSA028-120 HNbeta-CSA030-120
]
```

```
for {set delta 80} { $delta<=120 } { incr delta 2 } {
for {set bet 0} { $bet<=30 } { incr bet 2 } {
set f [fsimpson [ list [list dipole_1_2_beta $bet] [list shift_1_aniso [expr $Nfreq*$delta ] ]
]]
```

```
fphase $f -scale 0.2
```

```
faddlb $f 10 0
```

```
fzerofill $f 1048576
```

```
fft $f
```

```
set [list ar1 ] [fint $f [list [list 100. 297.5] [list -97.5 100. ] ] ]
```

```
set [list ar3 ] [fint $f [list [list 147.5 297.5] [list -97.5 52.5 ] ] ]
```

```
puts " delta= $delta beta= $bet "
```

```
puts "$ar1"
```

```
puts "$ar3"
```

```
puts $outfile1 "$delta $bet $ar1 $ar3 [expr [lindex $ar1 0]/[lindex $ar1 1] ] [expr [lindex
$ar3 0]/[lindex $ar3 1] ] [ expr [lindex $ar1 0]/[lindex $ar1 1]/ [lindex $ar3 0]*[lindex
$ar3 1] ]"
```

```
puts $outfile2 " $delta $bet [expr [lindex $ar3 0]/[lindex $ar3 1] ] "
```

```
fextract $f 297.5 -97.5
```



```
fsave $f [lindex $name $i]
funload $f
incr i
}
}
}
```

## *Appendix 2.1. Simulation of $^{15}\text{N}$ line width.*

Here we give SIMPSON input file to simulate data presented in Figure 4.3.1. File gives  $^{15}\text{N}$  line width in net of interacting protons and can be modified to get spectrum without mutual proton-proton interaction.

```
spinsys {
  channels 15N 1H
  nuclei 15N 1H 1H 1H 1H
  dipole 1 2 10828.1 0 10 0
  jcoupling 1 2 -95 0 0 0 0
  shift 2 1p 7.7p 0.65 40 0 0
  shift 1 100 100p 0.2 0 0 0
  shift 3 0p 7.7p 0.65 20 10 50
  shift 4 2p 7.7p 0.65 4 23 58
  shift 5 3p 7.7p 0.65 88 71 31
  dipole 2 3 -1000 12 210 33
  dipole 2 4 -1200 72 12 210
  dipole 2 5 -800 23 44 71
  dipole 3 4 -800 17 0 56
  dipole 3 5 -200 54 56 88
  dipole 4 5 -1111 37 88 59
}
par {
  spin_rate 10000
  gamma_angles 40
  sw 100000
  crystal_file zcw986
  np 36000
  start_operator I1x+I2x
  detect_operator I1p
  proton_frequency 600e6
  method gcompute
}
proc pulseseq {} {
  global par
  maxdt 1
  delay 100000
}
proc main {} {
  global par
  set f [fsimpson ]
  fphase $f -scale [ expr 0.2*96/100]
```

```
faddlb $f 10 0
fzerofill $f 1048576
fft $f
fextract $f 297.5 -97.5
fsave $f Lw3-1H-10kHz.spe
funload $f
}
```

## Appendix 2.2 Experimental values for $T_1$ , $T_2$ and $\eta$ for SH3.

Relaxation data, presented in Chapter 4 are listed below:

Here are  $T_1$ (s) measured at 600 MHz and 900MHz, the results of monoexponential double parametrical fit are given below:

res600 - residue name for 600 MHz results

T1m600 -  $T_1$  (s) values obtained on 600 MHz instrument

rmsT1m600 - fitting error for 600 MHz data

res900 - residue name for 900 MHz results

T1m900 -  $T_1$  (s) values obtained on 900 MHz instrument

rmsT1m900 - fitting error for 900 MHz data

res600	T1m600	rmsT1m600	res900	T1m900	rmsT1m900
L8	4.65122	0.55357	L8	5.36274	0.75442
V9	34.49652	4.4205	V9	49.35347	3.38694
L10	20.24588	7.64212	L10	23.93327	5.10801
A11	28.53027	6.05962	A11	18.47348	3.93767
L12	19.78929	4.08874	L12	43.53311	13.23298
Y13	49.31829	4.26401	Y13	41.39503	5.78818
D14	15.5703	3.74983	D14	19.35336	1.9613
Y15	29.9036	1.36573	Y15	37.5575	2.52793
Q16	15.35992	1.70167	Q16	19.7283	1.94812
E17	17.86445	2.32283	E17	32.21341	4.04229
K18	34.65028	2.00623	K18	38.9366	4.16906
S19	11.02079	0.86132	S19	12.74473	0.56572
R21	1.88915	0.03026	R21	1.87723	0.04017
V23	18.71523	0.27578	V23	14.61347	2.59048
T24	10.3015	0.40404	T24	17.23294	1.24016

M25	30.42302	3.06346	M25	32.89406	2.4795
K26	30.68446	2.5618	K26	33.59218	3.12812
K27	16.21695	3.43673	K27	22.5766	2.51842
G28	27.70589	1.12555	G28	34.47533	2.85962
I30	18.7838	1.31456	I30	28.05375	2.06242
L31	24.90612	3.37559	L31	47.74123	11.12265
T32	5.83826	1.09314	T32	9.85698	1.30392
L33	39.81106	3.81586	L33	47.66893	7.48523
L34	7.40778	0.82943	L34	11.08549	0.14222
N35	36.70529	2.11795	N35	54.62919	10.2861
S36	10.23215	4.41405	S36	1.23309	0.72999
K39	7.85471	0.55624	K39	12.8825	0.76761
D40	17.72376	8.07643	D40	12.5363	4.01969
W41	16.48384	2.52876	W41	20.75727	4.54966
K43	21.94894	1.96619	K43	25.58464	2.42105
V44	14.15855	3.27695	V44	23.6864	4.38537
E45	5.17612	0.42789	E45	7.56929	0.94315
V46	23.96791	0.24613	V46	23.91198	0.66379
R49	18.58777	3.30262	R49	25.92933	3.16032
Q50	6.07359	0.17378	Q50	9.7956	0.30869
G51	17.12147	1.71814	G51	29.71033	3.11572
F52	26.64148	1.69641	F52	39.14954	4.27127
V53	45.35447	2.09126	V53	60.19296	18.01921
A55	27.52659	2.64574	A55	41.01593	2.11826
A56	15.43669	6.45111	A56	20.49128	3.37275
Y57	11.73353	4.93633	Y57	27.69486	4.67284
V58	37.32621	5.33921	V58	53.34332	8.45611
K59	17.27467	3.17124	K59	34.19614	8.31288
K60	5.37541	0.48357	K60	9.30321	0.51437
L61	6.35323	0.34614	L61	7.61761	0.86798
D62	1.32981	0.11112	D62	1.90392	0.1198

### Tabellenbeschriftung 6.3.1

Here are  $T_2$  values measured at 600 MHz, the results of monoexponential double parametrical fit are given below:

Fit  $Y=A1*\exp(-t/T2)$

residue - residue name: index “u”–upfield component and index “d”–downfield component.

$T_2$  - fitted  $T_2$  values, given in ms

rms $T_2$  - fitting error

residue	$T_2$	rms $T_2$
L8u	16.43704	2.70341
L8d	39.19565	5.96228
residue	$T_2$	rms $T_2$
V9u	58.23465	6.04686
V9d	63.64111	11.1999
L10u	50.20194	11.62402
L10d	51.08688	13.27561
A11u	50.79323	8.6638
A11d	42.82496	4.89224
Y13u	85.03502	6.51391
Y13d	109.91327	10.7556
D14u	123.10333	16.08263
D14d	129.67558	19.11829
Y15u	120.23911	8.88771
Y15d	147.92812	18.4476
Q16u	106.74434	11.94045
Q16d	160.65726	19.82059
E17u	69.37638	11.3982
E17d	101.74927	20.59008
S19u	74.91788	6.04814

S19d	109.52491	10.55787
R21u	32.79999	5.99448
R21d	38.00433	6.1894
E22u	91.44308	11.21602
E22d	116.37239	12.85235
T24u	51.77266	10.19356
T24d	92.20754	9.02342
M25u	124.27129	7.38347
M25d	127.03479	11.66648
K26u	75.82919	8.72209
K26d	159.12953	23.8421
K27u	123.5899	21.02955
K27d	160.71246	29.60936
G28u	235.29155	128.00644
G28d	177.53701	69.53937
I30u	43.97566	3.65029
I30d	56.59404	8.23255
L31u	52.18956	10.37006
L31d	51.1269	6.38497
T32u	40.70137	2.87055
T32d	66.78183	8.08979

L33u	253.92497	62.14668
L33d	129.4832	47.54509
L34u	19.12764	3.1863
L34d	82.20574	12.432
S36u	31.73364	3.50604
S36d	47.41241	8.45216
T37u	54.01046	9.55827
T37d	52.85019	5.1266
D40u	62.71761	7.22669
D40d	65.05281	3.62276
W41u	71.09831	8.07984
W41d	132.48731	25.29049
K43u	31.68615	5.56534
K43d	39.50518	7.19582
V44u	46.57035	4.27749
V44d	36.85981	5.64242
E45u	27.27114	1.86436
E45d	67.57842	3.85929
V46u	35.9953	4.97092
V46d	66.76452	10.82971
R49u	58.70095	5.51544
R49d	76.11557	5.64984

Q50u	41.8958	3.71217
Q50d	109.03036	9.45569
G51u	99.88773	15.65227
G51d	114.48702	18.23962
F52u	59.33875	8.40816
F52d	103.93138	15.4367
V53u	55.41258	7.47038
V53d	57.35837	13.29579
A55u	47.22755	9.0972
A55d	43.94305	9.44126
A56u	155.22534	44.65558
A56d	472.23413	107.97382
Y57u	71.23618	6.0909
Y57d	188.40539	42.19341
V58u	118.5932	11.39635
V58d	107.81716	15.96831
K59u	73.34286	5.91156
K59d	91.47597	17.08946
L61u	46.8153	4.7525
L61d	110.9554	16.1608
D62u	7.65634	0.87838
D62d	94.29044	14.10393

Tabellenbeschriftung 6.3.2

Here are differential relaxation rates values measured at 600 MHz, the results of monoexponential double parametrical fit are given below:

Residue–residue

Eta–differential relaxation rate, given in Hz

RmsEta–fitting error

Residue	Eta	rmsEta
L8	17.66259	6.94351

V9	0.59	0.555
L10	0.615	0.505

A11	-2.475	0.52
Y13	1.16	0.205
D14	0.44	0.6
Y15	0.49	0.425
Q16	1.63	0.585
E17	2.8	0.595
S19	2.72	0.37
R21	12.135	2.235
E22	1.79	0.445
T24	8.515	0.895
M25	0.415	0.39
K26	2.595	0.25
K27	0.19	0.9
G28	0.2	1.55
I30	2.8	0.58
L31	-0.165	1.155
T32	5.185	0.655
L33	-2.16	1.565
Resisdue	Eta	rmsEta
L34	22.565	1.83

S36	3.53	1.2
T37	0.185	0.59
D40	2.915	0.88
W41	2.625	0.67
K43	2.875	0.54
V44	0.015	0.605
E45	10.64	1.035
V46	2.425	1.115
R49	1.64	0.345
Q50	6.745	0.545
G51	0.875	0.415
F52	6.705	1.25
V53	1.28	0.575
A55	-0.32	0.57
A56	1.715	0.575
Y57	4.37	0.37
V58	-0.405	0.545
K59	1.3	0.64
L61	6.515	0.645
D62	60	8.28

Tabellenbeschriftung 6.3.3



### *Appendix 2.3 SIMPSON input file to extract $^{15}\text{N}$ - $^1\text{H}$ dipolar coupling values.*

The input file below was used to extract dipolar couplings, which were discussed in Chapter 4.

```
spinsys {
  channels 1H 15N
  nuclei 1H 15N
  dipole 1 2 10828 0 20 0
  shift 1 0 0p 0.65 17 84 12
  shift 2 0 170p 0.2 0 0 0
  jcoupling 1 2 -93 0 0 0 0 0
}
par {
  spin_rate 25000
  gamma_angles 20
  sw 250000
  crystal_file rep678
  np 199
  start_operator I1x
  detect_operator I2p
  proton_frequency 600e6
  method gcompute
  variable rfn 39000
}
proc pulseseq {} {
  global par mn g
  maxdt 0.5
  reset
  pulse 1e6 64000 0 $par(rfn) 0
}
proc minuit {} {
  global par mn g k
  set k [expr $k+1]
  set f [fsimpson [ list [list dipole_1_2_aniso $mn(dipole)] ] ]
  set scale [ expr 100000*$mn(sc)]
  set lb $mn(lb)
  fphase $f -scale $scale
  faddlb $f $lb 0
  fsave $f mnHdd50Q50f3.fid
  puts "k= $k"
  set rms [frms $f $g -re]
  funload $f
  return $rms
}
proc main {} {
  global par mn g k
  set k 1
  set g [fload "cp50Q50-30f3.fid"]
  set expfidnp [fget $g -np]
  puts "np= $expfidnp"
```

```
# mnpar name val step [min max]
mnpar dipole 11000 2000 9000 12000
mnpar lb 90 200 0 250
mnpar sc 14 4 10 18

mnminimize
minuit
}
```

#### *Appendix 2.4. Fitting results for $^{15}\text{N}$ - $^1\text{H}$ dipolar coupling values.*

The results were obtained by employing SIMPSON package, the input file is given in Appendix 2.3.

Notations:

A–residue number

Res–residue

Hdd– $^{15}\text{N}$ - $^1\text{H}$  dipolar coupling

Lb–line broadening, according to SIMPSON standard. Simple exponential damping of the time domain data

Scale–scale.

Itter–number of iterations

Rms–error given by SIMPSON minimization routine.

Res	Hdd	Lb	Scale	Itter	rms
8 L8	10369	152.7	8.91	208	0.948
9 V9	10994	202.6	11.76	377	0.632
10 L10	11060.4	180.2	16.4	286	0.985
11 A11	10974	36.86	9.92	184	1.32
12 L12	10980	162.2	9.95	452	1.1
13 Y13	10987	136.3	11.78	237	0.7
14 D14	10607	168.2	13.68	817	0.532
15 Y15	11038	187.1	13.3	216	1.49
16 Q16	10585	148.72	15.1	498	0.856
17 E17	11028	111.38	15.84	223	0.998
18 K18	10974.2	146.9	17.48	396	0.787
19 S19	10713	227.2	13.9	284	1.18
21 R21	10834	125	5.93	390	1.37
23 V23	10797	250	13.81	382	0.637
24 T24	10122	181.5	11.62	378	0.932
25 M25	10990	147.8	13.6	303	0.899
26 K26	10857	153.4	12.1	452	0.852

27 K27 10962 171.9 11.02 260 0.927
28 G28 11178 228 11.28 668 1.25
A Res Hdd Lb Scale Itter rms
A Res Hdd Lb Scale Itter rms
30 I30 10901 102.97 9.47 459 0.966
31 L31 10917 207.6 10.55 337 1.06
32 T32 10512 222.3 10.91 1403 1.16
33 L33 10935 89 9.02 289 0.993
34 L34 10951.3 121.5 9.053 455 1.84
35 N35 10946 182.8 13.1 320 0.725
39 K39 10696 127.8 11.77 670 0.486
41 W41 10915 111.6 10.89 286 0.972
42 W42 10934 135 10.4 645 0.56
43 K43 11075 139.1 9.93 283 1.22
44 V44 11100 153.2 15.2 501 1.02
45 E45 10472 160.03 8.55 318 1.28
46 V46 10999 158.4 10.8 328 1.22
49 R49 10978 149.9 11.34 366 1.09
50 Q50 10391.4 250 14.61 1368 0.74
51 G51 10836 207.3 10.57 756 0.631
52 F52 10956.3 158 9.88 878 0.905
53 V53 11116 148.3 12.63 257 0.953
55 A55 10973 129.6 12.1 478 0.637
56 A56 10908 175.2 12 379 1.06
57 Y57 11004 149.3 7.47 254 1.33
58 V58 11073 140.7 11.2 372 1.01
59 K59 11051 148.6 10.63 691 0.914
60 K60 10762 216.2 15.7 359 0.905
61 L61 10521 218.2 12.5 556 0.486
62 D62 6513 292.6 12.05 705 1.01

Tabellenbeschriftung 6.3.4

## *Appendix 2.5 C++ code to fit correlation parameters.*

This program was employed for grid search, described in Chapter 4, Equation 4.5.1.

```
char chX;
char *outfile[63][5], *resname[63]; // 6 -experemental , 1 - output

double x2, tf, s2s, ts, wN, wH, wdHN, VdHN, pi, wns, wN900, wH900, wns900, S2f;
double T16exp, Etaexp, T16,eta2, RMST1, RMSetaT1, RMStriple , T19, T19exp;
double tsstep, tsmax, s2sstep, tfstep;
double optTriple[63][10], optetaT1[63][9], optT1[63][9]; // S2s, ts, rms, T1600, eta600, T1900,
tf
double datain[63][5];
int valid[50];
int n, k, m;

double J(double s2s1,double ts1,double w1) ;
double R16(double s2s1,double ts1);
double R19(double s2s1,double ts1);
double eta(double s2s1,double ts1);
void data(void );

void main()
{
    data();
    tsmax=800;
    tsstep=0.2; // nanoseconds
    s2sstep=0.004; // s2slow step
    tfstep=20./1000000./1000000.;
    cout<<1e-9*1000000000.<<"\n"; cout<<"cos= "<<cos(20./180.*pi)<<"\n" ;
    ofstream writeGeneral; writeGeneral.open("_GeneralRelaxSH3all.dat",ios::out); // triple RMS
    file
    if (!writeGeneral) {cout<<"file error";} else {cout<<"\n output file
    "<<"GeneralRelaxSH3.dat"<<"is open \n";};
    writeGeneral<<"Here results for relaxation, all residue and combinations, 1st Triple results,
    2nd T1+T2, 3d T1+T1, tf="<<tf<<"\n";
    writeGeneral<<"ResName ResNum S2general T1600Ex etaExp T1900ex S2slow ts1 tf1(ns)";
    writeGeneral<<" rmsTriple1 T16001 eta1 T19001 S2slow2 ts2 rmsEtaT12 T16002 eta2
    T19002";
```

```

writeGeneral<<" S2slow3 ts3 rmsT1T13 T16003 eta3 T19003"<<"\n";
ofstream writeRes; writeRes.open("_GeneralRelaxSH3Kall.dat",ios::out); // triple RMS file
if (!writeRes) {cout<<"file error";} else {cout<<"\n output file
"<<"GeneralRelaxSH3.dat"<<"is open \n";};
writeRes<<"Here results for relaxation, all residue and combinations, 1st Triple results, 2nd
T1+T2, 3d T1+T1, tf="<<tf<<"\n";
writeRes<<"ResName ResNum S2general T1600Ex etaExp T1900ex S2slow ts1 tf1(ns)";
writeRes<<" rmsTriple1 T16001 eta1 T19001 S2slow2 ts2 rmsEtaT12 T16002 eta2 T19002";
writeRes<<" S2slow3 ts3 rmsT1T13 T16003 eta3 T19003"<<"\n";

```

```

ofstream writeCheck; writeCheck.open("Check.dat",ios::out); // triple RMS file

```

```

for (m=1; m<47; m++)
{
n=valid[m];
optTriple[n][3]=optetaT1[n][3]=optT1[n][3]=1000.;
T16exp=datain[n][2];
T19exp=datain[n][3];
Etaexp=datain[n][1];

```

```

x2=pow(datain[n][4]/VdHN,2); // general order parameter
s2s=x2+0.0002; // slow order parameter
tf=0./1000000./1000000.;
optTriple[n][3]= optetaT1[n][4]= optT1[n][5]=100.;

```

```

for (k=0; k<500; k++)
{
s2s=x2+0.0002; // slow order parameter
cout<<pow(2,5)<<"\n"<<"S2="<<x2<<"\n"<<"s2f=x2/s2s="<<x2/s2s<<" "<<"\n";
cout<<"s2s "<<"ts "<<"RMST1 "<<"RMSEtaT1 "<<"RMSTriple "<<"T1 "<<"eta2 "<<"\n";

```

```

do{
ts=0.2;;
do

```

```

{
T16=1./R16(s2s, ts);
T19=1./R19(s2s, ts);
eta2=eta(s2s, ts);

```

```

RMST1=sqrt(pow( (1./T19-1./T19exp)*T19exp,2)+ pow( (1./T16-
1./T16exp)*T16exp,2)+0*pow( (Etaexp-eta2)/Etaexp,2) );

```

```

RMSetaT1=sqrt(pow(      0*(1./T19-1./T19exp)*T19exp,2)+      pow(      (1./T16-
1./T16exp)*T16exp,2)+pow( (Etaexp-eta2)/Etaexp,2) );
RMStriple=sqrt(pow(      (1./T19-1./T19exp)*T19exp,2)+      pow(      (1./T16-
1./T16exp)*T16exp,2)+pow( (Etaexp-eta2)/Etaexp,2) );

// cout<<tf<<" "<<resname[m]<<s2s<<" "<<" "<<ts<<" "<<RMST1<<" "<<RMSetaT1<<"
"<<RMStriple<<" "<<T16<<" "<<eta2<<" "<<T19<<" "<<"\n";
// writeCheck<<tf<<" "<<resname[m]<<s2s<<" "<<" "<<ts<<" "<<RMST1<<"
"<<RMSetaT1<<" "<<RMStriple<<" "<<T16<<" "<<eta2<<" "<<T19<<" "<<"\n";

if( RMStriple<optTriple[n][3])
{
optTriple[n][1]=s2s; optTriple[n][2]=ts; optTriple[n][3]=RMStriple;
optTriple[n][4]=T16; optTriple[n][5]=eta2; optTriple[n][6]=T19;
optTriple[n][7]=tf;
}

if( RMSetaT1<optetaT1[n][3])
{
optetaT1[n][1]=s2s; optetaT1[n][2]=ts; optetaT1[n][3]=RMSetaT1;
optetaT1[n][4]=T16; optetaT1[n][5]=eta2; optetaT1[n][6]=T19;
optetaT1[n][7]=tf;
}

if( RMST1<optT1[n][3])
{ optT1[n][1]=s2s; optT1[n][2]=ts; optT1[n][3]=RMST1;
optT1[n][4]=T16; optT1[n][5]=eta2; optT1[n][6]=T19;
optT1[n][7]=tf;
}
ts=ts+tsstep;
} while (ts<=tsmax) ;
cout<<"\n";
s2s=s2s+s2sstep;
} while (s2s<=1.) ;

writeGeneral<<resname[n]<<" "<<valid[m]<<" "<<x2<<" "<<datain[n][2]<<"
"<<datain[n][1]<<" "<<datain[n][3]<<" ";
writeGeneral<<optTriple[n][1]<<" "<<optTriple[n][2]<<" "<<1e9*optTriple[n][7]<<"
"<<optTriple[n][3]<<" ";
writeGeneral<<optTriple[n][4]<<" "<<optTriple[n][5]<<" "<<optTriple[n][6]<<" ";
writeGeneral<<optetaT1[n][1]<<" "<<optetaT1[n][2]<<" "<<optetaT1[n][3]<<" ";

```

```

writeGeneral<<optetaT1[n][4]<<"      "<<optetaT1[n][5]<<"      "<<optetaT1[n][6]<<"      ";
writeGeneral<<optT1[n][1]<<" "<<optT1[n][2]<<" "<<optT1[n][3]<<" ";
writeGeneral<<optT1[n][4]<<" "<<optT1[n][5]<<" "<<optT1[n][6]<<" "<<"\n";
tf=tf+tfstep;
}
writeRes<<resname[n]<<" "<<valid[m]<<" "<<x2<<" "<<datain[n][2]<<" "<<datain[n][1]<<"
"<<datain[n][3]<<" ";
writeRes<<optTriple[n][1]<<"      "<<optTriple[n][2]<<"      "<<1e9*optTriple[n][7]<<"
"<<optTriple[n][3]<<" ";
writeRes<<optTriple[n][4]<<" "<<optTriple[n][5]<<" "<<optTriple[n][6]<<" ";
writeRes<<optetaT1[n][1]<<" "<<optetaT1[n][2]<<" "<<optetaT1[n][3]<<" ";
writeRes<<optetaT1[n][4]<<" "<<optetaT1[n][5]<<" "<<optetaT1[n][6]<<" ";
writeRes<<optT1[n][1]<<" "<<optT1[n][2]<<" "<<optT1[n][3]<<" ";
writeRes<<optT1[n][4]<<" "<<optT1[n][5]<<" "<<optT1[n][6]<<" "<<"\n";
}
writeGeneral.close();
writeCheck.close();
writeRes.close();
}
double J(double s2s,double ts,double w)
{
double Jint;
Jint=(1.-x2/s2s)*tf/(1.+w*w*tf*tf)+x2/s2s*(1.-s2s)*ts*1e-9/(1.+w*w*ts*1e-9*ts*1e-9);
Jint=Jint*1.;
return Jint;
}
double R16(double s2s1,double ts1)
{
double R1int ;
R1int=wdHN*wdHN*(J(s2s1, ts1,(wH+wN)) + 3.*J(s2s1, ts1,(wN))+6.*J(s2s1, ts1,(wH-
wN)))/10.+2.*wns*wns*(J(s2s1, ts1,(wN)))/15.;
return R1int;
}
double R19(double s2s1,double ts1)
{
double R1int900 ;
R1int900=wdHN*wdHN/10.*(J(s2s1,      ts1,(wH900+wN900))      +      3.*J(s2s1,
ts1,(wN900))+6.*J(s2s1,      ts1,(wH900-wN900)))      +2.*wns900*wns900/15.*(J(s2s1,
ts1,(wN900)));
return R1int900;
}

```



```

double eta(double s2s1,double ts1)
{
double etaint, P2 ;
P2=1./2.*(3.*cos(20./180.*pi)*cos(20./180.*pi)-1.);
etaint=P2*wns*wdHN*(4.*J(s2s1, ts1, 0.)+3.*J(s2s1, ts1, wN))/15.;
return etaint;
}

void data (void )
{

pi=3.14159;
tf=0./1000000./1000000.;
wdHN=10828.*2.*pi*(pow(1.04/1.02,3));
wN=60.817345*2.*pi*1000000.;
wH=600.1275*2.*pi*1000000.;
wns=wN*170./1000000;
VdHN=10828.*(pow(1.04/1.02,3));

wN900=91.2*2.*pi*1000000.;
wH900=900.19*2.*pi*1000000.;
wns900=wN900*170./1000000;

outfile[24][4]="_ResultsT24.dat"; outfile[24][1]="_RmstrippleT24.dat";
outfile[24][2]="_RmsetaT1T24.dat"; outfile[24][3]="_RmsT1T24.dat";

datain[24][1]=17./2.; // in Herz, Etaexp
datain[24][2]=10.3; //in seconds T16exp=
datain[24][3]=17.23; // T19exp=
datain[24][4]=10122.2; //Hdd
resname[24]="T24";

datain[8][1]=17.66259; // in Herz, Etaexp
datain[8][2]=4.65122; //in seconds T16exp=
datain[8][3]=5.36274; // T19exp=
datain[8][4]=10369;

datain[9][1]=0.59; // in Herz, Etaexp
datain[9][2]=34.49652; //in seconds T16exp=
datain[9][3]=49.35347; // T19exp=
datain[9][4]=10994;

```

```
/* input for all residues*/
```

```
datain[61][1]=6.515; // in Herz, Etaexp  
datain[61][2]=6.35323; //in seconds T16exp=  
datain[61][3]=7.61761; // T19exp=  
datain[61][4]=10521;
```

```
datain[62][1]=60.00259; // in Herz, Etaexp  
datain[62][2]=1.32981; //in seconds T16exp=  
datain[62][3]=1.90392; // T19exp=  
datain[62][4]=6513;
```

```
outfile[8][1]="_RmstripleL8.dat";  
outfile[9][1]="_RmstripleV9.dat";  
/*the same for all reidues*/
```

```
outfile[61][1]="_RmstripleL61.dat";  
outfile[62][1]="_RmstripleD62.dat";  
outfile[8][2]="_RmsetaT1L8.dat";  
outfile[9][2]="_RmsetaT1V9.dat";
```

```
/*the same for all reidues*/
```

```
outfile[61][2]="_RmsetaT1L61.dat";  
outfile[62][2]="_RmsetaT1D62.dat";
```

```
outfile[8][3]="_RmsT1L8.dat";  
outfile[9][3]="_RmsT1V9.dat";
```

```
/*the same for all reidues*/
```

```
outfile[61][3]="_RmsT1L61.dat";  
outfile[62][3]="_RmsT1D62.dat";
```

```
outfile[8][4]="_ResultsL8.dat";  
outfile[9][4]="_ResultsV9.dat";
```

```
/*the same for all reidues*/
```

```
outfile[61][4]="_ResultsL61.dat";  
outfile[62][4]="_ResultsD62.dat";
```

```
valid[1]=8;  
valid[2]=9;
```

```
/*the same for all reidues*/
```

```
valid[45]=61;  
valid[46]=62;
```

```
resname[8]="L8";  
resname[9]="V9";
```

```
/*the same for all reidues*/
```

```
resname[61]="L61";  
resname[62]="D62";  
}
```

## Appendix 2.6. Simulated results for motional parameters.

The results are obtained using grid searched presented in Appendix 2.5.

Experimental data:

ResName—residues name

S2genera—generalized order parameter, obtained from direct  $^{15}\text{N}$ - $^1\text{H}$  dipolar couplings measurements

T1600Ex— $T_1(\text{s})$  experimental data, obtained on 600 MHz instrument

EtaExp—differential transversal relaxation rate (Hz), obtained on 600 MHz instrument

T1900ex— $T_1(\text{s})$  experimental data, obtained on 900 MHz instrument

Simulated data:

S2slow—order parameter for slow motion.

ts1—correlation time of slow motion, ns.

tf1n - correlation time of fast motion, ns.

rmsTriple1—difference between experimental and calculated data, given by Equation 4.5.1

T16001 - calculated in grid search simulations  $T_1(\text{s})$  value for 600 MHz field.

eta1—differential transversal relaxation rate  $\eta$  (Hz), calculated in grid search simulations, for 600 MHz field.

T19001 - calculated in grid search simulations  $T_1(\text{s})$  value for 900 MHz field.

ResName	S2general	T1600Ex	etaExp	T1900ex	S2slow	ts1	tf1ns	rmsTriple1	T16001	eta1	T19001
L8	0.81617	4.65122	17.6626	5.36274	0.88037	152.8	2.02	0.01771	4.59975	17.6833	5.29038
V9	0.91752	34.4965	0.59	49.3535	0.96972	19	0.02	0.04594	35.5194	0.57046	50.0342
L10	0.92857	20.2459	0.615	23.9333	0.97277	22.4	0.14	0.02969	20.3528	0.61724	23.2588
A11	0.91419	28.5303	-2.475	18.4735	0.99839	0.8	0.08	1.0361	25.0817	0.01421	23.3129
Y13	0.91635	49.3183	1.16	41.395	0.99655	353.2	0.04	0.17986	54.1772	1.15904	49.0404
D14	0.85406	15.5703	0.44	19.3534	0.96226	12.2	0.04	0.00977	15.4825	0.4429	19.2679
Y15	0.92488	29.9036	0.49	37.5575	0.97708	21.6	0.06	0.07027	30.6088	0.49373	35.234
Q16	0.85052	15.3599	1.63	19.7283	0.93472	26.4	0.06	0.04833	15.7781	1.63672	18.9658

E17	0.92321	17.8645	2.8	32.2134	0.94741	47.8	9.42	0.06262	18.7688	2.79029	30.9788
S19	0.87122	11.0208	2.72	12.7447	0.92742	38.2	0.26	0.01063	10.9952	2.72059	12.6139
R21	0.89101	1.88915	2.5	1.87723	0.99521	492.6	2.04	0.67116	3.36301	2.49908	3.81801
T24	0.77775	10.3015	8.515	17.2329	0.78195	37.8	5.26	0.00178	10.314	8.50825	17.2151
M25	0.91685	30.423	0.415	32.8941	0.98105	22.4	0.06	0.0307	29.7666	0.41975	32.3117
K26	0.8948	30.6845	2.595	33.5922	0.951	54	0.06	0.02058	30.7445	2.57555	34.2452
K27	0.91219	16.217	0.19	22.5766	0.97239	6	0.02	0.05679	16.3543	0.18151	23.3723
G28	0.94849	27.7059	0.2	34.4753	0.98069	9.8	0.06	0.04744	26.6781	0.20149	35.4199
I30	0.90206	18.7838	2.8	28.0538	0.91026	30.4	0.3	0.00531	18.7062	2.80487	27.9747
L31	0.90471	24.9061	-0.165	47.7412	0.97291	0.2	0	1.14199	43.5659	0.00906	43.8492
T32	0.83883	5.83826	5.185	9.85698	0.94703	82	9.9	0.02014	5.92478	5.18791	9.72222
L33	0.9077	39.8111	-2.16	47.6689	0.9719	0.2	0	1.01423	41.8118	0.00944	42.0837
L34	0.91036	7.40778	22.565	11.0855	0.96656	684.6	5.08	0.00511	7.37307	22.5638	11.1076
S36	0.93717	10.2322	3.53	1.23309	0.99337	535.6	0.82	0.86355	9.22807	3.53006	8.60271
D40	0.93717	17.7238	2.915	12.5363	0.96937	94.6	0.72	0.21435	15.6678	2.92878	15.0935
W41	0.90438	16.4838	2.625	20.7573	0.92458	34.2	0.4	0.00193	16.4539	2.62571	20.7454
K43	0.93109	21.9489	2.875	25.5846	0.94329	49.2	1.04	0.01837	22.2321	2.86562	25.2605
V44	0.9353	14.1585	0.015	23.6864	0.9995	0.2	0.14	0.37913	21.8042	0.01636	21.2977
E45	0.83246	5.17612	10.64	7.56929	0.89666	103.8	4.38	0.0046	5.16119	10.6495	7.59563
V46	0.91836	23.9679	2.425	23.912	0.97856	116.2	0.12	0.0176	24.3605	2.42303	24.0816
R49	0.91485	18.5878	1.64	25.9293	0.93505	24.4	0.14	0.01711	18.6923	1.61616	26.1139
Q50	0.81963	6.07359	6.745	9.7956	0.88783	57.2	7.36	0.0015	6.07313	6.74208	9.78155
G51	0.89134	17.1215	0.875	29.7103	0.93954	14.4	0	0.02798	17.464	0.87121	29.1426
F52	0.91119	26.6415	6.705	39.1495	0.91939	81.2	3.9	0.02051	26.1796	6.73156	39.532
V53	0.938	45.3545	1.28	60.193	0.9622	33	0.04	0.03619	45.0501	1.26035	62.1875
A55	0.91402	27.5266	-0.32	41.0159	0.96622	0.2	0	1.07114	34.3387	0.01149	34.562
A56	0.90322	15.4367	1.715	20.4913	0.93142	24.8	0.18	0.00852	15.3632	1.72263	20.38
Y57	0.91919	11.7335	4.37	27.6949	0.96339	107.8	9.98	0.25022	14.5505	4.37469	23.9055
V58	0.93075	37.3262	-0.405	53.3433	0.97495	0.2	0	1.04963	45.8936	0.0086	46.1921
K59	0.92706	17.2747	1.3	34.1961	0.93126	18.6	0	0.1193	18.6712	1.33015	31.3727
L61	0.84027	6.35323	6.515	7.61761	0.88047	54.4	1.9	0.02026	6.30015	6.53639	7.48194
D62	0.32201	1.32981	60.0026	1.90392	0.44221	140	4.02	0.00344	1.32666	59.9656	1.90852

Tabellenbeschriftung 6.3.5



## *Summary.*

Understanding the mechanisms how biological systems work is an important objective of current structural biology. Nuclear magnetic resonance (NMR) spectroscopy is a well suited technique to approach these goals and to study structure and dynamics of biomolecules in order to obtain complimentary information for understanding functionality of proteins. Recently, rapid progress has been made in the field of biological solid state NMR (ssNMR), which resulted in complete structure elucidation of several peptides and small proteins, the characterization of protein complex formation and the characterization of dynamic properties of small proteins. Solid state NMR is the method of choice for structural and dynamic characterization of membrane proteins and aggregated amyloidogenic systems, which are poorly soluble and can not be easily studied by solution state NMR and X-ray spectroscopy. Modern solid state NMR is still limited in resolution and sensitivity, and requires developments in sample preparation and pulse sequence design.

In my thesis, I study the potential use of deuteration in protein solid state NMR for sensitivity, as well as for resolution enhancement in  $^{15}\text{N}$ - $^1\text{H}$  correlation experiments. Achieved progress in these fields allows to monitor backbone motion with high accuracy, which has not been available before. We show for the first time that TROSY type experiments can be beneficial for solid state NMR. In addition, a pulse sequence for  $^{13}\text{C}$ - $^{13}\text{C}$  J decoupling was developed to increase resolution in the carbon dimension.

Chapter 2 describes proton detected experiments of the  $^{15}\text{N}$  labeled protein  $\alpha$ -SH3 at different levels of deuteration. This sample preparation technique allows proton detection without homonuclear and heteronuclear decoupling at moderate spinning frequencies, resulting in ultrahigh resolution in both the  $^{15}\text{N}$  and  $^1\text{H}$  dimensions.

In Chapter 3, we employed ultrahigh resolution to analyze TROSY effects in ssNMR, which can be exploited to study dynamic effects in the solid state and to relate their influence on line width. These studies might have significant impact for the further improvement of resolution for solid state NMR investigations of large biomolecules.

The dynamics of the protein backbone are investigated by measurements of  $^{15}\text{N}$   $T_1$  and  $T_2$  in Chapter 4. Transversal relaxation measurements were introduced for the first time in ssNMR. These experiments allow to describe internal dynamics of a protein in the solid state, which are responsible for the functionality of biomolecules.

Another aspect of functionality and structure stability of proteins is their interactions with water molecules, which were studied in Chapter 5. The introduced experiments allow the site specific detection of water molecules in the solid state and the estimation of their mobility. This approach might be used to study water channels or water molecules in amyloid fibrils.

Chapter 6, shows the pulse sequence to decouple the  $^{13}\text{C}$ - $^{13}\text{C}$  homonuclear scalar couplings during stroboscopic detection. This technique can be successfully applied in order to increase the spectral resolution up to a factor of 2-2.5 and sensitivity up to a factor of 1.2. We expect that this approach will be useful for the study of larger biomolecular systems like membrane proteins and amyloidogenic peptides and proteins where spectral overlap is critical.

**Keywords:**

Solid state NMR spectroscopy, Linewidth, Perdeuteration, Dynamics of proteins

## *Zusammenfassung.*

Das Verständnis der Mechanismen, nach denen biologische Systeme ablaufen, ist ein wichtiger Fokus der aktuellen Strukturbilogie. Kernmagnetische Resonanzspektroskopie (NMR) ist eine geeignete Technik, um solche Ziele anzustreben sowie Struktur und Dynamik von Biomolekülen zu erforschen, um komplementäre Informationen zum Verständnis von Proteinfunktionalität zu erhalten. Rasante Fortschritte sind vor nicht langer Zeit auf dem Gebiet biologischer Festkörper-NMR (ssNMR) erzielt worden, was zu vollständiger Strukturaufklärung zahlreicher Peptide und kleiner Proteine, der Beschreibung von Protein-Komplexbildung sowie der dynamischen Eigenschaften kleiner Proteine geführt hat. Festkörper-NMR ist die Methode der Wahl bei struktureller und dynamischer Charakterisierung von Membranproteinen und aggregierten amyloidogenen Systemen, die schwer löslich und kaum mit Lösungs-NMR oder Röntgenkristallographie zugänglich sind. Moderne Festkörper-NMR ist noch immer limitiert, was Auflösung und Empfindlichkeit betrifft, und macht weitere Entwicklungen auf den Gebieten der Probenpräparation und des Pulssequenz-Designs erforderlich.

In meiner Arbeit untersuche ich die potenzielle Verwendung von Deuterierung in der Protein Festkörper-NMR zur Erhöhung von Empfindlichkeit und Auflösung in  $^{15}\text{N}$ - $^1\text{H}$  Korrelationsexperimenten. Der erzielte Fortschritt auf diesen Gebieten erlaubt die Verfolgung von Proteinrückgratbewegungen mit hoher Genauigkeit, die vorher nicht verfügbar war. Wir zeigen zum ersten Mal, dass TROSY Experimente für Festkörper-NMR gewinnbringend sind. Außerdem wurde eine Pulssequenz für  $^{13}\text{C}$ - $^{13}\text{C}$  J Kopplung zur Erhöhung der Auflösung in der Kohlenstoff-Dimension entwickelt.

Kapitel 2 beschreibt protonendetektierte Experimente am  $^{15}\text{N}$  markiertem Protein  $\alpha$ -SH3 bei unterschiedlichem Deuterierungsgrad. Diese Technik der Probenpräparation erlaubt Detektion von Protonen mit homonuklearer und heteronuklearer Entkopplung bei moderaten spinning-Frequenzen, was zur ultrahohen Auflösung sowohl in der  $^{15}\text{N}$ -Dimension als auch in der  $^1\text{H}$ -Dimension führt.

In Kapitel 3 nutzten wir die ultrahohe Auflösung zur Analyse von TROSY Effekten in der ssNMR, welche dazu genutzt werden können, um dynamische Effekte im



festen Zustand zu untersuchen und ihren Einfluss mit der Linienbreite in Beziehung zu setzen. Diese Studien könnten signifikanten Einfluss auf zukünftige Verbesserungen der Auflösung für Festkörper-NMR an großen Biomolekülen haben.

Die Dynamik des Proteinrückgrates wird über Messung der  $^{15}\text{N}$   $T_1$  und  $T_2$  Zeiten in Kapitel 4 ergründet. Messung transversale Relaxation wurde zum ersten Mal in der ssNMR einbezogen. Diese Experimente erlauben eine Beschreibung der inneren Dynamik eines Proteins im festen Zustand, welche für die Funktionalität von Biomolekülen verantwortlich ist.

Ein anderer Aspekt von Funktionalität und struktureller Stabilität von Proteinen ist ihre Wechselwirkung mit Wassermolekülen, was im Kapitel 5 untersucht wird. Die eingeführten Experimente erlauben die ortsspezifische Detektion von Wassermolekülen im festen Zustand und die Erfassung ihrer Mobilität. Dieser Ansatz könnte genutzt werden, um Wasserkanäle oder Wassermoleküle in amyloiden Fibrillen zu untersuchen.

Kapitel 6 zeigt die Pulssequenzen zur Entkopplung von  $^{13}\text{C}$ - $^{13}\text{C}$  homonuklearen skalaren Kopplungen während stroboskopischer Detektion. Diese Technik kann erfolgreich eingesetzt werden, um die spektrale Auflösung um bis zu 2-2.5 fach und die Empfindlichkeit um bis zu 1.2 fach zu erhöhen. Wir erwarten, dass dieser Ansatz nützlich für Studien an größeren biomolekularen Systemen wie Membranproteinen und amyloidogenen Peptiden und Proteinen sein wird, bei denen spektraler Überlapp kritisch ist.

**Schlagwörter:**

Festkörper-NMR-Spektroskopie, Linienbreite, Perdeuterierung, Dynamik von Proteinen